SCUOLA DI DOTTORATO
UNIVERSITÀ DEGLI STUDI DI MILANO-BICOCCA

Department of Physics

PhD program Physics and Astronomy Cycle XXIX

Curriculum in (se presente / if it is)

Prompt photon emission- A novel approach towards highest time resolution with scintillators

Surname Martinez Turtos Name Rosana

Registration number 787919

Tutor: Marco Paganoni

Co-tutor: Alessio Ghezzi

Supervisor: Paul Lecoq

Coordinatore / Coordinator: Giberto Chirico and Marta Calvi

ACADEMIC YEAR 2017

PROMPT PHOTON EMISSION-
A NOVEL APPROACH TOWARDS HIGHEST TIME RESOLUTION WITH SCINTILLATORS

Dissertation

Rosana Martinez Turtos

Università degli Studi di Milano Bicocca

Rosana Martinez Turtos

PROMPT PHOTON EMISSION-

A NOVEL APPROACH TOWARDS HIGHEST TIME RESOLUTION WITH SCINTILLATORS

Submitted for the degree of Doctor of Physics and Astronomy

January 16^{th}, 2017

Summary

Generating a prompt response to the passage of ionizing particles has emerged as a critical requirement for next-generation scintillator-based radiation detectors in high energy physics (HEP) and time-of-flight positron emission tomography (TOF-PET). State-of-the-art time resolution values are of the order of 100 ps FWHM for 511 keV gamma excitation, single channel readout and 160 ps for multichannel HEP calorimeters. Going down to sub-20 ps coincidence time resolution (CTR) implies a major technological challenge that could be overcome by increasing photostatistic, reducing rise and decay-time or using an intense prompt signal as a time tag in the readout chain.

The first part of this thesis will focus on the impact of the scintillating crystal optical signal as the key factor to reduce timing. The main parameters, i.e. light yield ($\propto$ to the number of detected photoelectrons N_{pe}), rise- and decay-time (τ_r, τ_d) will be put into perspective in order to know their present contribution to the CTR and therefore, find ways to improve their current values. In the second part of the manuscript, we identify and characterize a new class of Auger suppressed semiconductor nanocrytals (NCs) with enhanced timing characteristics under ionizing radiation.

The implementation of nanocrystal-based scintillators as a new generation of ultrafast particle detectors is explored using two main lines: (1) nanocrystals as part of a heterostructure and (2) nanocomposites, where the NCs are embedded in a host matrix. In conclusion, the present contribution proposes a feasible way to overcome the technological challenge that sub-20 ps time resolution implies.

to my friend
James K. Jordan (1922-2003)

It is our responsability as scientists,
knowing the great progress which comes
from a satisfactory philosophy of ignorance,
the great progress which is the fruit of freedom of thought,
to proclaim the value of this freedom;
to teach how doubt is not to be feared but welcomed and discussed;
and to demand this freedom as our duty to all coming generations.

Richard Feynman,
on The Value of Science, 1955.

Abstract

Generating a prompt response to the passage of ionizing particles has emerged as a critical requirement for next-generation scintillator-based radiation detectors in high energy physics (HEP) and time-of-flight positron emission tomography (TOF-PET). In the search for rare events in the future high luminosity colliders (like HL-LHC, FLC), event discrimination by vertex identification will require a sub-20 ps time resolution due to considerable pileup of particle bunches (in HL-LHC for instance: 140 interactions per beam crossing). Similarly, precise time tagging of 511 keV gamma rays is needed in TOF-PET in order to confine the e^+-e^--annihilation point along the line of response (LOR) to the level of a few millimeters. Only then the time consuming, iterative, or back projection algorithms could be replaced by a fast and direct, "real time", image reconstruction, benefiting from more than a ten-fold increase in sensitivity.

State-of the-art time resolution values are of the order of 160 ps for multichannel HEP calorimeters and 500-600 ps in commercial TOF-PET scanners. The best value obtained in an integrated system is 316 ps by the Philips Vereos machine which employs digital silicon photomultipliers (SiPMs) instead of analog technology. Under optimized laboratory conditions, on the other hand, 10 mm long cerium-doped $(Lu_{1-x}Y_x)_2SiO_5$ crystals with nanosecond photon emission rates, coupled to modern solid state photodetectors (e.g. FBK analog silicon photomultipliers, SiPMs) and fast front-end electronics, deliver coincidence time resolution (CTR) of 117 ps FWHM for 511 keV gamma excitation and 60 ps for minimum ionizing particles with a dE/dx $\sim$ 1 MeV/mm. A different approach, using digital SiPMs and $22 \times 32 \times 32$ mm^3 bulk LYSO together with maximum-likelihood techniques to estimate the time of interaction, reaches CTR values of 147 ps under 511 keV for dual-side-readout and 215 ps for single-side-readout. Exploiting the Cherenkov prompt emission has lead to CTR values of 270 ps using $2 \times 2 \times 3$ mm^3 BGO crystals (τ_d=300 ns).

Going down to sub-20 ps time resolution implies a major technological challenge that could be overcome by increasing photostatistic, reducing rise and decay times or using an intense prompt signal as a time tag in the readout chain. Assuming Poisson statistic of the photon emission process and in the case of $\tau_d \gg \tau_r * N_{pe}$, where N_{pe} is the number of detected photoelectrons, the CTR can be simplified as $CTR \propto \sqrt{(\tau_r \tau_d / N_{pe})}$. Hence, the photoelectron density of the scintillating emission would need to be increased by two orders of magnitude if a CTR of O(10)ps was to be reached. On the other hand, if a prompt photon emission along with the scintillating signal will be available, one would require between 500-1000 photons and an advancement in the single photon time resolution of modern solid-state photodetectors from 50 to 10 ps to obtain a CTR of 10 ps.

The first part of this thesis will focus on the impact of the scintillating crystal optical signal as the key factor to reduce timing. The main parameters, i.e. light yield ($\propto N_{pe}$), rise- and decay-time (τ_r, τ_d) will be put into perspective in order to know their present contribution to the CTR and therefore, find ways to improve their actual values. In the second part of the manuscript, we characterize a new class of Auger suppressed semiconductor nanocrystals with enhanced timing characteristics due to a giant oscillator strength transition.

The study starts with the validation of the simulation framework used to track optical photons inside and outside the scintillating crystals. Simulations are used to (1) estimate the light transfer efficiency of 20 mm long LYSO crystals with different coupling configurations, (2) to calculate the light extraction maximum gain obtained by shaping the readout face of cuboid scintillating crystals and (3) to evaluate the potential of a new highly pixelated PET module for higher spatial resolution and DOI encoding information.

To the simulation studies follows the quantification of the LYSO intrinsic light yield, which sets a limit to the value that N_{pe} could theoretically reach using state-of-the-art photodetectors. The results are 40'000 $\pm$ 3% (stat) $\pm$ 9% (syst) ph/MeV, which indicate that around 50% of the photons are lost in a 20 mm long crystal. This corresponds to a factor of 0.7 in CTR improvement if all the light produced will be extracted, which is unable to provide an order of magnitude leap in the time resolution. In this way, the identification of potential materials for prompt photon emission is carried out by looking into Auger suppressed nanocrystals (NCs).

Three different classes of colloidal nanocrystals were investigated: two-dimensional CdSe nanoplatelets (NPLs), spherical CdSe/CdS core/giant shell quantum dots (GS QDs) and two-dimensional core/shell CdSe/ZnS nanoplatelets. We demonstrated that the emission rates of the first two NCs under pulsed X-ray excitation are much faster than traditional mechanisms in bulk scintillators, i.e. 5d-4f transitions. CdSe NPLs have a sub-100 ps effective decay time of 77 ps and CdSe/CdS GS QDs exhibit a sub-ns value of 849 ps. Further, the respective CdSe NPL and CdSe/CdS GS QD X-ray excited photoluminescence have the emission characteristics of excitons (X) and multiexcitons (MX), with the MXs providing additional prospects for fast timing with substantially shorter lifetimes. Inferred light yield values for these two materials are in the order of 10^3 and 10^4 ph/MeV for NPLs and GS QDs, respectively. This feature defines them as a potential material class to generate a prompt photo-response at the level of CTR $\sim$ O(10)ps. The different multiexcitonic dynamics seen for both types of NCs under ionizing excitation, makes CdSe NPL the best performing material due to its red-shifted MX population. The study using CdSe/ZnS core shell NPLs showed spectral and timing deteriorated properties along the timeline of this thesis.

The implementation of nanocrystal-based scintillators as a new generation of ultrafast particle detectors was explored using two main lines: (1) nanocrystals as part of a heterostructure and (2) nanocomposites, where the nanocrystals are embedded in a matrix host. In the first approach, CdSe NPLs and GS QDs films were deposited on the surfaces of LSO:Ce and LuAG:Ce, respectively. The study confirmed the simultaneous emission from both scintillating systems with the presence of an additional longer decay component due to absorption of the bulk scintillator light by the NC film. In both cases, the secondary excitation by the bulk scintillator and the intrinsic longer lifetime components of the NCs can be reduced by isolating the fast MX emission via spectral filtering. Simulations were performed to test the efficiency of a sampled crystal using a LYSO+CdSe NPLs heterostructure, yielding layers of maximum 200 μm thickness. The timing performance of a ZnO:Ga nanopowder-based composite was tested for a sample where the NCs are embedded in a polystyrene matrix. The decay time measured is of the order of 500 ps. CTR measurements using 511 keV excitation present a FWHM of 200 $\pm$ 30 ps for events with maximum energy deposition and 30 detected photoelectrons. An efficiency and transparency boost when placing nanopowders in a denser host still constitutes the main challenge in order to benefit from sub-nanosecond recombination times.

In conclusion, the present thesis proposes a feasible way to overcome the technological challenge that sub-20 ps time resolution implies. We demonstrate the large development potential of NC technology and justify the rigorous research in this field to make NCs a viable option for superfast timing in domains such as HEP and medical imaging.

Acknowledgments

I am especially grateful for have been given the opportunity of obtaining my PhD education in the framework of a multidisciplinary and welcoming research program. The professional and socially integrating environment created by the PicoSEC MC-NET [1] fellowship in collaboration with Milano-Bicocca university has built an excellent network to develop and advance state-of-the-art research. Therefore, I would like in first place to thanks the people who setup the network and made possible my participation in such a nice project. In particular, I would like to thanks Dr. Etiennette Auffray and Dr. Marco Paganoni for their kindness and collaborative spirit, trying always their best to make things happen. A special acknowledgment goes to Dr. Paul Lecoq for his everlasting determination and energetic guidance.

To both groups from Milano and CERN, I say thanks for their support and cooperation along the last four years, especially the Italian team, in which I identify many features from my home culture. It has been a pleasure to see them share life and food as a very big family. I especially thanks Marco Pizzichemi for contacting me to be part of the group and Alessio Guezzi for his lessons and his contagious laugh.

This thesis is largely influenced by the work of my colleague Dr. Stefan Gundacker. I thanks him for the scientific method, the experimental precision and his sourdough bread. The discussions with him have also contributed to my work in a team formation and I am very much thankful for his company.

I am also very grateful for all the help I got from part of Dr. Thomas Meyer in the writing of the research proposal preceding the submission of this thesis. His patience and hard working has largely contributed to the clearness and methodology followed in the present manuscript.

Furthermore, I would like to thanks Kristof Pauwels, Marco Lucchini, Matteo Salomoni, Dominique Deyrail, Rosalinde Pots and Gianluca Stringhini for the everyday help. I specially thanks to my ex-PicoSEC fellows Myhtra Varun Nemallapudi for the mind-blowing conversations, to Farah Ben Mimuon Bel Hadj and Pawel Modrzynski, Liu Zheng and Rita Giufredi for the colorful picture, the different points of view and the music.

[1] Pico-second Silicon photomultiplier-Electronics & Crystal research Marie Curie Innovative Training Network, `http://picosec.web.cern.ch`.

In addition, I would like to mention collaborators as Joel Grim, Sergey Omelkov and Lenka Prochàzkovà that came to the lab in the frame of the STSMs[2] program of the FAST [3] Cost Action. Working with them has lead to a good part of the experimental results so I am thankful for their cooperation and for the visiting opportunity provided by the FAST Cost Action.

At last, I would like to thanks mom and dad for their unconditional support to my education. It has been incredibly easy for me just to look up to them and take my own decisions. I thanks sister for her infinite friendship and husband for the everyday happiness and the technical support. They also read the entire thesis and help me in the edition process.

I dedicate this thesis to a family friend which contributed to my life in many ways. James K. Jordan was a black man born in USA in the nineteen twenties. He earned his right to education only after coming back from piloting planes in the Viet-Nam war, finishing his degree in Philosophy in 1960 when he was almost 40. After many years, his economic situation allowed him to travel to Cuba and help many families, including mine. He died from prostatic cancer after more than 80 years of an incredible and inspiring life.

To my fellows, family and friends a big thanks for their support and encouragement along the transatlantic journey.

Rosana Martinez Turtos

[2]Short Term Scientific Mission
[3]Fast Advanced Scintillator Timing

Contents

Introduction

State-of-the-art and Motivation

Over the last few decades, radiation detector research has largely been directed towards the discovery and development of scintillators with improved energy resolution via increased light yield and better proportionality [1, 2, 3]. More recently, generating a 'prompt' response to the passage of ionizing particles has emerged as a critical requirement for next-generation radiation detectors, notably in high energy physics (HEP) and time-of-flight positron emission tomography (TOF-PET) applications. In the search for rare events in the planned high luminosity large hadron collider at CERN[4] (HL-LHC), for example, event discrimination would require a sub-20 ps time resolution to mitigate the problem of particle bunch pileup [4]. Similarly, precise time tagging of 511 keV γ-rays is needed in TOF-PET in order to confine the e^+-e^--annihilation point along the line of response (LOR) to the level of a few millimeters [5], [6].

Current state-of-the-art time resolution values in large multichannel HEP detectors as the CMS[5] electromagnetic calorimeter (ECAL) are of the order of 160 ps[6] for channels belonging to the same electronic readout unit and around 300 ps for channels sharing different units [4]. In the low energy regime of 511 keV, state-of-the-art is of the order of 500-600 ps in commercial TOF-PET scanners [7]. However, the best value of 316 ps is reached by the Philips Vereos machine using digital silicon photomultipliers instead of analog technology. Under optimized laboratory conditions, on the other hand, 10 mm long cerium-doped Lu_2YSiO_5 crystals with nanosecond photon emission rates, coupled to modern solid state photodetectors (e.g. FBK analog silicon photomultipliers, SiPMs) and fast frontend electronics, deliver coincidence time resolution (CTR) of 117 ps for 511 keV gammas [8]. If instead the same scintillator was used for the detection of minimum ionizing particles (MIPs with $dE/dx \sim 1$ MeV/mm), the resolution improves to 60 ps with single-channel readout [9]. A different approach, using digital SiPMs and $22 \times 32 \times 32$ mm^3 bulk LYSO together with maximum-likelihood techniques to estimate the time of interaction, reaches CTR values of 147 ps under 511 keV for dual-side-readout [10] and 215 ps for single-side-readout [11].

[4] European Organization for Nuclear Research
[5] Compact Muon Solenoid
[6] All values are expressed in full-width-half-maximum (FWHM).

Such precision of 100 ps CTR corresponds to 15 mm spatial confinement along the line of response (LOR) of PET scanners, which allows to discriminate between organs under examination, e.g. prostate, pancreas or lymph nodes, and the background generated by other, marker-attracting organs such as, e.g., the heart or the bladder [6]. Despite being a significant improvement over standard TOF-PET cameras, this precision is still not sufficient to allow a direct 3D image of a PET image without reconstruction. To ultimately reach the level of true space points, i.e. not only in the traditional x-y coordinates in the plane of the detection pixels but also in z (along the LOR), calls for a CTR improvement as high as 10 ps, equivalent to 1.5 mm along the LOR. Only then the time consuming, iterative, or back projection algorithms could be replaced by a fast and direct, "real time", image reconstruction, benefiting from a minimum ten-fold increase in sensitivity.

An advancement from present state-of-the-art to O(10)ps CTR, however, entails a major technological challenge beyond conventional photon spectroscopy with its inherent scintillation mechanisms. Even a fast crystal brand, like LSO:Ce co-doped with 0.4% Ca^{2+}, with novel elementary stoichiometry and lowest emission rise- and decay-time (τ_r=20 ps, τ_{d-eff}=30 ns) is still far from reaching the 10-20 ps time domain. Single channel readout for this crystal presents CTR values in the order of 100 ps under 511 keV gamma excitation for 10 mm length and 34 ps under MIPs for 5 mm [8, 9].

Assuming Poisson statistic of the photon emission process and in the case of $\tau_d \gg \tau_r * N_{pe}$ [12], where N_{pe} is the number of detected photoelectrons, the CTR can be simplified to,

$$CTR = 2.36 * \sqrt{\frac{\tau_r \times \tau_d}{N_{pe}}} \tag{1}$$

This estimation only includes the scintillation statistics and does not take into account the photon travel spread in the crystal (PTS) and the single photon time resolution (SPTR) of photodetectors. If we assume PTS and SPTR remain constant, the photoelectron time density of the scintillating emission would need to be increased by two orders of magnitude if a CTR of O(10)ps is to be reached. This statement holds true when using state-of-the-art solid state photodetectors with an improved photon detection efficiency ($\sim$ 50%) and single photon time resolution ($\sim$ 60 ps). On the other hand, if a prompt photon emission along with the scintillating signal will be available it would be used as time tag in the readout chain. This method would require between 500-1000 photons and an advancement in the single photon time resolution of modern solid-state photodetectors from 50 to 10 ps to obtain a CTR of 10 ps.

The first part of this thesis will focus on the impact of the scintillating crystal optical signal as the key factor to reduce timing. The main parameters, i.e. light yield ($\propto N_{pe}$), rise- and decay-time (τ_r, τ_d) will be put into perspective in order to know their present contribution to the CTR and therefore, find ways to improve their actual values. In the second part of the manuscript the characterization of a new class of materials with unparalleled energy conversion efficiency will be presented. These materials already known for their sub-nanosecond

photoluminescence response due to a collective phasing of dipoles over many unit cells which permits a giant oscillator strength transition (GOST) [13, 14, 15], allows for enhanced timing characteristics which are rarely seen in bulk scintillators at room temperature. In this thesis, they will be proven to be a proliferating source of prompt photons under ionizing radiation.

So called nanocrystals (NCs), i.e. semiconductors grown at the nano-scale ($\lesssim$ 100 nm) with a size-dependent band-gap structure, are capable of solving many of the challenges in the current R&D of scintillating detectors. Their tunable optoelectronic properties, combined with recent advances in controlling their size, shape, heterostructure and surface chemistry, have enabled their use in a wide range of photonic applications, such as low-threshold lasing [15, 16, 17], photovoltaic cells [18] and single photon sources for quantum information [19, 20]. Their high quantum yields and ultrafast recombination time at the sub-nanosecond level have already generated interest in their use as low-cost, high-performance scintillators for radiation detection [21, 22, 23]. Earlier high energy excitation studies have identified several important issues and deficiencies that degrade the light emitting properties of NCs, predominantly photo-instability [24], losses due to the re-absorption of emitted light [25] and their intrinsic drawback, non-radiative Auger recombination [26]. However, significant progress has been made to overcome these barriers and to advance this technology for applications outlined above. Auger recombination, for example, has been considerably suppressed with the appearance of 2D-nanoplatelets [15] and heterostructured core/shell quantum dots [27]. Further improvements were made by embedding ZnO:Ga nanoparticles in a host material leading to a mechanically stable and efficient synthesis of composites using dry nanopowders [23]. This opens a new research line dedicated to energy transfer mechanisms between a host matrix and localized nano-emitters and allow to measure the coincidence timing response of this new nano-materials under gamma excitation.

Structure

The present manuscript is organized in the following way:

Chapter 1, the theoretical background is introduced starting with the description of conventional inorganic scintillators and basic radiative transitions allowed in these materials. The main parameters that characterize the scintillating pulse are described together with the scintillator's main applications. A review of fast recombination processes is presented with a short discussion of their light yield and potential usability in radiation detection.

Chapter 2 introduces nanocrystals are introduced as a new ultrafast scintillator. Quantum confinement, carrier multiplication and photoionization effects under optical excitation will be presented in order to understand the multiexcitonic dynamics exhibited by these systems under ionizing radiation. Special attention is given to nanocrystals that show a severe reduction of Auger recombination either by designing core/shell heterostructures or by engineering the dimensions of confinement.

Chapter 3 discusses the validation of the Monte Carlo code used to transport and track optical photons along the scintillator. These studies will be concluded in a through experimental validation with light output measurements. Once the simulations are proven to effectively reproduce the measurements using different coupling/wrapping conditions, the code will be used in the study of three particular cases. First, the intrinsic light yield of LYSO crystals is estimated using dry and grease coupling. Another section is dedicated to geometrically modified crystals, which are calculated to bring some gain in light extraction. Finally, the study of light sharing in crystal matrices to increase the spatial resolution of PET systems and to provide DOI information is presented.

Chapter 4, the experimental results using a setup designed to measure the intrinsic light yield of LYSO crystals will be showed. Knowledge of this quantity brings information regarding the limits faced by increasing photostatistic to its maximum value. The idea consists in confining light in a determined point in space by electron excitation and extracting this light in a well defined cone allowing for a purely geometric correction factor. A discussion regarding how to reduce the systematic uncertainties is done for general use of this bench.

Chapter 5 presents a full description of spectral-time resolved single photon counting system used to characterize the rise- and decay-time of scintillating materials. The experimental bench uses a pulsed picosecond X-ray tube as excitation source, which allows to resolve the first nanoseconds of the scintillation pulse. The intrinsic time resolution of the system is around 18 ps FWHM measured under femtosecond laser excitation and the impulse response function (IRF) is between 60-134 ps FWHM for X-ray irradiation. The rise time of several lutetium based scintillating crystals, with and without Ca^{2+} co-doping, was subjected to study under X-ray pulsed excitation. Time-resolved photoluminescence was carried out in order to determine the decay time of different scintillating systems.

Chapter 6 presents the characterization of different types of nanocrystals as a potential source of prompt photons for the development of ultrafast radiation detectors. They are CdSe nanoplatelets (NPLs), CdSe nanoplatelets with a ZnS shell and CdSe quantum dots with CdS giant shell. As first, their photoluminescence properties will be measured using a 372 nm picosecond laser excitation, followed by pulsed X-ray excitation. Effective decay times measured are of the order of sub-100 ps for CdSe NPLs and sub-1 ns for CdSe/CdS giant shells quantum dots under ionizing radiation. In order to optimize timing and efficiency performance, the same materials are coupled to silver nanoparticles with a plasmon resonance that matches the nanocrystal emission. Characterization of this plasmonic layers is done using laser excitation.

Chapter 7 presents the implementation of nanocrystals as a new particle detector. Two main lines of research will be presented: (1) nanocrystals as part of a heterostructure and (2) nanocrystals fabricated as a composite. At first, a dry deposition of colloidal nanocrystals is done on one of the faces of a conventional scintillator. The time resolved emission spectrum under pulsed X-ray excitation is measured and the light yield estimated via Geant4

simulations taking into account the energy deposition. The second approach presents ZnO:Ga nanopowder embedded in different hosts and measured in coincidence under gamma and minimum ionizing excitation

At the end, the manuscript concludes with a general discussion of the main results. Future lines of research to complement and follow-up the work developed during the present thesis are included as part of the Perspectives section.

In short, this thesis starts with the validation of the simulation framework used to track optical photons inside and outside the scintillating crystals. To the simulation studies follows the quantification of the LYSO intrinsic light yield, which sets a limit to the value that N_{pe} could theoretically reach using state-of-the-art photodetectors. At the end, the manuscript finishes with the characterization of new scintillating semiconductors and the implementation of nanocrystal-based scintillators as a new particle detector.

The present research has been develop in the frame of the PicoSEC[7] fellowship (2014-2016) and the network setup by FAST[8] Cost Action (2016-2017) and Crystal Clear Collaboration.

[7] Pico-second Silicon photomultiplier-Electronics & Crystal research Marie Curie Innovative Training Network, `http://picosec.web.cern.ch`.

[8] Fast Advanced Scintillator Timing

Chapter 1

Inorganic Scintillating crystals

1.1 Definition

Scintillation is defined as the emission of electromagnetic radiation, usually in the visible or UV range, as a result of the passage of ionizing radiation through a medium [28]. This could let to a misunderstanding with the Cherenkov effect but the nature of the radiative transition behind the emission is intrinsically different. The spontaneous recombination of an electron and a hole occupying two different states in the energy bands of a material leads to the emission of a photon in the visible or UV range. If the aforementioned electron-holes pairs are created as a consequence of the thermalization process of "hot" electrons coming from the interaction of high energetic particles with matter, then the consequent electromagnetic emission is known as scintillating light. This property is not exclusive of inorganic crystals, since it can also be found in liquid and plastic scintillators, however for the purpose of maximizing detection efficiency in a small volume and stopping power of high energetic particles we will focus on inorganic materials along this manuscript.

The term crystal refers to the definition used in solid state physics related to the periodic organization of the atoms in specific sites of the lattice, where a periodical potential can be used to describe the behavior of electrons bound to the lattice and carriers in general. The crystalline arrangement of the atoms along specific directions brings the possibility of calculating the energy bands that electrons and holes are allowed to occupy. In this way, we are dealing with light emission processes coming as a result of excitation which "travels" in a periodic and symmetric system. In general, electrons bound to the lattice can be described using Bloch functions, which state that every electron-like particle which can be modeled as a single particle wave function $\psi(\vec{r})$ finds its stationary state solutions in the form of a plane wave with wave-vector $\vec{k}$ multiplied by a periodic function $u(\vec{r})$ having $\vec{R_0}$ as a vector in the

Bravais lattice[1]:

$$\psi_{n\vec{k}}(\vec{r}) = e^{i\vec{k}\cdot\vec{r}} u_{n\vec{k}}(\vec{r}) \quad where, \quad u_{n\vec{k}}(\vec{r}+\vec{R_0}) = u_{n\vec{k}}(\vec{r}) \tag{1.1}$$

The periodic function $u_{n\vec{k}}$ is known as the envelope function. The name derives from the deduction that physical properties can be derived from the slowly varying envelope function, identified here as $u_{n\vec{k}}(\vec{r})$, rather than the total wavefunction. The validity of the envelope function approximation is still an active area of research and can be thought of as an approximation on the material and not the quantum mechanics.

Crystalline solids are also characterized by a non-continuous electronic energy distribution with a band gap $E_g \gg kT$ separating a filled valence electronic band from higher energy and generally not populated levels forming the conduction band. The width of the band gap between valence and the conduction band determines whether the material is a semiconductor ($<$ 2-3 eV) or an insulator ($>$3 eV).

The crystalline structure of a scintillator gives rise to very interesting properties which will be reviewed and discussed in the following sections. At first, the crystalline structure of scintillating inorganic materials will be described, together with highlighted concepts of band theory. Second, we will review the main macroscopic observables used to characterize them. At the end, we dedicate a separate section to fast radiative transitions and time-of-flight applications.

1.2 Crystalline structure and band theory

Introducing the many-particle Schrödinger equation with operator $\hat{p} = -i\hbar\nabla$ as the momentum components allows for the determination of the energies of the system:

$$H(\hat{p}; \vec{r_1}, \vec{r_2}..., \vec{r_n}; \vec{R_1}, \vec{R_2}..., \vec{R_n}; t)\Psi = -\frac{\hbar}{i}\frac{\partial\Psi}{\partial t} \tag{1.2}$$

Here, $\vec{r_n}$ and $\vec{R_n}$ are the vector position for electrons and ions, respectively. The wavefunction can normally be factorized as:

$$\Psi(\vec{r_1}, \vec{r_2}..., \vec{r_n}; \vec{R_1}, \vec{R_2}..., \vec{R_n}; t) = \psi(\vec{r}, \vec{R})\phi(\vec{R})\varphi(t), \tag{1.3}$$

where $\phi(\vec{R})$ is the wavefunction for all the ions and $\psi(\vec{r}, \vec{R})$ is the wavefunction for all the electrons dependent on the ionic position. The difference of mass between electrons and ions for most semiconductors is at least a factor of 1.8×10^3. Therefore, the electrons can move 100 times faster than the ions which allows for the previous approximation where the electrons can be regarded as instantaneously adjusting their motion with respect to the ions.

[1] Defined as the lattice obtained by applying a set of discrete translations operations, i.e. linear combinations using the primitive cell vectors.

Dividing the electrons into core and valence electrons (leaving out magnetic effects) [29] leads to the following expression for the time-independent crystal Hamiltonian:,

$$H = \sum_l \frac{\vec{p}_l^2}{2M_l} + \sum_{l,m} U(\vec{R}_l - \vec{R}_m) + \sum_i \frac{\vec{p}_i^2}{2m_i} + \sum_{i,l} V(\vec{r}_i - \vec{R}_l) + \sum_{i,j} \frac{e^2}{4\pi\epsilon_0 |\vec{r}_i - \vec{r}_j|}, \tag{1.4}$$

where l and m label the ions, i and j label the electrons, $\vec{p}$ is the momentum, M is the ionic mass, m is the mass of the electrons, $U(\vec{R}_l - \vec{R}_m)$ is the inter-ionic potential and $V(\vec{r}_i - \vec{R}_l)$ is the valence-electron-ion potential. Substituting equation 1.3 in equation 1.2, we have

$$\frac{H\psi(\vec{r},\vec{R})\phi(\vec{R})}{\psi(\vec{r},\vec{R})\phi(\vec{R})} = -\frac{\hbar}{i}\frac{\partial\varphi/\partial t}{\varphi} \tag{1.5}$$

The left-hand side depends only on the coordinates. Meanwhile, the right-hand side is only time dependent, so that each side is equal to one and the same constant. We shall denote it by E as it is dimensionally an energy. The time-dependent part of the previous equation is:

$$\frac{\partial\varphi/\partial t}{\varphi} = -\frac{i}{\hbar}E \tag{1.6}$$

whence

$$\varphi(t) = Ae^{-iEt/\hbar} \tag{1.7}$$

In this way we have separated spatial and time dependencies and the wavefunction can be written in the form of stationary equations:

$$\Psi(\vec{r},\vec{R};t) = \sum_{j,l} c_j\psi_j(\vec{r},\vec{R})\phi_l(\vec{R}) \cdot e^{\frac{-iE_jt}{\hbar}} \tag{1.8}$$

Writing the previous equation as the solution of a general class of problems assumes that the set of functions ψ_n are orthonormal and that they form a complete set. The time-independent Schrödinger equation for $\psi(\vec{r},\vec{R})$ and $\phi(\vec{R})$ can be written isolating the ionic and electronic contribution by introducing a mixed term given by H':

$$\psi(\vec{r},\vec{R})H_L\phi(\vec{R}) + \phi(\vec{R})H_e\psi(\vec{r},\vec{R}) + H'\psi(\vec{r},\vec{R})\phi(\vec{R}) = E\Psi(\vec{r},\vec{R},t) \tag{1.9}$$

where,

$$H'\psi(\vec{r},\vec{R})\phi(\vec{R}) = H_L\psi(\vec{r},\vec{R})\phi(\vec{R}) - \psi(\vec{r},\vec{R})H_L\phi(\vec{R}) \tag{1.10}$$

The relative contribution of H' is of the order of m/M_l. The adiabatic approximation allows to neglect this term. In this case equation 1.9 splits into a purely ionic and electronic equation.

$$H_L\phi(\vec{R}) = E_L\phi(\vec{R}) \qquad H_e\psi(\vec{r},\vec{R}) = E_e\psi(\vec{r},\vec{R}) \tag{1.11}$$

where,

$$H_e = \frac{\vec{p}_i^2}{2m_i} + \sum_{i,l} V(\vec{r}_i - \vec{R}_l) + \sum_{i,j} \frac{e^2}{4\pi\epsilon_0|\vec{r}_i - \vec{r}_j|} \tag{1.12}$$

In this way, the solution for the wavefunction of the free electron at a position $\vec{r}$ with zero electromagnetic potential, i.e. $\vec{V}(\vec{r}) = 0$, is as follows:

$$\Psi(\vec{r}, t) = e^{i(\vec{k}\cdot\vec{r} - \frac{Et}{\hbar})} \tag{1.13}$$

with the energy eigenvalue (in this case it is just the kinetic energy) given by:

$$E = \frac{\hbar^2 k^2}{2m} \tag{1.14}$$

This solution can be considered as a very simplistic solution for an electron in the conduction band of a semiconductor considered as "free" and occupying a non-degenerate state, under the adiabatic approximation . The dispersion or energy versus momentum (which is proportional to the wavevector $\vec{k}$) curves are parabolic just as for classical free particles, as shown in Figure 1.1. We will use this definition of parabolic band later on.

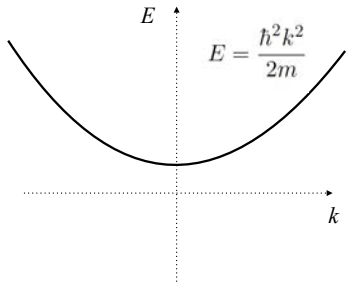

Figure 1.1: Energy in the k-space for a free electron.

Regarding the spatial distribution of the ions within the lattice, we find that the vast majority of the mainstream semiconductors have a face-centered cubic Bravais lattice [30], as shown in Figure 1.2. The lattice points are defined in terms of linear combinations of a set of primitive lattice vectors such as:

$$\vec{a}_1 = \frac{A_0}{2}(\hat{j} + \hat{k}), \qquad \vec{a}_2 = \frac{A_0}{2}(\hat{k} + \hat{i}), \qquad \vec{a}_3 = \frac{A_0}{2}(\hat{i} + \hat{j}) \tag{1.15}$$

The complete crystal structure is obtained by placing the atomic basis at each Bravais lattice. For materials such as Si, Ge, GaAs this consists of two atoms, one at ($\frac{1}{8}$,$\frac{1}{8}$,$\frac{1}{8}$) and the other at (-$\frac{1}{8}$,-$\frac{1}{8}$,-$\frac{1}{8}$) in units of A_0. For the group IV materials, such as Si and Ge, as the atoms within the basis are the same, the crystal structure is equivalent to diamond. For III-IV and II-IV compounds such as CdSe, CdS, PbSe and ZnO the cation sits on the (-$\frac{1}{8}$,-$\frac{1}{8}$,-$\frac{1}{8}$) site and the anion on ($\frac{1}{8}$,$\frac{1}{8}$,$\frac{1}{8}$). Sometimes, the same compounds grown as nanocrystals can form a different structure, known as wurtzite (Figure 1.2 b)). The wurtzite structure is non-centrosymmetric, i.e. lacks inversion symmetry. Due to this, wurtzite crystals can (and generally do) have properties such as piezoelectricity and pyroelectricity, which centrosym-

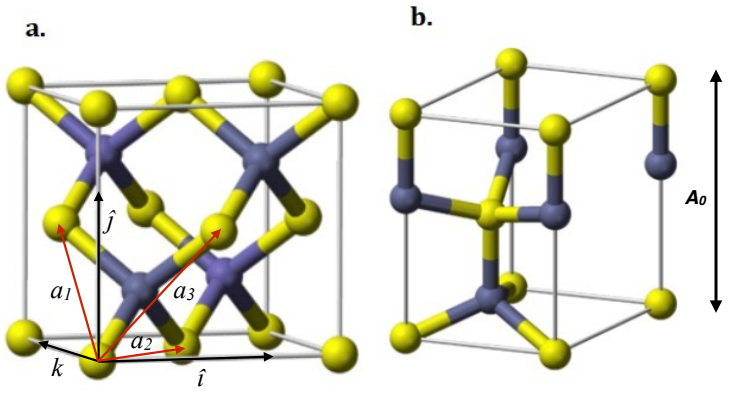

Figure 1.2: The zinc-blend (a) and wurtzite (b) crystal structures represented in a unit cell. The colors represent the different ions conforming the primitive cell. The vectors forming the basis of the unit cell are shown in black. The vectors forming the primitive cell are shown in red.

metric crystals lack. Each of the two individual atom types forms a sub-lattice which is HCP-type (short for hexagonal close-packed). When viewed altogether, the atomic positions are the same as in the hexagonal diamond. The property of inversion symmetry is crucial when the momentum operator is applied to calculate the matrix element of a transition.

1.2.1 The effective mass approximation

From an electrostatic point of view, the crystal potential consist of a three-dimensional lattice of symmetric ionic core potentials screened by the inner shell electrons, which are surrounded by the covalent bond charge distribution that holds the structure together. Solving the previous Schrödinger equation for many-body system results in a complicated expression, regardless of the periodic potential. One simplified solution is to assume $V(\vec{r})$ as a constant and includes its contribution in the form of an empirical fitting parameter called the effective mass m^*. This approximation is indeed suitable for relatively low electron momenta, as occurs with low electric fields and is a widely used parametrization. The effective mass is, as expected from the different crystal potential along particular axis, anisotropic and has been calculated for most of the semiconductors. In GaAs, for example, the reported effective mass of electrons in the conduction band is around $0.067 * m_0$ [30], where m_0 is the rest mass of an electron. The energy eigenvalue can be expressed as,

$$E = \frac{\hbar^2 k^2}{2m^*} \tag{1.16}$$

This expression in the k-space will looks exactly like in Figure 1.1 but with a narrower parabola when using the effective mass for GaAs (Figure 1.3).

There are two distinct bands within the semiconductors. The lower band is almost full of electrons and the conductivity in this band is defined by the movement of empty spaces. This band originates from the electron states which constitute the covalent bonds holding the

atoms together in the crystal. In some way, electric charge in a solid resembles a fluid, and the analogy for the *valence band* is that the empty states behave like bubbles within the fluid and they are known as *holes*. The other band, known as *conduction band* is almost devoided of electrons. It represents excited electron states which are occupied by electrons promoted from localized covalent bonds into extended states in the body of the crystal. Figure 1.3 illustrates these two bands and the gap separating them known as the band gap. Notice how the valence band is inverted which implies the lowest energy states for the holes are at the top of the band. The aperture of the parabola is also different, which indicate the different values for the effective mass approximation of electrons and holes. In this case, the representation implies a heavier hole compared to the effective mass of the electrons.

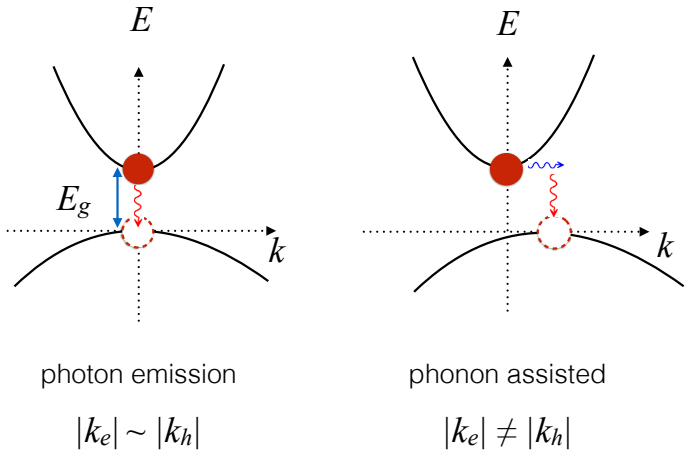

Figure 1.3: Direct and indirect band gap semiconductors with their corresponding photon emission processes.

The minimal-energy state in the conduction band and the maximal-energy state in the valence band are each characterized by a certain crystal momentum (k-vector) in the Brillouin zone. If the k-vectors are the same, it is called a 'direct gap' semiconductor. If they are different, it is called an 'indirect gap'. In an indirect gap, a photon can not be emitted because the electron must pass through an intermediate state and transfer momentum to the crystal lattice, which usually happens through phonon relaxation. This classification is presented in Figure 1.3 using the energy in the k-space diagram.

1.2.2 The reciprocal lattice

As shown in the previous sections, considering the electron wavefunction as a plane wave ($e^{i\vec{k}\cdot\vec{r}}$) but with a correction factor called effective mass, is a useful method to approximate the electronic band structure. In general, such a wave does not have the periodicity of the crystal lattice. However, it can be proven that the periodicity will be maintained when choosing the proper vector basis. This set of vectors is usually called vectors of the reciprocal lattice.

They form the primitive cell of a lattice obtained after applying a Fourier transformation to the vectors of the Bravais lattice.

They can be obtained using the following relations:

$$\vec{b}_1 = 2\pi \frac{\vec{a}_2 \times \vec{a}_3}{\vec{a}_1 \cdot (\vec{a}_2 \times \vec{a}_3)} \qquad \vec{b}_2 = 2\pi \frac{\vec{a}_3 \times \vec{a}_1}{\vec{a}_1 \cdot (\vec{a}_2 \times \vec{a}_3)} \qquad \vec{b}_3 = 2\pi \frac{\vec{a}_1 \times \vec{a}_2}{\vec{a}_1 \cdot (\vec{a}_2 \times \vec{a}_3)} \tag{1.17}$$

When expressing the reciprocal lattice vectors in the basis of $(\hat{i}, \hat{j}, \hat{k})$, we obtain:

$$\vec{b}_1 = \frac{2\pi}{A_0}(-\hat{i} + \hat{j} + \hat{k}) \qquad \vec{b}_2 = \frac{2\pi}{A_0}(\hat{i} - \hat{j} + \hat{k}) \qquad \vec{b}_3 = \frac{2\pi}{A_0}(\hat{i} + \hat{j} - \hat{k}) \tag{1.18}$$

which are equivalent to the body-centered cubic Bravais lattice vectors. Thus the reciprocal lattice constructed from the linear combinations:

$$\vec{G} = \beta_1 \vec{b}_1 + \beta_2 \vec{b}_2 + \beta_3 \vec{b}_3 \tag{1.19}$$

is a body-centered cubic lattice with lattice constant $2\pi/A_0$.

It was shown by von Laue [31] that waves will diffract in a periodic structure when:

$$\vec{k} \cdot \vec{G} = \frac{1}{2}|\vec{G}| \tag{1.20}$$

In this way, the free electron dispersion curves of Figure 1.1 will be perturbed when the electron wave vector satisfies the previous condition. Figure 1.4 illustrates the effect that such diffraction would have on the free electron curves. At a wave vector which satisfies von Laue's condition, i.e. $\vec{k} = \frac{2\pi}{A_0}\hat{k}$, the energy bands are disturbed and an energy gap opens. Such effect on the parabolic dispersion is known as the *nearly free electron model*.

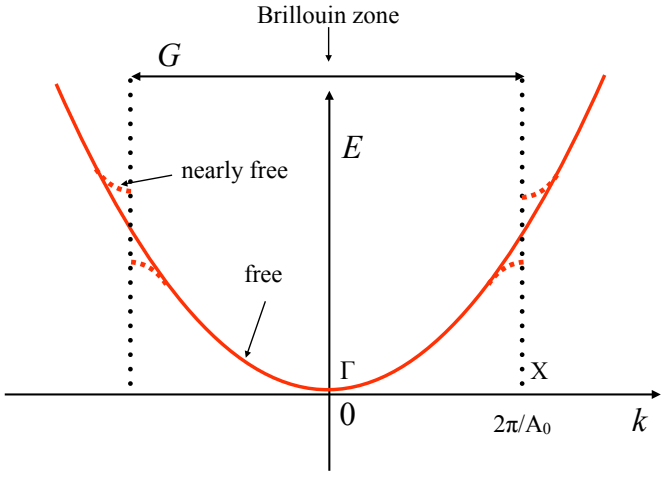

Figure 1.4: Comparison of the "free" and "nearly free" electron model. At a wave vector which satisfies von Laue's condition, i.e. $\vec{k} = \frac{2\pi}{A_0}\hat{k}$, the energy bands are disturbed and an energy gap opens.

The space between the lowest wave vector which is the solutions to von Laue's condition is called the first Brillouin zone. Note that the reciprocal lattice vector in any particular direction spans the Brillouin zone. As mentioned before, a face-centered cubic lattice has a body-centered cubic reciprocal lattice, and therefore, the Brillouin zone is a 3D solid, which happens to be a truncated octahedron. High symmetry points around the Brillouin zone are often labeled for ease of reference, with the most important of these, being the k=0 point, referred to as Γ, and the $< 001 >$ zone edges, which are called the X points.

1.2.3 $\vec{k} \cdot \vec{p}$ perturbation

In practice the important regions of the band structure are those which are most commonly populated by the mobile excitation of the crystal: electrons in the conduction band valley and holes at the top of the valence band. Finding the solution for the one-electron Schrödinger equation at these points in the Brillouin zone, it is possible to obtain solutions in the immediate neighborhood by including the scalar product $\vec{k} \cdot \vec{p}$ as a perturbation.

Suppose that the eigenvalues and Bloch functions are known for all bands at the center of the zone, Γ. Then the Schrödinger equation:

$$\{\frac{\vec{p}^2}{2m} + \sum_l V(\vec{r} - \vec{R_{l0}})\}\, e^{i\vec{k}\cdot\vec{r}} u_{n\vec{k}}(\vec{r}) = E_{n\vec{k}}\, e^{i\vec{k}\cdot\vec{r}} u_{n\vec{k}}(\vec{r}) \tag{1.21}$$

can be transformed to an equation containing only the periodic part of the Bloch function with $\hat{p} = -i\hbar\nabla$ [29]:

$$\{\frac{1}{2m} + (\vec{p} + \hbar\vec{k})^2 + V(\vec{r})\}\, u_{n\vec{k}}(\vec{r}) = E_{n\vec{k}}\, u_{n\vec{k}}(\vec{r}) \tag{1.22}$$

where $V(\vec{r})$ is a simpler notation for the periodic potential.

In the limit of $\hbar\vec{k} \ll \vec{p}$, the equation 1.22 can be written as:

$$(H_0 + H_1 + H_2)\, u_{n\vec{k}}(\vec{r}) = E_{n\vec{k}}\, u_{n\vec{k}}(\vec{r}) \tag{1.23}$$

$$H_1 = \frac{\hbar}{m}\vec{k} \cdot \vec{p} \tag{1.24}$$

$$H_2 = \frac{\hbar^2\vec{k}2}{2m} \tag{1.25}$$

So, we have H_1 as a first-order and H_2 as a second-order perturbation.

To zero order,

$$u_{n\vec{k}} = u_{n0} \tag{1.26}$$

$$E_{n\vec{k}} = E_{n0} \tag{1.27}$$

To first order,

$$u_{n\vec{k}} = u_{n0} + \frac{\hbar}{m} \sum_{m \neq n} \frac{\vec{k} \cdot \langle m_0 | \hat{p} | n_0 \rangle u_{m0}}{E_{n0} - E_{m0}} \tag{1.28}$$

$$E_{n\vec{k}} = E_{n0} + \frac{\hbar}{m} \vec{k} \cdot \langle m_0 | \hat{p} | n_0 \rangle, \tag{1.29}$$

Here m_0 and n_0 represent different bands with $\vec{k}$=0. Crystals with inversion symmetry have symmetrical Bloch functions. Since $\hat{p}$ is antisymmetric there will be no first-order correction to the energy. Where inversion symmetry is lacking, as in wurtzite structures, the correction may be non-zero and a term proportional to $\vec{k}$ appears. This indeed occurs at the top of the valence band and at the X point in the conduction band in these materials and results in a shift of the extreme in $\vec{k}$.

However there is always a first-order correction to the Bloch function. For example, the Bloch functions of the conduction band and valence band are respectively $|s\rangle$ and $|p\rangle$ orbital like and have a strong momentum matrix element connecting them. The second-order correction is not as important for the Bloch functions as it is for the energy. Neglecting the first-order correction equation 1.30 is obtained:

$$E_{n\vec{k}} = E_{n0} + \frac{\hbar^2 \vec{k}^2}{2m} + \frac{\hbar^2}{m^2} \sum_{i,j} \frac{|\vec{k} \cdot \langle m_0 | \hat{p} | n_0 \rangle|^2}{E_{n0} - E_{m0}} \tag{1.30}$$

This result can be expressed in terms of an effective mass as follows:

$$E_{n\vec{k}} = E_{n0} + \sum_{i,j} \frac{\hbar^2 \vec{k_i} \vec{k_j}}{2m^*_{ij}} \tag{1.31}$$

where m^* is a second-order tensor

$$\frac{m}{m^*_{ij}} = \delta_{ij} + \frac{2}{m} \sum_{m \neq n} \frac{\langle n_0 | p_i | m_0 \rangle \langle m_0 | p_i | n_0 \rangle}{E_{n0} - E_{m0}} \tag{1.32}$$

Applying degenerated perturbation theory it is possible to calculate the energy eigenvalues for the valence band, where in dependence of the effective mass we can have light holes, heavy holes and an split off (product of the spin orbit interaction) of the bands.

Oscillator strength

Since we are interested in radiative transitions between conduction and valence band, it is useful to introduce a term that express the probability of an allowed transition. Following the relation $P = \frac{1}{\tau_d}$, it is clear that a high probability of carriers recombination brings a faster decay time. In a radiative transition between band n and band m the perturbation writes as [29]:

$$H_\nu = -\frac{e}{m}\vec{A}\cdot\vec{p} \tag{1.33}$$

where $\vec{A}$ is the vector potential of the electromagnetic wave. Consequently, the matrix element which determines the transition rate contains the momentum matrix element $\hat{p}_{mn}$ connecting the two bands at k=0:

$$\hat{p}_{mn} = \langle m_0|\hat{p}|n_0\rangle \tag{1.34}$$

which are exactly the quantities that appear in the $\vec{k}\cdot\vec{p}$ perturbation theory and determine the curvature of band extrema. The probability of transition is usually described by a dimensionless quantity known as the oscillator strength which is defined as:

$$f_{mn} = 2\frac{|\hat{p}_{mn}|^2}{m\hbar\omega_\nu}, \tag{1.35}$$

where $\hbar\omega_\nu = E_{m0} - E_{n0}$. A reasonable approximation for interband transitions between conduction and valence band is,

$$f_{cv} \approx 1 + \frac{m}{m_v^*}, \tag{1.36}$$

where m_v^* is the hole effective mass for the given valence band.

One way to increase the oscillator strength for a radiative transition between carriers in the conduction and valence band, i.e. energy gap in the visible $\sim$ 1.7-3.4 eV will be to have a system where the electron-hole pair will form a strong bound state that is coherent over few unit cells. In this way, we introduce and develop the concept of exciton.

1.2.4 Excitons

An exciton is defined as the bound state of an electron and a hole that interact with each other through the electrostatic Coulomb force. Since it is a neutrally charged bosonic quasi-particle (formed by two fermions), excitons are the elementary excitation of condensed matter that can transport energy without transporting net electric charge. Even though the hole is not a standard elementary fermion but corresponds to a full valence band minus one electron; the hole is a many-body object in itself. It is possible to show that a full valence band with an empty state does behave as a single fermion, called hole, against a large number of effects, including exciton formation [32]. From the total charge and the force linking both particles, the exciton could be understood as an hydrogen atom with a center of mass move far from the nucleus due to the difference in the effective mass. In this way and comparing to the atomic

properties of Hydrogen, the binding energy of the excitonic bound state will be smaller and the particle size will be bigger. Basically, the distance between electron and hole is going to depend on the dielectric constant of the material, which will screen the Coulomb force between the electron and the hole.

Excitons can be classified according to two limiting cases [32]: (1) Frenkel excitons, first proposed by Yakov Frenkel in 1931, are typical in materials with a small dielectric constant like in organic molecular or alkali halide crystals. The Coulomb interaction is therefore strong and the excitons are highly localized in space, sometimes entirely located in the same molecule. (2) Wannier-Mot excitons, named after Gregory Wannier and Nevill Francis Mott, are typical in inorganic semiconductors where the dielectric constant is quite large. This reduces the Coulomb force attracting electrons and holes making the radius of the exciton particle longer than the interatomic space. These are also known as *large excitons*. The main differences among Frenkel and Wannier excitons regarding particle radius and binding energy are shown in Figure 1.5.

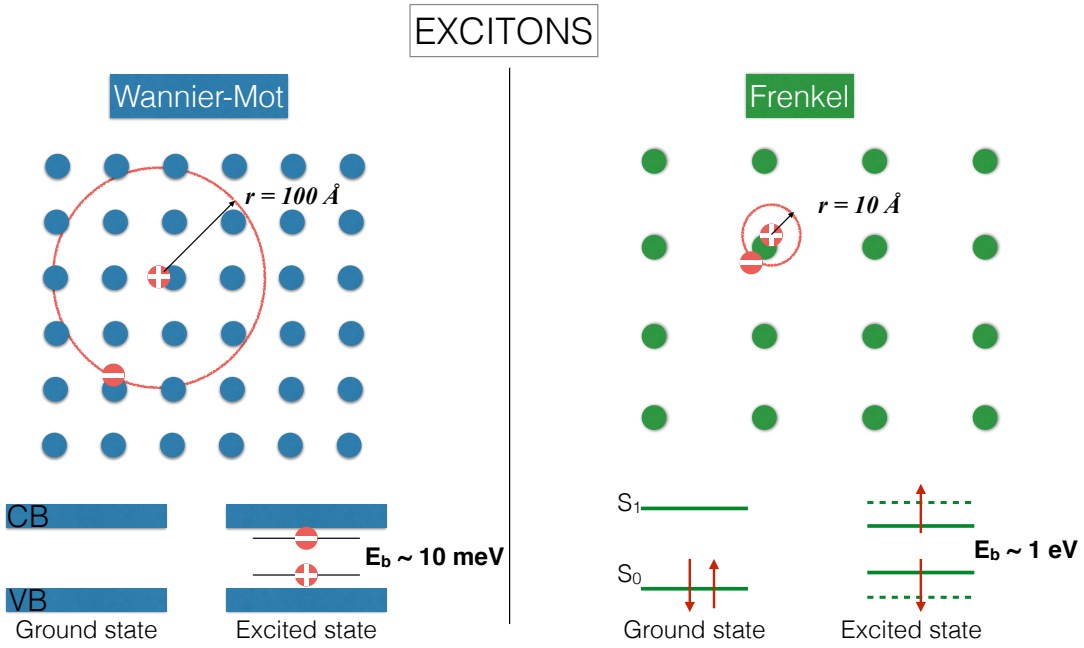

Figure 1.5: The two limiting exciton states, i.e. Wannier-Mot (left) and Frenkel (right). Main differences are shown regarding radius and binding energy.

From the wave-like behavior of particles, excitons can also be considered as coherent excitation that extends over a macroscopic volume. These coherent excitations can result either from atomic excitation delocalized by intersite interatomic-level Coulomb processes, as in the case of Frenkel excitons or from the excitation of valence electrons into the conduction band, as in the case of Wannier excitons.

The exciton energy states in semiconductors can be obtained, often very accurately, within the effective mass approximation. If we assume spherical bands at $\vec{k}$=0, the effective mass Hamiltonian writes as follows [29]:

$$H^* = \frac{\vec{p}_e^{\,2}}{2m_e^*} + \frac{\vec{p}_h^{\,2}}{2m_h^*} - \frac{e^2}{4\pi\epsilon|\vec{r}_e - \vec{r}_h|} = \frac{\vec{P}^2}{2(m_e^* - m_h^*)} + \frac{\vec{p}^2}{2\mu^*} - \frac{e^2}{4\pi\epsilon r} \tag{1.37}$$

Here m_e^* and m_h^* are the effective masses of the electron and hole, respectively. Meanwhile, $\vec{r}_e$ and $\vec{r}_h$ are their position vectors, $\vec{P}$ is the momentum of the exciton conjugated to the center-of-mass coordinate $\vec{R}$.

$$\vec{R} = \frac{m_e^*\vec{r}_e + m_h^*\vec{r}_h}{m_e^* + m_h^*} \tag{1.38}$$

$\vec{r} = \vec{r}_e - \vec{r}_h$, and μ^* is the reduced effective mass given by

$$\frac{1}{\mu^*} = \frac{1}{m_e^*} + \frac{1}{m_h^*} \tag{1.39}$$

In this way, the envelope wavefunction must be of the form $u(\vec{r})e^{i\vec{k}\cdot\vec{R}}$, where $u(\vec{r})$ obeys

$$\{\frac{\vec{p}^2}{2\mu^*} - \frac{e^2}{4\pi\epsilon r}\}u(\vec{r}) = Eu(\vec{r}) \tag{1.40}$$

The total energy is then,

$$E_k = E + \frac{\hbar^2 k^2}{2(m_e^* + m_h^*)} \tag{1.41}$$

Equation 1.40 is the hydrogenic wave equation and consequently

$$E_n = -\frac{(e^2/4\pi\epsilon)^2}{2(\hbar^2/\mu^*)n^2} \tag{1.42}$$

where n is an integer and the envelope wavefunction takes the hydrogenic form

$$u_n(\vec{r}) = R_{nl}(\vec{r})Y_l^m(\theta,\phi) \tag{1.43}$$

Here, $R_{nl}(\vec{r})$ is the radial function, $Y_l^m(\theta,\phi)$ are the spherical harmonics and l and m are the orbital and magnetic quantum numbers, respectively. Compared with the hydrogen atom the radius of the ground state is generally large because $\epsilon > \epsilon_0$ and $\mu^* < m_H$. The effective Bohr radius is given by,

$$\lambda_B^* = \frac{m\epsilon}{\mu^*\epsilon_0}\lambda_B \tag{1.44}$$

Here, λ_B is the Bohr radius and is equal to $\hbar^2/(me^2/4\pi\epsilon_0) = 0.528$ $\mathring{A}$. The factor multiplying λ_B in equation 1.44 is about 200 for bulk GaAs and the ground state binding energy is about 5 meV. For small binding energies typical of excitons in bulk semiconductors the oscillator strength of free excitons is usually of the order of 10^{-4}.

1.3 Macroscopic observables

From the macroscopic point of view, the interaction of a highly energetic particle with a scintillating crystal leads to the emission of a bunch of less energetic particles: optical photons. In a very simplistic way, the scintillator could be understood as a high dynamic range "wavelength shifter" which converts high energetic ionizing particles into light that is commonly readout with photodetector. This exact property is what allows to use scintillators as particle detectors, especially when operated in the linear regime where the optical signal is proportional to the deposited energy in the crystal. Some inorganic materials are usually also rather dense, they are able to stop most of the electromagnetic radiation, giving the possibility of not only detecting the passage of ionizing particles but also to measure their total energy. Measuring the total energy of high energetic particles, a technique known as calorimetry, finds plenty of application in society, mainly for national security, industry, monitoring of sealed containers used in nuclear reactors, medical imaging devices for cancer diagnostic and research facilities all around the world.

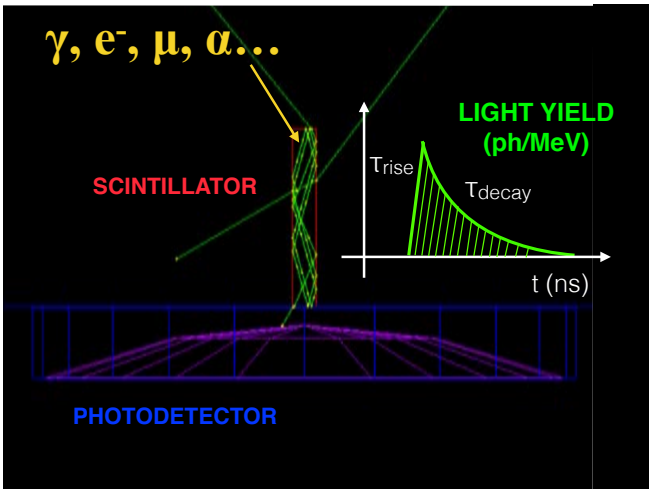

Figure 1.6: Basic components of a scintillator-based particle detector. The crystal acts as the producer and transporter of the light towards the readout face which is eventually coupled to a photodetector, in this case a photomultiplier tube. The main characteristics of the optical scintillating signal are displayed next to the crystal, i.e. light yield (ph/MeV), rise- (τ_r) and decay-time (τ_d) .

1.3.1 Light yield and energy resolution

A very simplistic schematic of the detection chain and its main components are shown in Figure 1.6 together with the main parameters characterizing the scintillation. Light yield is defined as the amount of photons produced per unit of energy deposited in the scintillator. Since access to this magnitude comes after coupling the light emitted to the photodetector, we will define two different terms, light output and intrinsic light yield, which distinguish respectively the light that exits the crystal and the total amount of photons created. To have a better idea of how these two terms are related when considering the energy deposition process we define the theoretical limit for light output:

$$LY_{out}^{lim}[ph/MeV] = LTE \times \frac{S \cdot Q}{b \cdot E_G[MeV]} \tag{1.45}$$

Here, the term LTE stands for the light transfer efficiency of the scintillating crystal and depends on the transparency to its own emission, index of refraction and the crystal's attenuation length. Basically the LTE reflects the waveguide properties of the scintillator to transport the light created to the photodetectors. S is a factor representing the energy transfer efficiency from the bulk energy deposited in the medium to the luminescent centers and Q is defined as the quantum efficiency of those centers. The denominator represents the energy necessary to create and electron-hole (e-h) pair, which is the bang gap energy (E_G) corrected by the phonon losses in the thermalization stage (b). As an example, we can take the figure of merit among scintillators used for medical imaging application, lutetium oxy-orthosilicate Lu_2SiO_5 doped with Ce^3, which has E_G=7.2 eV and b=2 [33]. If we substitute these values into the formula 1.45 and assume a perfect scintillator with S × Q × LTE = 1, the theoretical upper limit for the light output is 70'000 e-h pairs/MeV.

In a real scenario, S × Q × LTE ∼ 0.3 for a 2×2×20 mm^3 LYSO crystal coupled to a photodetector using the 2×2 mm^2 face, grease coupling and teflon wrapping. For this amount of light detected ∼ 20'000 ph/MeV, the energy resolution of a scintillating LSO crystal (defined as the full width half maximum of the total energy peak in pulse height spectra divided by the mean energy of that peak), would be around 2% assuming 662 keV energy deposition. However, when looking at the energy resolution of few inorganic scintillators, i.e. halides, oxides, garnets, (see Figure 1.7) we find that the maximum energy resolution is achieved by $LaBr_3$:Ce with R=3%, which presents a light yield two times larger compared to LSO. It is clear that some energy is being dissipated by non-radiative channels. This constitutes the principal cause of the non-proportionality seen in scintillators. The red stars in the energy resolution line of Figure 1.7 represent the limit set by photon statistics for both SrI_2:Eu and $LaBr_3$:Ce which are the scintillators with the highest light yield known so far.

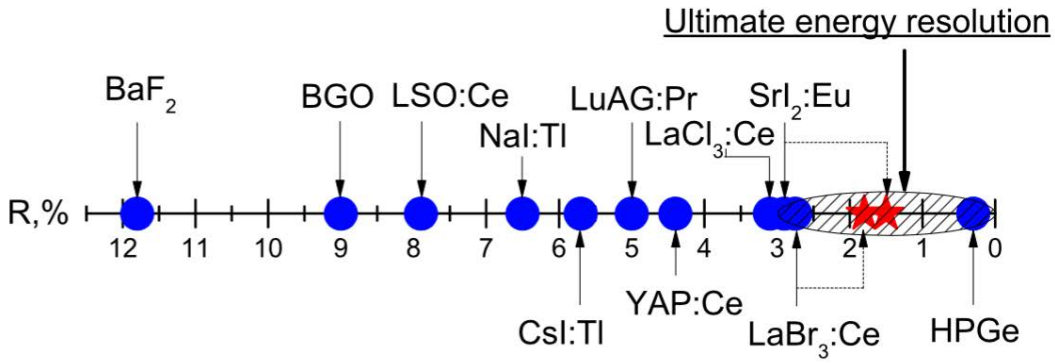

Figure 1.7: Energy resolution (R,%) of inorganic scintillators and of a HPGe detector for the detection of 662 keV gamma photons as reported in [34].

Non-proportionality in inorganic scintillators has been widely studied and described by the scientific community with a successful experimental validation of the theory for almost every type of crystal [35, 36, 37]. The model uses coupled rates and transport equations describing both the movement and the linear and non-linear interactions of the charge carriers deposited along an ionized track. As the "hot" electron slows down, it produces e-h pairs with higher density near the end of the track, ultimately reaching values as high as $10^{20}\ \frac{e-h}{cm^3}$. As represented in Figure 1.8, e-h pairs will be created almost in a straight line at the very end of the track. In this way, the carriers will undergo track-dilution either by diffusion or thermal quenching. The non-proportionality is explained as a competition of whether excitation will move more quickly reducing their initial concentration by the quenching itself (a loss of light emission) or by diffusion to larger radius (preserving the possibility of light emission later at lower concentration).

Considering $n(\vec{r},t)$ as the excitation density distribution with $n_0 = 10^{20}\ \frac{e-h}{cm^3}$, the second order transport equation is given by:

$$\frac{\partial n(\vec{r},t)}{\partial t} = D_{eff}\nabla^2 n(\vec{r},t) - K_2 n^2(\vec{r},t) \tag{1.46}$$

$$D_{eff}\nabla^2 n(\vec{r},t) - K_2 n^2(\vec{r},t) \propto \frac{K_2}{\pi^2 r^4}(dE/dx)^2 \tag{1.47}$$

where x is the line defining the ionization track as shown in Figure 1.8.

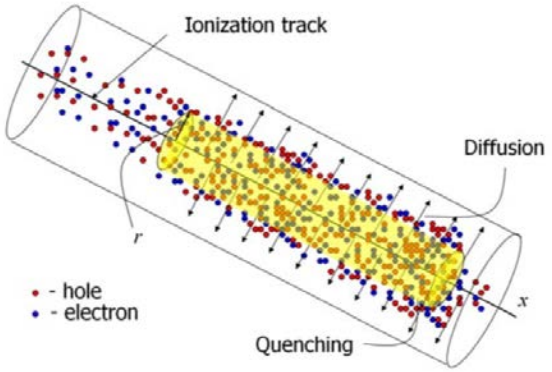

Figure 1.8: Sketch of an ionization track formed by a primary electron starting from the left creating free electrons and holes that diffuse radially away from the track, as reported in [34].

This model of ambipolar diffusion of electrons and holes (D_{eff}) and second order thermal quenching (K_2) is enough to explain the carrier recombination process happening in oxides scintillators and most semiconductors. However, it changes to a third order model for thermal quenching present in monovalent and multivalent halides. One physical phenomenon affecting halides more than oxides and semiconductors is spatial charge separation when the electron and hole mobilities are widely unequal, especially due to the presence of self-trapped holes and differences regarding the hot-electron thermalization range.

Experimental measurements of the radius of the region of non-linear quenching (NLQ) near the end of the track report that $r_{NLQ} \sim 3$ nm in NaI:Tl [35], which is also taken as the radius for self-trapped holes spatial distribution. In contrast to this tight radius of hole concentration, calculations of the thermalization range of conduction electrons in the heavier halides (mostly iodides) indicate that some of the hot electrons should travel much farther radially, of the order of 100 nm in CsI and NaI [38, 39]. Roughly half of the hot electrons were found to interact promptly with self-trapped holes in their 3-nm radius track, however the other half showed a larger distribution in CsI and NaI. The electron thermalization time increases roughly inversely with the optical phonon frequency, and was found to be about 7 ps in CsI, 2 ps in NaI, and 0.5 ps in CaF_2 [39].

It is clear that the carrier recombination process leading to scintillation is a complex problem with many variables, where light yield and timing profile of the signal are the macroscopic parameters commonly used to characterize the material.

1.3.2 Rise- and decay-time of the scintillating pulse

Concerning the rise- (τ_r) and decay-time τ_d characterizing the scintillating pulse, we might think intuitively that these correspond to the time constants of a positive and a negative exponential functions, respectively, since the light emission comes as a result of the recombination of electrons and holes populating specific states. However, the full picture that is needed to understand these parameters is a lot more complicated and differs from intrinsic to doped scintillators, having sometimes not even an exponential parametrization. A general description of how the thermalization process of "hot" carriers occurs and how they migrate through the crystal populating the energetic bands along time is shown in Figure 1.9 (as published in [40]). Basically the whole process can be described in three main steps: (1) creation of electronic excitations (from 10^{-16}-10^{-10} seconds in Figure 1.9), (2) transfer to luminescent centers (from 10^{-10}-10^{-8} seconds in Figure 1.9) and (3) e-h recombination leading to scintillation emission (last stage in Figure 1.9).

A gamma of 511 keV which interacts with the material through either photoelectric effect or Coulomb scattering (pair production is energetically forbidden). This interaction will produce a "hot" highly energetic electron taken from the core band of the material. In the very first 0.1-10 fs after the interaction, this "hot" electron and hole will start a multiplication process through inelastic electron-electron scattering and Auger process, causing the ionization of the medium until the energy of each electron is just above the e^--e^- scattering threshold and the energy of the holes is below the Auger relaxation threshold. After this, the thermalization of carriers happens mostly through phonon interaction in a time range from 10 fs to 1 ps, where each electron in the conduction band moves towards the minimum energetic level and the holes localize at the top of the valence band. Once the momentum of each carrier is near zero and in dependence on the kind of scintillator (intrinsic or activated), the localization of excitations may arise with formation of self- trapped excitons and self-

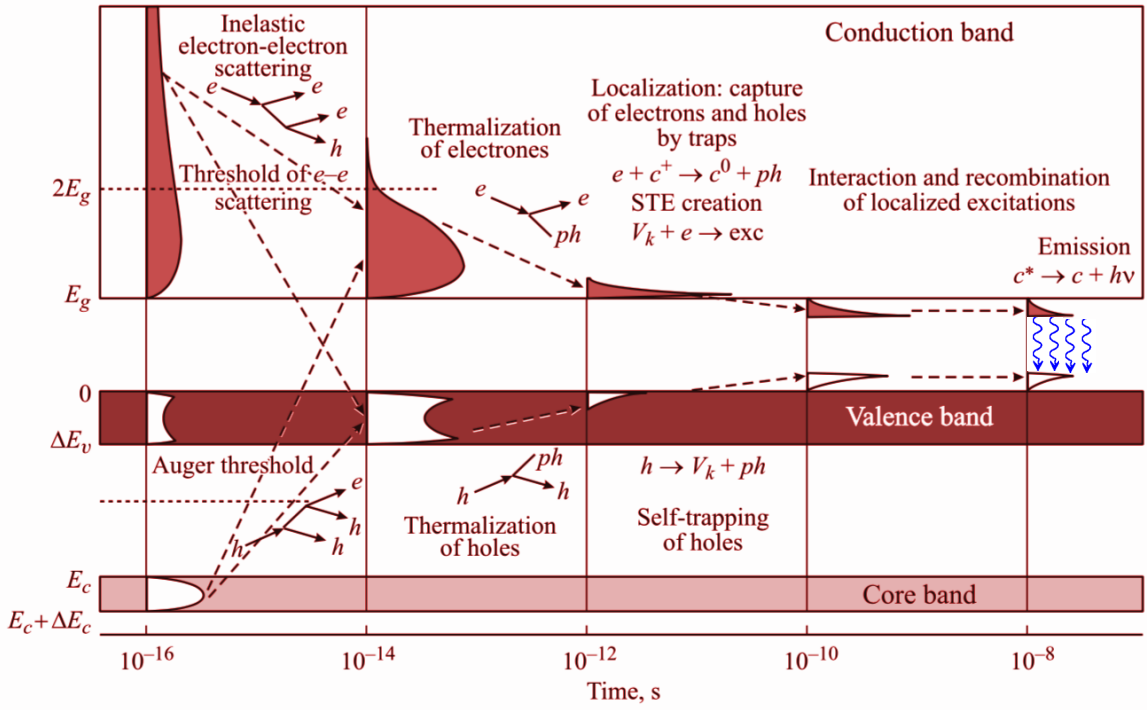

Figure 1.9: General scheme of relaxation of electronic excitation in an insulating material as published in [40].

trapped holes, capture of electrons and holes by traps and similar events. As a result, these centers have localized states located in the band gap. After interaction and recombination of localized excitations ($\tau_r \sim$ 1-100 ps), the luminescent centers will emit photons (τ_d >10 ns).

A slightly different process happens for scintillators which are doped with rare earths ions RE^{3+} as Ce^{3+}, Eu^{3+} or Pr^{3+}, just to mention an example. The luminescence in this kind of materials comes after a specific transition localized in the 5d-4f orbitals. In this way, the 4f band of the activator is localized within the band gap of the scintillator which in this case acts as a transparent host for the 5d-4f transition. For this particular case, there could be two ways of exciting the RE^{3+} centers. The first one is a direct excitation from "hot" electrons with energies between the threshold for e-e and e-RE scattering as shown in the first multiplication stage in Figure 1.10. The emission centers will be populated without having to wait for the thermalization process and this will give rise to a very fast τ_r. The second way follows the process already explained before, where the thermalization occurs through phonon interaction, followed by the localization of the excitation (self-trapped electrons and holes, capture, etc.) and eventually light emission. This doping technique not only provides with a very strong luminescence of the RE^{3+} centers which show a relatively short decay- and rise-time but usually shows a large thermal stability of the light output and high transparency in a wider spectral range.

The stage introducing the longest delay in the scintillation mechanism is the one where charge carriers are recaptured at trapping levels in the material's forbidden gap. This stage is the least predictable because material point defects, flaws, surfaces and interfaces can introduce energy levels within the forbidden gap and strongly modify and/or degrade the otherwise high intrinsic scintillation performance [3].

Another interesting case is cross-luminescent crystals. Cross-luminescence is due to a radiative electronic transition from the valence band to the uppermost core band, providing the Auger relaxation of the uppermost core band hole is strictly forbidden. This situation occurs when the energy difference between the uppermost core level and the valence band is less than the band gap so that re-absorption processes can be avoided. The archetype of cross-luminescent crystals is BaF_2. Such crystals give rise to very short sub-nanosecond luminescence decays which can be of interest for fast timing applications. Unfortunately, the light yield is relatively weak because usually only a few number of excitations created in the crystal are useful to produce cross- luminescence and the light emitted is in the deep UV. To describe the relaxation of excitations, it is therefore necessary to involve the uppermost core band in the scheme shown in Figure 1.10.

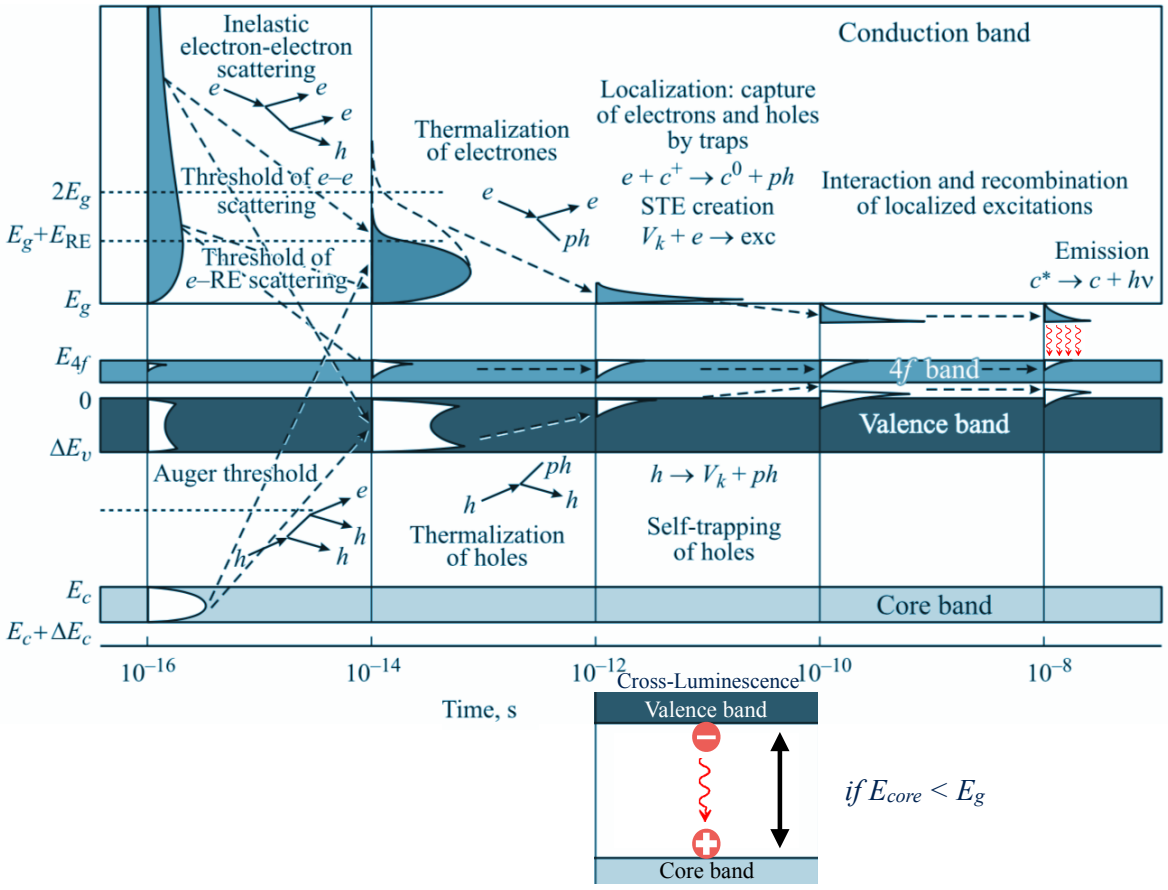

Figure 1.10: Top: Relaxation of electronic excitations in RE^{3+} activated crystals as published in [40]. Bottom: The cross-luminescence mechanism between the core and valence band is illustrated within its time of emission.

In general, if the scintillation process happens mostly through radiative transitions, i.e. quenching is suppressed, the light pulse can be parametrized using a sum over all the exponential components [12].

$$f(t) = \sum_{i}^{N} \frac{A_i}{\tau_{d,i} - \tau_{r,i}} \cdot e^{\frac{(\theta - t)}{\tau_{d,i}}} - \sum_{i}^{N} \frac{A_i}{\tau_{d,i} - \tau_{r,i}} \cdot e^{\frac{(\theta - t)}{\tau_{r,i}}} \tag{1.48}$$

Each parameter A_i is divided by the total amount of photons emitted under their corresponding timing characteristics, so that at the end the factor multiplying the exponential function is the number of photons emitted under their rise and/or decay constants. Here, θ takes into account any possible delay between the energy absorption and light emission. A typical time-resolved photoluminescence spectrum of a LSO:Ce co-doped with Ca^{2+} crystal taken under 372 nm laser excitation is shown in Figure 1.11 together with the fit parameters for the rise and decay times. In the case of laser excitation, its energy is only capable to populate the Ce^{3+} centers so we can measure the intrinsic recombination time of the luminescence. In this case, we have a decay time of nearly 32 ns (Figure 1.11 left) and a rise time near zero (Figure 1.11 right), which confirms the fact that the thermalization process of hot carriers is not occurring.

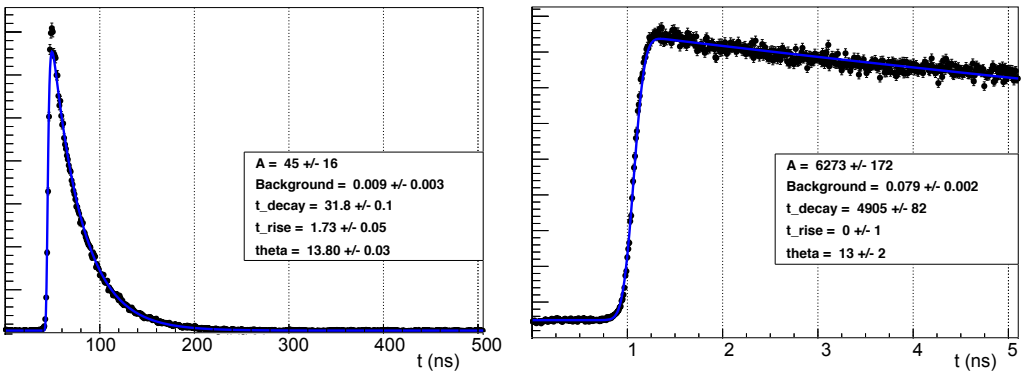

Figure 1.11: Time-resolved photoluminescence measured under laser excitation using a LSO:Ce Ca^{2+} co-doped crystal.

The crystal in question is not only doped with Ce^{3+} but co-doped with Ca^{2+}, which is responsible for a second and faster decay time as it can be seen in Figure 1.11, right. This technique of co-doping with another aliovalent ion(s) which do(es) not participate in the energy transfer and storage processes is usually applied to mitigate the intrinsic defects of the scintillator. Due to the mismatch between their charge state and that of the original substituted lattice ion, the Coulombic equilibrium in the lattice is changed and this usually induces changes in the concentration of intrinsic point defects as well [3]. In the process of material optimization, the minimization or inactivation of such defects is one of the main goals. This can be done either by changing the carrier dynamic which populates the trapping centers or by material purification and optimization of the technological process.

1.4 Fast radiative transitions

A review [41] of common and fast radiative transitions which are present in scintillating materials are presented in Table 1.1.

Table 1.1: **Review of fast radiative transitions present in scintillating materials**.

Material	Process	Lifetime	Theory
Any	X-ray transition	$\sim 10^{-15}$ s	$\frac{1}{\tau} = \frac{4e^2}{3\hbar c^3}\omega_{21}^3 \lvert\vec{M}_{21}\rvert^2$
BaF_2	Cross-luminescence F2p→Ba5p	880 ps	core-valence, 220 nm
$PbWO_4$	Thermal Quenching	$\sim$ 10 ns	$\frac{1}{\tau} = \frac{1}{\tau_r} + \frac{1}{\tau_{nr}}$
Ce^{3+}:LaF_3	Activator ion RE^{3+} (5d→4f)	$>$ 16 ns	$\frac{1}{\tau} = \frac{4e^2}{3\hbar c^3}\omega_{21}^3 \lvert\vec{M}_{21}\rvert^2$
$CaWO_4$	Hot-Intraband Luminescence	$\sim$ 0.1-10 ps	$\frac{1}{\tau} = \Sigma(h\nu)^2 \mid \langle f \mid \hat{M} \mid i\rangle \mid^2$
ZnO:D°X	Bound exciton	50-300 ps	
ZnO	Exciton	$\sim$ 400 ps	Giant oscillator strength
CdSe Nanocrystals	Biexciton stable at RT Multiexciton	$\sim$ 100 ps $<$ 100 ps	Giant oscillator strength

Looking at the radiative transition rate for spontaneous emission:

$$\frac{1}{\tau} = \frac{4e^2}{3\hbar c^3}\omega_{21}^3 |\vec{M}_{21}|^2 \tag{1.49}$$

We can find extremely short recombination times as the ones exhibited by an X-ray transition, if the energy (frequency-ω) of the transition is high enough. For optical transitions from atoms, molecules and bulk materials the typical recombination time following the previous equation is of the order of 10^{-9} s. An accepted standard of fast timing among scintillators is Auger-free cross-luminescence in BaF_2, where the Ba5p-F2p core-valence transition at $\sim$ 220 nm has a lifetime of 880 ps [42]. An optical transition between activator ions, specifically between 5d-4f orbitals, will yield a minimum decay time of $\sim$ 16 ns. This number could decrease to less than 10 ns if the crystal present some quenching, as suggested by the following equation:

$$\frac{1}{\tau} = \frac{1}{\tau_r} + \frac{1}{\tau_{nr}}, \tag{1.50}$$

where τ_r is the radiative decay time and τ_{nr} is the non-radiative one. However, this will lead to a decrease of the total number of photons, as in $PbWO_4$ where the light yield is as low as 200 ph/MeV.

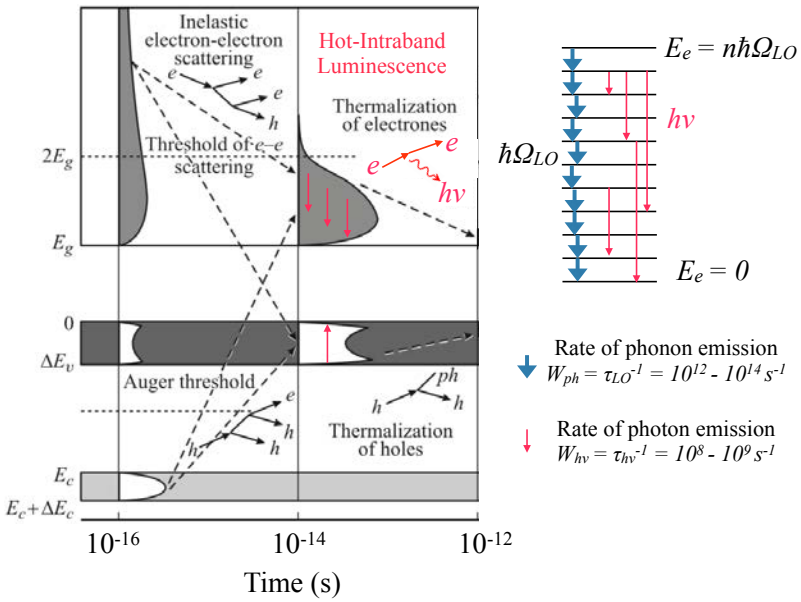

Figure 1.12: Hot intraband luminescence relaxation scheme as published in [43].

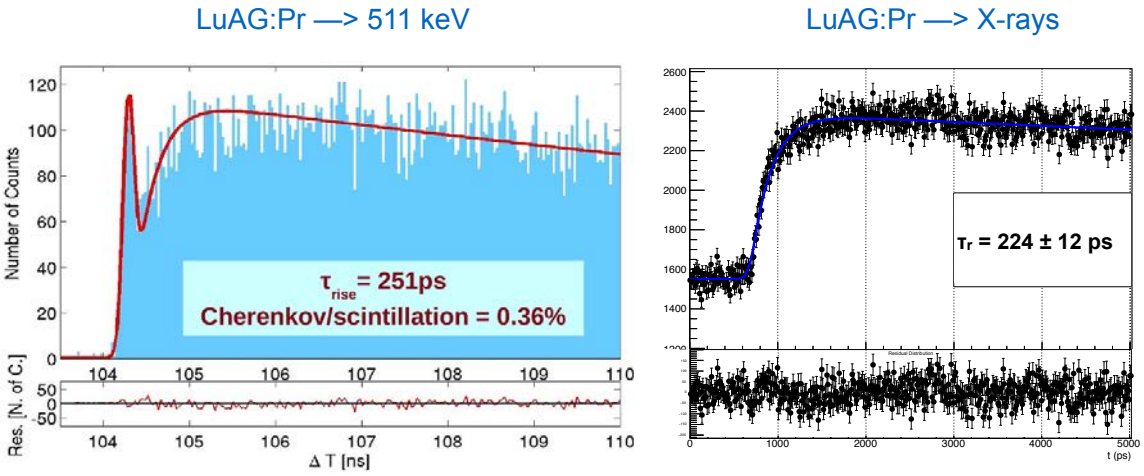

Figure 1.13: Cherenkov versus hot intraband luminescence prompt emission seen in LuAG:Pr

A prompt emission, within 0.1-10 ps, could be obtained from "hot" electrons which recombine during the thermalization process as presented in Figure 1.12. This emission known as hot intraband luminescence (IBL) has proven to present a light yield of maximum 3 to 5 order of magnitude less compared to Ce^{3+} doped scintillators and is also distributed along a broad spectral range. Recent studies [44] have shown hot intraband luminescence monitored under low-power X-ray excitation, which confirmed the absence of a power threshold of its mechanism and completely ruled out the role of excitation density effects in IBL formation. Whether this prompt emission could contribute to lower the state-of-the-art of coincidence time resolution values is still under investigation. However, time-resolved measurements of LuAG:Pr scintillator performed with 511 keV excitation and pulsed X-rays confirmed that the efficiency of this process is much less when comparing to prompt Cherenkov photons as

shown in Figure 1.13. The prompt peak emission seen for 511 keV excitation disappears when changing to X-ray irradiation, which indicates that all the prompt emission seen in the first plot is due to Cherenkov.

The remaining radiative transitions appearing in Table 1.1 with a sub-nanosecond timescale have an excitonic origin. Since this transition looks promising for fast timing research and there is no intrinsic limit for the light yield, the following Chapter 2 will be dedicated to materials which exhibit a giant oscillator strength.

1.5 Applications

Among inorganic scintillating crystals, we can find a quite large diversity regarding crystal growth techniques and sample preparation specialized for the different applications. They can be grown in the form of powders, optical ceramics, microstructured materials and single bulk crystals, being the last one the figure of merit for calorimetry and PET scanners. The most important characteristics for bulk scintillators are the following:

1. Light yield, usually in the range of few hundreds to few thousand photons per MeV.
2. Stopping power, given by the density and the thickness of the material.
3. Time response: rise time is usually in the sub-nanosecond scale however the decay time varies widely with the scintillator type.
4. Transparency, highly dependent on the Stokes shift of the crystals and the attenuation length.
5. Chemical stability and radiation hardness.
6. Linearity of light response and energy resolution.
7. Spectral matching between light emission and photodetector quantum efficiency.

Table 1.2 summarizes the main properties of significant materials which have been or are widely applied in different fields. They all show excellent energy resolution at 662 keV, except $PbWO_4$ which has a very low light yield, however its radiation hardness makes it an excellent candidate for harsh environments.

As shown in the previous list, choosing the right scintillator for electromagnetic calorimeters is highly application dependent, when considering the broad energy regime, count rate, radiation environment and the most recent feature, coincidence time resolution. The time-of-flight (TOF) technique using inorganic scintillating crystals has been studied and developed for the last 20 to 30 years, especially in the field of positron emission tomography with the replacement of NaI:Tl, CsI:Tl and BGO by lutetium oxy-orthosilicate and garnet families.

Table 1.2: **Review of single crystal inorganic scintillators commonly used in medical imaging devices, high-energy physics and industrial applications** as reviewed in [3].

Crystal	Density (g/cm^3)	Light yield (ph/MeV)	Decay time (ns)	λ_{max} (nm)	$\Delta E/E$ at 662 keV (%)
CsI:Tl	4.51	66 000	800	550	6.6
NaI:Tl	3.67	41 000	230	410	5.6
$LaBr_3$:Ce	5.3	61 000	35	358	2.9
K_2LaI_5:Ce	4.4	55 000	24	420	4.5
BaF_2 (only cross luminescence)	4.88	1 500	0.6-0.8	180-220	7.7
$Bi_4Ge_3O_{12}$	7.1	8 600	300	480	9.0
$PbWO_4$	8.28	300	2-3	410	30-40
$CdWO_4$	7.9	20 000	5 000	495	6.8
$YAlO_3$:Ce	5.6	21 000	20-30	360	4.6
$LuAlO_3$:Ce	8.34	12 000	18	365	∼15
$Y_3Al_5O_{12}$:Ce	4.56	24 000	90-120	550	7.3
$Lu_3Al_5O_{12}$:Ce	6.67	12 500	55	530	11
Gd_2SiO_5:Ce	6.7	8 000	60	420	7.8
Lu_2SiO_5:Ce	7.4	26 000	30	420	7.9

Basically, the TOF technique uses the time-of-flight information of the particles interacting with the detector to identify and reconstruct the particle vertexes. The time resolution, i.e. FWHM or sigma of the distribution built from t_2-t_1 when measuring in coincidence, defines the spatial resolution along the line of response. This technique can be extrapolated to basically any calorimeter system either for measuring back-to-back 511 keV gammas from the e^+-e^- annihilation or detecting the jets created by p-p, p-Pb collision in big accelerators. Figure [2] 1.14 illustrates the inorganic scintillating crystal's main applications in two different energetic regimes, at low energy < 1 MeV and higher energies of the order of hundreds of GeV. The TOF technique is applied in a PET ring or to identify pileup events when the proton bunches are crossing and colliding at the LHC. For the low energetic regime, applications are mainly in the field of medical imaging devices like Computed Tomography (CT), Single Photon Emission Computed Tomography (SPECT) and positron emission tomography, with the last one holding the best values in terms of sensitivity per dose received by the patient.

For high energy physics the clearest examples are the electromagnetic calorimeters surrounding the collision point. As an example, let's take ECAL (Figure 1.14), the electromagnetic calorimeter from the CMS experiment at the LHC. ECAL is formed by 75'000 $PbWO_4$ 22 cm long crystals, which is equivalent to $24X_0$, being X_0 the radiation length. The crystals are arranged in a central barrel and two endcaps almost closing the 4π space around the collision point. The scintillation decay time of the crystals is comparable to the LHC bunch crossing interval of 25 ns, and about 80% of the light is emitted in 25 ns. Time resolution evaluated during test beam using electrons was estimated to be lower than 20 ps sigma for

[2] Courtesy of EndoTOFPET-US and CMS collaborations

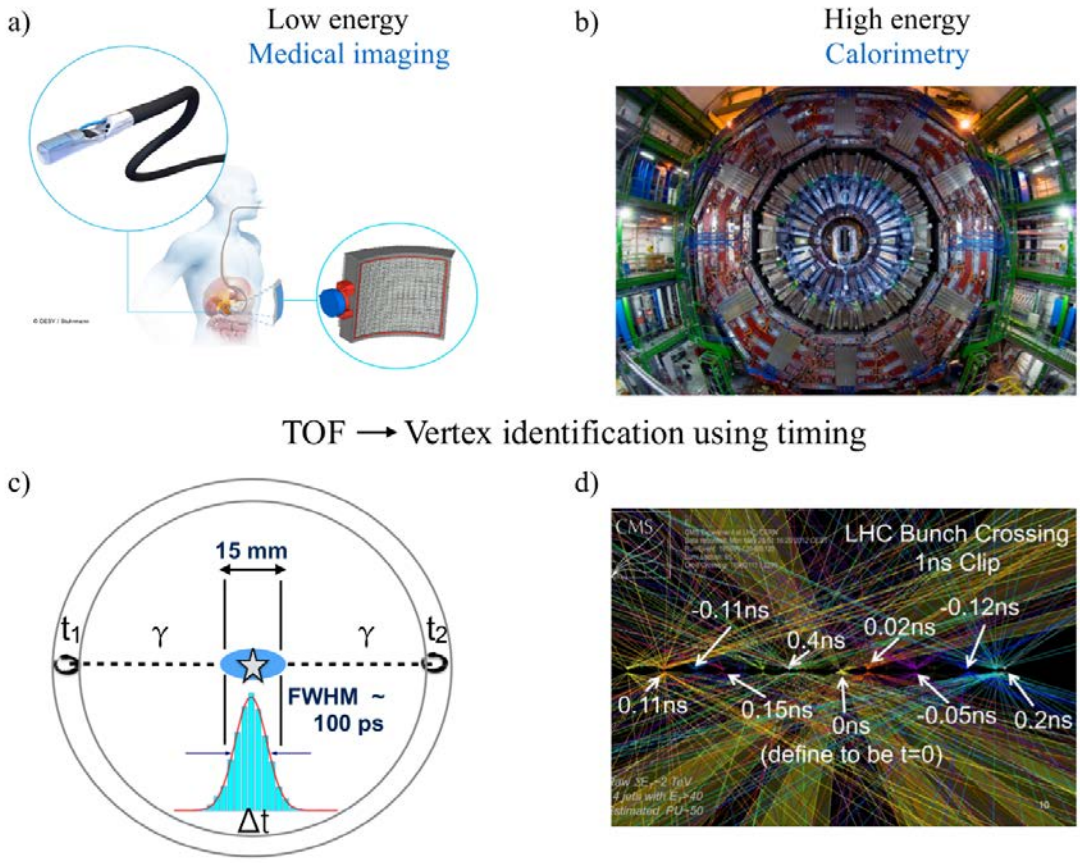

Figure 1.14: Main applications of inorganic scintillating crystals in different energetic regimes. a) Endoscopic time-of-flight PET device from the EndoTOFPET project which uses a time resolution of 200 ps to reject background events from a 3 cm diameter region. b) The electromagnetic calorimeter of the CMS experiment at the LHC contains more than 75'000 PWO crystals. Bottom: The time-of-flight technique used for vertex identification. c) e^+-e^- annihilation along the line of response of a PET ring. d) Pileup events per bunch crossing in proton-proton collisions at the LHC with around 20 interactions distributed along 6 cm.

energies > 50 GeV, however this resolution deteriorates to around 150 ps when the data are taken during the actual runs of the LHC [4]. The new experimental phases in HEP at future accelerators foresee a large increase in luminosity, i.e. $>10^{35}\text{cm}^{-2}\text{s}^{-1}$ at extreme collision frequencies, to explore and elucidate new phenomena at low cross section. Bunch separation can then be as small as 500 ps, and the bunches themselves carry such a high density of particles that each bunch crossing will generate several collisions. At such beam intensities, e.g. $\sim$ 200 pileup events can be produced in each bunch crossing. Precise identification of collision tracks or jets is necessary to mitigate this pileup. In this case only TOF techniques and event tagging with a precision of <30 ps can achieve pileup suppression by more than a factor of 10.

In the next subsection, we will focus on the time-of-flight technique as applied in positron emission tomography giving an overview of the parameters affecting the time resolution performance of the scintillator-based detectors.

1.5.1 Time-of-flight in PET

As mentioned before, time-of-flight positron emission tomography, TOF-PET, constitutes the figure of merit among molecular imaging devices. Its progress was limited for around a decade, however the rapid development in the past 15 years of efficient and fast photodetectors, i.e PMTs and analog or digital Silicon photomultipliers (SiPMs), the introduction of very bright, relatively fast and dense scintillators as LSO, together with fast readout electronics have pushed forward the TOF technique in the medical imaging community. A summary of the state-of-the-art of commercially available systems from different producers is detailed in Table 1.3 as published in [45].

Table 1.3: **Specifications of commercially available and recently introduced new clinical TOF-PET/CT systems**.

Company / **System name**	Philips Ingenuity TF [46]	Siemens Biograph mCT [47]	GE Discovery 690 [48]	Philips Vereos digital [7]	Toshiba Celesteion [49]
Scintillator	LYSO	LSO	LYSO	LYSO	LYSO
Photo-detector	PMT	PMT	PMT	dSiPM	PMT
Crystal size, mm^3	4×4×22	4×4×20	4.2×6.3×25	4×4×19	4×4×12
Total # crystals	28,336	32,448	13,824	23,040	30,720
Patient bore, cm	71.7	78	70	70	78
Axial length, cm	18	21.8	15.7	16.4	19.6
Resolution, mm transaxial, 1 cm/10 cm	4.8/5.1	4.4/4.95	4.7/5.06	4.1/4.5	5.1/5.1
Resolution, mm axial, 1 cm/10 cm	4.73/5.23	4.4/5.9	4.74/5.55	3.96/4.3	5.0/5.4
Energy resolution, %	11.1	11.5	12.4	11.1	NA
Sensitivity, cps/kBq	7.3	9.7	7.4	5.7	NA
Scatter fraction, %	36.7	33.2	37	30	42.7
Coincidence window, ns	4.5	4.1	4.9	4	NA
TOF resolution, ps	**502**	**527.5**	**544.3**	**316**	**∼410**

The principal motivation to include the time-of-flight information in the reconstruction algorithm is the obtained improvement in signal-to-noise ratio of the image. This could lead eventually to a reduction in acquisition time or lowering the injected dose. This gain is difficult to quantify into one single factor, because TOF improves the imaging performance of a PET scanner in several ways comparing to non-TOF-PET:

- Increases effective sensitivity;
- Increases rate of reconstruction algorithm convergence;
- Makes convergence more uniform;
- Improves contrast recovery at matched noise;

A fair approximation of the signal-to-noise ratio (SNR) gain expected is given by the following relation [50]:

$$G = \frac{SNR_{TOF}}{SNR_{non-TOF}} = \sqrt{\frac{2D}{c \cdot CTR}} = \sqrt{\frac{NEC_{TOF}}{NEC}} \tag{1.51}$$

where, D is the diameter of the patient, c is the speed of light and CTR stands for coincidence time resolution expressed in FWHM. When substituting state-of-the-art CTR values from commercially available scanners we get a gain of 2.9 using D=40 cm and a CTR=316 ps. Looking at the formula, larger patients in which the probability of scattered events is higher will benefit more than normal patients when the gain is only a factor ~ 3. However, a CTR of 100 ps could bring a gain of a factor 5.2 in image signal-to-noise ratio, which already represents a significant improvement for every patient. Calculations done to determine the gain in imaging time are shown in Figure 1.15 following data published in [51, 45]. Here, NEC stands for noise equivalent counts.

Currently new research work is underway that has already achieved coincidence time resolution (CTR) values as low as 100 ps and below [5, 12] for single channel readout. In terms of spatial resolution, such precision corresponds to 15 mm along the LOR, now allowing to discriminate between organs under examination (e.g. prostate, pancreas or lymph nodes) and the background generated by other, marker-attracting organs such as the heart or the bladder [6]. Coincidence time resolution measurements between two single scintillating pixels using single channel readout have helped considerably to understand the main factors influencing timing [52]. As the first approach and as an approximation for the very first detected photons, the CTR can be parametrized as equation 1.

Hence, the CTR is proportional to the density of photons emitted by the scintillator, which leads to the selection of brighter and faster scintillators for TOF-PET with LYSO as the figure of merit. Among the different factors which are directly affecting the amount of photons coupled to the photodetector, we have the crystal attenuation length, matching index of refraction and detection efficiency of the photodetector. From the timing point of view, apart from the rise- and decay-time of the optical signal, there are other parameters shuffling the time of arrival of the first emitted photons. First, the photon time spread (PTS) within the scintillator due to multiple internal reflections increases considerably the travel path of each photon. Second, the single photon time resolution (SPTR) of the photodetector with state-of-the-art values around 50 ps FWHM. Both PTS and SPTR contribute to the spread of the timing signal and the uncertainty involved in the coincidence measurement.

Under laboratory conditions, $2 \times 2 \times 10$ mm^3 cerium-doped $Lu_2(Y)SiO_5$ crystals with nanosecond photon emission rates, coupled to modern solid state photodetectors (e.g. FBK analog Silicon Photomultipliers, SiPMs) and fast frontend electronics, deliver CTRs of $\sim$117 ps for an estimation of 5'000 photoelectrons detected [8]. If instead the same scintillator was used for the detection of minimum ionizing particles (MIPs with dE/dx $\sim$ 1 MeV/mm), the

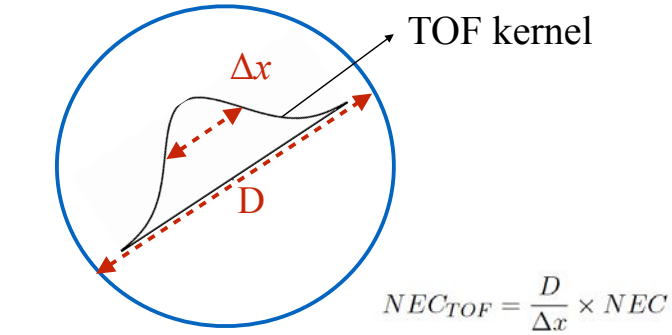

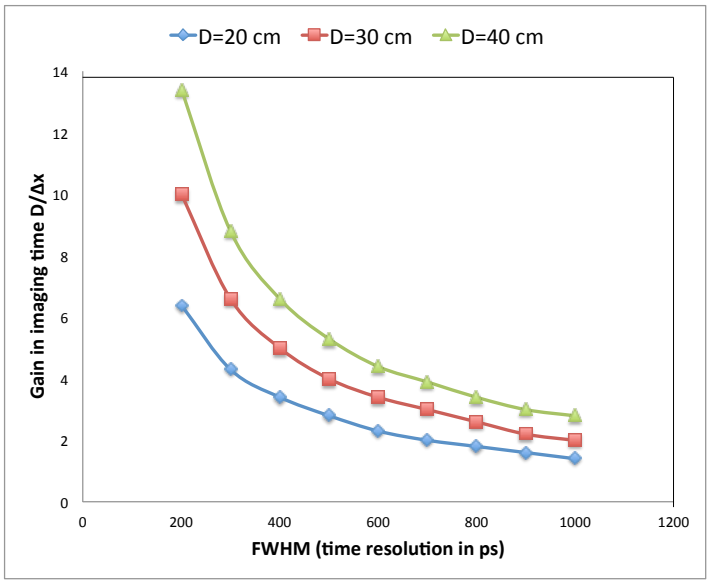

Figure 1.15: TOF-PET gain in imaging time as a function of CTR expressed in FWHM for different patient sizes. This calculation [51] assumes analytical reconstruction and a simple uniform cylinder of activity.

resolution improves to 60 ps with single-channel readout [9]. There is a slight improvement if a LSO:Ce:Ca co-doped scintillators are used instead, with values of 100 ps for 511 keV using 10 mm long crystals and 34 ps using MIPs and a 5 mm long crystal [8, 9].

A different approach, using digital SiPMs and $22 \times 32 \times 32$ mm^3 bulk LYSO together with maximum-likelihood techniques to estimate the time of interaction, reaches CTR values of 147 ps for dual-side-readout [10] and 215 ps for single-side-readout [11]. Dual-side-readout is also able to provide with a depth-of-interaction (DOI) resolution of 2.4 mm FWHM, which is essential to decrease the parallax error. A novel method to obtain DOI information has been achieved using an 8×8 LYSO pixelated matrix with crystals of $1.5 \times 1.5 \times 15$ mm^3 coupled to a 4×4 multipixel photon counting (MPPC) detector from Hamamatsu. The method exploit the light shared among different pixels together with the light attenuation over the length of the crystals to identify the point of gamma interaction with and spatial resolution close

to 1.5 mm (size of the individual pixels) and a DOI resolution of 2.9 mm [53]. Single-side-readout and 4:1 crystal-photodetector coupling allow for CTRs values measured between the matrix and a single pixel of the order of 350 ps [54].

The need for fast timing and the development of SiPMs with an excellent photodetection efficiency in the near UV has brought back to the scene scintillators as BGO, which was widely used in PET before LYSO became the figure of merit. BGO has a light yield of a factor 5 less when comparing to LYSO and it also quite slow, i.e. decay time of 300 ns. However, it is an excellent Cherenkov radiator due to its high optical index and good transparency in the UV region. CTR values measured using $2 \times 2 \times 3$ mm^3 BGO crystals present a FWHM of 270 ps [55], which could rapidly improve if the photodetection efficiency of SiPMs increases in the UV/blue area.

A CTR of 100 ps, despite being a significant improvement over standard TOF-PET cameras, is still not sufficient to allow a direct 4D reconstruction of a PET image. To ultimately reach that level of true space points, i.e. not only in the traditional x-y coordinates but also in z (along the LOR), calls for a CTR improvement to as high as 10 ps, equivalent to 1.5 mm along the LOR. Only then the time consuming, iterative, or back projection algorithms could be replaced by a fast and direct, "real time", image reconstruction, benefiting from at least a ten-fold increase in sensitivity.

A study of the influence of 10 ps coincidence time resolution in TOF-PET image reconstruction carried out by Nikos Efthimiou [56] shows the incredible potential of such resolution. For this, a complex voxelized XCAT phantom was simulated using GATE v6.2. A normal ^{18}F-FDG distribution was used and the simulation took place for one bed position in the thorax area. The reconstructed images using non-TOF and TOF information with 600 ps and 10 ps FWHM are shown in Figure[3] 1.16. The images from top and bottom are only different in the number of counts recorded, which is twenty times higher for the picture in the bottom. As expected, datasets with higher number of counts present better noise properties. However the use of TOF, especially the 10 ps, strongly improves the image quality in low count statistics. While the number of iteration has a positive effect on the image quality for non-TOF and 600 ps TOF, for 10 ps the best images are acquired on the very first iteration. More iterations increase the noise level which confirm a direct creation of the image in "real time".

Going down to sub-20 ps time resolution implies a major technological challenge that could be overcome by increasing photostatistic, reducing rise and decay times or using an intense prompt signal as a time tag in the readout chain. Assuming Poisson statistic of the photon emission process and in the case of $\tau_d \gg \tau_r * N_{pe}$, where N_{pe} is the number of detected photoelectrons, the CTR can be simplified as $CTR \propto \sqrt{(\tau_r \tau_d / N_{pe})}$. Hence, the photoelectron density of the scintillating emission would need to be increased by two orders of magnitude if a CTR of O(10)ps was to be reached. According to Cràmer-Rao lower bound calculations,

[3]Courtesy of Nikos Efthimiou

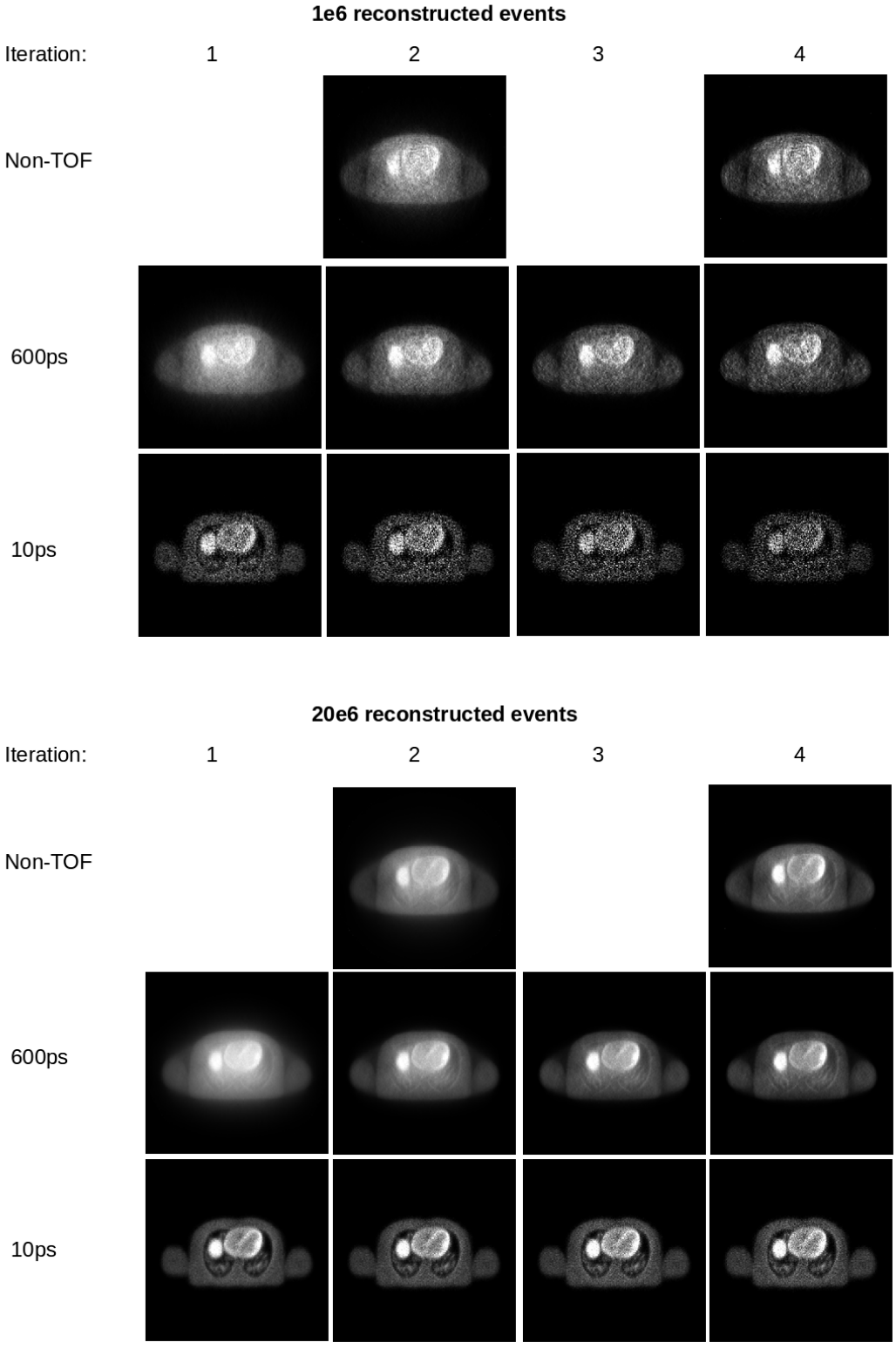

Figure 1.16: Reconstructed images of an anthropomorphic XCAT phantom with and without TOF, after the first 4 iterations, for 1 million (top) and 20 millions (bottom) true events. The image includes the lower part of the heart (two ventricles) and a portion of the upper part of the liver.

the number of prompt photons needed along with the scintillation emission in the crystal is as high as 500-1000 photons if a CTR of 10 ps is to be reached [12, 57]. These numbers already assume a considerable improvement of the SPTR of state-of-the-art photodetectors as low as the SPTR of a single SPAD (single photon avalanche diode) which is around 10 ps. Therefore, the need for fast emitting materials or a source of sufficiently prompt photons under ionizing radiation is essential in the research path of sub-20 ps time resolution detectors.

Chapter 2

Scintillating Nanocrystals

2.1 Definition

Semiconductor nanocrystals (NCs) are nanometer-sized crystalline particles that contain approximately 100 to 10'000 atoms, which are characterized by the same crystal lattice structure as the corresponding bulk semiconductor. Using chemical syntheses, they can be fabricated with almost atomic precision as nearly spherical nanoparticles (quantum dots) [58], [59], elongated nanosized crystals (quantum rods) [60], or nanostructures of other more complex shapes such as tetrapods [61]. The particle size of the aforementioned crystallites is usually in the range of the Bohr radius for a bulk semiconductor, which is typically 1-10 nm for most materials. When the particle size is smaller or comparable to the Bohr radius, the electron-hole pairs and/or excitons can not longer be considered as free particles, but instead due to the quantum confinement effect the carriers are only able to occupy specific and quantized energy levels. As a consequence the whole electronic structure of the semiconductor is modified and the energy of the band gap will increase with decreasing particle size as shown in Figure 2.1.

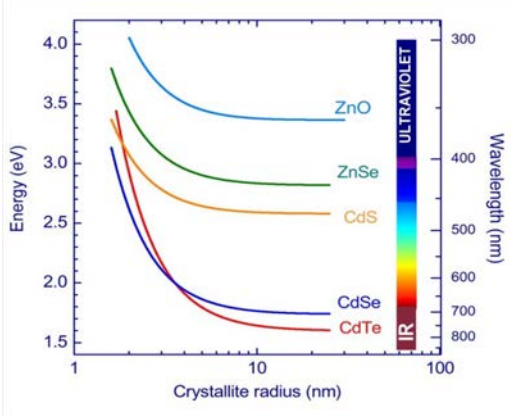

Figure 2.1: Bandgap energy of different semiconductor materials as a function of the crystallite size.

Let's take CdSe as example. This semiconductor has a band gap of 1.74 eV as a bulk material. When synthesized as a nanocrystal, CdSe is not only able to emit visible light, but the emission could be tuned from green to red by controlling the particle size from 1 nm to 5 nm, respectively.

Furthermore, by combining different materials in one nanocrystal, it is possible to produce various types of heterostructures, including all-semiconductor hetero-nanoparticles [62, 63, 64] or hybrid semiconductor-metal structures [65]. The ability to precisely control the composition, size, and shape of NCs provides great flexibility in the engineering of their electronic and optical properties by directly manipulating the electronic wave functions (wavefunction engineering). For instance, colloidal synthesis is able to provide semiconductor nanocrystals with nearly single atomic layer precision with sizes of few tenths of nanometers and a size dispersion under 4-5%.

This Chapter will give an overview on the quantum confinement effect and the multi-excitonic dynamics present in nanocrystals as a consequence of a significant enhancement of carrier-carrier Coulomb interactions in these materials. Strong carrier-carrier interactions in NCs have a number of important spectral and dynamical implications. They result in large, tens-of-milli-electron-volt spectral shifts of multiexciton emission bands with respect to single-exciton transition energies [66]. They also have a strong effect on carrier dynamical behaviors. Specifically, Auger-type e-h energy transfer mediated by Coulomb coupling becomes an efficient channel for electron intraband relaxation, which can compete with phonon-assisted relaxation mechanisms [67, 68, 69, 70]. Furthermore, strong carrier-carrier interactions can lead to the direct photogeneration of multiexcitons by single photons, referred here as carrier multiplication (CM) [71]. This process is extremely efficient in quantum confined NCs and leads to internal quantum efficiencies of converting light quanta into charge carriers that can greatly exceed 100%.

The understanding and manipulation of both processes, Auger recombination (AR) and carrier multiplication (CM) are key parameters in order to assess the promising application of nanocrystals in the field of radiation detectors. The suppression of the non-radiative recombination (AR) is fundamental in order to profit from an enhanced rate of carrier multiplication.

2.2 Quantum confinement effect

As discussed in section 1.5, the Bohr radius for the excitonic state in the GaAs bulk semiconductor is around 5 nm. This quantity, λ_R varies between 1-10 nm for most semiconductors giving rise to a high quantum confinement for electron-hole pairs created in nanocrystals of the same size. A "weak" quantum confinement effect is seen in wide-band gap semiconductors when the particle size is one order of magnitude higher and the exciton state is coherent over the particle volume.

The quantum confinement effect can be better understood when solving the problem of the particle in a box, where the walls are represented as an infinite potential and the particle moves freely within the boundaries of the well. The schematic of the quantum well problem is shown in Figure 2.2. Solving the Schrödinger equation in one dimension simplifies the calculations, having the following boundary conditions:

$$V(x) = \begin{cases} 0 & for \quad 0 < x < a \\ \infty & otherwise \end{cases}$$

Substituting the Hamiltonian operator by $\hat{p}^2/2m + V(\vec{r}) = -\frac{\hbar^2}{2m}\nabla^2 + V(\vec{r})$ in the left-hand side of the equation 1.5 leads to:

$$\frac{-\hbar^2}{2m}\frac{d^2\psi}{dx^2} + V(x)\psi = E\psi \tag{2.1}$$

Equation 2.1 in and outside the well takes the following form:

$$for \quad 0 \geq x \geq a \qquad V(x) = \infty \rightarrow \psi(x) = 0 \tag{2.2}$$

which refers to the zero probability of finding the particle out of the well/box, whereas equation 2.3 defines the wavefunctions inside the box.

$$for \quad 0 < x < a \qquad V(x) = 0 \rightarrow \frac{-\hbar^2}{2m}\frac{d^2\psi}{dx^2} = E\psi \tag{2.3}$$

Defining $k = \sqrt{\frac{2mE}{\hbar^2}} > 0$, equation 2.3 will then look like:

$$\frac{d^2\psi}{dx^2} = -k^2\psi \tag{2.4}$$

which has a general oscillatory solution,

$$\psi(x) = Asin(kx) + Bcos(kx); \tag{2.5}$$

To find A and B we match the solutions at the boundaries x = 0 and x = a by imposing continuity:

$$\psi(0) = \psi(a) = 0 \tag{2.6}$$

So $\psi(0) = 0 \rightarrow$ B=0, and $\psi(a) = 0 \rightarrow Asin(ka) = 0$ with $ka = n\pi$, which implies the following set of solutions:

$$\psi_n(x) = \begin{cases} A_n sin(\frac{n\pi x}{a}) & for \quad 0 < x < a \\ 0 & for \quad 0 \geq x \geq a \end{cases}$$

Normalizing the eigenfunctions according to equation 2.7 leads to the values of A_n in equation 2.8.

$$\int_{-\infty}^{\infty} |\psi_n|^2 dx = |A_n|^2 \int_0^a sin^2(\frac{n\pi x}{a}) dx = \frac{|A_n|^2 a}{2} = 1 \tag{2.7}$$

$$|A_n| = \frac{2}{a}, \quad \forall \quad n. \tag{2.8}$$

Hence the energy eigenfunctions of the infinite square well are a discrete series of *sine* functions labeled by n (Figure 2.2). An eigenfunction labeled by n has n-1 zero crossings, called nodes.

Since n is a discrete spectrum, a quantum particle inside an infinite square well can only take specific, quantized values of E, unlike classical mechanics. The energy levels are found by substituting $k_n = n\pi/a$ in equation $k = \sqrt{\frac{2mE}{\hbar^2}}$. The discrete energy levels are represented until n=4 on the right hand side of Figure 2.2.

$$E_n = \frac{n^2\pi^2\hbar^2}{2ma^2} \qquad for \quad n = 1, 2, 3... \tag{2.9}$$

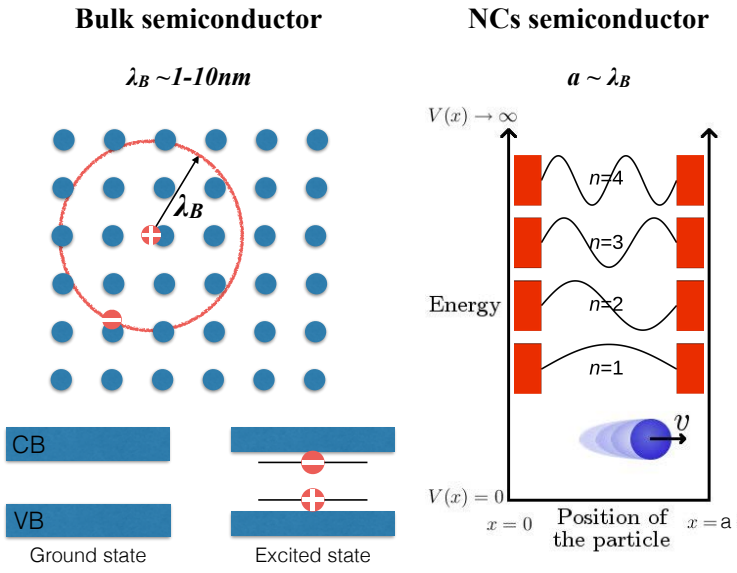

Figure 2.2: Main differences between electron-hole space separation in bulk and nano-semiconductors. Left: Spatial coherence of the excitonic state in bulk semiconductors (not to scale) Right: Schematic representation of a particle confined in a crystallite of the size of the Bohr radius with its consequent discrete energy levels.

Notice that the smaller the dimension of the quantum well, i.e. higher quantum confinement, the larger will be the separation between energetic levels. This property is directly correlated with the light emission observed in nanocrystals. There is a blue shift of the emission wavelength of smaller particles and a red shift for bigger ones.

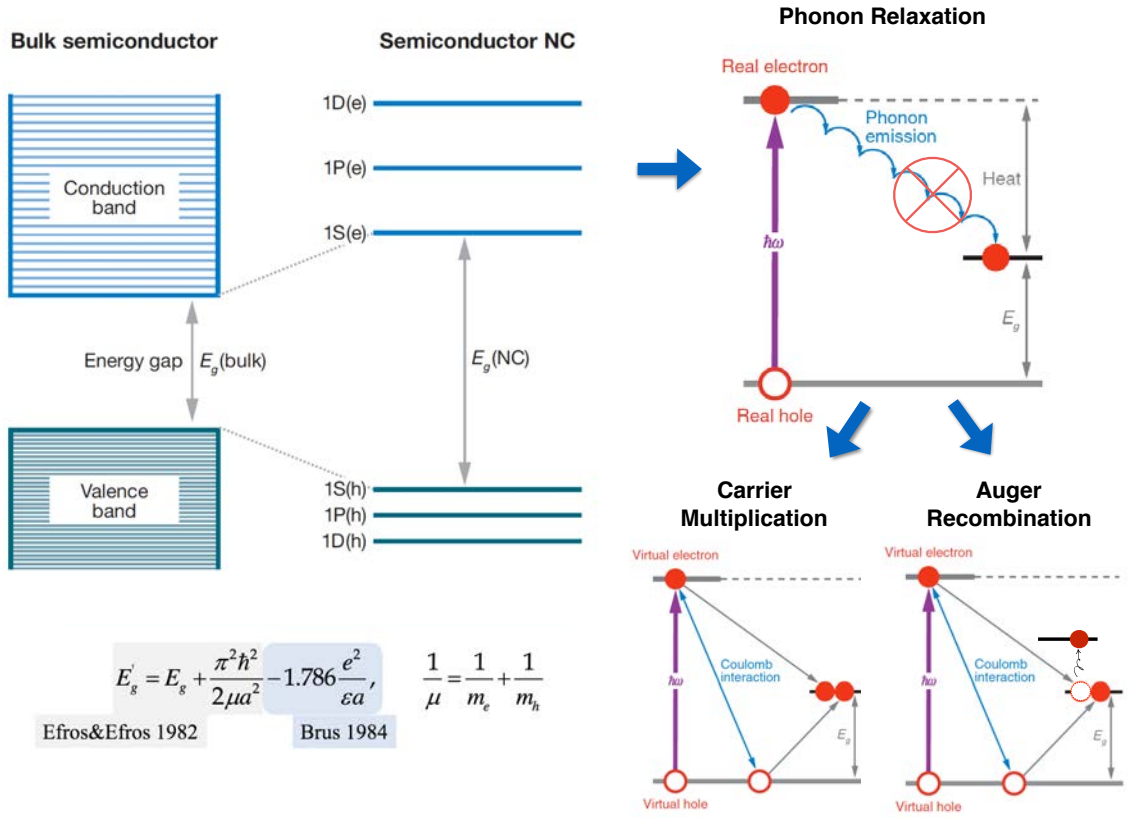

Figure 2.3: Schematics of the main differences in the electronic structure of bulk and semiconductor nanocrystals and subsequent interband transitions as published in [72, 73]. The reduced phonon recombination rate and Coulomb carriers interactions give rise to carrier multiplication (CM) and Auger recombination (AR).

Quantum confinement is not only responsible for a larger band gap but also for the discretization of the energy levels in the conduction and valence band, which is usually a continuum spectrum for bulk semiconductors. One of the main implications of this atomic-like conduction and valence band is the suppression of the phonon-assisted relaxation of the electrons thermalizing within the conduction band, since not all phonon transitions are allowed. Basically, the energy between different levels of the same band is larger than the thermal energy of the crystal $\sim$ 25 meV. This property promotes two very interesting processes: carrier multiplication (CM) through impact ionization and Auger recombination (AR). Both processes are represented in Figure 2.3 and they are basically the main source of open decay channels and non-radiative transitions within nanocrystals under high energy excitation.

Previous experimental [74, 75] and theoretical studies [76] indicate that in zero dimensional (0D) NCs, Auger recombination is a three-particle decay process, which is a result of the fact that Coulombic e-h interaction energies in NCs are much smaller than carrier confinement energies, and hence, electron and hole motions in these NCs are not correlated. The electron-hole pair binding energy in bulk PbSe is 0.6 meV, while confinement energies in the NCs under investigation are 1 eV.

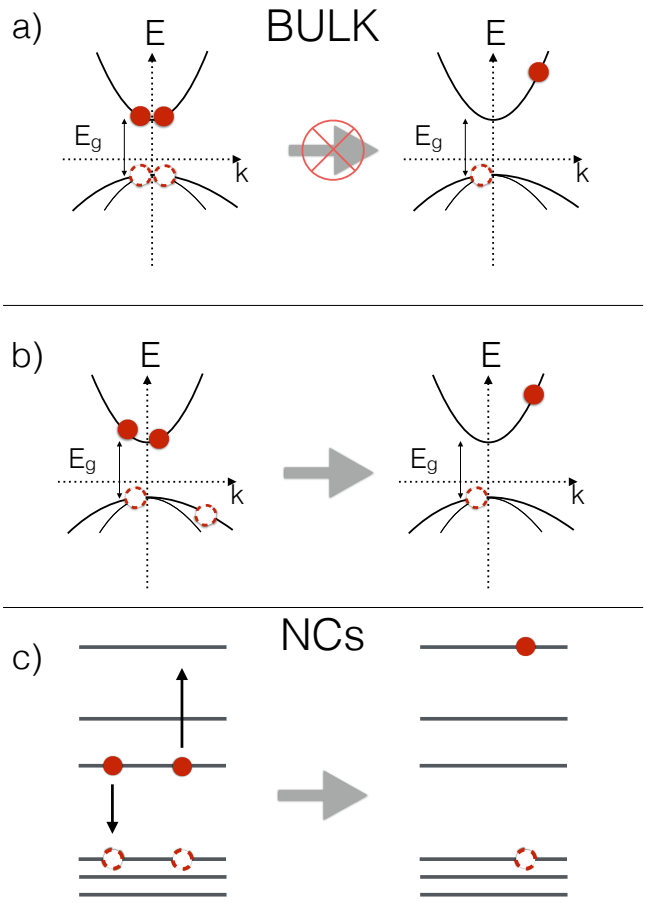

Figure 2.4: Main differences between Auger recombination processes in bulk and nano-semiconductors. (a) Low energy carriers in a bulk semiconductor with energy gap E_g can not undergo Auger recombination (AR) due to requirements that energy (E) and momentum (p) are conserved simultaneously. (b) Higher energy carriers can undergo AR in a bulk semiconductor. (c) Low-energy carriers in a semiconductor NC can undergo AR due to the discrete character of the energy levels, which results in relaxation of translational momentum conservation.

The constraints imposed upon AR by momentum conservation in the bulk are expected to be relaxed in nanocrystals [76]. Carriers contained within NCs reside in discrete, atomic-like levels (see Figure 2.4), which are classified according to angular momentum (J) but not translational momentum [77]. Thus, it is expected that AR in NCs must conserve total carrier energy and angular momentum but not translational momentum. In this case, AR should occur without an energetic barrier because carrier energy and M are not directly related, and hence, the carrier that is re-excited can easily access an energy-conserving state with an appropriate value of J [78]. This difference from bulk semiconductors has several implications. The lack of a barrier to AR in NCs means that (i) low-energy e-h pairs are available for Auger recombination whereas in the bulk they are not (compare Figure 2.4(a) and (c)), (ii) temperature does not influence the Auger recombination rates, (iii) the nanocrystal's size (which defines Coulomb coupling) and wave function overlap determine AR rates rather than the energy gap, and (iv) the inverse-AR process of impact ionization may also be barrierless.

Another main difference between bulk and semiconductor nanocrystals is given by the number of electron-hole pairs which are created as a function of the excitation density. Table 2.1 summarizes the density of carriers for low, moderate and high excitation. We can see that creating one e-h pair per nanocrystal is enough to reach a very high carrier density. If the number of electron-hole pairs reaches a mean value of two per each crystallite the regime of population inversion can be reached, where the system may exhibit optical gain.

Table 2.1: **Number of electron-hole pairs created as a function of excitation density in bulk and semiconductor nanocrystals**.

Excitation	Bulk 10^{22} atoms/cm^3	Nanocrystal ~ 1000 atoms
low	$n_{eh} < 10^{16}$ cm^{-3}	$<n_{eh}>_{dot} \ll 1$
moderate	$n_{eh} = 10^{16} - 10^{17}$ cm^{-3}	$<n_{eh}>_{dot} = 1$ $n_{eh} \sim 10^{19}$ cm^{-3}
very high	$n_{eh} > 10^{18}$ cm^{-3}	$<n_{eh}>_{dot} = 2$

2.3 Density of states and energy structure

The density of states $\rho(E)$is defined as the number of states per energy per volume unit of real space and determines the energy and momentum distribution of a particular number of electrons (holes) within a subband. It follows the expression:

$$\rho(E) = \frac{dN}{dE} \tag{2.10}$$

In the $\vec{k}$-space, the total number of states N is equal to the volume of a sphere of radius $|\vec{k}|$, divided by the volume occupied by one state and divided by the volume of the real space:

$$N = 2\frac{4\pi k^3}{3}\,\frac{1}{2\pi R^3}\,\frac{1}{R^3} = 2\frac{4\pi k^3}{3(2\pi)^3} \tag{2.11}$$

The term $\frac{1}{2\pi R^3}$ is obtained after imposing the periodicity condition of the envelope function when calculated for a vector from the Bravais lattice R. The factor 2 has been introduced to allow for double occupancy of each state by different carrier spins. The density of states can be expressed as following:

$$\rho(E) = \frac{dN}{dE} = \frac{dN}{dk}\frac{dk}{dE} \tag{2.12}$$

$$\frac{dN}{dk} = 2\frac{4\pi k^2}{(2\pi)^3} = (\frac{k}{\pi})^2 \tag{2.13}$$

In addition, the parabolic bands of the effective mass approximation give:

$$k = \sqrt{\frac{2m^*E}{\hbar^2}} \tag{2.14}$$

$$\frac{dk}{dE} = \left(\frac{2m^*}{\hbar^2}\right)^{\frac{1}{2}} \frac{E^{-\frac{1}{2}}}{2} \tag{2.15}$$

which finally gives the density of states for a bulk semiconductor:

$$\rho(E) = \frac{1}{2\pi^2}\left(\frac{2m^*}{\hbar^2}\right)^{\frac{3}{2}} \frac{E^{\frac{1}{2}}}{2} \tag{2.16}$$

Thus, the density of states within a band and around a minimum where the energy can be represented as a parabolic function of the momentum, is a continuous function and is proportional to the square root of the energy.

If we do the same analysis for 1D, 2D and 3D highly confined systems, i.e. quantum wells (nanoplatelets), wires and dots, we obtain the density of states summarized in the following Table 2.2.

Table 2.2: **The density of states for reduced-dimensionality systems**.

Dimension of confinement	$\rho(E)$
3D	series of δ functions
2D	$\frac{1}{\pi^2}\left(\frac{2m^*}{\hbar^2}\right)^{\frac{1}{2}} \frac{E^{-\frac{1}{2}}}{2}$
1D	$\frac{1}{2\pi^2}\left(\frac{2m^*}{\hbar^2}\right)^{1} E^0$
0D	$\frac{1}{2\pi^2}\left(\frac{2m^*}{\hbar^2}\right)^{\frac{3}{2}} \frac{E^{\frac{1}{2}}}{2}$

If there are many (n) confined states within the quantum wire with subband minima E_i, then the density of states at any particular energy is the sum over all the subbands below that point, which can be written as:

$$\rho^{2D}(E) = \sum_{i=1}^{n} \frac{1}{\pi^2}\left(\frac{2m^*}{\hbar^2}\right)^{\frac{1}{2}} \frac{(E-E_i)^{-\frac{1}{2}}}{2}\Theta(E-E_i) \tag{2.17}$$

The situation for quantum dots as reflected in Table 2.2 is very different. As the particles are confined in all directions, then there are no dispersion curves, and thus the density of states is just dependent upon the number of confined levels. One single isolated dot would therefore offers just two (spin-degenerate) states at the energy of each confined level, the plot of the density of states versus energy would be a series of δ-functions.

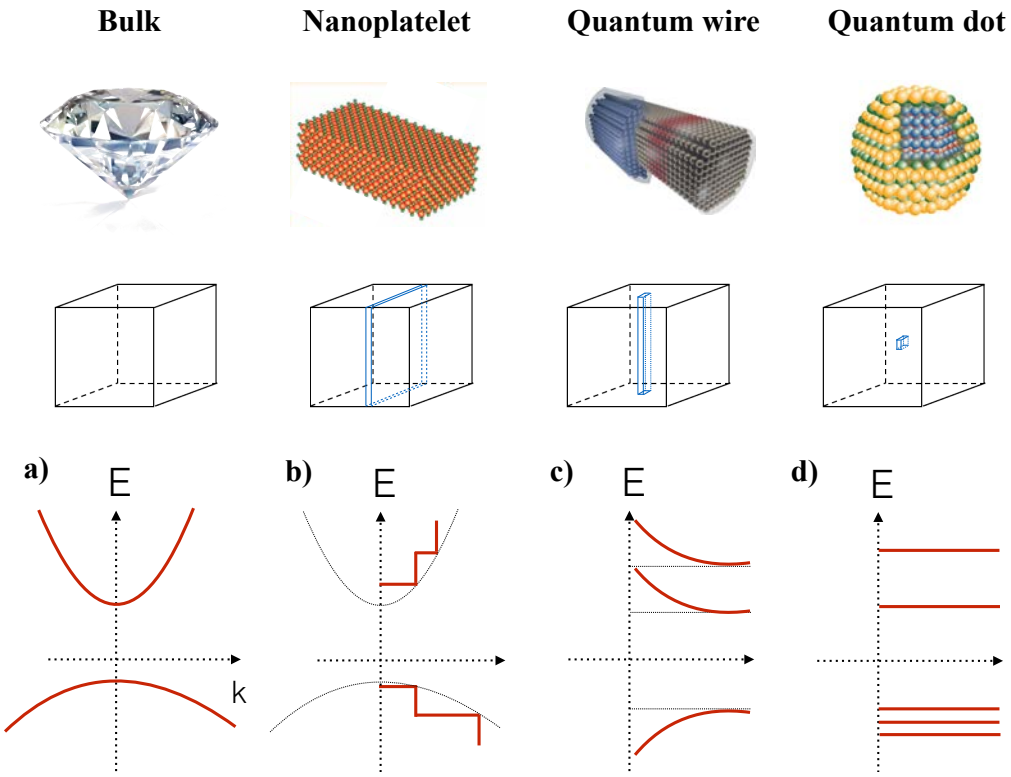

Figure 2.5: Schematic of density of states as the system dimensionality is reduced. The density of states in different confinement configurations: (a) bulk; (b) quantum well or nanoplatelet; (c) quantum wire; (d) quantum dot. Adopted from [79]. Not to scale.

Figure 2.5 illustrates the density of states for bulk and semiconductor nanocrystals with different degrees of confinement. The conduction and valence bands split into overlapping subbands that become successively narrower as the electron motion is restricted in more dimensions. As illustrated for the quantum wire and quantum dots, these confined systems can present different heterostructures like a core/shell fabrication. However the curves of density of states presented in Figure 2.5 are representative of an ideal nanocrystal with one layer or core, as illustrated for the nanoplatelets or quantum wells.

One way to experimentally visualize the density of states for a quantum dot system is to look at the absorption or excitation spectrum of these materials. For instance, a better understanding of the valence subbands is necessary. Basically, the formulations developed in the previous section are enough to understand the electronic states of the conduction band. However, because of the complex, multi-subband character of the valence band typical for many semiconductors, one can only explain the NC valence-band structure by considering confinement-induced mixing between different subbands [80]. In the case of a quantum dot, the valence-band Hamiltonian contains both the crystal-lattice and NC-confinement potentials. For this situation, the true quantum number is the total angular momentum, $\vec{F}$, which is a sum of the Bloch-function angular momentum, $\vec{J}$, and the orbital momentum of the hole envelope function, $\vec{L}$, hence $\vec{F} = \vec{J} + \vec{L}$. Usually, the valence band states will be denoted by nL_F. Calculations of the size-dependent hole energies in CdSe quantum dots taking into

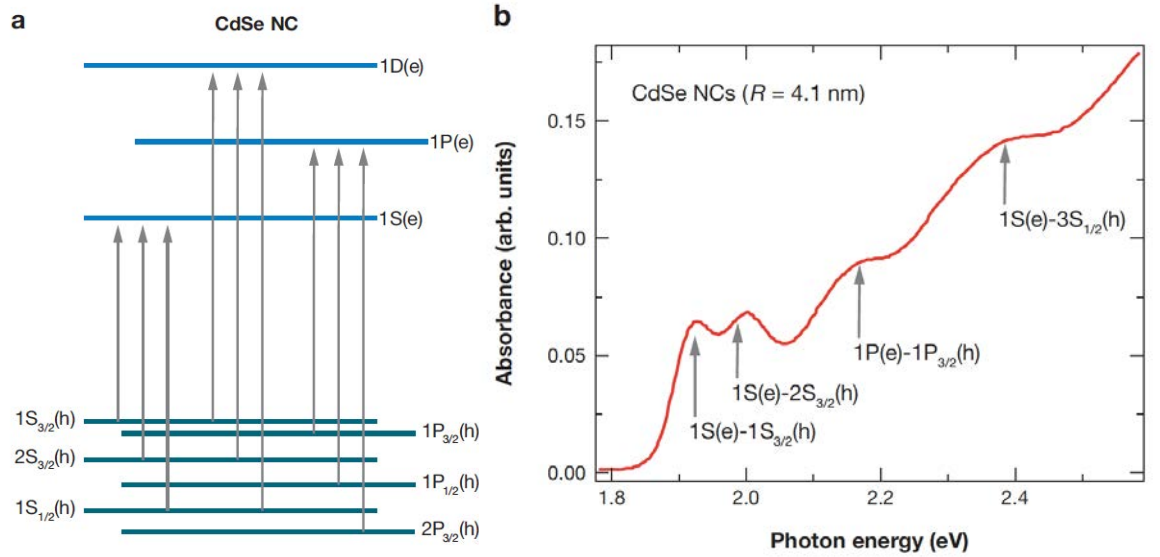

Figure 2.6: Interband optical transitions of colloidal CdSe nanocrystals a) The arrows indicate the allowed transitions between conduction and valence subbands. (b) A linear (ground-state) absorption spectrum of CdSe NCs with a mean radius of 4.1 nm. Arrows mark the positions of four well-resolved transitions that involve either the 1S or 1P electron states. As published in [72]

.

account the mixing between heavy, light, and spin-orbit split-off valence subbands present the levels $1S_{3/2}$, $1P_{3/2}$, and $2S_{3/2}$ as the three lowest states. Optical transitions that involves these states are well resolved in a linear absorption spectrum of colloidal CdSe NCs as shown in Figure 2.6.

2.4 Multiexcitonic dynamics

The creation of multiexcitons and its subsequent radiative recombination increase the quantum efficiency of the NC and reduce the emission time due to the creation of many decay channels. However, it is not a condition strictly necessary to achieve fast recombination time. Another way would be to increase the oscillator strength of the radiative transition since decay time (τ) and oscillator strength are both inversely proportional as stated in the following equation:

$$\frac{1}{\tau} = \frac{2ne^2\omega_{21}f_{21}}{mc^3} \tag{2.18}$$

A fast emission due to the giant oscillator strength has been experimentally observed in excitons weakly bound to impurities and defects. Since the matrix element of the transition is a volumetric weighted integral along all possible states, the localization of the exciton in a

region of the lattice which involves several unit cells contributes to a significant increase of the oscillator strength. This spatial coherence of the excitation can be achieved either by a defect-bound e-h pairs or by reducing the size of the semiconductor in the form of nanocrystals. Up to a limited particle size, the exciton wavefunction is assumed to be coherent over the whole particle, so particle size replaces the range of the exciton and the coherent phasing of dipoles over many unit cells results in a dipole matrix element much larger than that achieved by a single atom.

The giant oscillator strength is manifested by the fast single-exciton photoluminescence decay kinetics present in CdSe nanoplatelets and quantum dots in the order of a few hundreds of picoseconds. Furthermore, single-exciton binding energies in the order of ∼100 meV for these systems guarantee a stable excitonic population at room temperature which contributes considerably to the high quantum efficiency of fast emission under laser excitation.

The dynamics of the multicarrier interaction and eventual recombination exhibited in nanocrystals will be analyzed on the basis of Auger recombination (AR) and carrier multiplication (CM) as reviewed in [72, 73].

2.4.1 Carrier multiplication

In a conventional gamma absorption scenario, a photon with an energy $\hbar\omega \geq E_g$ results in a single electron-hole pair, whereas the photon energy in excess is dissipated through phonon relaxation in the lattice. Strong carrier-carrier interactions can in principle open a new relaxation channel, in which the excess energy does not dissipate via electron-phonon scattering, but it is instead transferred to a valence band electron, exciting it across the band gap in a collision-like, impact ionization event. As result, a gamma absorption ends up with the creation of two electron-hole pairs instead of one, if energy conservation allows it. This process is usually known as carrier multiplication and finds plenty of application in the photovoltaic technology to increase the power conversion efficiency of solar cells.

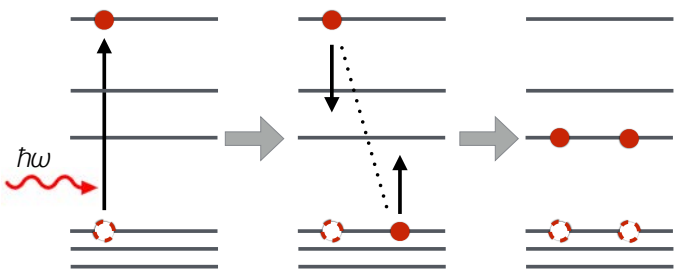

Figure 2.7: A sequence of events leading to carrier multiplication. Left: Absorption of a high-energy photon producing a hot conduction-band electron. Middle: this electron transfer its excess energy to a valence band electron via an impact-ionization-like event, exciting it across the band gap. Right: photogeneration of two electron-hole pairs.

The ideal case for carrier multiplication yield is described by a staircase in which each increment of the incident photon energy by the band gap results in a new e-h pair, which increases the quantum efficiency (QE) by 100%. QE is defined as the number of photons emitted product of a radiative recombination of electron-hole pairs. This ideal behavior is shown in Figure 2.8 together with the real scenario obtained using bulk semiconductors. In contrast to the theoretical limit where the threshold energy to create two e-h pairs is exactly two times the band gap energy, bulk semiconductors exhibit a $\hbar\omega_{th} \geq 4E_g$ and the linear growth is much slower. The inverse slope of this dependence represents a measure of the e-h pair creation energy, i.e. ϵ_{eh} is the energy required to generate a new e-h pair at spectral energies above $\hbar\omega_{th}$. According to a large body of experimental data we can conclude in,

$$\hbar\omega_{th} = \epsilon_{eh} + E_g \tag{2.19}$$

For the ideal case (dashed line in Figure 2.8), $\hbar\omega_{th}$=2E$_g$ and ϵ_{eh} = E$_g$. However, due to momentum conservation a new e-h pair produced through impact ionization must carry non-zero kinetic energy. This means ϵ_{eh} increases by the value of the kinetic energy E$_k$, which in the free carrier approximation can be expressed as E$_k$ = 1.8E_g. Phonon losses (E$_{ph}$) also increase the realistic ϵ_{eh}, approximately between 0.5-1 eV. In conclusions, we have that at least $\epsilon_{eh} = E_g + E_k + E_{ph} \sim 3E_g$, instead of the ideal value of E_g. Respectively, the carrier multiplication threshold is at least 4E$_g$ as shown by the solid black line in Figure 2.8, starting at 4.5 and finishing at 8 $\hbar\omega/E_g$.

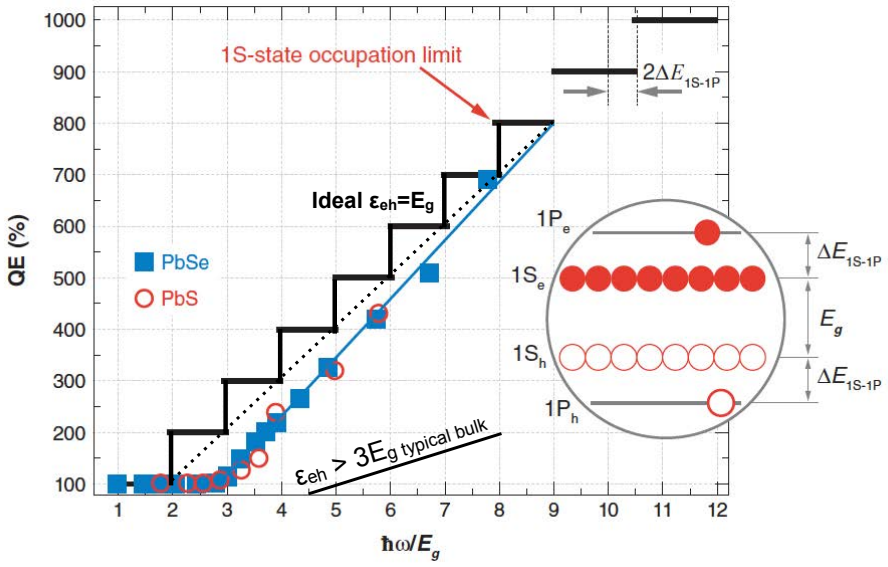

Figure 2.8: Theoretical and experimental quantum efficiency (QE) of photon absorption to e-h pair conversion as a function of pump-photon energy normalized by the energy gap. The black dashed line represents the energy-conservation-defined-limit which assumes all the excess energy above the band gap could be used to create of a new e-h pair. The black solid line is the typical dependence observed for bulk semiconductors which contrasts with experimental QEs measured for PbSe (blue solid squares) and PbS (red open circles) nanocrystals. As published in [72] and [73].

Having analyzed the bulk semiconductor case, let's have a look at semiconductor nanocrystals. Here, the phonon losses are highly reduced due to a discrete energy levels in the conduction band. These discrete, atomic-like levels are classified according to angular momentum but not translational momentum so there is a relaxation of translational momentum, conservation rules which also reduces E_k. In this way, measurements done using PbSe and PbS quantum dots have proven to considerably decrease $\hbar\omega_{th}$ to 3 times E_g as shown in Figure 2.8, with the outstanding result of 700% QE for a gamma absorption. In this case, there is not Auger recombination taking place and all the e-h pairs created by CM are able to decay radiatively.

A biexciton (XX) created via CM in a neutral nanocrystal could decay radiatively or through Auger recombination (AR), in which case the overall decay rate will be faster but the quantum efficiency will decrease considerably. If we assume only radiative decay, looking at the probability of recombination ($P_r = \frac{1}{\tau_r}$) of two electron-hole pairs, we find that the biexciton radiative recombination time (i.e. τ_{r-xx} as shown in Figure 2.9) is 4 times faster than that of the radiative exciton (τ_{r-x}). Each electron will be able to recombine with 2 holes, so that will open 4 different channels. This factor 4 is characteristic of quantum dots where the confinement is high in 3D dimensions, however studies suggest a factor 2 for nanoplatelets where the confinement is 1 dimensional and the electron-hole pairs are allowed to move in a plane. The distance between e-h pairs will allow each electron just to recombine with one hole, opening 2 channels instead of 4. This fact has been experimentally confirmed in [75] where a series of CdSe elongated NCs (nanoplatelets) were used to study the effect of the 0D to 1D transition of non-radiative Auger recombination.

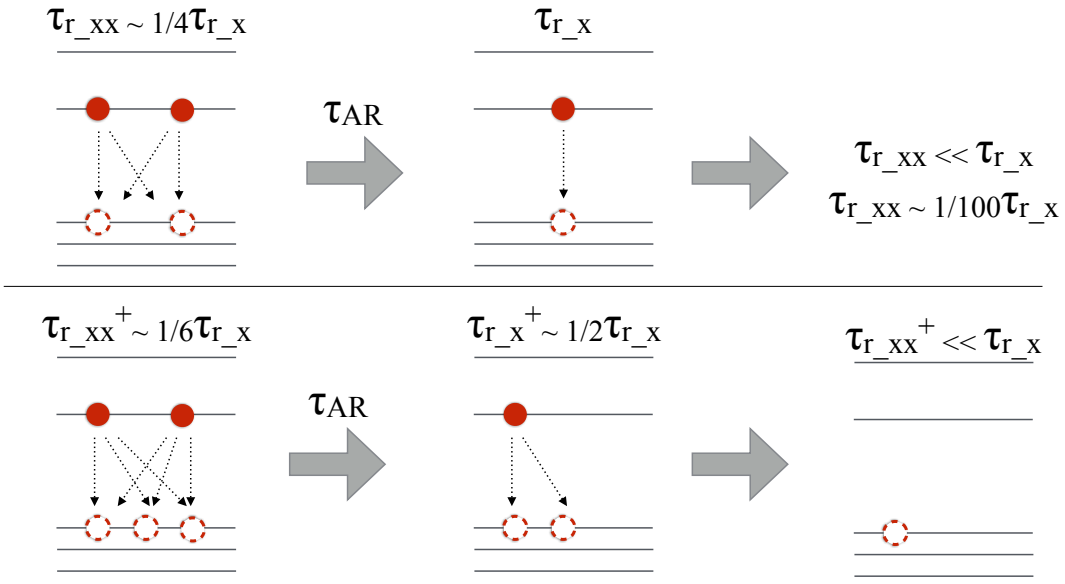

Figure 2.9: Sequence of recombination events in the case of carrier multiplication in a neutral (top) and charged (bottom) nanocrystal.

In this way, the comparison between the single-excitonic (X) and biexcitonic (XX) decay times offers a quantitative path to determine if carrier multiplication is happening in an

efficient way or whether Auger recombination is dominating. Single-excitonic decay time τ_X is usually determined under low excitation density, where the number of e-h pairs per nanocrystal is much less than one. Incrementing the excitation density will usually shorten the decay rate with the consequent spectral shift in the wavelength of emission by the value of the binding energy of the multiexcitons created.

One of the most direct approaches of determining the biexciton binding energy is based on the analysis of relative spectral positions of the biexciton and single-exciton emission lines. Radiative recombination of a biexciton (XX) produces a photon ($\hbar\omega_{XX}$) and an exciton (X): $XX \longrightarrow X + \hbar\omega_{XX}$. Because the final exciton can be in either its ground or excited state, the shift of the biexciton emission band with respect to the single-exciton peak, in addition to being affected by the exciton-exciton interaction energy, can also be contributed by the excess energy of the surviving exciton with respect to the ground-state single-exciton level (E_X^0). If we assume that the biexcitons preferentially decay into ground-state excitons, the shift of the biexciton line ($\hbar\omega_{XX} = E_X^0 + \Delta_{XX}$) with respect to the single-exciton band ($\hbar\omega_X = E_X^0$) provides a direct measure of the exciton-exciton binding energy: $\Delta_{XX} = \hbar\omega_X - \hbar\omega_{XX}$.

When the excitation density increases, the probability of having a charged e-h pair, i.e. trion, X^+, 1 electron and 2 holes or viceversa X^-, 2 electrons and 1 hole also increases. This can lead to a shortening in the decay rate of the charged biexciton τ_{XX^+} due to a different number of channels which will be open, as illustrated at the bottom of Figure 2.9. In this case, a factor of 6 between single-excitonic and biexcitonic recombination decay times is characteristic of a charged biexciton population. As a conclusion, a factor of 100 between biexcitonic and single-excitonic emission is usually accepted as a signal of prominent Auger recombination in the dynamic of the multiexcitonic population [81].

2.4.2 Auger recombination

Auger recombination is a process in which the e-h recombination energy is not emitted as a photon but is transferred to a third carrier instead, usually another e^-. This third carrier is then promoted to a higher-energy level, which can be within or outside the nanocrystal (Auger photoionization). Basically, we are talking of two-electron process collision in which a substantial energy change occurs. The efficiency of Auger processes, which are mediated by Coulomb electron-electron interactions differ greatly between the atomic and bulk semiconductor cases. In atomic systems, for which the electron-electron coupling is much stronger than the electron-photon coupling, the rates of Auger transitions are significantly greater than the rates of the radiative transitions. As a result, the decay of the multi-electron states in atomic systems is dominated by Auger processes. In bulk semiconductors, Auger recombination is inhibited by kinematic restrictions imposed by energy and translational-momentum conservation. However, because of relaxation of momentum conservation and the spatial proximity of the carriers, Auger recombination rates increases dramatically in nanocrystals, especially in quantum dots where the confinement is in 3D.

The five basic processes of Auger recombination are shown in Figure 2.10. In process 1 two electrons collide in the vicinity of a hole, resulting in the e-h recombination and the excess energy absorbed by the other electron. Process 2 involves a phonon whose momentum helps to relax conditions in the energy and momentum of the colliding particles. In process 3 and 4 a localized state is involved and process 5 describes an internal transition in a donor-acceptor pair.

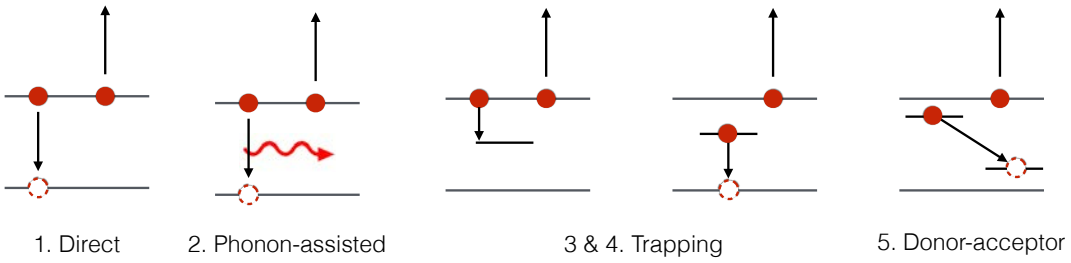

Figure 2.10: Five basic Auger processes. Five more exits in which a hole carries away the energy. The reverse of these processes lead to ten basic processes of impact ionization.

The rate for the direct Auger effect is closely related to the electron-electron scattering rate with the only difference that one of the electrons have its final state in another band. The rate will be given by the familiar equation of first-order perturbation theory:

$$W_{recomb} = \int_f \frac{2\pi}{\hbar} |M|^2 \delta(E_f - E_i) dS_f \tag{2.20}$$

where, f and i refer to the final and initial states, the integral is over all final states S_f, and the time dependence is subsumed in the delta function conserving energy. M is the matrix element of the transition.

In order to calculate the Auger recombination rate, let's assume that the incident electron in the conduction band, which has a wavevector $\vec{k}_1$ and a defined spin, collides with a second electron in the conduction band, which has a wavevector $\vec{k}_2$ and either an identical spin or its opposite. Assuming the wavevector $\vec{k}_1'$ refers to the valence band state and the wavevector $\vec{k}_2'$ refers to the high-energy state in the conduction band. The matrix element for process 1, the direct collision of two electrons of identical spin, is:

$$M_{12} = \frac{1}{V^2} \int\int u^*_{v\vec{k}_1'}(\vec{r_1}) e^{-i\vec{k}_1'\cdot\vec{r_1}} u^*_{c\vec{k}_2'}(\vec{r_2}) e^{-i\vec{k}_2'\cdot\vec{r_2}} \times \frac{e^2 \cdot e^{-q_0|\vec{r_1}-\vec{r_2}|}}{4\pi\epsilon|\vec{r_1}-\vec{r_2}|} u^*_{c\vec{k}_1}(\vec{r_1}) e^{-i\vec{k_1}\cdot\vec{r_1}} u^*_{c\vec{k}_2}(\vec{r_2}) e^{-i\vec{k}_2\cdot\vec{r_2}} d\vec{r_1}\cdot d\vec{r_2} \tag{2.21}$$

Therefore, determining the matrix element for all the different processes can be a very long and tedious calculation. So, let's just apply some basic statistic in order to get the feeling about the recombination rate for the Auger effect.

Let's assume that state $|\mathbf{k}_2\rangle$ is full (electron in the conduction band before being transferred to a more energetic level), $|\mathbf{k}_1'\rangle$ is empty (occupied by a hole since it is in the valence band) and $|\mathbf{k}_2'\rangle$ is empty (electron in the more energetic level). Assuming non-degenerated statistics, we can calculate the following weighting factor as the probability of having an electron with wavevector $\vec{k_2}$ and a hole with wavevector $\vec{k_1'}$,

$$P(\mathbf{k}_2, \mathbf{k}_1') = f(\mathbf{k}_2)(1 - f(\mathbf{k}_1')) \tag{2.22}$$

where for near thermal equilibrium,

$$f(\mathbf{k}_2) = \frac{n}{N_c} e^{-\frac{E_{c\mathbf{k}1'}}{k_B T}} \tag{2.23}$$

$$1 - f(\mathbf{k}_1') = \frac{p}{N_v} e^{-\frac{E_{v\mathbf{k}2}}{k_B T}} \tag{2.24}$$

Here, n and p are the electron and hole densities, N_c and N_v are the effective densities of states in the conduction and valence bands, respectively.

The recombination rate will be proportional to the density of electron-hole pairs created in the material which makes it an important loss process in semiconductors in which carriers densities are of the order of 10^{18} e-h/cm^3, particularly at room temperature or above. Due to the high carrier density exhibited in nanocrystals $\sim 10^{19}$ e-h/cm^3, when there is an average of 1 e-h pair per crystallite, Auger recombination is one of the main non-radiative processes. This has been experimentally proven by [74] where CdSe quantum dots of different sizes were used to study confinement-induced modifications in Auger-type interactions during the transformation from bulk crystalline to atomic regimes. Experimental data for the Auger effect in QDs were analyzed within a bulk semiconductor approach by introducing an effective carrier concentration in the nanocrystal ($n_{eh} = \frac{N}{V_0}$ where N is the number of e-h pairs per dot and V_0 is the dot volume) and a cubic carrier decay rate $C_A n_{eh}^3$ (with C_A the Auger constant).

Experimental data of multiexcitonic recombination were successfully found to follow the model proposed and the time-constant ratios predicted by the bulk semiconductor model held for all QDs sizes. Simple bulk material reasoning would suggest that the enhancement in the Auger decay in smaller particles is caused by an effective increase in carrier concentrations resulting from the increased spatial confinement. However, the R^3 size dependence of relaxation times measured experimentally was different from the R^6 dependence predicted by the bulk semiconductor model, which shows that in QDs, the Auger constant depends on the particle size. This is also indicated by calculations of QD Auger ionization.

Previous studies [75] have shown a transition from cubic to quadratic Auger recombination decay from quantum dots to nanoplatelets, especially as the nanocrystal aspect ratio is increased above 8. This observation indicates that in long quasi-1D nanoplatelet, Auger decay occurs as a result of bimolecular, exciton-exciton interactions. The effect of sample

dimensionality on its optical-gain performance was also observed, concluding that the use of elongated NCs allows to reduce non-radiative carrier losses arising from Auger recombination compared to spherical NC emitting at the same wavelength. This reduction leads to an increased optical-gain lifetime and an extended gain spectral range.

2.4.3 Heterostructures

As explained in the previous section, the multiexciton Auger recombination rate is linearly proportional to the particle volume, which is sometimes known as V-scaling. Although Auger lifetimes exhibit a quick increase with quantum dot size, they are still in the sub-nanosecond timescale, even in large QDs, with sizes reaching that of a bulk exciton. An alternative approach to reduce Auger decay rate is to delocalize the electron-hole pair inducing its spatial separation. This reduces the wavefunction overlap for the ground-state electron and hole participating in the transition. This approach involves the growth of core/shell structures, known as type II quantum dots [82] and dot-in-rod nanostructures. Figure 2.11 illustrates the difference between type I and II showing the spatial distributions of electron (ρ_e) and hole (ρ_h) charge densities, which are nearly identical in type-I NCs. In type-II core/shell NCs, electrons are primarily localized in the core, while holes reside in the shell, which lead to a significant difference in radial distributions of ρ_e and ρ_h.

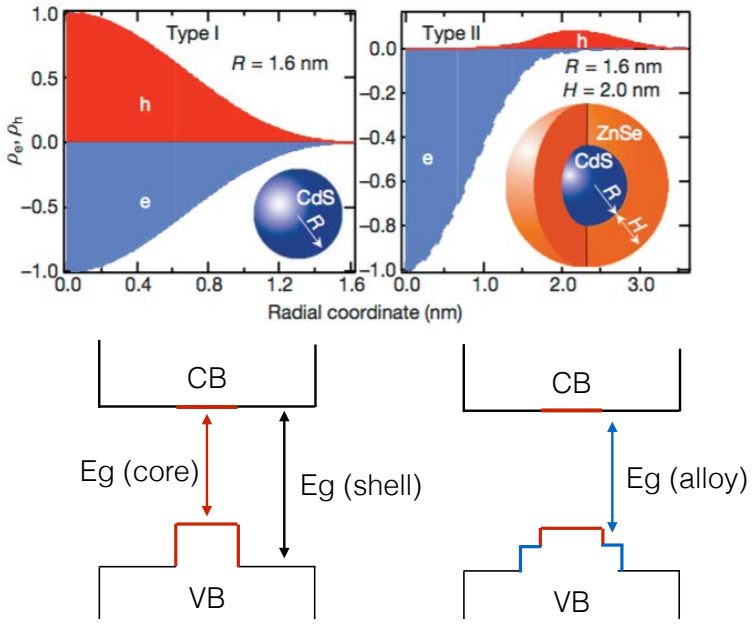

Figure 2.11: Spatial distribution of the charge densities of electrons and holes in quantum dots Top: QDs of type I (calculated for R=1.6 nm) and type II (core/shell heterostructure with R=1.6 nm and H=2.0 nm) as published in [82]. Bottom: Schematic of the band energy diagram for the core/shell and core/alloy/shell heterostructures.

Reduced e-h overlap is one of the main reasons for the suppression of Auger recombination in core/shell heterostructures. However, increasing the shell thickness produces an unexpected and very rapid lengthening of the Auger time constant not explained by the

V-scaling nor the e-h delocalization. This observation suggests that other structural characteristic of the QDs, such as the properties of its interface might play an important role in the decay rate of AR. Theoretical calculations have proven that the shape of the confinement potential has a significant effect in the Auger recombination rate, which was experimentally evaluated by smoothing the potential with the use of alloys between core and shell. This fabrication modifies the shape of the potential from a sharp step-like to a more parabolic profile as shown at the bottom of Figure 2.11. Core/shell heterostructures not only have a significant impact in Auger recombination rate but are widely used to gain in photostability since reduce the blinking considerably [83], i.e. photoluminescence intermittency.

2.5 Applications

Nanocrystals have proven to be an emerging technological platform which offer cheap, versatile production for many optoelectronic components. Their size-dependent electronic band structure together with recent advances in controlling their size, shape, core/shell heterostructure, and surface chemistry have enabled their use in a wide range of photonic applications. Their unique multicarrier dynamic based on wavefunction manipulation and engineering brings the possibility of controlling the properties of semiconductors materials almost at the atomic level.

Industrial applications are new digital plasma displays and white LEDs [84], optical filters, laser modulators [85], electro-optical modulators [86] and further fundamental research developed for quantum computation. Nanocrystals have been applied in the field of biolabeling [87], low-threshold lasing [15, 16, 17] using colloidal solutions, photovoltaics cells [18], direct-injection LED [88], photodetectors [89], and single photon sources for quantum information [19, 20]. Furthermore they are extensively used as sensors in the nanoplasmonic field, which brings an enhancement of the nanocrystal performance and allows to increase their sensitivity to the molecular level [90].

The high quantum yields (QYs) of NC quantum dots (QDs) and fast recombination times under laser excitation have also generated interest in their use as low-cost, high-resolution scintillators for radiation detection [21, 22]. Towards this end, the response of QDs under alpha [91], soft X-ray [92] and γ-ray [25] irradiation has been investigated. Previous studies have lead to the identification of the main bottlenecks when applying semiconductor nanocrystals as radiation detectors such as low stopping power, low transparency due to small Stokes shift and in particular low quantum efficiencies providing an ultrafast but inefficient response under ionizing radiation.

One of the first studies under time-resolved electron excitation [26] has found that highly energetic excitation of CdSe/ZnS core/shell quantum dots produces high yields of weakly emissive multiexcitons and trions, suggesting significant roles of processes such as CM, and scattering-type or Auger-assisted ionization in energy relaxation. These processes result in an

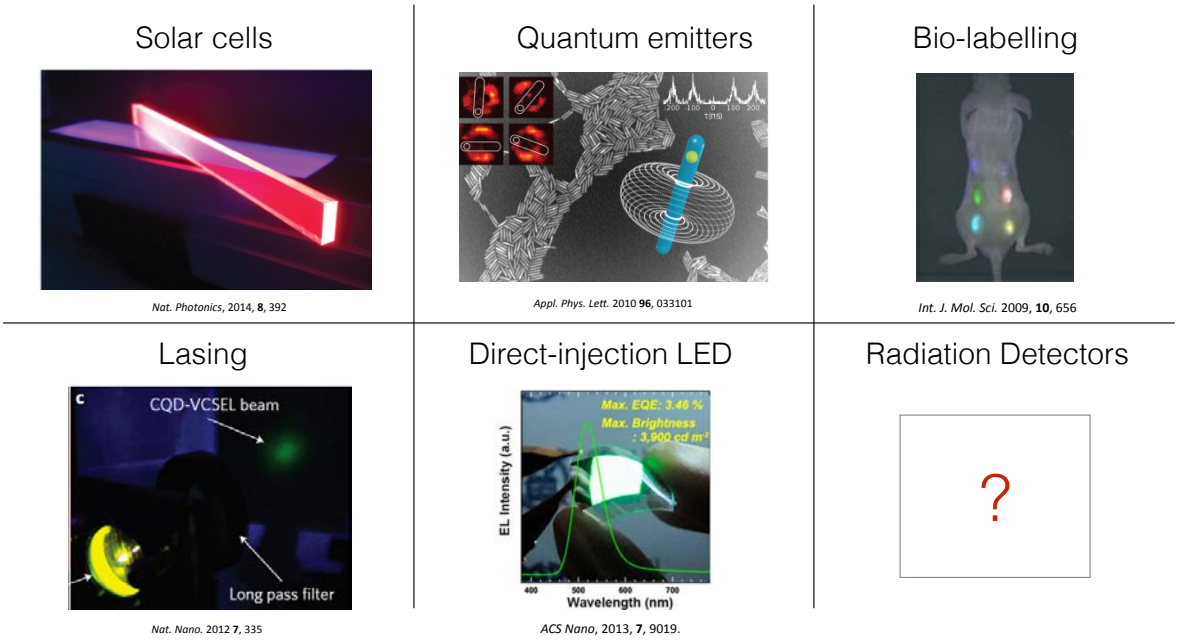

Figure 2.12: Application of nanocrystals in dissimilar fields.

excited-state population that presents a heretofore under-appreciated and in fact dominant channel for loss of absorbed energy in previously reported NC-based gamma-ray scintillation experiments. In this way, its conclusion points towards the possible improvement of future NC-based detectors performance not by using materials with large Stokes shift (as is the prevailing view), but rather through the use of a specific, emerging class of engineered nanomaterials exhibiting suppressed Auger recombination.

As a follow-up of the previous studies, in this thesis we will identify Auger suppressed nanocrystals under laser excitation and determine whether this suppression holds true under ionizing irradiation. The present research will extend to different types of nanocrystals synthesized either in a wet solution or by irradiation methods in the form of dry nanopowders. But first, we need to have a look to the properties of conventional scintillating materials.

Chapter 3

Light transport in scintillating crystals

3.1 Introduction

In this chapter, light output measurements are performed using a set of LYSO crystals with lengths between 5 and 30 mm and 2×2 mm^2 cross section. In this way, the attenuation length of the LYSO will be evaluated as a function of crystal size using different masking, coupling and wrapping configurations. Light yield experimental data is used to validate the light ray tracing Monte Carlo code based on Geant4 classes and libraries. The comparison is done for most configurations showing good agreement with the experiment. This "validation" allows us to use the simulations as a modeling framework in the study of three particular cases:

1. The estimation of the light transfer efficiency for different coupling configurations is done in order to indirectly determine the intrinsic light yield of LYSO crystals. The study uses both analytical and Geant4-based simulation approaches, yielding error bars of 13% around an average value of 39'000 ph/MeV. This result will be experimentally confirmed in the next chapter as a very accurate approximation. Knowledge of the intrinsic light yield sets a quantitative limit to the maximum gain that can be obtained after light extraction optimization.

2. Light output optimization will be considered for geometrically modified crystals in which the readout face is shaped accordingly to Monte-Carlo based simulations. The modification introduced breaks the symmetry for the angle of total internal reflection and allows a maximum gain in light extraction of 30%, which is experimentally confirmed for some samples.

3. Light sharing among different crystals conforming a highly pixelated matrix will be evaluated in order to increase the spatial resolution by changing the crystal-photodetector coupling factor from 1:1 to 4:1. The possibility of obtaining DOI information is also investigated using the same light-sharing guide. One configuration is found to be a promising module candidate for PET systems with encoded DOI information and a spatial resolution about 1.5 mm.

3.2 Light output

The determination of the crystal light output is usually the conventional method to characterize and quantify the scintillators' performance in terms of photons per MeV and energy resolution [93]. Once the photodetector response has been calibrated, i.e. single electron and quantum efficiency, the photopeak signal is used to calculate the number of photons emitted per energy deposited in the crystal. The standard procedure uses a PMT to measure the energy spectrum together with a gamma source, usually ^{137}Cs or ^{22}Na. One of the faces of the crystal is placed with dry or grease contact on the PMT window. For a single LYSO crystal, 2×2×20 mm^3 with all faces polished, the energy spectrum looks like shown in Figure 3.1.

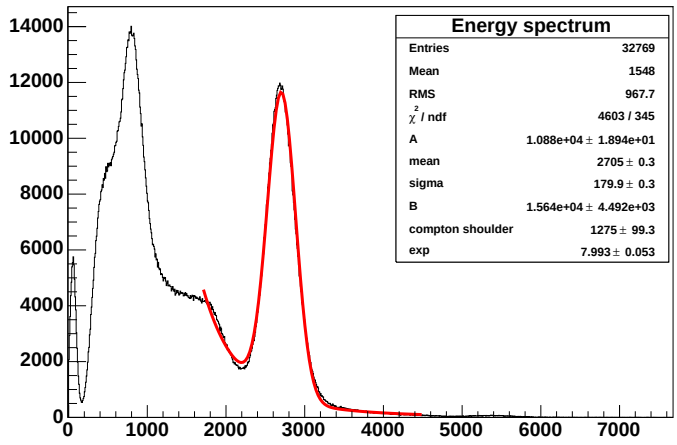

Figure 3.1: Energy spectrum of ^{137}Cs measured with an LYSO scintillator coupled to a PMT. From left to right: noise peak, backscattered peak, the Compton continuous, Compton shoulder and photopeak.

Furthermore, light output measurements under different wrapping and coupling conditions for several crystal lengths allow us to understand deeper the light transport efficiency (LTE). When modeled correctly, LTE is also able to provide information about the scintillator intrinsic light yield (the initial amount of photons emitted in the crystal) following the equation:

$$LY_{out} = LY_{int} \times LTE \tag{3.1}$$

where LTE can take values from 0 to 1.

A complete understanding of the photon dynamic from creation to absorption is fundamental in order to quantify the LTE upper limits. This sets a maximum value for the amount of light that can be extracted if loss processes were minimized or if the light within total internal reflection could be untrapped. To tackle this task, a light transport code that uses Geant4 libraries and classes [94] will be implemented as model for the tracking and transport of optical photons in the crystal in order to estimate LTE values.

3.2.1 Experimental bench

Figure 3.2 shows the main components of the light yield bench. The whole setup is placed inside a temperature controlled light tight box. The PMT used is a Hamamatsu R2059, with a 30 mm diameter fused silica window operated at 2200 V. The charge pulse created is send to the multichannel analyzer which in this case is a 4 channel CAEN Digitizer DT5720D (12 bit 250 MS/s ADC). The trigger is set on the negative edge of the signal and the charge pulse is recorded in a gate as long as ten times the decay time of the scintillator.

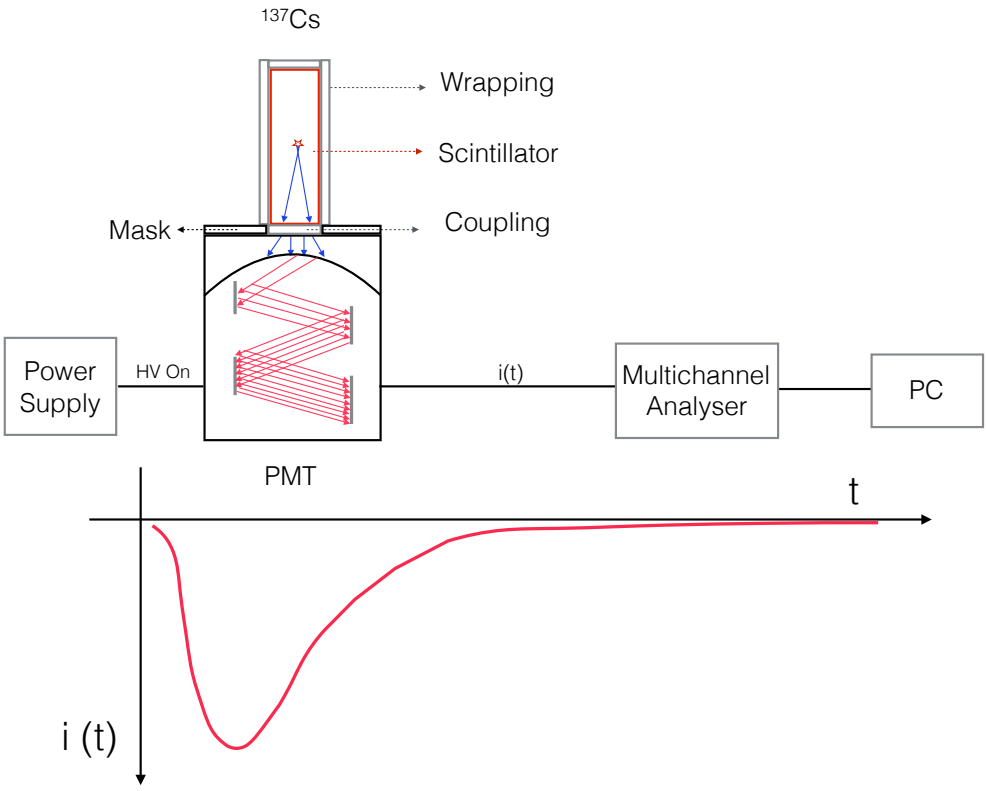

Figure 3.2: Schematic view of the experimental setup used to measure the light output of scintillating crystals.

The light output (expressed in ph/MeV) is calculated using the following equation:

$$LY_{out} = \frac{N_{pe}}{QE_{PMT} \cdot E_{\gamma}} = \frac{Channel \cdot 10^{Atten/20}}{SE_{PMT} \cdot QE_{PMT} \cdot E_{\gamma}} \tag{3.2}$$

Here, the channel used is the one corresponding to the photopeak. SE_{PMT} refers to the single photo-electron signal of the PMT and QE_{PMT} stands for its quantum efficiency. E_γ is the energy of the gamma source used, in this case 662 keV.

PMT Single Photoelectron Response

The signal arising from one single photoelectron is analyzed in order to calibrate the multi-channel digitizer response. The PMT is operated with the high voltage on and no source of light reaching the window. The spectrum is shown in Figure 3.3 (left) and the mean of the Gaussian fit corresponds to the channel of one photoelectron. After this, the energy spectrum of a gamma source is acquired by coupling the crystal to a PMT and the photopeak channel is divided by the single photoelectron channel. The next step, uses the quantum efficiency of the system to convert from photoelectrons to number of photons. The stability of the PMT is monitored by checking the photopeak position for some interval of time as shown to the right-hand side of Figure 3.3. After some minutes the PMT is ready to use.

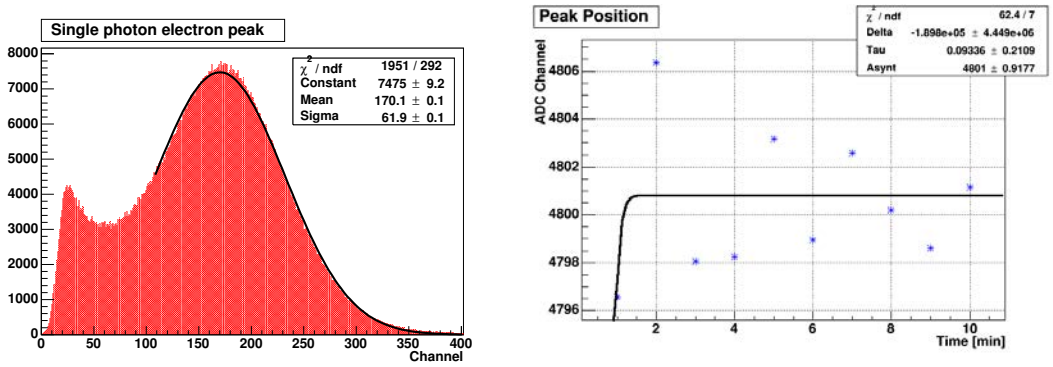

Figure 3.3: PMT calibration and stability. Left: PMT single photoelectron response. Right: PMT stability measured for 10 minutes.

3.2.2 Measurements

Light output measurements were carried out using the setup explained in the previous section and two sets of LYSO crystals from *Crystal Photonics Inc.*[95] between 5 and 30 mm long and cross section of 2×2 mm^2. The first configuration consisted in placing one of the 2×2 mm^2 crystal face dry coupled and not wrapped in contact with the PMT window using two mask sets: a circular holder of 3 mm diameter and a square tight mask with 2.1×2.1 mm^2 hole. This configuration will be identified in the future as dry coupling and is the one which present less statistical uncertainties. Values are reproducible within a 5% deviation, mostly arising from the surface/edges state of different crystals. The rest of the configurations are: 2. grease coupling using both sets of masks and no wrapping, 3. Teflon wrapping, dry coupling using the circular holder, 4. Vikuiti [96] wrapping, dry coupling using also just the circular holder. For all the aforementioned configurations the statistical fluctuation lays within 10% around

the mean value.

The results of these measurements are shown in Table 3.1, where each value is an average of measurements done using two different crystals of the same length. Figure 3.4 shows the same values normalized to the dry and unwrapped configuration of 20 mm crystal length, where the attenuation reaches a plateau after 20 mm. For the dry configuration, using circle or squared mask, the light output deviation for 20 to 30 mm long crystals is around 3% and 2%, respectively. The light attenuation is almost completely saturated and a waveguide behavior is appearing. Also noticeable is a difference in light output when measuring with the different masks, especially for very short crystals where the gamma interaction has a bigger probability to happen at the end of the crystal. The reason for these differences will be discussed in the next section.

Table 3.1: **Light output values for LYSO CPI crystals as a function of its length using different coupling/wrapping configurations**.

	No wrapping (ph/MeV)				**Dry coupling (ph/MeV)**	
Crystal	**Dry**		**Grease**		**Teflon**	**Vikuiti**
length (mm)	□*	◯*	□	◯	◯	◯
5	4911	6773	14936	19582	14664	16474
10	4164	5351	13439	17341	12185	13436
15	3916	4587	13310	15820	9201	12019
20	3693	4195	12693	14100	8404	10607
25	3684	4252	13100	14538	8769	9140
30	3582	4019	11041	13628	7631	8792

* Mask used in the measurements

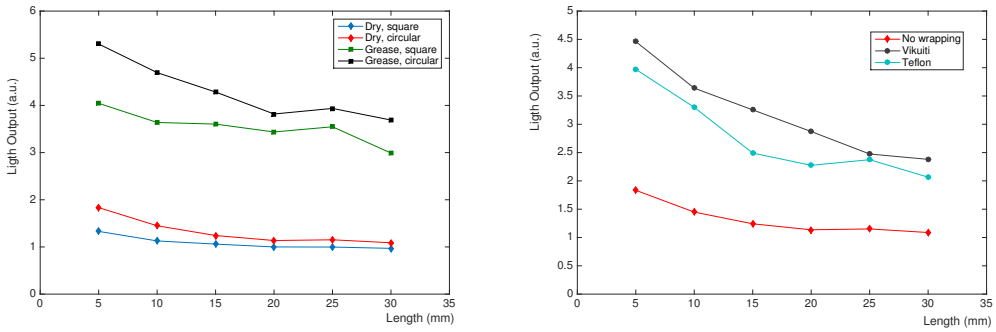

Figure 3.4: Normalized light output trend of LYSO crystals as a function of its length. Left: crystals were measured unwrapped using dry and grease coupling and both set of masks. Right: crystals were measured using dry coupling, two kind of wrapping and the circular mask.

For the wrapped configurations, one can notice the difference in light attenuation when using different reflecting materials. Teflon, as a Lambertian reflector preserves the trend imposed by the crystal intrinsic attenuation. However, Vikuiti with its specular reflections among the different refractive layers is not able to keep the wave-guiding effect seen for the crystals between 20-30 mm length. There is indeed more light lost when using longer crystals wrapped with Vikuiti.

3.3 Physical modeling

3.3.1 Simulations using Geant4

Geant4 simulations were performed in order to validate the Monte Carlo framework by comparing to experimental data. Optical photons are treated following the equations of classical optics when λ is much bigger than typical interatomic distances. The transport across materials and surfaces will depend just on the characteristics of the medium regarding index of refraction, absorption length and Rayleigh scattering. The latter is usually unimportant, since for $\lambda = .2\mu m$ we have $\sigma_{Rayleigh} \approx .2b$[1] for N_2 or O_2 which gives a mean free path of ≈ 1.7 km in air and ≈ 1 m in quartz. Absorption is important for optical photons because it determines the lower λ limit in the window of transparency of the radiator. Absorption competes with photo-ionization in producing the signal in the detector, so it must be treated properly in the tracking of optical photons.

When a photon arrives at the boundary of a dielectric medium, its behavior depends on the nature of the two materials which join at that boundary:

1. Case dielectric $\rightarrow$ dielectric. The photon can be transmitted (refracted ray) or reflected (reflected ray). In case where the photon can only be reflected, total internal reflection takes place.

2. Case dielectric $\rightarrow$ metal. The photon can be absorbed by the metal or reflected back into the dielectric. If the photon is absorbed it can be detected according to the photoelectron efficiency of the metal.

3. Case dielectric $\rightarrow$ black material. A black material is a tracking medium for which the user has not defined any optical property. In this case the photon is immediately absorbed undetected.

With these basic rules for tracking in mind, simulations are designed shooting gammas of few hundreds keV into a material which creates optical photons following energy conservation. The energy deposited is converted to a certain amount of photons according to the value set for the intrinsic light yield. Afterwards the photons are tracked until they reach the volume declared as photodetector, deposit energy and, they are by this means, absorbed.

The simulation basic geometry includes the crystal coupled to a PMT (glass window and the photocathode). The LYSO emission spectrum and timing properties are included as inputs, as well as the absorption and scattering lengths [97]. The material properties table for the PMT window and photocathode are taken from measurements reported in [98] and [99] for fused silica and bialkali, respectively. The surfaces of the crystal and PMT are considered as polished, as first approximation, with the selection of the unified model [94]

[1] 1b = 10^{-24} cm^2

for each interface. The histogram of hits produced by the optical photons collected in the photodetector is shown in Figure 3.5, together with the geometrical visualization presented as inset.

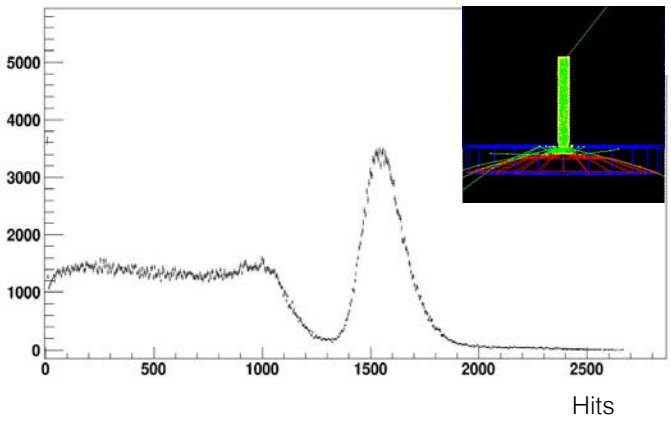

Figure 3.5: Simulated energy spectrum using a 2×2×30 mm^3 LYSO crystal coupled to a PMT as shown in the inset.

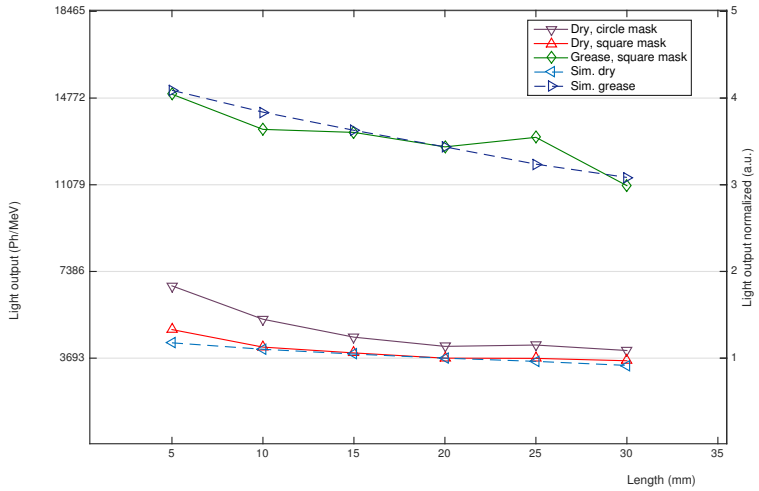

Figure 3.6: Light output for dry and grease coupled LYSO crystals obtained by experiment and simulations. The simulated values are normalized to the 20 mm long crystal.

The light output values obtained by simulation are compared to the previous measurements performed with LYSO crystals and are shown in Figure 3.6 normalized to the 20 mm long crystal. For the square mask a better agreement with the simulations is seen when compared to the circle mask. In this way we can conclude that the absorption parameters are able to reproduce experimental values if the contribution from the edges and/or corners is minimized. The comparison to absolute values implies a previous knowledge of the intrinsic light yield which gives us a reason to compare only normalized values.

3.3.2 Light Transfer Efficiency estimations

Using just geometrical analysis of the light that can be extracted out of the crystal without considering Fresnel reflections, a very simplistic estimation can be done [52].

$$LTE_{dry} = \frac{2\pi(1 - cos\theta_1)}{4\pi} = \frac{1 - cos\theta_1}{2} = 8.2\% \tag{3.3}$$

$$LTE_{grease} = \frac{4\pi\{1 - cos\theta_2\} - 2\pi\{1 - cos\theta_1\}}{4\pi} = 29\% \tag{3.4}$$

Where,

$$\theta_1 = asin(\frac{n_{air}}{n_{LYSO}}) \tag{3.5}$$

and

$$\theta_2 = asin(\frac{n_{grease}}{n_{LYSO}}) \tag{3.6}$$

This approximation, however does not consider Fresnel reflections which will increase the values for the LTE and does not include either light losses due to the diffusion through the edges/corners. In this way, it can be considered as a LTE minimum value and constitutes an underestimation of 25% compared to the maximum value of LTE that can be obtained, assuming crystals perfectly polished when running Geant4 simulations.

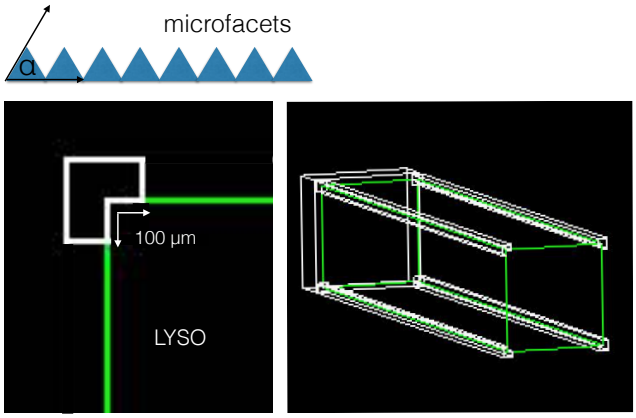

Figure 3.7: Schematic of the rough surfaces declared for the crystal vertical edges using the unified model.

The main difficulty for simulations to accurately estimate the scintillators light output is the modeling of surface/edge defects [100]. When mathematically considering a totally polished crystal, photons impinging at the edges will be reflected as if they were impinging in one of the two perfect surfaces that coincide in space. Randomizing the normal vector that corresponds to the photons reflected back at the edges would give a more realistic situation and it could account for light diffusion.

After a careful examination of the crystal edges with a microscope, we have defined a 100 μm rough interface at the 4 vertical edges of the crystal with different depolishing levels defined by α standard deviation (σ_α) (unified model established in [94], where α constitutes the angle defined by the microfacets and the polished surface). The schematic representation of the new surface declaration is shown in Figure 3.7. The different cases are 1. completely polished, 2. etched corners, where the degree of depolishing is very small with $\sigma_\alpha = 1.8°$ and 3. ground corners, where the vertical edges are defined with $\sigma_\alpha = 12°$. This correlation between σ_α and surface roughness is taken from [101]. We have found that even declaring the 4 vertical edges as completely unpolished, the simulated LTE still lies within the analytic estimation (that does not consider any Fresnel or internal reflections) and the perfect polished case.

In this way, we will set a 25% error bar as first approximation for the LTE estimation, going from 8.2-11% for the dry coupled configuration and from 29-38% for the grease coupled case with no wrapping. LTE values are presented in Table 3.2. The ratio between the LTEs calculated for grease and dry coupling using the analytic and simulations approaches is around 3.45. This value is in very good agreement with the factor seen for the light output using grease and dry coupling as it can be inferred from Table 3.1 and Figure 3.6 which is also around 3.5 for the 20 mm long crystal.

Table 3.2: **Estimations of Light Transfer Efficiency (%) for dry and grease coupling case using different approaches**.

LTE %/**Coupling**	**Dry**	**Grease**	Ratio
Analytic (no Fresnel)	8.2	29.0	3.5
Sim. (polished crystal)	11.2	38.3	3.4
Sim. (etched corners)	10.6	36.8	3.5
Sim. (ground corners)	9.0	30.6	3.4

Comparing with the light output measurements $< LY_{out} >$ for crystals between 20-30 mm where the attenuation shows saturation, estimations of the LYSO intrinsic light yield can be done and are shown in Figure 3.8.

Estimations of the LTE using different approaches and combined with light output measurements show that the LY_{int} has to be within a range of 34'000-44'000 ph/MeV. Looking at the trend that LTE proposes for the treatment of the crystal edges, the experimental value is reproduced where the crystal edges are defined as ground surfaces within 100 μm. Simulations using Geant4 have shown good comparative results for the 5-30 mm long crystals. Light output measurements have proven to be highly dependent on the amount of light exiting the crystals by the lateral faces, especially for crystals shorter than 10 mm. The way to mask this light in the naked configuration or reflect it using Teflon or Vikuiti wrapping is crucial in order to reproduce experimental data.

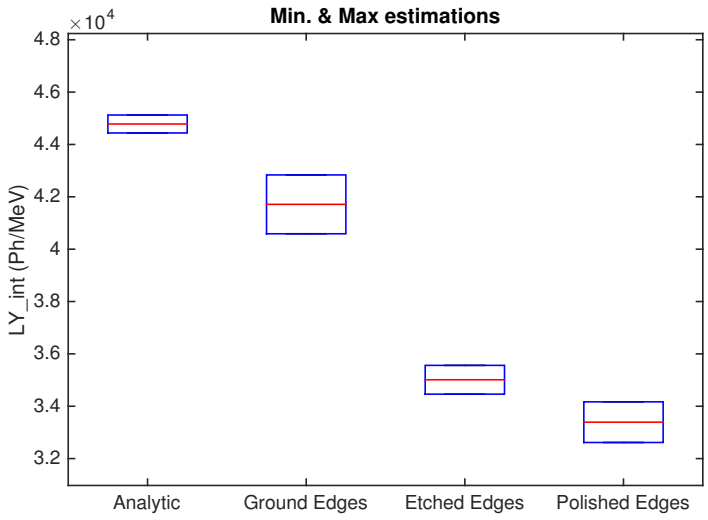

Figure 3.8: Intrinsic light yield estimations using dry and grease coupling LTE calculations.

3.4 Increasing light output

3.4.1 Conceptual idea

Scintillating light produced in the crystal impinges on the exit face with an angular distribution as shown in Figure 3.9 (left). Due to the reference system used in the simulations where the gamma particles are flying towards z-negative, the photons reaching the exit face will have an impinging angle between $\pi/2$ and π radians. Considering a LSO:Ce crystal with 1.82 as index of refraction and depending on the refractive index of the coupling medium, the critical angle for total internal reflection usually varies between $33.3° - 60°$. This angle defines the amount of light being extracted. Light arriving to the exit face with an impinging angle bigger than the critical angle will bounce back and forth, trapped in the crystal, contributing to the photon time spread and eventually being absorbed after multiple reflections. These photons are represented in the angular distribution plot (Figure 3.9) to the left of the arrow representing the critical angle for the air coupling case, and as the area indicates, those are the majority of the total number of photons. Changing the critical angle or reducing the amount of light trapped in the scintillator improves the scintillator light extraction, consequently the number of photoelectrons created.

Several methods have previously been proposed in order to increase light extraction by recuperating these trapped modes. Among others, there are techniques such as microstructuration [102], photonic crystals [103] and nanostructures. Gains up to a 100% have been reported for air coupling in those studies. These structures are complex and often need specialized equipment to implement. Furthermore, most of the previously referred methods offer a clear enhancement of light extraction only with air coupling whereas experiments, which could potentially benefit from an increased light extraction tend to employ a coupling medium such as silicone grease which significantly reduces the effect of the observed gain.

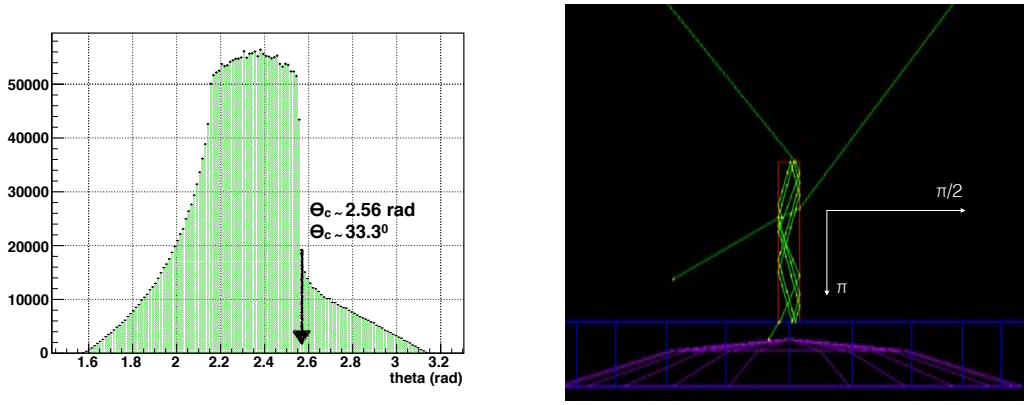

Figure 3.9: Angular distribution of the light impinging on LSO:Ce exit face when coupled to air for a crystal with a rectangular shape and $2 \times 2 \times 15$ mm^3 size.

But, what if we could benefit from the light which is untrapped when changing the reference plane of the exit face as represented in Figure 3.10 (top)?

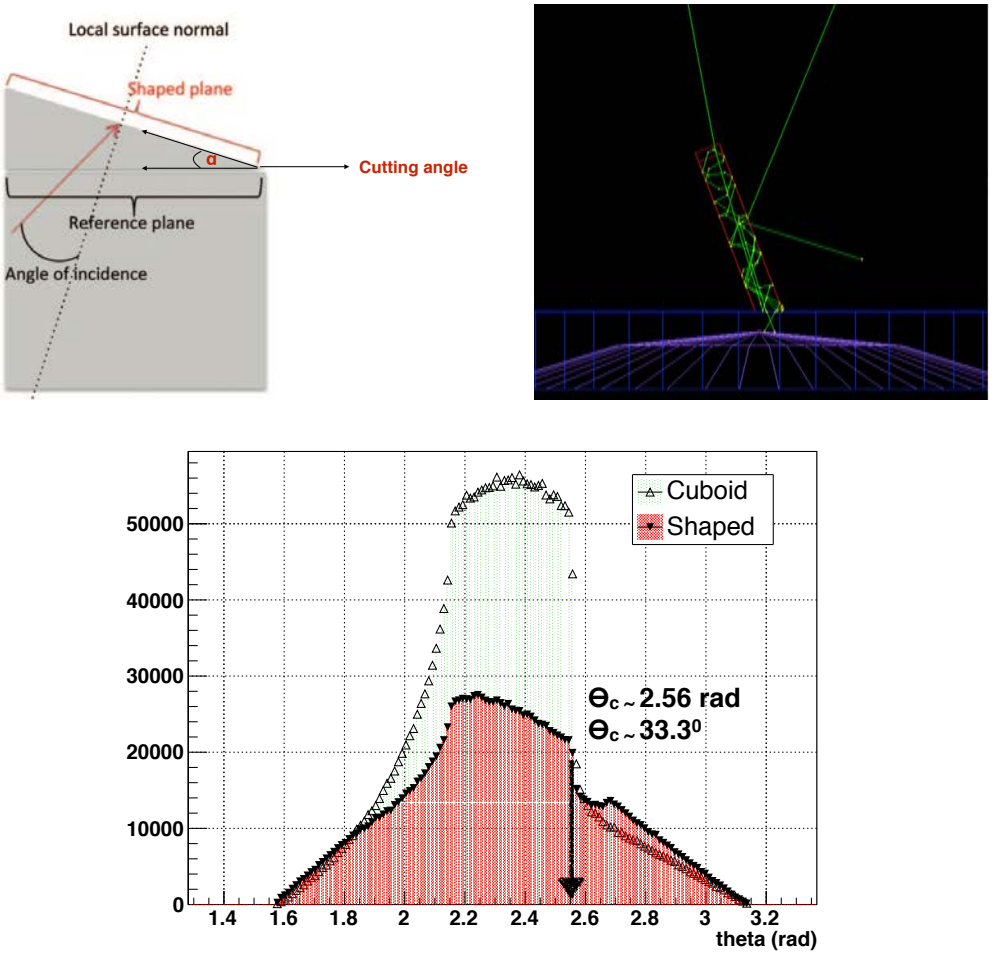

Figure 3.10: Angular distribution and readout face coupling for a non cuboid crystal. Top left: Schematics and cutting angle of the readout face of a shaped crystal. Top right: Crystal coupled to a PMT using the shaped face as described in the front configuration. Bottom: Angular distribution for a cuboid and a shaped crystal, where the exit face is cut from side to side with a 30° angle.

If the angular distribution is calculated for this new shaped crystal, the critical angle will be, of course the same, but due to the new asymmetric geometry, the bouncing angle will not be preserved and a fraction of the trapped photons will have some chance to arrive to the exit face with an angle of incidence $\theta < \theta_c$, managing to escape. If one superposes the angular distribution of the cuboid and the shaped crystal, which have been built with the same amount of photons, the number of photons which are trapped (to the left of the critical angle arrow) is significantly bigger for the cuboid crystal, meanwhile the distribution to the right of the critical angle is smaller when compared to the shaped configuration.

3.4.2 Simulations

Simulations are run in order to determine the optimum cutting angle which could provide the highest gain for light extraction. The geometrical representation of the cutting angle as a function of crystal axis is presented in Figure 3.10, left. Due to space constraints on crystal-SiPM coupling area, the simulations were carried out using both faces, front and back, preserving the cross section of the crystal as the coupling area. In this way, the front configuration will not have the whole shaped surface in contact with the photodetector but instead, it is placed with the longest axis perpendicular to the PMT. The results are shown in Figure 3.11, where for the dry coupling non-wrapping case, the expected gain has its maximum when the cutting angle reaches 30°. Simulations predict a top of 20% gain for the back configuration and maximum 40% for the front configuration. Cutting one of the faces of the crystal with a 30° plane could be done easily in our workshop either from edge to edge or from corner to corner. The former will be called wedge-cut and the latter, diamond-cut. Both shapes are shown to the left-hand side of Figure 3.12, whereas the final cut crystals are shown to the right.

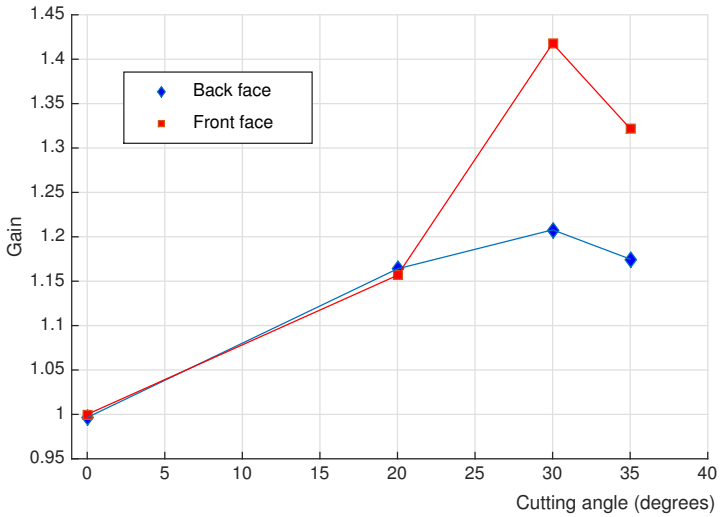

Figure 3.11: Gain in light extraction when shaping the coupling face of the crystal for different angles as obtained by Geant4 simulations.

Measurements of the crystal light output were carried out in the light yield bench described in section 3.2 and they are subsequently compared to simulations. Both configurations are taken into consideration: back and front, when the coupling face is unshaped and shaped, respectively. The gain is reported comparing to the reference cuboid crystal of $2 \times 2 \times 15$ mm^3. Grease and dry coupling, together with Vikuiti (specular reflector [96]) and Teflon wrapping are the configurations used for measurements. However, simulations will only be run using Teflon, declared as a material with a Lambertian reflection. The gain values obtained from simulations are summarized in Table 3.3, together with the values obtained for the reference cuboid crystal.

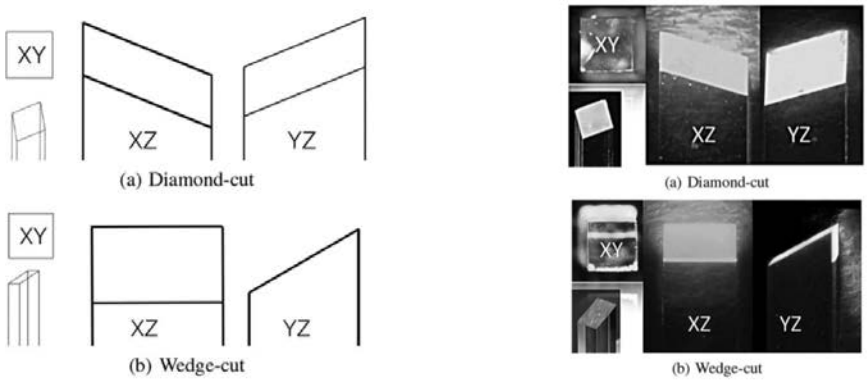

Figure 3.12: Shaped crystals with two different exit face modification [104]. Left: Schematic setup used in the simulations. Right: Pictures taken of the two types of crystals after cutting.

Table 3.3: **Light output gain for shaped crystals according to Geant4 simulations for different coupling and wrapping configurations**.

		Light output Gain (%)			
Sample	Coupled face	Air coupling		Glue coupling	
		Naked	Teflon	Naked	Teflon
Diamond	Back	20	37	3	12
	Front	37	40	21	17
Wedge	Back	16	38	1	13
	Front	34	15	10	10
Reference crystal		Light Output (ph/MeV)			
		4470	13810	15120	22840

From the simulation point of view, there is not a big difference between the gain reported for a diamond-cut shape nor a wedge-cut shape. However, the diamond configuration shows gain as high as 40% for the Teflon wrapped configuration with no glue coupling. In general, a factor 10-17% is reported as total gain for the wrapped, glue coupled configuration, which offers the maximum light output values.

3.4.3 Light output measurements

Light output measurements performed with the cut crystals are summarized in Table 3.4. Two samples were produced with the diamond-cut shape and only one for the wedge-cut crystal. Diamond-cut geometry showed an increase in light extraction for most configurations. Between 20% and 40% gain was measured for air coupling and between 10% and 34% gain for glue coupling for most wrapped configurations in the case of the diamond-cut geometry. Diamond-cut crystal sample 2 however showed a lowered light output when coupled with the back face and wrapped with Vikuiti ESR. The measured improvements in the light output are lower than the values predicted by simulations.

Table 3.4: **Measurements of the light output gain for shaped crystals**.

		Light output Gain (%)					
Sample	Coupled face	Air coupling			Glue coupling		
		Naked	Teflon	$Vikuiti^{TM}$	Naked	Teflon	$Vikuiti^{TM}$
Diamond 1	Back	0	26	33	-19	19	27
	Front	30	40	43	-7	10	34
Diamond 2	Back	-1	22	25	-12	25	-6
	Front	34	32	22	-7	15	12
Wedge	Back	17	-20	-12	-14	-9	11
	Front	-5	-1	-13	-7	-9	-6

Simulations of Geant4 predicted an improved light output also for the wedge-cut geometry but first, this depends on the configuration (front or back), and second, the percentage increase is lower in comparison with the 'diamond-cut' geometry. Measurements on the 'wedge-cut' geometry do not show an increase in the light extraction for most of the configurations as illustrated in Table 3.4. We attribute this discrepancy, at least in part, to the measurement uncertainties and the limitations of crystal machining. While simulations are performed under controlled settings, the samples prepared and polished in the laboratory could deviate from the ideal geometry in ways we do not fully understand yet. Studying more samples can offer us an insight into this. Non-uniformity of crystal wrapping and optical coupling affect the measurement and this can be overcome by utilizing a precise glue dispenser and a standardized wrapping procedure through pre-fabricated Vikuiti ESR boxes.

3.5 High resolution crystal matrix

As presented in section 1.5, scintillating crystals are widely used as the sensitive detector in electromagnetic calorimeters and PET scanners, which are usually quite compact. From high to low energy applications, the detector area covers a considerable amount of space in order to increase the detection efficiency of the system. Specifically for PET scanners,

scintillating crystals can be used as a bulk material or in a pixelated configuration in the form of matrices. Single crystals are placed next to each other, usually separated by a reflector foil, which reduces cross talk and allows to identify the point of interaction. Therefore, the spatial resolution of the whole system will be proportional to the size of the pixelated array which is usually 4×4 with pixels of 3×3 mm^2 since it can be coupled to commercially available SiPM matrices also with a 4×4 array and the same pixel cross section.

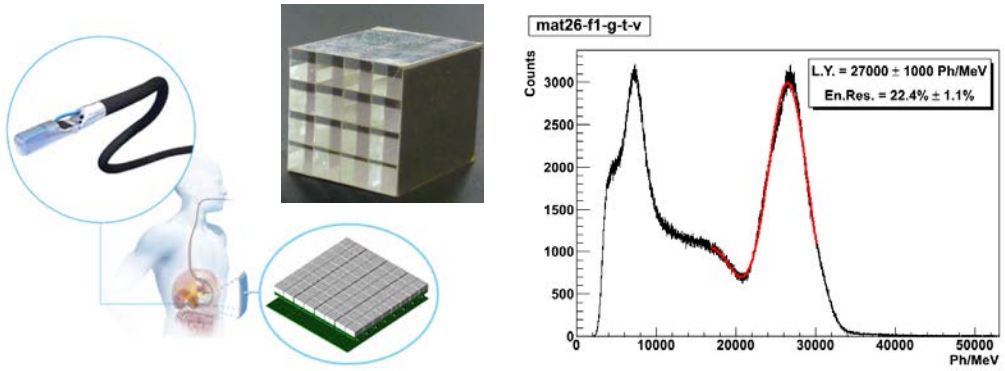

Figure 3.13: Scintillating crystals matrices for radiation detector system and their performance in terms of light output and energy resolution.

SiPM matrices, known as multipixel photon counter, MPPC, combines the fast response of SiPMs with a compact solution for multichannel readout. Each SiPM in the matrix is a square of 3.0×3.0 mm^2 with 3464 active SPADs (50×50 μm^2 each). The distance between two adjacent SiPMs in the matrix (center to center) is 3.6 mm. These SiPMs exploit the Through Silicon Via (TSV) technology, leading to less dead space and a reduced connection length as compared to conventional wire-bonded SiPMs. This specific readout of 4×4 pixelated matrix coupled to 4×4 MPPC has been used in the external plate of the EndoTOPPET-US system [6] as shown in the left of Figure 3.13. The scintillating matrix should fulfill some requirements in order to guarantee good homogeneity among different channels. The energy resolution of the matrix as a block detector is one of the parameters which can be used to check for an inhomogeneous response. The matrix will usually presents larger values for energy resolution compared to single crystals , i.e. $\sim 20\%$ as shown in the right of Figure 3.13, however a clear Compton edge followed by a single peak should be features to maintain.

3.5.1 Light sharing to achieve higher spatial resolution

A simulation study was done in order to evaluate the performance of a new module, i.e. scintillating matrix coupled to MPPC, where the coupling factor has changed from 1:1 to 4:1. In this case, the simulation includes a 8×8 matrix with 1.5×1.5 mm^2 pixels coupled to a 4×4 photodetector matrix with 3×3 mm^2 pixels as shown in Figure 3.14. A glass slab of 1 mm is placed in two different positions, either between the matrix and the MPPC or at the back of the matrix. This glass will share the light between different pixels which constitute the basic strategy to reconstruct the point of interaction.

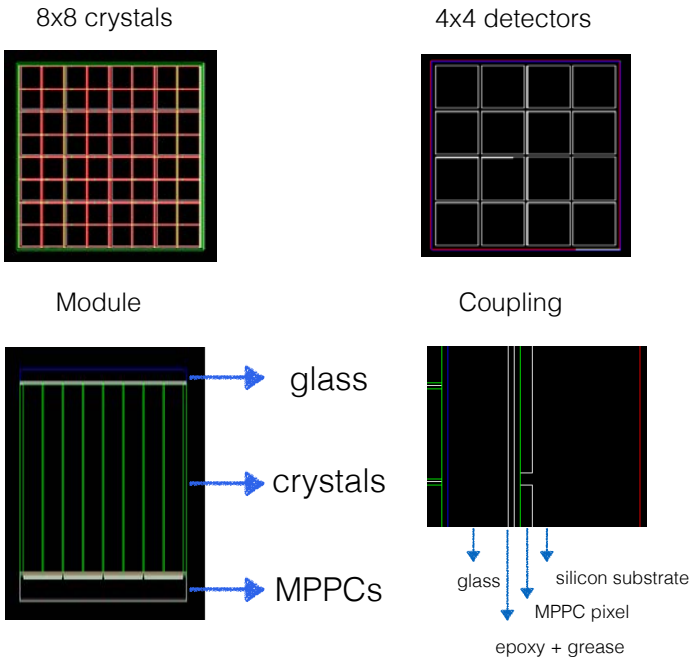

Figure 3.14: High pixelated matrix new module as built in the simulations. The 8×8 crystal matrix with 1.5×1.5 mm^2 pixels is coupled to a 4×4 photodetector matrix with 3×3 mm^2 pixels. The light sharing glass slab is located in two positions: 1. at the back of the matrix as the 'Module' schematic (bottom left) or 2. between the matrix and the photodetector as the 'Coupling' cross section (bottom right).

The reconstruction of the crystal position where the gamma interaction takes place is based on the Anger logic, which uses the ratio of the number of hits in each MPPC cell p_i by the total number of hits. Hits are photons depositing energy in the photodetector so they are the analog to photoelectrons in a real system. The reconstruction shown in Figure 3.15 can be obtained following the relation:

$$x = \frac{1}{P}\sum p_i X_i \qquad \& \qquad y = \frac{1}{P}\sum p_i Y_i \tag{3.7}$$

where $P = \sum_{i=1}^{N} p_i$ (i=1,..8) and X_i and Y_i correspond to the physical coordinates of each MPPC pixel.

Simulations are run using an isotropic point source placed at some distance from the front face of the scintillating matrices and the Anger logic is applied using the two configurations mentioned above. A reflecting surface is defined to account for the matrix wrapping. The reconstructed image is shown in Figure 3.15 where the identification of the point of interaction for each single pixel is clear. Differences in the shape of the reconstructed matrix is seen when comparing both configurations. Even though the configuration with the glass at the back of the matrices shows a less accurate reconstruction for the outer pixels, the crystals at the corner can be still identified.

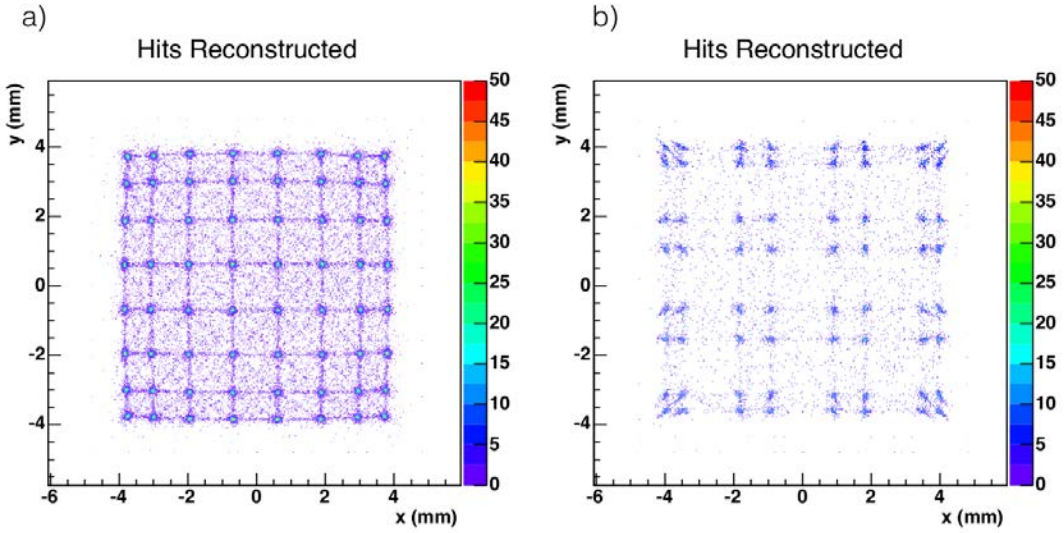

Figure 3.15: Reconstructed hits following the Anger logic for two different configurations. a) glass slab between the scintillating crystal matrix and the photodetector and b) light sharing glass slab placed at the back of the matrix.

3.5.2 Light sharing to extract DOI information

DOI (depth of interaction) resolution constitutes one of the main methods to avoid the parallax error in PET reconstruction. One of the first techniques was based on a phoswich detector where different scintillating materials are connected to build a single pixel. The difference in pulse shape is then used to identify in which half of the detector the interaction actually took place. Another solution is to use dual-side-readout, however this increases the number of channels and therefore complicates the electronic readout scheme and also magnifies the cost.

One novel way is to use the light spread among neighbor pixels to evaluate the sharing factor called R0 and find a correlation with the gamma interaction point. In this way, simulations will be used to evaluate the correlation between R0 and the DOI as defined at the top of Figure 3.16. The correlation between these two variables is plotted and shown in Figure 3.16 for one quarter of the scintillating matrix, which is representative for the rest of the pixels. From the two glass configurations simulated in the previous section, only the one with the glass placed at the back of the matrix is able to show some correlation between R0 and the DOI. Notice that R0 is analogous to the Anger logic shown previously but the weighted factor extends only to the adjacent pixels and not to the totality of the channels. A change of 10% for R0 might be not at all representative at the level of a real measurement, however this R0 vs. DOI correlation can be shaped by de-polishing the pixel faces.

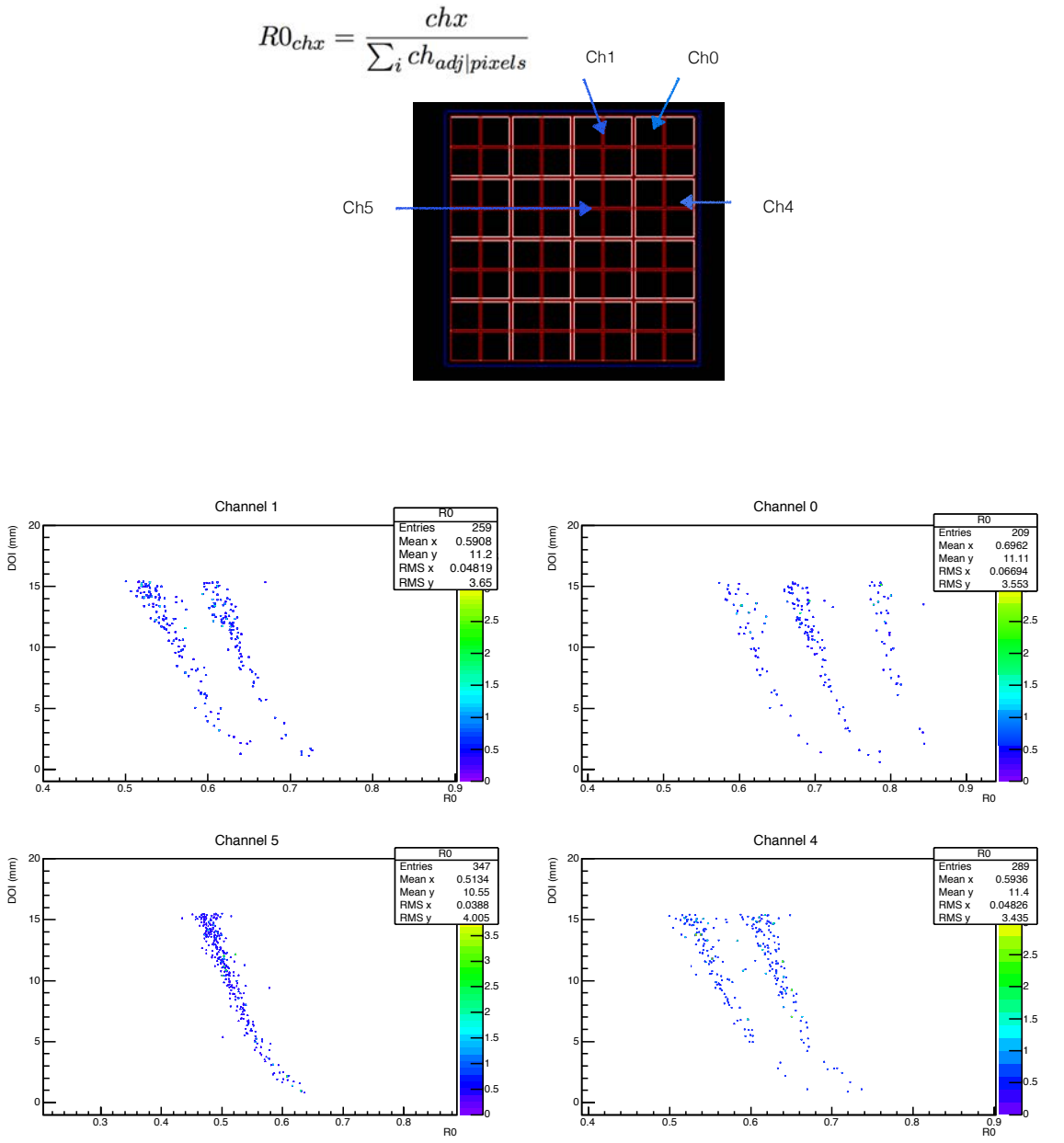

Figure 3.16: Extraction of DOI information by looking at the correlation of the light sharing R0 factor and the interaction point in the crystal. The simulations are done for the first quarter of the matrix which involves four MPPC channels using the configuration with the glass slab in the back.

3.6 Conclusions

In this chapter, the simulation framework used to track optical photons in the scintillator has been validated for LYSO with length between 5 and 30 millimeters. The comparison with experimental data is successful only for the tight square mask which minimizes the effect of edges and corners.

Estimations of the LTE using different approaches and combined with light output measurements show that the LY_{int} has to be within a range of 34'000-44'000 ph/MeV. Looking at the trend that LTE proposes for the treatment of the crystal edges, the experimental value is reproduced where the crystals edges are defined as ground surfaces within 100 μm. Light output measurements have proven to be highly dependent on the amount of light exiting the crystals by the lateral faces, especially for crystals shorter than 10 mm. The way to mask this light in the naked configuration or reflect it using Teflon/Vikuiti wrapping is crucial in order to reproduce experimental data [105].

When the crystal extraction face with a simple cuboid geometry is modified into various alternative geometries the simulations predict a clear improvement in the light collection. Measurements with the shaped crystals published in [104] show an improvement for one of the two tested geometries. The improvements seen are not uniform among the two samples from the same geometry. The observed increase in light output for shaped crystals both from simulations and measurements is due to the introduction of an asymmetry into the cuboid crystal geometry. Such an asymmetry disrupts the propagation of trapped modes of light and causes them to exit with a finite probability while preserving the portion of generated light that reaches the exit face at an angle less than the critical angle for the pair of media at the extraction face. Since a part of trapped light will be extracted, this implies that the light output for a shaped crystal will be higher than the reference crystal. We arrive at this conclusion through simulations and measurements of the light angular distribution. However, the coupling configuration when the shaped face is at the back does not necessarily preserve the portion of light that would arrive at the exit face within the critical angle, and therefore does not necessarily have a positive value of gain.

The evaluation of a new highly pixelated module for higher spatial resolution and DOI encoding information done by means of simulations has been followed-up with a successful experimental corroboration and is published in [53, 54].

Chapter 4

LYSO intrinsic light yield

4.1 Introduction

The performance of scintillating crystal in terms of light output constitutes the basis in order to improve the energy and time resolution of radiation detector systems, especially in the low energy regime of medical imaging [106]. Increasing the light output in order to improve the photostatistic has been proven as an effective way to increase coincidence time resolution which scales with the square root of it. In this way, a coincidence time resolution (CTR) improvement of one order of magnitude would need and increase in the number of photoelectron detected in a factor of 100, if the photodetector single photon time resolution is kept as a constant. One way to increase the photostatistic will be to optimize the light transfer efficiency of the scintillator, theoretically up to 100%, which implies there is no light loss processes in the crystal and the totality of light created is transmitted out of the crystal. Henceforth, the photostatistical improvement limit will be given by the intrinsic light yield of the scintillator.

Usually, when estimating or measuring the intrinsic light yield of a scintillating crystal, LY_{int}, a deep understanding and characterization of the photon dynamics in the scintillating crystal is needed. Measurements of this quantity remain in the literature as a wide approximation based on Light Transfer Efficiency (LTE) simulations [107], as presented in Chapter 3, or underestimate light absorption for certain geometries [108]. Another method relies on long calibration processes [109], [110] in order to account for all the factors that contribute to light losses. However, these calibration methods are highly dependent on the surface state and geometry of the crystal and so far, they do not report values for LYSO scintillators, which represent our main interest because of their high light yield and relatively fast decay.

In the present chapter, we will focus on the determination of LY_{int} and LTE by means of experimental measurements. A bench has been set up in order to have a direct measurement of the LY_{int} using electron excitation and restricting the light extracted in a narrow cone that allows a simple analytic relation between LY_{int} and the measured values.

4.2 Conceptual idea

The idea consists in minimizing all the factors that contribute to light losses when optical photons are transported in the crystal and correcting only for a very simple Fresnel transmission through a polished surface and a pure geometrical factor. Light will be emitted within a determined area and not all along in the crystal, creating a cloud of optical photon emission which will spread isotropically in a 4π solid angle. However, the photons that will be detected are the ones traveling forward and exiting the crystal within a pre-defined solid angle set by two pinholes, one at the crystal exit face and a second one placed at the PMT window. To avoid the multiple reflection effect present in crystals with a high aspect ratio, a 1 cm^3 LYSO crystal has been chosen and the crystal is measured in dry coupling and no wrapping. Decreasing the solid angle and the size of the emission cloud will increase the accuracy of the experiment which is only limited by the photodetector used. The 10 mm long cube has been chosen in order to minimize the losses through attenuation since the optical photons will travel for 20 mm as maximum. Processes like absorption or Rayleigh scattering have an almost negligible contribution for distances around 20 mm since the minimum value reported is 138 mm for μ_s [111]. The geometrical factor will be just a weighted ratio between the solid angle of light extraction, analog to the measured light output, and 4π, related to the intrinsic light yield. A more explanatory drawing is shown as the inset of Figure 4.1. The following relation is the basic idea followed in this measurement:

$$\frac{LY_{out}}{LY_{int}} \propto \frac{d\Omega}{4\pi} \tag{4.1}$$

The scintillation emission is confined approximately within a volume of $1{\times}1{\times}0.5\ mm^3$, according to the energy deposition tracking of the electron excitation. For this, an electron beam of 1 mm diameter and 1.5 MeV was used to excite a cubic LYSO crystal at the center of one of its faces. An excitation energy > 1 MeV has been chosen in order to have minimum ionizing particles which yield a number of photons similar to the gamma interaction. In this way, quenching due to high density excitation is minimized. Following this line, a test is carried out in order to have maximum count rate of electrons, since a signal above the LYSO background is needed. However, having a penetration range of 0.5 mm will enlarge the systematic uncertainties.

The experimental bench which schematic is presented in Figure 4.1, consists of a custom made electron monochromator that uses a magnetic field to bend the electrons coming from a $^{90}Sr/^{90}Y$, 34.22 MBq source with energies up to 2.3 MeV. The curvature radius is fixed to

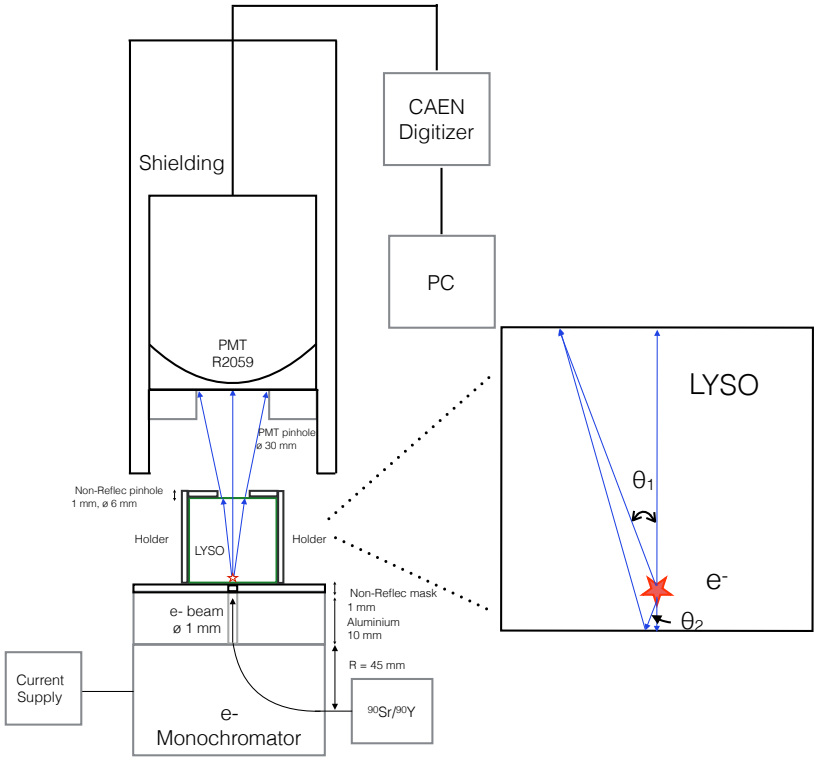

Figure 4.1: Schematic view of the experimental setup for the intrinsic light yield measurements. The geometrical solid angles defining the light extraction are shown as inset where the electron excitation point is marked with a red start. (Not to scale.)

45 mm and the energy of the electrons is chosen according to the coil current. The monochromator shielding plates are made of 10 mm thick aluminum, to guarantee only electrons with the desired energy can pass through the 1 mm hole. A black-non reflective crystal holder is attached to the electron exit plate, ensuring that scintillating photons escaping through the lateral and top faces are not reflected back by the aluminum plate. The 1 mm hole of the shielding plate is aligned with the center of the light extraction pinhole. The PMT R2059 used is enclosed in a set of iron tubes shielding the magnetic field created in the coils. The PMT together with its pinhole is placed at a distance which preserves the extraction solid angle.

The formula to reconstruct the total number of photons per energy deposited based on the amount of photoelectrons detected N_{pe} is the following,

$$LY_{int} = LY_{out} \times F_{geom} \tag{4.2}$$

Where,

$$LY_{out} = \frac{N_{pe}}{QE_{PMT} \cdot E_{e-}} = \frac{Channel \cdot 10^{Atten/20}}{SE_{PMT} \cdot QE_{PMT} \cdot E_{e-}} \tag{4.3}$$

and

$$F_{geom} = \frac{1}{(1-R) \cdot (\frac{d\Omega_1}{4\pi} + R\frac{d\Omega_2}{4\pi})} = 70 \tag{4.4}$$

Here, SE_{PMT} refers to the single photo-electron signal of the PMT and QE_{PMT} stands for its quantum efficiency. E_{e-} is the energy of the electron beam. R, is the Fresnel reflection coefficient for the light impinging at back and front surfaces of the crystal. The terms $\frac{d\Omega_1}{4\pi}$ and $\frac{d\Omega_2}{4\pi}$ correspond to the solid angle defined by θ_1 and θ_2, respectively as shown in the inset of Figure 4.1. θ_1 is defined as $atan\frac{r_{pinhole}}{h}$, where h is determined using Geant4 simulations of the electron deposition within the crystal. Accounting for the fraction of photons reflected back at the top face of the crystal and exiting within solid angle θ_1, the factor $d\Omega_2$ is determined using θ_2. These two angles will depend on the size of the cubic crystal, the energy of the electron beam and the pinhole radius. For a 1 cubic centimeter LYSO, an energy $\sim$ 1.5 MeV and a pinhole radius of 3 mm, θ_1 is equal to 14° and θ_2 is calculated to be 13.6°.

4.3 Simulations

Simulations are set in order to recreate the experiment features, identify the main source of uncertainties and minimize them. Figure 4.2 shows the geometry visualization of the whole system, 1 mm diameter source represented by a yellow star, a cubic LYSO crystal (in red) and two set of pinholes (in blue) in order to maintain the solid angle seen by the PMT (green glass window and a red photocathode).

Using low energy electromagnetic libraries in Geant4 we are able to track the energy deposited by electrons inside the LYSO crystal in function of the penetration depth as shown in Figure 4.3. After 0.5 mm the electron has deposited all its energy and light will be emitted then from this zone in the crystal. We are basically simulating the Bragg peak for an electron beam of exactly 1.46 MeV ($\sim$ 1.5 MeV), since electrons are not heavy particles they will deposit energy in a broader peak compared to ions but narrow enough to being able to confine the light in a 0.5 mm depth region. Figure 4.3 right shows the histogram of energy deposited vs. depth (Z) inside the crystal, so after 0.5 mm from the edge of the crystal, the amount of energy deposited is negligible.

The ionization distribution is used to define the solid angle vertex given by θ_1 (see Figure 4.1) and its dispersion allows us to calculate the uncertainties on the determination of the solid angle. This gives results of 8.7% when doing the error propagation of the arctangent function with two variables. Following the energy deposition profile, h in the arctangent function is defined as the crystal length minus 0.1 mm (taken from Figure 4.3), the region where most of the energy is released. A geometrical representation of both solid angles used to build the geometric correcting factor is shown to the right of Figure 4.1, where θ_1 is responsible for the light traveling forward and θ_2 for light reflected back and still able to exit. The light detected is collimated within a 14.0° cone of extraction using a black non-reflective pinhole, which assures the bouncing of optical photons under θ_2, to contribute less than 20%. Processes like absorption or Rayleigh scattering, despite the very different values reported in literature concerning absorption length (μ_a) and scattering length (μ_s), have an almost

negligible contribution for distances around 20 mm since the minimum value reported for μ_s is 138 mm [111].

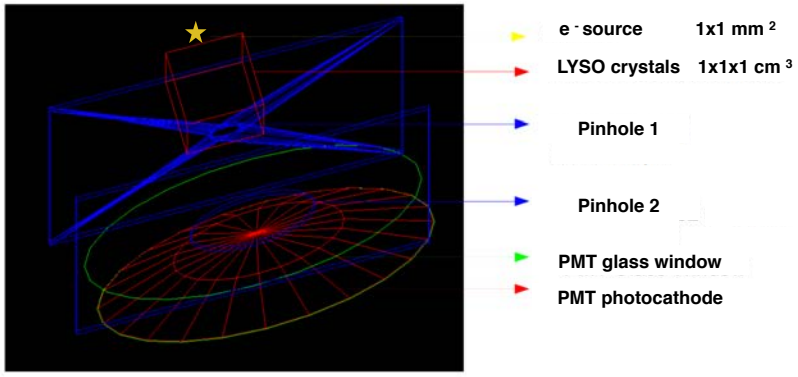

Figure 4.2: Geant4 geometrical visualization of the experimental setup conformed by the cubic crystal, the two set of pinholes and the PMT.

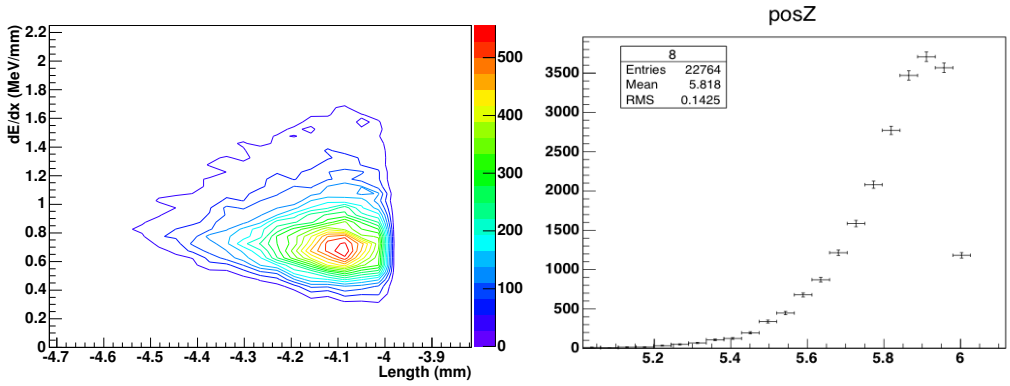

Figure 4.3: Ionization cloud created by the electron track along the crystal length as obtained by simulations.

The optimum pinhole radius is determined applying the equation 4.2 to the number of photons detected in the simulations and comparing to the real number of photons created in the scintillating crystal. The results are shown to the left of Figure 4.4 where the error bars correspond to the peak energy resolution. For pinhole radius between 2 and 3 mm the intrinsic light yield is accurately reproduced within a 3% with respect to the real value. When simulating the step number of the photons that manage to reach the photodetector with the conditions described in the experimental setup, one can see to the right of Figure 4.4 a first peak related to photons traveling straight (the ones corrected under θ_1) and a peak with a step number which is 2 times bigger, reflected on the back and exiting, with a height $< 20\%$ as compared to the ones traveling straight, which are corrected under θ_2.

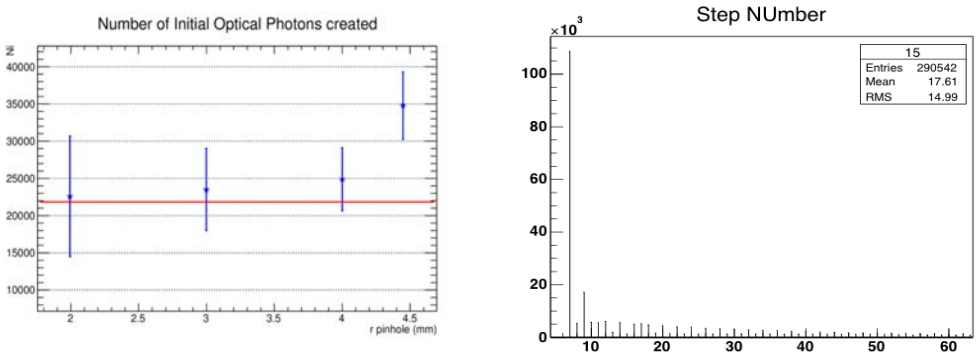

Figure 4.4: Simulation study to determine the optimum pinhole radius. Left: Calculation of the number of photons created by using the equation 4.4 with the photoelectrons detected in the simulations for different pinhole radius. Right: Step number coming from the tracking of optical photons that are transported through the pinhole set (pinhole 1 with radius of 3 mm) before reaching the photodetector

4.4 Electron beam calibration

The electron beam diameter of 1 mm was chosen to minimize the energy resolution of the monochromator to 2.2%. The curvature radius was set to 45 mm in order to maximize the count rate of the source for energies around 1-1.5 MeV which are minimum ionizing energies for electrons. The ^{90}Sr/^{90}Y electron source is placed with the output aligned with the input hole as shown in Figure 4.5 and the electron beam is obtained from the output slit, where the non-reflective holder is placed to position the cubic crystal. The first test is to check the linearity of the readout system when measuring with the electron source. For this, the energy spectrum of a ^{22}Na source is taken with a GaGG pixel crystal of $2 \times 2 \times 8$ mm^3 in order to avoid the intrinsic background of the LYSO. The energy spectrum of the electron source is superposed and the linearity is check to be correct, giving a 2274 keV energy for the last channel which correspond with the 2.3 MeV energy of the ^{90}Sr/^{90}Y. The spectra of both sources is plotted using the energy calibration and shown to the left of Figure 4.6. The energy resolution of the 511 keV peak is around 20%.

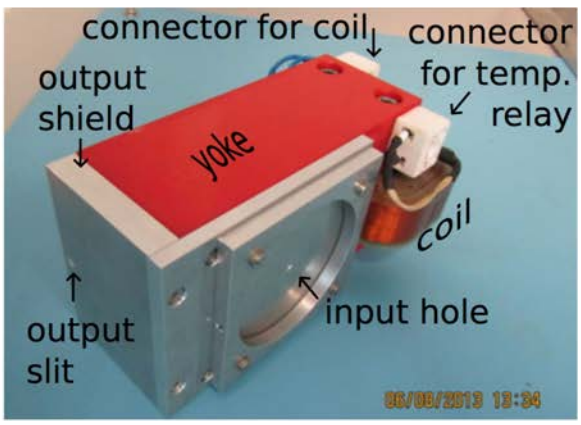

Figure 4.5: Electron monochromator and its main features.

A study of the PMT response with respect to the current applied to the monochromator coils was made using a ^{137}Cs source, increasing and decreasing the current and checking the displacement in the photopeak [112]. A magnetic hysteresis effect can be observed to the right of Figure 4.6. For this reason the monochromator is always set with a current of 1 A, ramping up direct to this value. When applying the magnetic field, the photopeak position is moved by a maximum of 6% to the smaller energies, which is part of the calibration factors of our system.

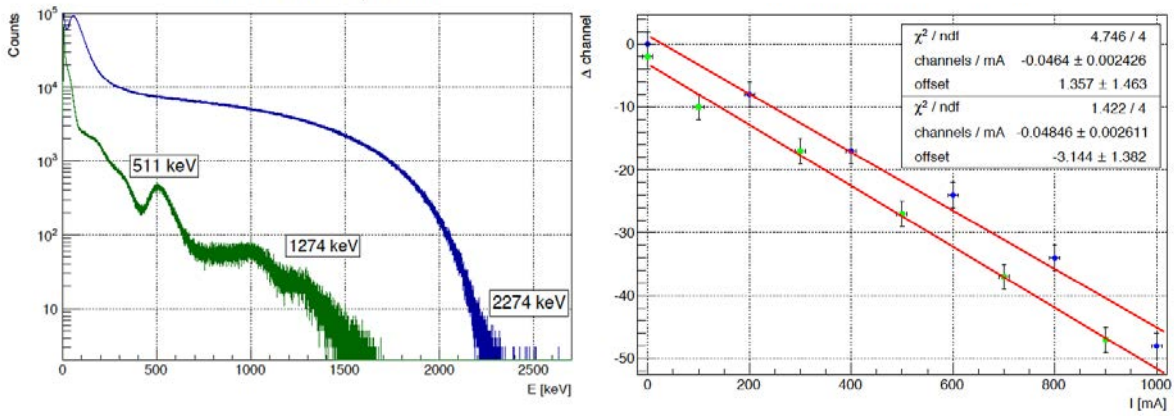

Figure 4.6: Electron beam energy calibration [112]. Left: ^{90}Sr/^{90}Y and ^{22}Na energy spectra measured using a PMT and a GaGG:Ce crystal. Right: Effect of the magnetic field in the displacement of the photopeak position when decreasing (blue dots) or increasing (green dots) the current.

Measurements of the angular distribution of the light output using either gamma or electron excitation reported the same isotropic distributions. This avoids corrections for the distance between the crystal and the PMT.

Due to the dependency of the light output as a function of the interaction point and different crystal geometries, the electron beam energy calibration is not a straightforward process. At first, a linear ADC (analog-to-digital converter) calibration is made using a set of gamma sources (^{57}Co,^{137}Cs,^{22}Na), and the electron energy is given by a linear fit. However, this procedure consider a homogeneous interaction all along the crystal, meanwhile for electrons, the interactions are concentrated in the upper central part of the crystal. To account for this effect, simulations were run with the same experimental features in order to calculate a depth of interaction (DOI) factor given by photopeak position divided by electron peak position when gammas and electrons have the same energy. For crystals with dimensions of 2×2×10 mm^3 and using a tight square mask this factor is 1 so we can measure the energy of the electron beam using this configuration, which gives a result of 1.46 MeV. In principle, a lower energy for the electron beam is desirable since the beam penetration would be considerably reduced.

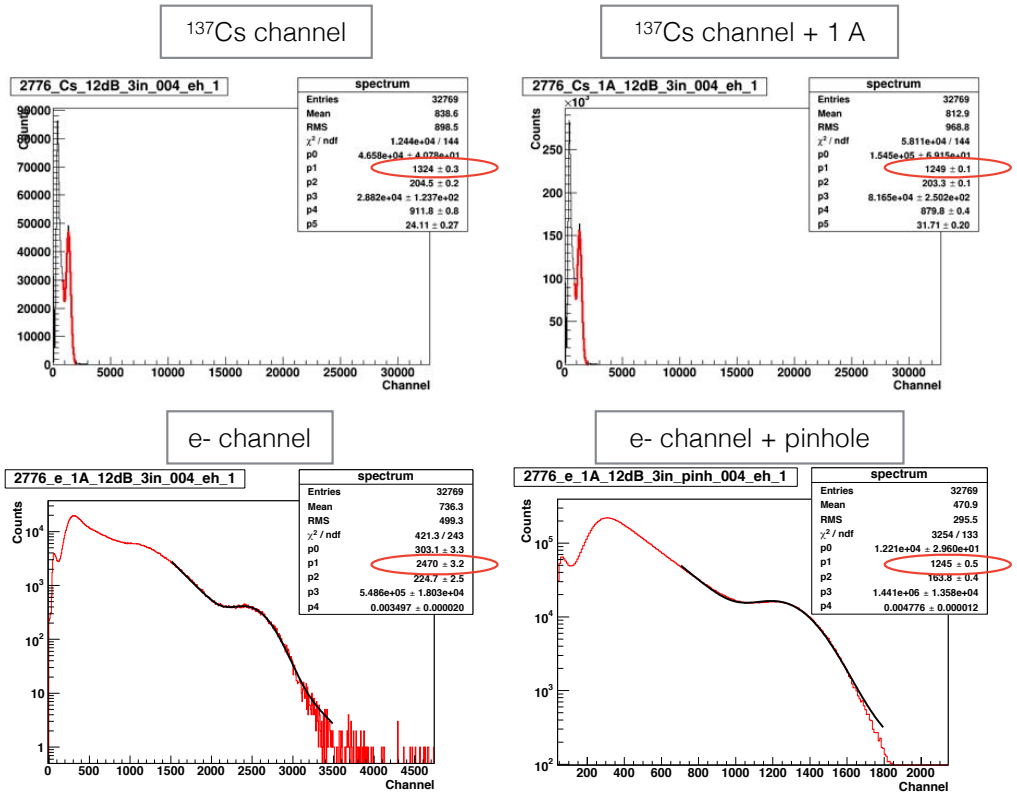

Figure 4.7: Set of measurements performed to find the magnetic field correction factor and the energy calibration done for the electron beam.

The magnetic field correction factor to be applied is found by direct comparison of the ^{137}Cs 662 keV photopeak measured with and without current passing thorough the coils as shown in Figure 4.7 top. The bottom part of the Figure 4.7 shows a typical energy spectrum taken with the LYSO cubic crystal in place using the monochromator with a current of 1 A with and without pinhole. Dividing the e- channel by the photopeak channel when the current is 1 A yields an electron energy of around 1.3 MeV. However, there is a DOI correction factor of around 0.9 for a cubic LYSO crystal when comparing electron and gamma excitation, which sets the energy back to 1.46 MeV.

4.5 Results

Measurements of the intrinsic light yield (LY_{int}) taken with 5 different 10×10×10 mm^3 LYSO crystals have been done in dry coupling and non wrapping configurations, using the pinhole that collimates the light exiting within the defined solid angle. The electron peak is fitted as shown in Figure 4.8. We calibrated the single photoelectron response and calculated the convolution of the LYSO emission spectrum with the PMT quantum efficiency to a value of 0.21. The final results for the intrinsic light yield are calculated according to equation 4.2 and are shown in Table 4.1 together with the measured light output.

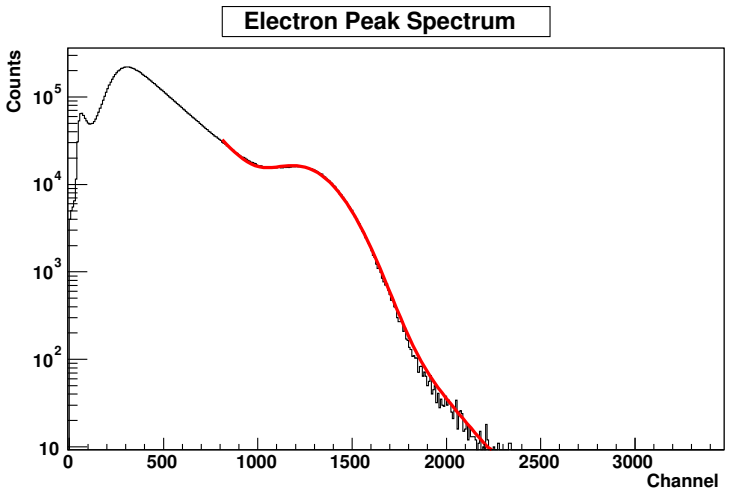

Figure 4.8: Electron peak spectrum using a black non-reflective 3 mm diameter pinhole in front of cubic LYSO crystal and a second pinhole in front of the PMT window.

Table 4.1: **Values of intrinsic light yield and light output for LYSO cubic crystals**.

Crystal ID	LY_{out} *(ph/MeV)*	LY_{int} *(ph/MeV)*
1	574	39045
2	595	41437
3	561	39044
4	576	39757
5	530	40125
Average	568	40000
STD	24	1153
STD/Average	3%	

The main contribution to the uncertainties arises from the quadratic error propagation of the geometric factor that, in a simplified way follows this function:

$$F = cos(atan\frac{x}{y}) \tag{4.5}$$

Where x is the pinhole diameter and y is the distance from the light emission point to the crystal exit face. Basically we are propagating the error of a solid angle where the vertex is not a point in the space but a cloud of probability. Using electrons of 1.5 MeV creates an ionization cloud that extends for 0.5 mm inside the crystal with a denser zone at 0.1 mm from the crystal upper face as already shown in the previous section. When propagating and substituting the uncertainties for x (0.08 mm, instrumental precision on the pinhole production) and y (0.4 mm), the relative error for the geometric factor is 8.7% $\sim$ 9%. Basically, the main source of uncertainty is coming due to the energy of the electron beam, smaller the energy, shorter the range of penetration, the accuracy on determining the solid angle increases considerably.

The light output measurements of the same cubic crystals we used for measuring the intrinsic light yield LY_{int} were carried out following the method reported in the previous chapter. The measured face is the entire 10×10 mm^2, dry coupled to the PMT. Light output results for the five different cubes have an average of 4820 ph/MeV and a standard deviation of 8%.

It is noteworthy that the statistical uncertainties for the intrinsic light yield setup have been reduced to basically the fluctuations of the PMT and the bench itself (3%). Meanwhile, the light output values of one entire face for the same crystals are showing a bigger statistical error (8%) arising from the surface state of different crystals. This confirms our method to determine an intrinsic magnitude independently of the surface state of the crystals.

4.6 Conclusions

The intrinsic light yield of LYSO crystals has been measured with results of 40'000 ph/MeV ± 9% (syst) ± 3% (stat) by means of electron excitation using a beam of 1 mm diameter and an energy of around 1.5 MeV [105]. This value is still pending to the PMT QE precise measurements. The systematic uncertainties can be considerably reduced when using a lower energy electron beam, which is especially suitable for crystals with no intrinsic background. Reducing the electron range from 0.5 mm to 0.1 mm decreases the geometric factor uncertainty to 5.5%, which could be feasible even for LYSO using a higher electron count rate. In this specific case, we are limited by the activity of the $^{90}Sr/^{90}Y$ source.

However, the method previously described can be extended to every single type of scintillating crystal and the uncertainties could be reduced by using different pinhole apertures and a stronger electron source. The presence of intrinsic background radiation is another factor which deteriorates the systematics of the experiment.

Measurements of $2\times2\times10$ mm^3 crystals with all polished faces using optical grease and Teflon wrapping show light output values of around 28'000 ph/MeV, giving LTE values of 70%. In general around 20-30% of the light created in a 10 mm long crystal is trapped, which gives some room for light extraction optimization. Alternative methods such as readout face shaping or photonic crystals coatings could be used for this purpose as proposed in the section 3.4 or as previously published in [113, 114]. However, even though some effort could be dedicated to increase the light output of a crystal there is an intrinsic limit in the maximum number of photons that are available for extraction. If we chose crystals of 20 mm, as the ones used in PET scanners, the LTE is around 50%, which could bring an increase in a factor of two if all the photons were extracted. Increasing the photon detection efficiency of the SiPM could also deliver another factor two in the number of photoelectrons detected. These two properties, light extraction and photodetection efficiency, have a limiting optimization factor of 4, which translates to an improvement in CTR of 0.5. We could reduce CTR to half of its present value however this will not bring a CTR of 10 ps.

Looking for materials with a faster decay- and rise-time is needed to open new ways in the optimization path of the scintillating crystal's performance in terms of time resolution. We have shown in this chapter that improving the light transfer efficiency will not bring an order of magnitude change in coincidence time resolution.

Chapter 5

Spectral-time resolved single photon counting system

5.1 Introduction

The measurement of the timing kinematics of radiative transitions is one way to characterize the carrier excitation and recombination processes which have taken place in the scintillator under different kinds of excitation. The time profile of the light emitted is not only related to the de-excitation of emission centers but carries the information related to the energy transfer efficiency between the host and the luminescent centers in the case when the excitation energy is much higher than the band gap of the scintillating material. In this way, the rise time will be the time constant signature of an fast (efficient) or delayed population of the recombination centers. Meanwhile, the decay time will be ruled by an exponential function describing the depopulation of the excited centers. A typical way to characterize the decay of luminescent centers located within the band gap of an inorganic scintillator is to perform time-resolved photoluminescence, where the sample is excited by a laser. The rise time, since it is usually excitation-dependent will vary from zero in the case of laser excitation to O(1)ns values which are typical of ionizing excitation.

The situation described before could vary considerably for the recombination processes happening within the discrete-like energy levels characteristic of scintillating nanocrystals. Having a system able to measure the aforementioned timing kinematics is essential in the R&D process involved in the characterization of new scintillating materials.

Coming back to conventional inorganic scintillators, their intrinsic rise time under ionizing radiation shows still some controversy among literature. One of the first studies made by Derenzo *et. al.*, [115] have shown two components for the rise time of LYSO crystals: the first one at the level of the impulse response function of the system and a second one at around 350 ps. However, there is not a follow-up study of these two rise time components with dif-

ferent crystals, neither discussion regarding the slow component. More recent measurements using also X-ray excitation [116] showed only one rise time component and no significant difference between Ca^{2+} co-doped or non co-doped crystals. However, rise time measurements made using time-correlated single photon counting technique and 511 keV gammas [12] show remarkable differences between Ca^{2+} co-doped and non co-doped crystals not only for LYSO but also when measuring LuAG:Ce and LuAG:Pr samples. These differences in rise time are able to explain the enhancement in coincide time resolution values of co-doped crystals as previously reported in [8].

The main source of discrepancy regarding the rise time measured under X-ray excitation comes as a result of a poor description of the impulse response function (IRF) of the photodetection system which is usually due to the impossibility to measure the time profile of the X-ray excitation pulse. For some time-resolved single photon counting systems using either MCPs (multi-chamber plates) or other X-ray sensitive photodetector, the determination of the excitation source time profile is a straightforward measurement, as simple as measuring background. For other systems which are insensitive to X-rays, the measurement of the IRF needs to be done using a material that converts the X-rays into light with a decay time constant much shorter than the full width half maximum (FWHM) of the excitation pulse. Finding a material with a monoexponential decay component of few picoseconds is not an easy task which leaves the IRF measurement as a bare approximation.

This chapter describes the technicalities of the spectral-time resolved single photon counting system used to perform rise and decay time measurements along the second part of this manuscript. The system is a Hamamatsu C10910 universal streak camera which handles a repetition rate of 4 MHz and has an intrinsic time resolution of 18 ps FWHM when operated using the slow single sweeping unit M10913-11. The system is built to perform time-resolved measurements under optical and ionizing excitation and the light from the excited sample is detected in transmission mode. The laser is a 372 nm picosecond pulsed diode from PiLAS with a FWHM of 51 ps when operated at 70% intensity. It is used to perform time-resolved photoluminescence and to trigger an N5084 X-ray tube which generates X-rays pulses following the laser temporal shape. The pulsed X-ray tube has a tungsten photocathode with an energy spectrum up to 40 keV and an intrinsic time resolution of around 50 ps FWHM. The IRF of the system is determined by experimental measurements up to the first decay component and by modeling in order to approximate the possible second decay component.

In section 5.4, the time resolved measurements of the energy transfer arising from X-ray irradiation of scintillating crystals, i.e. rise time, together with time resolved photoluminescence to characterize the decay time will be presented. Eight different lutetium oxyorthosilicate Ce^{3+} doped crystals with and without Ca^{2+} co-doping were tested, together with a LGSO and LFS samples. A set of garnets (YAG, GaGG and LuAG) with and without Mg^{2+} co-doping were also analyzed using the same IRF model presented in this chapter. However due to the preliminary nature of the results, the measurements are summarized in the annexed section A.

5.2 Model for the intrinsic rise- and decay-time

Data analysis under laser excitation is the easiest one to perform since the impulse response function (IRF) is a symmetric Gaussian where the only important parameter is sigma. This allows us to analytically solve the convolution integral and the fit is carried out using the following formula which was previously obtained in [12]:

$$F(t) = \sum_{i}^{N} \frac{A_i}{\tau_{d,i} - \tau_{r,i}} \cdot exp^{\frac{2\tau_{d,i}(\theta-t)+\sigma_{IRF}^2}{2\tau_{d,i}^2}} \cdot (1 - erf[\frac{\tau_{d,i}(\theta - t) + \sigma_{IRF}^2}{\sqrt{2}\sigma_{IRF} \cdot \tau_{d,i}}]) \\ - \sum_{i}^{N} \frac{A_i}{\tau_{d,i} - \tau_{r,i}} \cdot exp^{\frac{2\tau_{r,i}(\theta-t)+\sigma_{IRF}^2}{2\tau_{r,i}^2}} \cdot (1 - erf[\frac{\tau_{r,i}(\theta - t) + \sigma_{IRF}^2}{\sqrt{2}\sigma_{IRF} \cdot \tau_{r,i}}]) \tag{5.1}$$

Here, θ stands for the time zero of gamma/X-ray detection. Each parameter A_i is divided by the timing constants difference, which yield the total amount of photons emitted under their corresponding timing characteristics. An extra term was added to account for the background coming from the MCP (multichannel plate) noise. The sum stands for the number of components characterizing rise- and decay-time.

When analyzing X-ray excited data the fit can not be done analytically since the IRF is not a symmetric function either a Gaussian. The convolution is done by using a fast Fourier transformation where the functions are both built as probability density functions (p.d.f.). Therefore, the p.d.f. defining the impulse response function is the key factor in the fitting procedure. The function used to convolve with the asymmetric impulse response function (IRF) is the following:

$$f(t) = \sum_{i}^{N} \frac{A_i}{\tau_{d,i} - \tau_{r,i}} \cdot exp^{\frac{(\theta-t)}{\tau_{d,i}}} - \sum_{i}^{N} \frac{A_i}{\tau_{d,i} - \tau_{r,i}} \cdot exp^{\frac{(\theta-t)}{\tau_{r,i}}} \tag{5.2}$$

Parameter errors are calculated using the MINOS algorithm which has been designed to calculate the correct errors in all cases, especially when the functions are non-linear. The theory underlaying the 'non-parabolic log-likelihood' method used is described in [117] (pp. 204-205). MINOS actually follows the function out from the minimum to find where it crosses the function value (minimum + UP), instead of using the curvature at the minimum and assuming a parabolic shape. This method not only yields errors which may be different from those of HESSE, but in general also different positive and negative errors (asymmetric error interval). Indeed the most frequent result for most physical problems is that the (symmetric) HESSE error lies between the positive and negative errors of MINOS. The difference between these three numbers is one measure of the non-linearity of the problem (or rather of its formulation). In practice, MINOS errors usually turn out to be close to, or somewhat

larger than errors derived from the error matrix, although in cases of very bad behavior (very little data or ill-posed model) anything can happen. In particular, it is often not true in MINOS that two-standard-deviation errors (UP=4) and three-standard-deviation errors (UP=9) are respectively two and three times as big as one-standard-deviation errors, as is true by definition for errors derived from the error matrix (MIGRAD or HESSE).

5.3 Streak camera

5.3.1 Description

The schematic of the experimental setup used to measure time-resolved laser and X-ray excited emission is shown in Figure 5.1 a), where the spectral-time resolution is modulated by a system of horizontal and vertical slits. The time resolution of the camera under femtosecond laser excitation is 18 ps and the repetition rate can go up to 4 MHz. Pulsed X-rays with energies up to 40 keV are triggered by a picosecond diode laser PiLAS at 372 nm. Samples are mounted at few millimeters from the X-ray window of a Hamamatsu N5084 X-ray tube. The resulting photoluminescence or radioluminescence is spectrally dispersed with a 50 g/mm-150g/mm-300g/mm grating in a spectrograph 2300i spectrometer and strikes into a few micrometer thin photocathode. These photons are subsequently converted to photoelectrons and deflected in a C10910 Hamamatsu streak camera tube, which is operated in single photon counting mode by setting the MCP gain to maximum and counting only the signal above threshold. This readout procedure guarantees that the source of noise of the system is not coming from the CCD but only from thermal electrons amplified by the MCP. The single photon counting mode is guarantee if the number of pixels fired in one shot is less than 5% of the total amount of pixels. This is of course calculated for an area representative of the measurement in question and not for the totality of pixels available. The maximum aperture for the spectrograph slit is 3000 μm and 200 μm is the width of the photocathode itself.

A delay generator (represented by the clock in Figure 5.1 a) provides the trigger signal for the laser and the sweeping unit in order to synchronize the light time of arrival and the ramping edge of the voltage between sweeping plates. The dynamical range goes from 1 ns gate to 1 ms gate, however the time resolution is limited to the constant number of bins available in the CCD that is placed after the phosphor screen, which is 508. This implies a bin as short as 2 ps for the 1 ns gate or as long as 2 μs for the 1 ms gate.

A typical streak image obtained when exciting a CdSe nanoplatelets (NPLs) thin film with X-rays is shown in Figure 5.1 b), with time increasing downward along the vertical axis and photon energy increasing to the right along the horizontal axis. The emission centered at 380 nm is the laser stray light which bounces around and reaches the spectrograph slit multiple times (IRF_{laser}). The X-ray excited CdSe NPLs is the signal centered at 530 nm, which first decay component characterizes the setup IRF_{X-rays} for the 5 ns sweeping range.

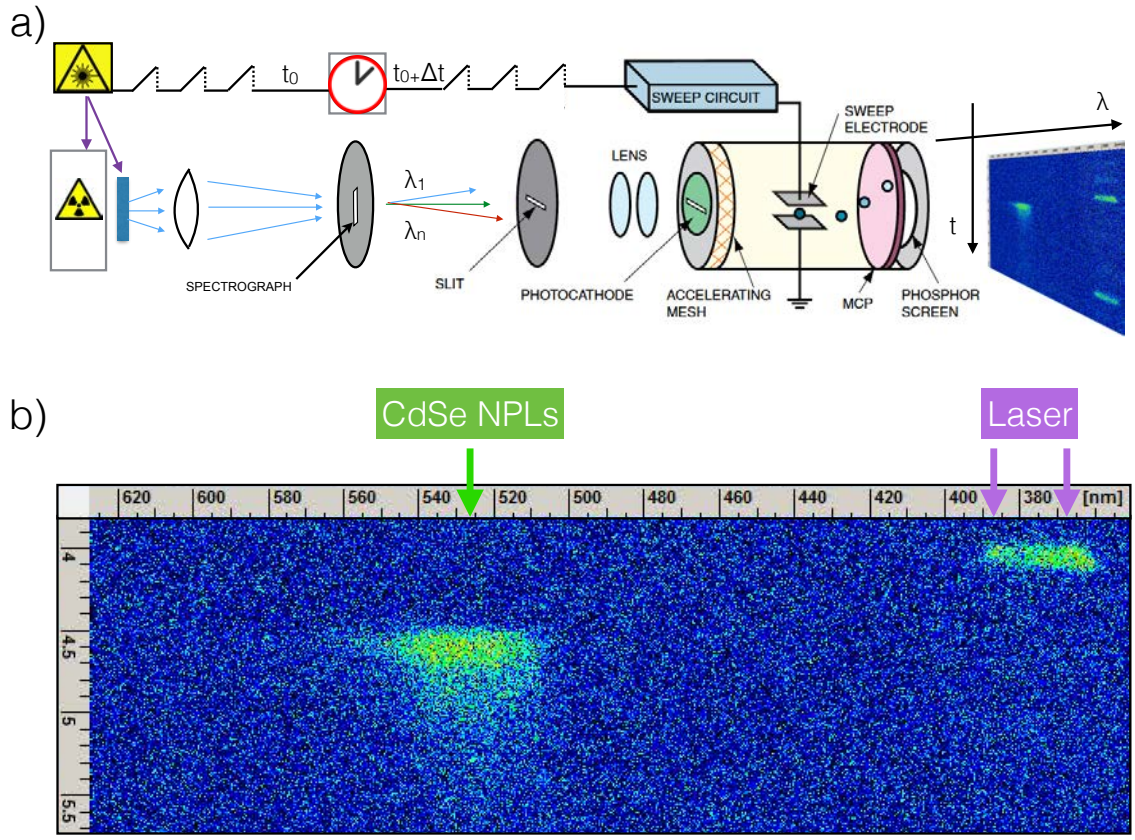

Figure 5.1: a) Schematic view of the instrumental setup main components. b) Streak camera image of CdSe nanoplatelets sample on a glass substrate excited by X-rays and sweeping at 5 ns.

Measuring with the streak camera requires three main steps:

1. Alignment → in order to focus the light created near the X-ray tube window into the spectrograph slit. The protocol to follow is explained in the Annex section B.1 and basically is a 2 lenses-2 mirrors of 2 inches diameter system. Maximizing the amount of light reaching the spectrograph slit at a height equal to the photocathode slit determines the signal-to-noise ratio of the measurement and for the case of X-ray excitation it might even define whether the measurement can be done or not.

2. Background calibration → in order to correct for the spectral-time response of the CCD and the sweeping range used. Basically, the background time response is not a flat function and furthermore is wavelength dependent as shown in Figure 5.2. This means that a specific calibration file needs to be acquired for each type of crystal by de-synchronizing the light emitted under continuous wave (c.w.) laser or LED excitation from the triggering signal provided by the streak camera. The aperture of both slits needs to be also the same since the spectral-time resolution is slit dependent. These calibration files can be directly stored in the streak camera software as shading and background corrections. The files should contain more than 10'000 counts per bin in a significant spectral region so that the statistical error is less than 1%.

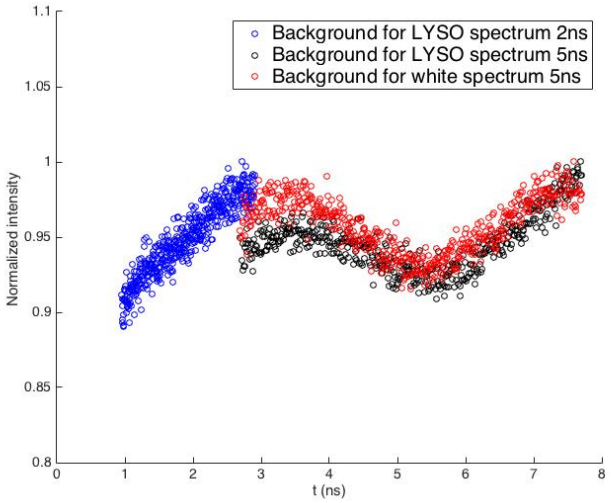

Figure 5.2: Spectral-time resolved background measured for different sweeping ranges and emission wavelengths.

3. Laser IRF calibration → in order to know the time resolution of the measurement in question. This calibration will be dependent on the sweeping range, the photocathode slit aperture and the optical path followed by the light. To correct for the optical path the laser is reflected by a layer of Teflon from the same spot that the crystal is placed later on. The drift associated with long measurements of 12 or more hours is negligible as demonstrated in Figure 5.3, where the difference in the sigma of the distribution is less than 1 picosecond.

   The main source of uncertainty is the photocathode slit aperture which is manually controlled and has steps of 5 μm which can introduce a maximum error of 10 ps. The systematic uncertainty in the determination of the laser IRF measured along different days has a standard deviation of 4 ps. To avoid the apparition of second peaks next to the main laser peak, the intensity is always set to 70%, so that the system can be triggered at 1-4 MHz. The laser IRF is not dependent on the triggering mode chosen, i.e. internal for a repetition rate f $<$ 1 MHz or external TTL for f $>$ 1 MHz.

Once the crystal has been aligned and the slits aperture and sweeping range are set, the measurement is carried out by integrating over a long number of exposures when using X-ray excitation. Signal-to-noise-ratio when using laser excitation can be 3 order of magnitude meanwhile for the case of X-ray irradiation is reduced to 1 order of magnitude. Estimations of the background over the whole spectral range resolved by the 50 g/mm grating is around 60 counts per hour for the 5 ns gate.

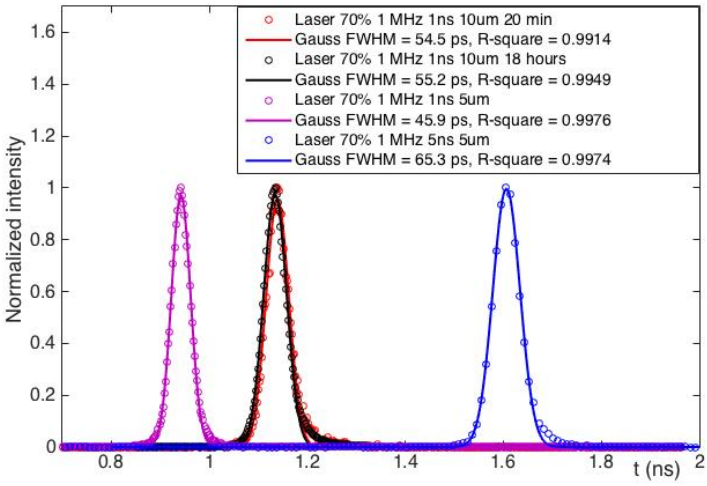

Figure 5.3: Laser IRF measured during 20 minutes and 18 hours using 1 ns and 5 ns gate and different slits aperture of 5 μm and 10 μm.

5.3.2 Impulse response function

The impulse response function (IRF) of the system has been determined using two different models: 1. a simplistic function describing the X-ray tube time profile which follows the information found in the data-sheet and 2. fitting the experimental data taken with a Hamamatsu X-ray streak camera and a 180 fs laser of a X-ray tube, type N5084 as the one we use in the lab. Both IRF models include different assumptions and are by no means a perfect representation of the actual IRF. However, the values obtained for the rise time of different scintillators are in good agreement with values measured using a different and well calibrated time-correlated single photon counting system [12]. For the nanocrystal case where the time profile already decays within the 5 ns gate, the influence of the model chosen for the IRF is negligible.

Models

The procedure starts by measuring the temporal profile of the laser under same measurement settings, sweeping range, optical path and photocathode slit aperture. Multiple reflections time spread contribution within the crystal is considered by measuring the laser light scattered by a LuAG undoped crystal positioned at the entrance of the X-ray tube window. Table 5.1 shows the values of FWHM for the laser measured under several configurations. For example, using 100 μm slit aperture and a 5 ns sweeping range, the laser shape is a Gaussian of 129 ps FWHM that is then convolved with the asymmetric X-ray tube time response. Due to the low signal-to-noise ratio characteristic of the X-ray excitation the photocathode slit can not be used with minimum aperture. The determination of the X-ray tube time profile is essential for the full characterization of the final IRF of the system.

Table 5.1: **Time resolution of the streak camera system expressed in FWHM when using laser excitation for different sweeping ranges and slits apertures.**

Sweeping range	Slit aperture	FWHM (ps)
1 ns	5 μm	54.5 $\pm$ 1
5 ns	5 μm	65.3 $\pm$ 2
200 ns	5 μm	700 $\pm$ 10
2 ns	100 μm	63 $\pm$ 3
5 ns	100 μm	129 $\pm$ 4

The first and simplest approach is to build the time response of the X-ray tube as an analytic non-continuous function with a first exponential rising component and a second monoexponential decay component. The X-ray tube time response is known to be asymmetric so a parameter θ can be used to define this asymmetry as suggested by the following function, which will be called fit I:

$$for \quad t \leq \theta \qquad f(t) = \frac{1}{e^{\theta/\tau_{xr}}} e^{t/\tau_{xr}} + background \tag{5.3}$$

$$for \quad t > \theta \qquad f(t) = e^{(\theta - t)/\tau_{xd}} + background \tag{5.4}$$

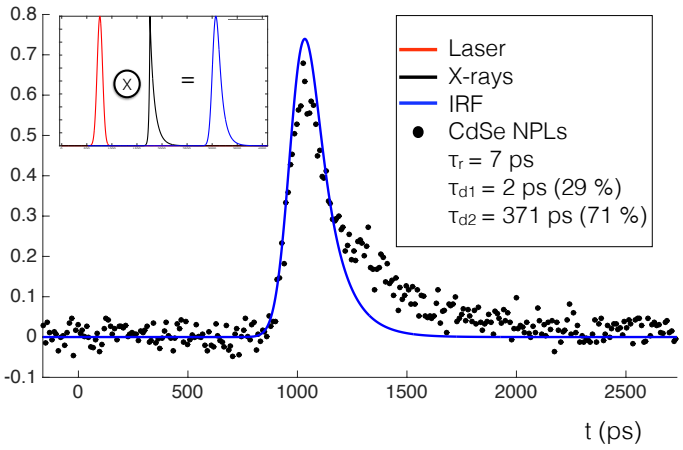

Figure 5.4: Instrumental response function of the system for 100 μm photocathode aperture and 5 ns sweeping range overlapping with the first component decay of the CdSe dynamic. The time profile of the tube is built analytically following the equations 5.3-5.4.

This function is represented by the black line function shown as inset of the Figure 5.4 which is convolved with the red line Gaussian function. The τ_{xr} and τ_{xd} constant are defined using the FWHM information of the tube specifications and the final IRF obtained by the convolution of the laser and X-ray IRF is the blue line curve (shown also in the referenced

figure). As can be seen in the CdSe decay of Figure 5.4 (these data are taken from the measurement shown in Figure 5.1 b), the first component of the CdSe NPL decay is limited to the time resolution of the tube when using τ_{xr} = 17 ps and τ_{xd}= 40 ps.

This method seems to reproduce correctly the CdSe NPLs time profile up to its first fast component. However, if the actual IRF of the X-ray tube presents a second low amplitude decaying component we will not be able to see it using this approach. For that reason a complementary study is done of the experimental data taken with a N5084 X-ray tube excited by a 180 femtosecond FWHM laser. Figure 5.5 shows the actual IRF of the X-ray tube which it is not exactly monoexponential in the rise or decay parts. These data have been provided by Hamamatsu in a private communication and have been measured using the C5680 X-ray special specification streak camera which has a golden photocathode which converts X-rays in photoelectrons.

The experimental data have been fit using the set of equations 5.3-5.4 (fit I in Table 5.2) and two other set of functions with biexponential rise and decay components (fit II and III in Table 5.2) in order to find the optimal scenario. Since the pedestal of the measurement is unknown the fit will include a free parameter in order to account for the background.

Fit I.I includes a monoexponential rise and decay times as in equations 5.3-5.4, however the continuity for x=θ is not imposed as in the case of fit I but parameters A and B are left free.

Fit II is defined with two rising components and one decaying parameter as described by the following equations:

$$for \quad t \leq \theta \qquad f(t) = Ae^{t/\tau_{xr1}} + Be^{t/\tau_{xr2}} + background \tag{5.5}$$

$$for \quad t > \theta \qquad f(t) = Ce^{(\theta - t)/\tau_{xd1}} + background \tag{5.6}$$

Fit III is including two rising and decaying parameters as described by the equations:

$$for \quad t \leq \theta \qquad f(t) = Ae^{t/\tau_{xr1}} + Be^{t/\tau_{xr2}} + background \tag{5.7}$$

$$for \quad t > \theta \qquad f(t) = Ce^{(\theta - t)/\tau_{xd1}} + De^{(\theta - t)/\tau_{xd2}} + background \tag{5.8}$$

These functions are then convolved with a Gaussian to account for the intrinsic time resolution of the streak camera used to measure the IRF. The sigma of this Gaussian is left as a free parameter and the fit value of 10 ps is in some agreement with the 13 ps time resolution reported for the streak camera. The values of the different parameters obtained when using the equations 5.3-5.8 are summarized in Table 5.2, where the fit is performed for the different cases.

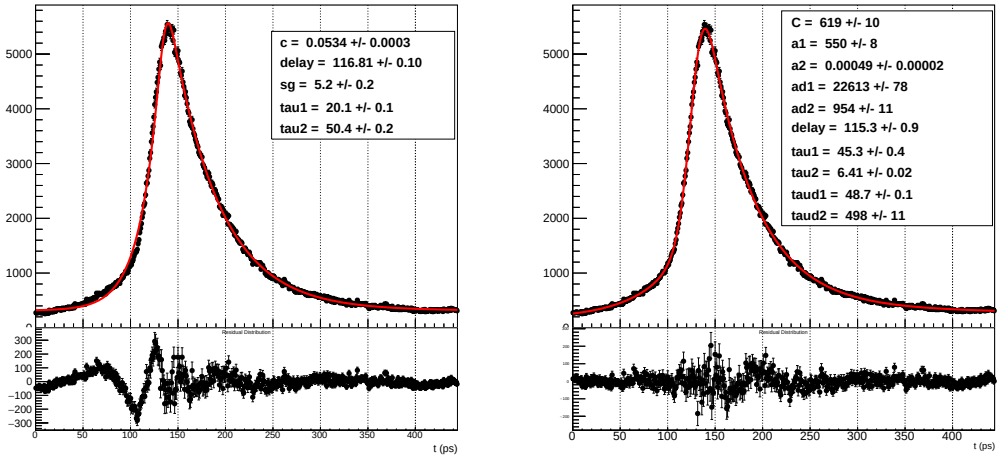

Figure 5.5: Time response of the X-ray tube as measured by Hamamatsu using a X-ray streak camera in a 440 ps gate. The data is fitted to a monoexponential (left, fit I) and biexponential (right, fit III) non-continuous functions following equations 5.3-5.4 and 5.7-5.8, respectively.

Table 5.2: **Fits parameters for the X-ray tube time response under femtosecond laser excitation after convolution with a Gaussian of 10 ps sigma**.

Fit	τ_{xr1} (ps)	τ_{xr2} (ps)	τ_{xd1} (ps)	τ_{xd2} (ps)	*back.*	χ^2
I	20.1 ± 0.1	-	50.4 ± 0.2	-	free	3.6
I.I	27.0 ± 0.1 (A)	-	50.4 ± 0.2 (B)	-	free	2.0
II	27.4 ± 0.6 (64.2%)	27 ± 1	51.2 ± 0.2	-	free	1.8
III	45.3 ± 0.4 (99.$\overline{9}$%)	6.41 ± 0.02	48.7 ± 0.1 (96.0%)	498 ± 11	free	1.2
III.upper	30.5 ± 0.1 (99.$\overline{9}$%)	3.97 ± 0.02	48.25 ± 0.06 (97.2%)	240 ± 2	fixed	1.6
III.lower	76 ± 4 (99.$\overline{9}$%)	9.05 ± 0.09	49.0 ± 0.3 (93.6%)	1074 ± 114	0	1.6

The main differences between fit I, II, III are the value of χ^2 and the fitting time which is obviously longer for the function with more parameters. Version III.lower seems to be unrealistic due to the value of 1 ns long decaying component (τ_{xd2}). Looking at the χ^2 values, fit II and III seem to be the best approximation, however this will need to be evaluated by fitting experimental data taken of representative cases. Furthermore for all the fits, when leaving the background as a free parameter or assuming the pedestal is at the level of the 10 first bins seem to underestimate the number of counts of the very last bins (look at the residual distribution for t>400 ps). When plotting the IRF data in log scale, the values are slowly rising for the time after 400 ps, which points towards a non-flat background as shown to the left of Figure 5.6. If we use the fit III which seems to give the best χ^2 values to reproduce the IRF experimental data when a linear fit has been applied to subtract the background, the long decay τ_{xd2} is found to be zero (Figure 5.6 right). In this way, we can understand the diversity of values reported in Table 5.2, where the background seems to play the key factor.

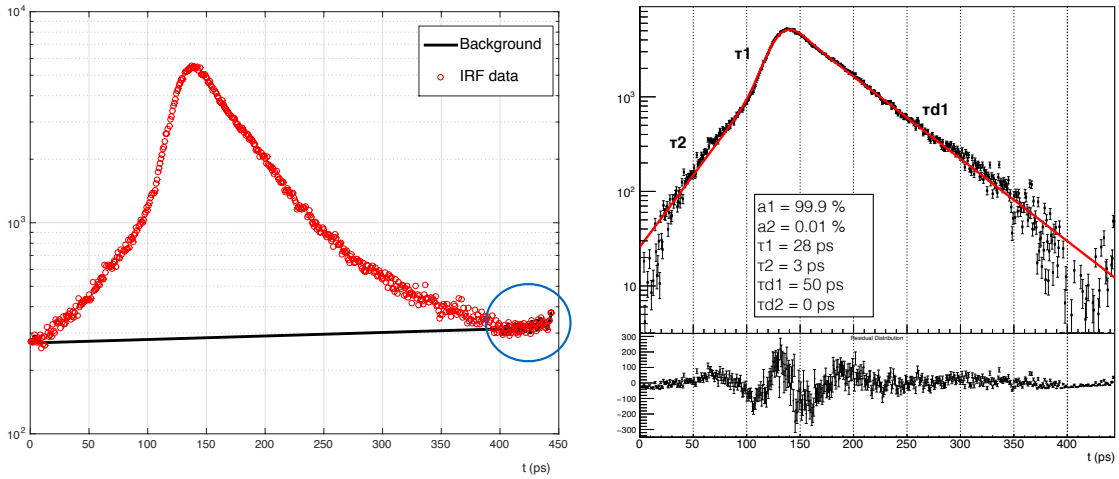

Figure 5.6: Left: IRF experimental data of a Hamamatsu N5084 pulsed X-rays tube with a non-flat background assumption. Right: Experimental data for which the background has been subtracted following the linear fit shown to the left and fit using equations 5.7-5.8.

Decay time of scintillating nanocrystals

When fitting the CdSe NPLs data previously presented in Figure 5.1 b), using as IRF the parameters from the very extreme cases of fit I and III, the values for the second decay time are different by 100 ps as shown in Figure 5.7 and summarized in Table 5.3. Even though fit I seems to have a very high χ^2 compared to fit III, the differences in decay times and abundances are not dramatic. In fact, the fit performed using the IRF information from the data-sheet seems to work quite nicely as an upper estimation of the decay components of a very fast decaying material. In this way, we justify the use of the simplest model when measuring time-resolved data of nanocrystals under X-ray excitation in the following chapters.

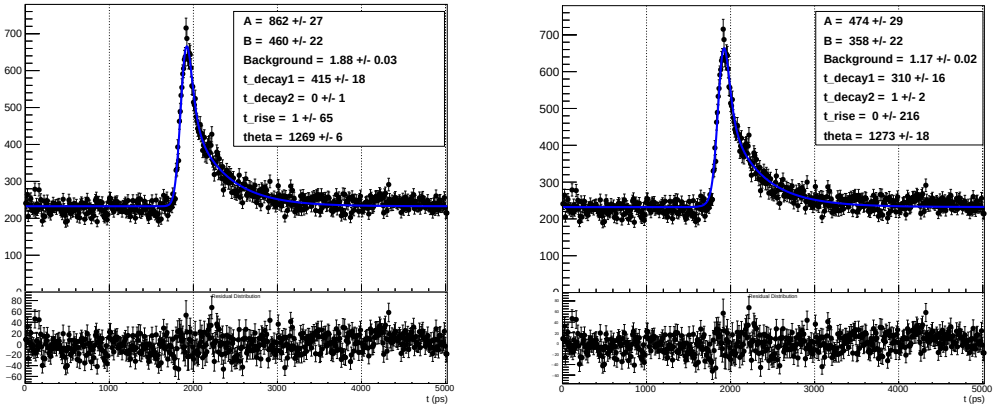

Figure 5.7: Fit of the CdSe NPLs X-ray excited data in the 5 ns gate using different IRF functions. Left: IRF fit using monoexponentials functions following equations 5.3-5.4. Right: IRF fit using biexponentials functions following equations 5.7-5.8.

Table 5.3: **Fit parameters for the time profile of CdSe NPLs using different IRF functions from the data-sheet or actual data**.

Fit	Parameters	τ_{d1} (ps)	τ_{d2} (ps)
data-sheet	τ_{xr}=17 ps τ_{xd}=40 ps	0 ± 1 (32%)	387 ± 27 (68%)
I	τ_{xr}=20 ps τ_{xd}=50 ps	0 ± 1 (35%)	415 ± 18 (65%)
III	τ_{xr1}=45 ps τ_{xr2}=6 ps τ_{xd1}=49 ps τ_{xd2}=498 ps	1 ± 2 (43%)	310 ± 16 (57%)

Rise time of inorganic scintillating crystals

Now, the question of how much the IRF fit under I, II and III equations is able to influence the value of the rise time of conventional scintillators measured under X-ray excitation, is still open. To compare, we evaluate the experimental data taken with the same LYSO scintillating crystals whose rise time values has been already measured and previously reported [12]. Taking the LYSO crystal CPI 2544 as an example, the rise time measured under 511 keV is 58 ps using a single photon time correlated setup with a Gaussian IRF of 63 ps sigma. One of the main differences between 511 keV and X-ray excitation is the presence of Cherenkov photons, which will modify the rise time reported. In principle, and as already explained [12], the absence of prompt photons in the rise time model will deliver slightly shorter values compared to the rise time which takes into account a very small fraction of prompt photons as it is the case of LYSO crystals. In this way, we expect that the rise time under X-ray excitation should be smaller than 58 ps when considering a model with only one rise time component. The laser IRF for the measurement of LYSO CPI 2544 was 54 ps sigma, which roughly convolved with a 21 ps sigma X-ray tube delivers a final IRF of around 58 ps sigma.

The different fits for the IRF were used to define the impulse response function and the data obtained when measuring the LYSO CPI 2544 under X-ray excitation were fit for several cases as shown in Figure 5.8. The values oscillates between 89 ps obtained with the fit I and 0 ps when using the fit III. The errors shown in each plot are just statistical uncertainties given by the MINOS algorithm which underestimates considerably the systematic errors. Comparing to the 58 ps rise time measured under 511 keV excitation, seems like the most appropriate value comes from the fit performed following I.I and II with results of 24 ± 5 ps and 53 ± 11 ps, respectively.

One way to confirm that fit III is an incorrect approach is to use it as IRF of a measurement performed using LSO:Ce:Ca co-doped scintillating crystal. This crystal has a rise time of the order of 20 ps measured under 511 keV excitation. 20 ps is also at the level of the systematic uncertainties arising from the time correlated single photon counting setup, so we could use it as a reference of zero or nearly zero rise time. Figure 5.9 shows several

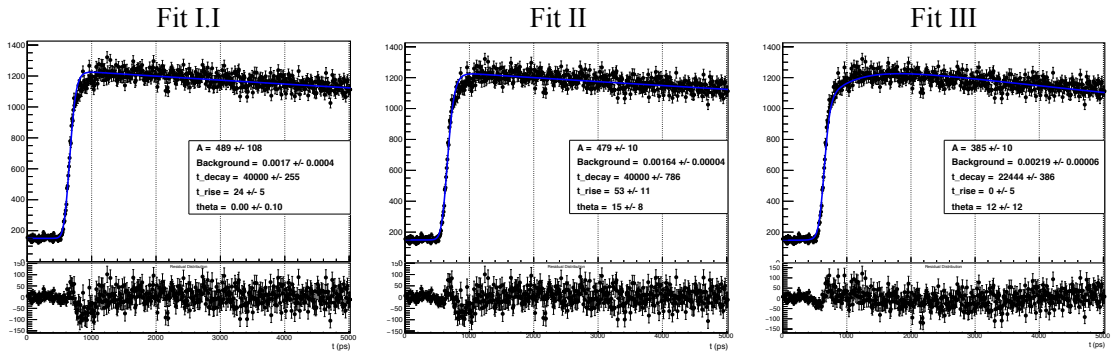

Figure 5.8: Rise time measured under X-ray excitation using a LYSO CPI $2 \times 2 \times 10$ mm^3 crystal and fit using different approximations of the IRF.

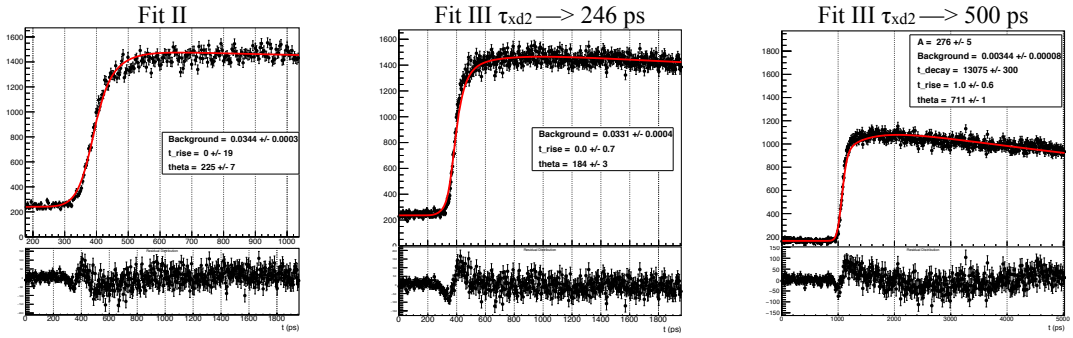

Figure 5.9: Rise time measured under X-ray excitation using a LSO:Ce Ca co-doped $2 \times 2 \times 10$ mm^3 crystal using fit II and III for the IRF de-convolution.

fits performed with the data obtained by measuring LSO:Ce:Ca co-doped crystal in the 2 ns gate using different fits for the IRF. The laser IRF has a sigma of around 26 ps. The best fit is obtained with fit II (χ^2=1.5) which is shown at the left-hand side of Figure 5.9 zooming in the first 800 ps of the signal. Fit III using a long decay of around 200 ps (center) has a χ^2=1.7. Fit III using 500 ps tail has a χ^2 >2 so we rule it out from this study.

Fitting the data obtained with LSO:Ce:Ca co-doped crystal in the 5 ns gate using fit II and fit III with 200 ps tail shows a χ^2=1.08 and 1.04, respectively. This points towards an actual presence of a long second tail different from 51 ps, however the decay constant and amplitude of this tail is not 246 ps and 4% as assumed from fit III.upper. In fact, the only way to get a χ^2 <1.5 when using fit II and III.upper is to make the rise time of the IRF zero. If we do this, both fits II and III.upper are able to reproduce the experimental data taken with a LSO:Ce:Ca co-doped with a χ^2 ~1.2. This points towards a tube time profile, which rises very fast following the laser and then decays either with a component of around 51 ps or two components of 51 ps and around 200 ps with an amplitude of less than 2%.

If we fit with the modified IRF which has a rise time near zero and either one or two decay components, the χ^2 of the fit is the same. We can go even further and fit using the amplitude of the second component as a free parameter and the value will decrease to less

than 2% compared to the amplitude of the 51 ps component. If we use both IRFs to fit the experimental data obtained with a LYSO CPI 2544 crystal taken at 5 ns, the determination of the two rise components has similar values, however the uncertainty in the determination of the second component is almost 80% as shown in Figure 5.10.

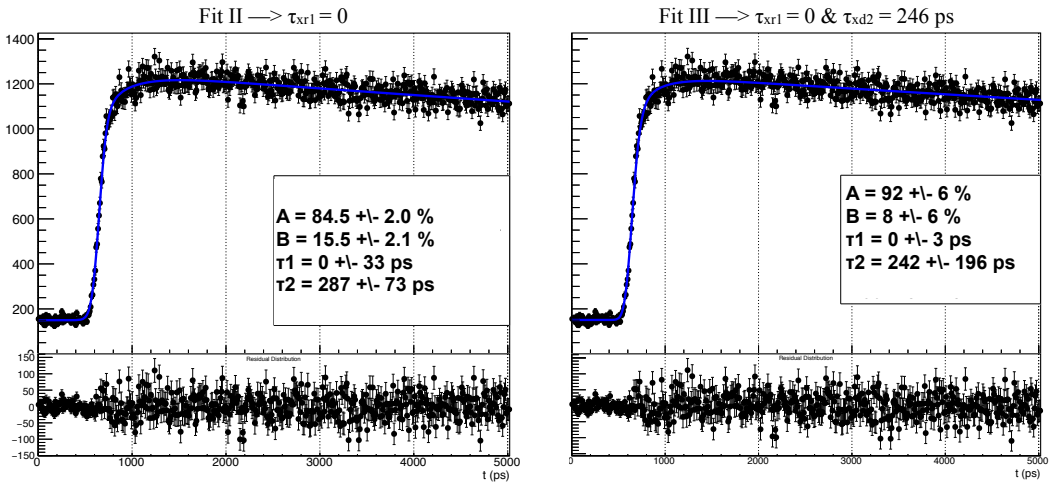

Figure 5.10: Rise time measured under X-ray excitation with a LYSO CPI crystal using a two components rise time model.

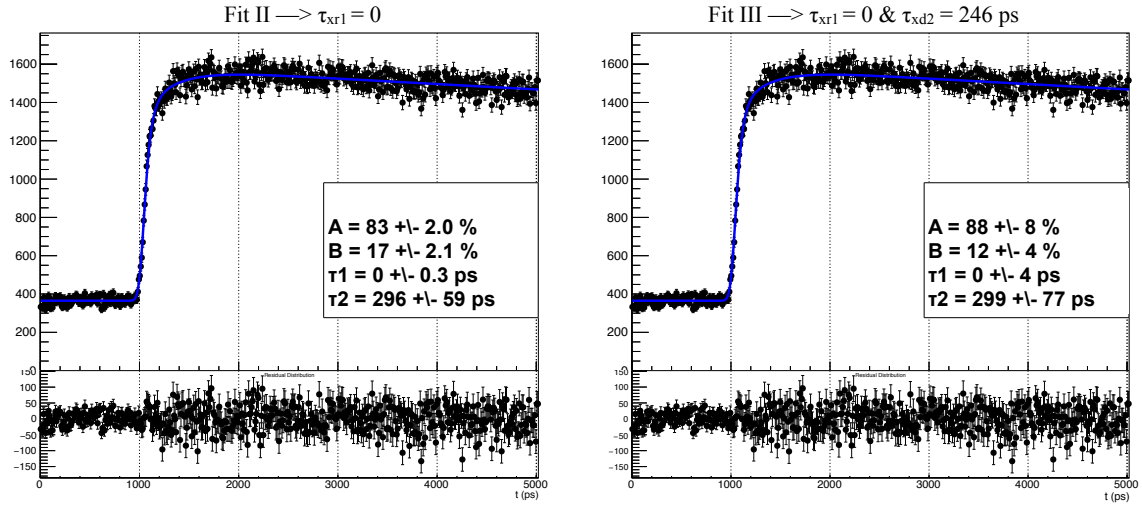

Figure 5.11: Rise time measured under X-ray excitation with a LSO CTI crystal using a two components rise time model.

The previous analysis show that using either the simplest fit approach or the one which assumes a possible extra long decay component as the fit III.upper, yields approximately the same results. However, the uncertainty in the determination of the second rise component is rather large when using fit III.upper. This is understood by looking at the correlation matrix which yields a very high value for the correlation between the second long component of the IRF and the second long component in the rise time. Measuring the crystals using a slit aperture of 50 μm which reduces the laser IRF to 34 ps sigma, the uncertainty related to the second rise time component decreases to a 25%, which is shown in Figure 5.11.

For simplicity we will work in the future chapters with the simplest first model, taking into account that the uncertainty of the second component in the two rise time model is very high.

5.3.3 Energy spectrum of the pulsed X-ray tube

The X-ray tube has a Tungsten photocathode with characteristic lines around 9 and 11 keV. The maximum voltage is 40 kV which defines the X-rays energy spectrum as shown in Figure 5.12. This spectrum is obtained by Geant4 simulations using a Beryllium window of 250 μm as reported in the data-sheet. If the tube has extra filters it is possible that the low energy region below 5 keV is actually different. X-rays are created and emitted in 2π exiting through a 30 mm diameter window. The operation current is around 2 μA when integrating the number of electrons triggered by the 372 nm picosecond laser with 4 MHz repetition rate.

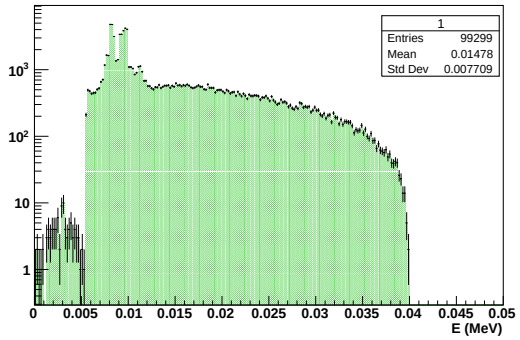

Figure 5.12: Energy spectrum of the tungsten X-ray tube used to excite the scintillating crystals.

The peak power of the laser is of the order of 10^7 photons per pulse, which reduces to 10^6 electrons per pulse due to the quantum efficiency of the X-ray tube photocathode. Integrating this amount of electrons per pulse in 1 second gives approximately a current of the order of μA. The lifetime of the tube, i.e. initial current reduced to 10% is around 1000 hours when setting the current at 50 μA. This gives us a factor of 25, so the tube could last 25'000 hours if operated at 2 μA, i.e. continuous operation for 2.85 years.

5.4 Rise- and decay-time of scintillating crystals

5.4.1 Laser excitation

The scintillating crystals were characterized using 372 nm laser excitation which gives information regarding Ce^{3+} intrinsic emission dynamics. The rise time under laser excitation is checked to be zero for all the crystals, which points towards sub-picosecond excitation time of the Ce^{3+} centers. Therefore, Table 5.4 is only reporting the decay time of several lutetium-based oxy-orthosilicates from different producers.

Table 5.4: **Decay time of lutetium oxy-orthosilicates Ce^{3+} doped scintillators using laser excitation**.

Crystal	$\tau_d \rightarrow$ IRF = 700 ps	
	τ_{d1}	τ_{d2}
LSO:Ce Ca 0.4%	33.7 ± 0.2 ns 94.3 ± 0.7%	9.2 ± 0.8 ns 5.7 ± 0.7%
LSO:Ce CTI 1802	35.2± 0.1 ns	-
LSO:Ce PML 1126	36.4± 0.04 ns	-
LYSO:Ce CPI 3051	37.7± 0.1 ns	-
LYSO:Ce CPI 2544	40.5 ± 0.1 ns 83.2 ± 1.4%	22.9 ± 0.1 ns 16.8 ± 0.2%
LYSO:Ce Proteus 2483	40.9 ± 0.1 ns 85.2 ± 6%	22.8 ± 0.5 ns 14.8 ± 1.9%
LYSO:Ce Sipat 2443	39.2± 1 ns	-
LGSO:Ce 2626	40.3 ± 0.2 ns 83 ± 6%	24.1 ± 0.5 ns 17 ± 2%
LFS:Ce 2798	36.5± 0.1 ns	-

5.4.2 X-ray excitation

Lutetium oxy-orthosilicates

A summary of all measurements is present in Table 5.5. The rise time values reported were obtained by using the simplest fit approach to describe the X-ray IRF where the decay time constant is around 50 ps. Using this fit the rise time of LSO:Ce Ca^{2+} co-doped crystals yields zero for either 2 ns or 5 ns sweeping range. The numbers reported can be considered as relative values to LSO:Ce Ca co-doped crystals. As demonstrated in the previous section the second rise time component seen for non co-doped crystals presents an underestimated error bar. The first rise time component which has usually values of 0 ± 1 ps is at the level of the IRF, so it is completely unresolved.

The second rise time component seen for lutetium oxy-orthosilicate non co-doped crystals could be an indication of a trapped population which eventually populates the activator levels with a decay time of ∼ 300 ps. If light emission comes as a result of this process, the scintillating pulse should follow the relation:

$$F(t) = \alpha * scint(t) + (1 - \alpha) * scint(t) \otimes excit(t) \tag{5.9}$$

where 1-α gives the population amplitude decaying at 300 ps which is represented as *excit(t)*. The function *scint*(t) stands for the direct excitation and emission from the Ce^{3+} centers. This mathematical model is indeed able to fit the experimental data when 1-α coincide with the amplitude of the second rise time component.

Table 5.5: **Rise time of lutetium oxy-orthosilicates Ce^{3+} doped scintillators with and without Ca^{2+} co-doping using pulsed X-ray excitation**.

	X-rays		
Crystal	IRF	τ_{r1}	τ_{r2}
LSO:Ce Ca 0.2%	63 ps	0 ps	-
LSO:Ce Ca 0.4%	134 ps	0 ps	-
LSO:Ce CTI 1802	80 ps	0 ± 2 83 ± 2.0%	296 ± 59 ps 17 ± 2.1%
LSO:Ce PML 1126	134 ps	0 ± 2 ps 86.7 ± 2.0%	376 ± 70 ps 13.2 ± 3.5%
LYSO:Ce CPI 2745	134 ps	0 ± 2 ps 82.9 ± 4.9%	400 ± 95 ps 17.1 ± 5%
LYSO:Ce CPI 3051	134 ps	0 ± 1 ps 82.4 ± 1.8%	276 ± 33 ps 17.6 ± 2.8%
LYSO:Ce CPI 2544	134 ps	0 ± 2 ps 82.7 ± 1.6%	227 ± 22 ps 17.3 ± 2.0%
LYSO:Ce Proteus 2483	134 ps	0 ± 2 ps 81.5 ± 1.6%	337 ± 41 ps 18.5 ± 2.0%
LGSO:Ce 2626	134 ps	2 ± 17 ps	-
LFS:Ce 2798	134 ps	0 ± 2 ps 83.2 ± 1.5%	202 ± 29 ps 16.8 ± 1.7%

5.5 Conclusions

In this chapter we have shown the potential of the streak camera to perform decay time measurements of fast scintillating nano-materials. Despite the impulse response function has not been measured accurately the model applied to describe the time profile of the X-ray tube allows us to estimate the rise time of conventional scintillating materials and to measure the timing kinematics of scintillating nanocrystals.

The rise time of a large set of lutetium oxy-orthosilicate Ce^{3+} crystals was measured using X-ray pulsed excitation and an impulse response function of 60-134 ps FWHM. Comparative measurements between doped and co-doped systems are able to confirm the existence of a second rise time component in non co-doped scintillators, except for the LGSO sample. These two rise time components could corresponds to a direct ($\tau_{r1} \sim$ O(10)ps) and delayed

($\tau_{r2} \sim$ O(100)ps) excitation of the activator centers. The study also included a set of garnets (YAG, GaGG, LuAG) with and without Mg^{2+} co-doping. Due to the preliminary nature of the rise time values obtained for the garnets study, their values are reported in the annex section A.

The dynamical range of the streak camera is suitable for time-resolved photoluminescence measurements. However the signal-to-noise ratio which corresponds to the time-resolved radio-luminescence measurements is very poor and the intrinsic time resolution of the system of 18 ps FWHM is highly deteriorated due to the low collection efficiency provided by optical devices. The spectral resolution is also deteriorated from 1 nm to 10 nm for the laser line.

Measuring the impulse response function (IRF) of the pulsed X-ray tube is absolutely necessary and essential in order to perform accurate rise time measurements. For this, the installation of an ID-quantique photodetector in front of the X-ray tube window is foreseen. The ID-quantique could also contribute to increase the signal-to-noise ratio of the radio-luminescence signal. As fast scintillator we could use a material known as malachite green used in [118] with an expected decay time of the order of 30-40 ps. Research of the time performance of ultrafast emitting materials could also serve for this purpose as we will see in the next chapter.

Chapter 6

Nanocrystals under optical and ionizing excitation

6.1 Introduction

Ultimate time resolution, one order of magnitude better than state-of-the-art values when using 511 keV gamma excitation [8], constitutes a major technological challenge among radiation detector systems. Sub-20 ps coincidence time resolution (CTR) in time-of-flight systems translates directly into a vertex identification area of a few millimeters which could highly impact medical imaging devices and high-energy physics detectors. In this way, producing a prompt photon signal [12] to the passage of ionizing radiation has become an essential feature for next generation scintillators used in high energy physics (HEP) and time-of-flight positron emission tomography (TOF-PET).

State-of-the-art CTR values on the order of 117 ± 3 ps have been achieved for 20 mm long LSO:Ce Ca co-doped crystals using 511 keV [8] γ-rays, which translates into a background rejection area of the order of a few centimeters. Reaching the millimeter level for vertex identification, however, necessitates CTR values of 10 ps or less. Lowering CTR values can be achieved via increasing the light yield, shortening scintillation signal rise and decay times, or introducing a strong prompt signal [12]. In the search for faster materials, co-doping with Ca^{2+} [119] or Mg^{2+} [120] species has proven to improve rise and decay time of the scintillating signal. However, this method finds poor impact on CTR measurements [8]. The intrinsic light yield measured for LYSO crystals is 40'000 ph/MeV ± 9% (syst) ± 3% (stat) under minimum ionizing electron excitation [105] and the decay times in cerium doped systems are limited to 16 ns [121]. This sets a limit to the improvement that photostatistic can bring to CTR measurements, requiring that new approaches to achieving a prompt photo-response must be explored.

Figure 6.1 presents Cràmer-Rao lower bound calculations for CTR values as a function of the single photon time resolution (SPTR expressed in sigma) and number of prompt photons produced along with the scintillation emission in the crystal (as published in [57]). For the calculations shown, we used the time profile of LSO:Ce, i.e. scintillation rise time of $\tau_r = 70$ ps and decay time of $\tau_d = 40$ ns, and crystals of 3 mm and 20 mm lengths with different light transfer efficiencies (LTEs). As shown in reference [12] and Figure 6.1, a coincidence time resolution of 10 ps FWHM can be achieved with a prompt signal of several hundreds of photons produced, providing that the SPTR of the SiPM is of the order of 10 ps sigma. Commercially available SiPMs do not provide this value. However, measurements performed on free standing single photon avalanche diodes of the SiPM showed SPTR values below 10 ps sigma. Consequently, the SiPM engineering has to be improved together with light production mechanisms to reach CTR values of 10 ps.

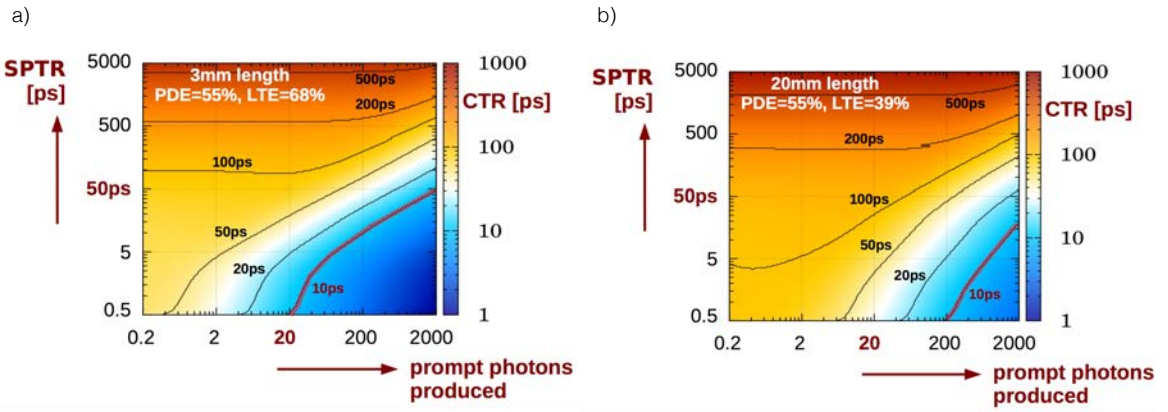

Figure 6.1: Cramèr-Rao lower bound calculations for CTR using a LSO:Ce scintillator of (a) 3 mm and (b) 20 mm length as function of SPTR and number of prompt photons. As reported in [12, 57].

Processes such as the Cherenkov effect [122, 123, 106] and hot intraband emission [124, 43] have been investigated for this purpose, though both suffer from poor light yield. This motivates research not only towards ultrafast sub-nanosecond performance but also to materials that have the potential to produce prompt photons with sufficiently high yield under ionizing irradiation.

In this chapter the ultrafast emission dynamics of colloidal semiconductor nanocrystals (NCs) as a new approach for prompt photon generation is presented. In Figure 6.2, the fast rise and decay for CdSe nanoplatelets (NPLs) and CdSe/CdS giant shell quantum dots (GS QDs) contrasted with the slower dynamics of LSO:Ce under pulsed X-ray excitation provides clear motivation for this work. CdSe NPLs are solution-processed quantum wells that are characterized by strong quantum confinement in only one dimension. Weak confinement in the lateral dimensions has two important consequences. First, in contrast to spherical NCs, momentum conservation rules apply more strictly, which reduces accessible states for Auger transitions. Second, a collective phasing of dipoles over many unit cells permits a giant oscillator strength transition (GOST) [13, 14, 15], resulting in ultrafast emission rates. We have also investigated spherical GS QDs. In addition to better photostability compared to

the core-only CdSe NPLs, their reduced emission/absorption band overlap (see Figure 6.3(b)) would be advantageous in real devices where light has to potentially travel through at least 20 mm of material before it is detected.

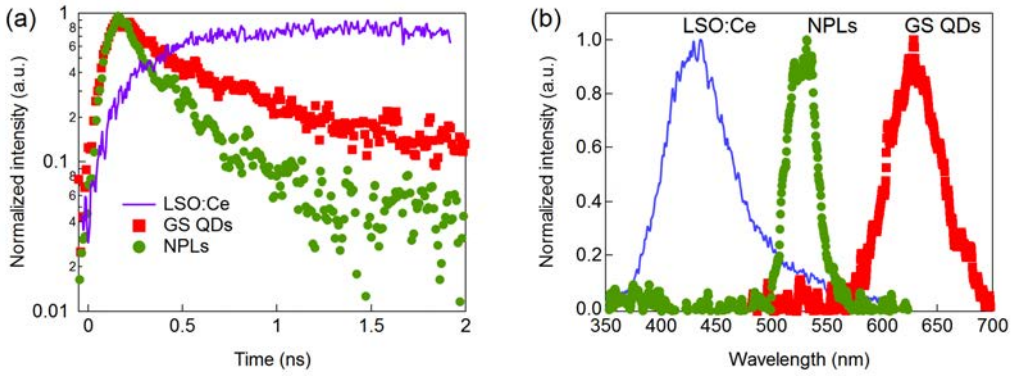

Figure 6.2: (a) Time-resolved photoluminescence and (b) steady-state spectra for LSO:Ce, CdSe/CdS GS QDs, and CdSe NPLs under pulsed X-ray excitation.

The tunable optoelectronic properties of NCs combined with recent advances in controlling their size, shape, core/shell heterostructure, and surface chemistry have enabled their use in a wide range of photonic applications. They have shown particular promise for bio-labeling [87], low-threshold lasing [16, 15, 17], photovoltaics [18], and single photon sources for quantum information [19, 20]. The high quantum yields (QYs) of NC quantum dots (QDs) has also generated interest in their use as low-cost, high-resolution scintillators for radiation detection [21, 22, 23]. Toward this end, the response of QDs under high energy electron [26], alpha [91], soft X-ray [92] and γ-ray [25] irradiation has been investigated. Initial high energy excitation studies have highlighted several important challenges that all degrade the light emitting properties of NCs, notably non-radiative Auger recombination [26], photo-instability [24], and losses due to the re-absorption of emitted light [25]. These challenges arise from the nature of NCs as small ($\lesssim$100 nm) semiconductors. On this size scale, strong carrier confinement results in efficient Auger recombination, high surface to volume ratios makes them sensitive to the external environment and damage, and small Stokes shifts result in significant re-absorption of emitted light. All of these issues degrade the performance of scintillators. For instance, nonlinear quenching such as Auger recombination that occurs at the high carrier densities created at electron track ends has been identified as a major cause of scintillator non-proportionality [125, 35, 121], and therefore degraded energy resolution.

Fortunately, significant effort has been devoted to overcoming these barriers to advance the development of NCs for the photonic applications mentioned above. Auger recombination, for example, has been mitigated with 2D NPLs [126, 15] and heterostructured core/shell NCs [127]. Similarly, CdSe/CdS core/shell and particularly core/giant shell quantum dots (GS QDs) have improved photostability due to reduced charge transfer to deep, non-radiative surface traps. Further, re-absorption can be circumvented by engineering large Stokes shifts in GS QDs, where emission from a CdSe QD core and absorption from the larger band gap CdS shell are well-separated [18, 127].

6.2 Laser excitation

6.2.1 Auger suppressed CdSe-based nanocrystals

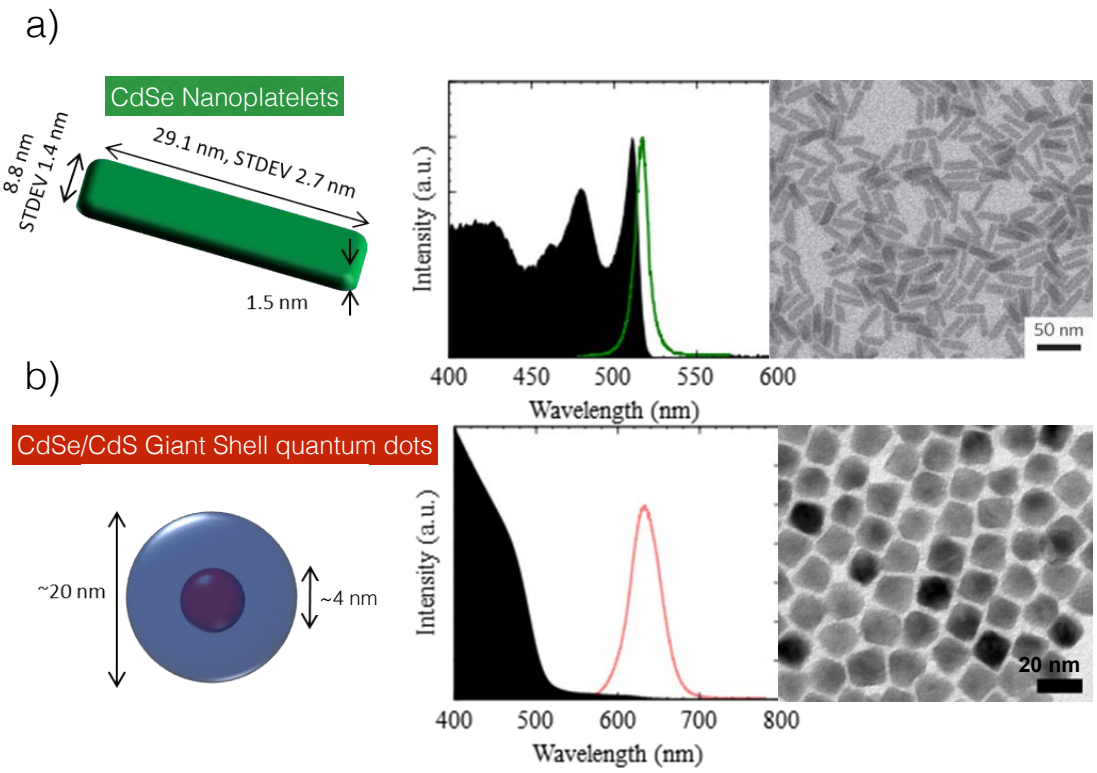

Figure 6.3: Structural and optical properties for (a) CdSe NPLs and (b) CdSe/CdS GS QDs (Left). Center: Absorption (black) and steady-state photoluminescence (green and red) spectra for both systems. Right: Nanocrystals TEM images as published in reference [15] and [27].

Auger recombination rates in nanocrystals are inversely proportional to the exciton volume and directly proportional to the electron-hole wavefunction overlap, and are therefore suppressed in nanocrystal heterostructures that allow for electron delocalization [127]. Electron delocalization can be reached either by engineering the band gap of the heterostructure with a smooth confinement potential between core and shell or by allowing for confinement in specific directions leaving one or two dimensions for the carriers to move freely. In this way, we will study two different systems whose both present high suppression of Auger recombination rate: CdSe nanoplatelets (NPLs) and CdSe/CdS giant shell quantum dots (GS QDs).

Details of the synthesis for the NPLs and GS QDs can be found in reference [15] and [27], respectively. The colloidal solutions used for all the measurements presented in this thesis were produced in the group of Iwan Moreels at Istituto Italiano di Tecnologia, Genova, Italy. The absorption and emission spectra and illustrations of the CdSe NPLs and CdSe/CdS GS QDs used in this section are shown in Figure 6.3. These spectra are typical of these NCs, and depict several of the characteristic features discussed above.

For the CdSe nanoplatelets, the 2.41 eV or $\sim$ 515 nm photoluminescence peak (Figure 6.3 (a) center) corresponds to a thickness of 1.5 nm, equivalent to five CdSe monolayers (ML) according to Achtstein and co-authors [128]. The lateral dimensions of 8.5×35.3 nm^2 imply that excitons only experience strong confinement in the z direction. The emission and absorption spectra in Figure 6.3 a) center reveals a Stokes shift of 24 meV. Excitonic transitions associated with the heavy holes (HH) and light holes (LH) are also visible at 2.43 eV and 2.57 eV, respectively. Figure 6.3 a) right presents a transmission electron microscope (TEM) image of the quantum wells. The quantum efficiency of these NPLs has been measured to be 25% under laser excitation. The timing characteristics are 400 ps decay time for the excitonic emission (X) centered at 515 nm with a binding energy of 132 meV and around 100 ps decay time for the biexciton (XX) which presents a binding energy of 32 meV and it is centered at 520 nm. These two very high binding energies allow excitons and biexcitons to co-exist at room temperature and decrease the stimulated emission threshold to one of the lowest values so far of 6 μmJ/cm^2. The stimulated emission peak is centered at 530 nm and shows sub-picosecond recombination times. Together with the sub-nanosecond emission of X and XX, a long tail of few nanoseconds which is characteristic of traps at the surface of the material is seen for CdSe NPLs (see Figure 6.4).

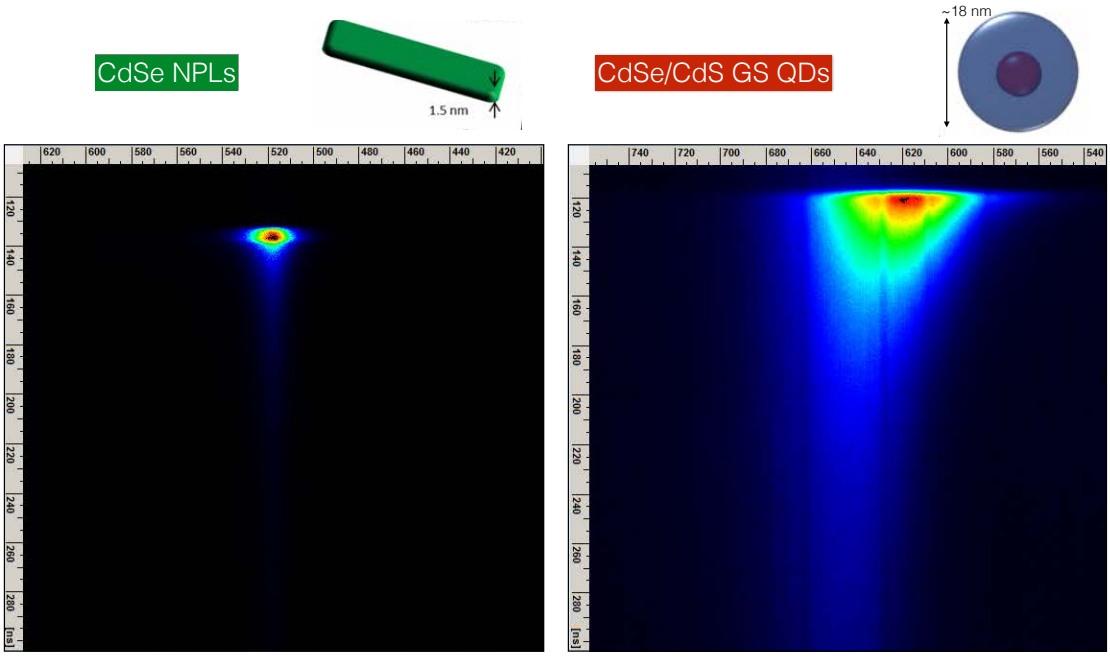

Figure 6.4: CdSe nanoplatelets (left) and CdSe/CdS giant shell quantum dots (right) characteristic excitonic photoluminescence emission measured with a gate of 200 ns. The NPLs emission overlaps with the IRF of the system for this sweeping range. The blue-shifted biexcitonic emission (centered at 620 nm) characteristic of the GS QDs dominates the signal for the first 10 ns.

Giant shell quantum dots were synthesized using a fast injection route which allows to epitaxially grow the shell in a nearly-free defect heterostructure. Both core and shell have a wurtzite structure and the quantum efficiency for these nanocrystals is reported to be close to 90%. The core is about 4-5 nm in diameter meanwhile the shell can grow up to 18 nm which is equivalent to around 18-20 CdS monolayers. The global Stokes shift is approximately

170 nm with the main excitonic emission centered at 640 nm as shown in Figure 6.4 (right) for the slowest emission. The lifetime of the biexcitonic emission has been reported as 15 ns with a quantum efficiency of 11%. In contrast to the CdSe NPLs, the biexcitonic population appears as a blue-shifted emission centered at around 620 nm. The blue-shift is characteristic from electron-hole pair bound states which repel each other as a result of the high degree of quantum confinement in every direction. The quantum dots used in this chapter have a CdSe core of 3.7 nm and a shell of 15 monolayers (MLs).

For both CdSe NPLs and CdSe/CdS GS QDs, thin films were prepared by drop-casting from O.D. (optical density) 30 toluene solutions. The deposition is done on microscope slips with thicknesses between 80-100 μm. There is no emission from this glass which makes the measurement background purely the thermal noise of the streak photocathode.

A near-UV 372 nm picosecond diode laser is used to trigger the X-rays and to directly excite the NCs films when deposited on a glass substrate. The features of the spectral-time resolved photon counting system was described in the previous chapter. The sweeping range for the laser excited measurements has been chosen to be the same that for X-rays excitation, together with slit aperture and laser settings. This guarantees the same laser IRF for both sets of measurements which allows us to make comparisons between laser and X-ray excited emission dynamics. A 2 ns gate is chosen for the CdSe NPLs for better resolution of the fast components. Meanwhile for GS QDs, the gate is open up to 5 ns since they present slower emission rates.

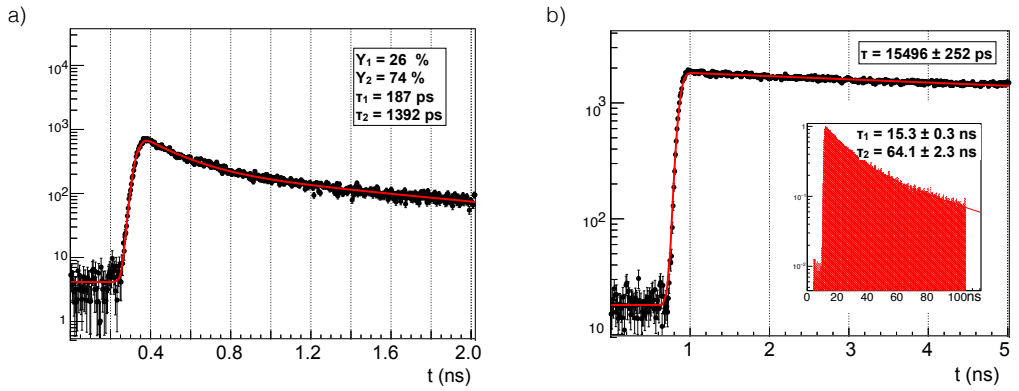

Figure 6.5: Nanocrystals timing performance under laser excitation measured under the same setup conditions used for X-ray excitation. a) CdSe nanoplatelets within a 2 ns gate. b) CdSe/CdS quantum dots giant shells within a 5 ns gate.

Timing performance under laser excitation from NPLs and QDs is shown in Figure 6.5. The results for NPLs point towards excitonic emission, consistent with laser excitation studies performed using similar materials as in reference [15]. Measurements of GS QDs PL within 100 ns gate are shown as inset of Figure 6.5 b), where two decay components with lifetimes of 15 ns and 64 ns, respectively, are required to fit the data. The 15 ns decay dominates the signal when a smaller window of 5 ns is used (Figure 6.5 b). These slow and fast components are consistent with the exciton and biexciton emission demonstrated in reference [27].

6.2.2 Core/shell CdSe nanoplatelets

While the absorption cross section and photostability of GS QDs are important features for high energy detection, the reduced oscillator strength due to electron delocalization in the shell leads to longer emission lifetimes as demonstrated in the previous section. On the other hand, CdSe NPLs are two-dimensional nanocrystals with both fast radiative emission and slow non-radiative emission rates. In this way, it seems natural to think in a system that combines both features, i.e. fast radiative emission and photostability. Growing shells to passivate emissive NC cores is a common strategy, and here we grow a ZnS shell on CdSe NPL cores. As shown in Figure 6.6, there is both a spectral shift and reduction in emission rate following ZnS shell growth. For both materials, the results were obtained by drop casting a thin film on a glass microscope slip and measuring in transmission mode using the streak camera. Although the emission rate slows down with shell growth, the fast component remains around 500 ps.

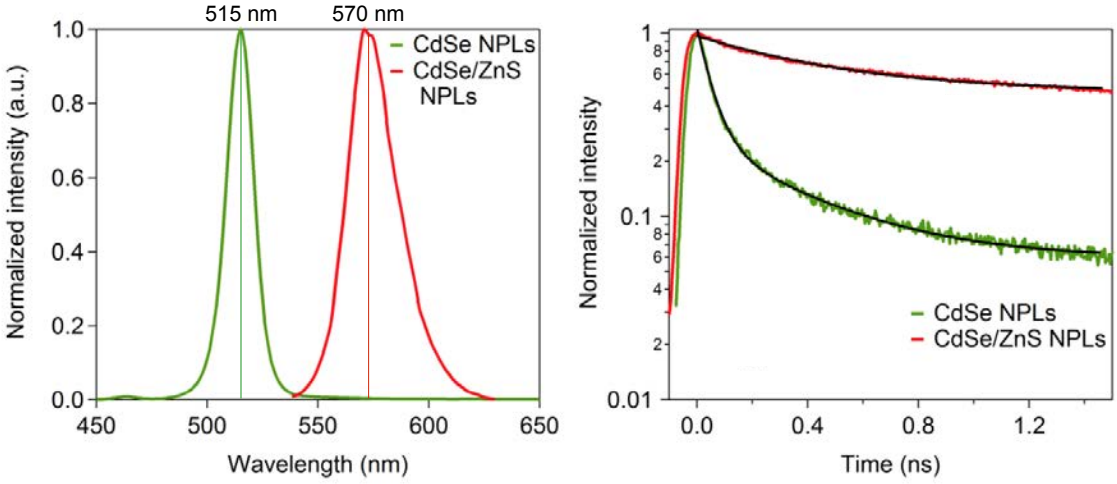

Figure 6.6: Photoluminescence spectra and spectrally-integrated decay from thin films of CdSe and CdSe/ZnS NPLs under picosecond laser excitation.

We present spectral-time resolved measurements (see Figure 6.7) of two different films composed by the same nanocrystals, CdSe/ZnS. However one of the solutions has been processed in order to remove the ligands and it is what we called "washed". The measurements presented here were performed in 2015 and 2016 with exactly one entire year in between. Significant differences in emission spectral and timing performance points towards an unstable syntheses of CdSe/ZnS NPLs that degrades with time.

In the measurements taken during 2015, a fast component of around 500 ps with an abundance of 10% is present in the film with less organic ligands. Meanwhile the normal film present a fast component of 600 ps with an abundance of 8% as shown in Figure 6.8. The long component between 7 to 8 nanoseconds can be even slower for both materials.

Figure 6.9 shows the time-integrated spectral profile of both films when measured in 2015 and 2016. A clear degradation is present in the samples measured in 2016, where the

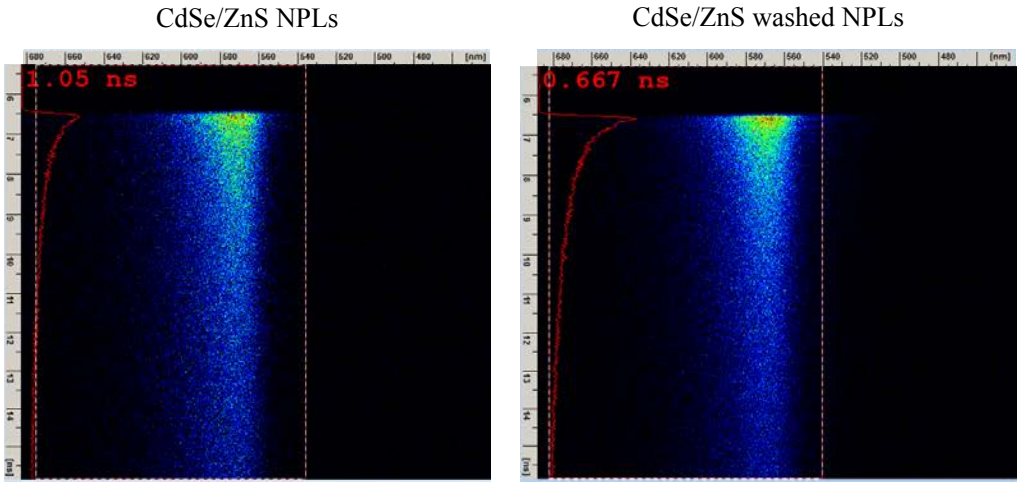

Figure 6.7: Time-spectral resolved photoluminescence of CdSe/ZnS nanoplatelets measured in the 10 ns gate in 2015.

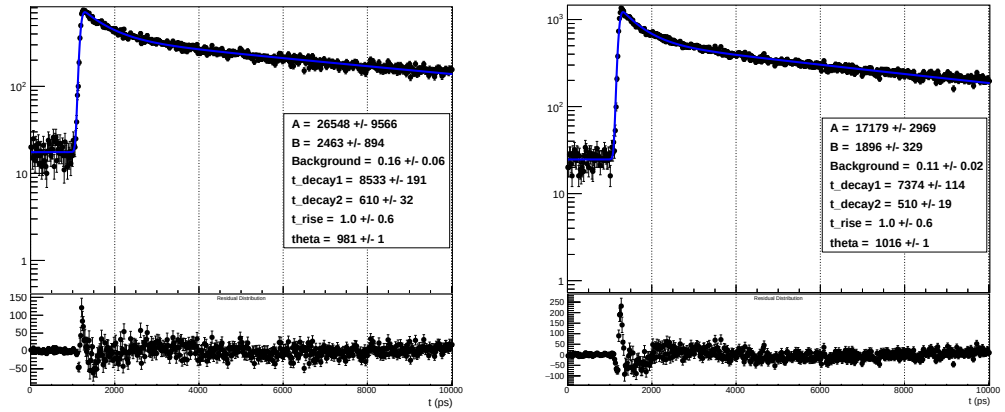

Figure 6.8: CdSe/ZnS NPLs timing performance under laser excitation measured in 2015 using the 10 ns sweeping range and an IRF of 50 ps. Left: CdSe/ZnS, Right: CdSe/ZnS with washed ligands.

luminescence spreads to the blue region and the main peak of emission is also broader. The degradation also affects the timing performance of the samples, showing a faster component at the level of 25 and 47 ps for the CdSe/ZnS and CdSe/ZnS "washed" films, respectively.

The possibility of synthesizing stable core/shell nanoplatelets would open a line of research oriented to the production of a proof of concept device using nanocrystals and scintillators in an integrated structure. However, they have not achieved good performance within the timeline of this thesis and therefore they will be considered as a very promising heterostructure to implement in the future.

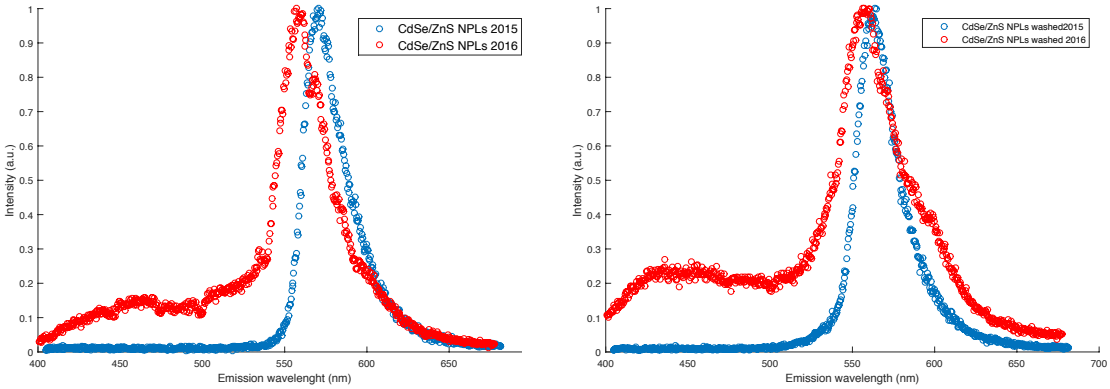

Figure 6.9: Emission spectra under 372 nm laser excitation of CdSe/ZnS core/shell nanoplatelets measured in different years. Left: CdSe/ZnS, Right: CdSe/ZnS with washed ligands.

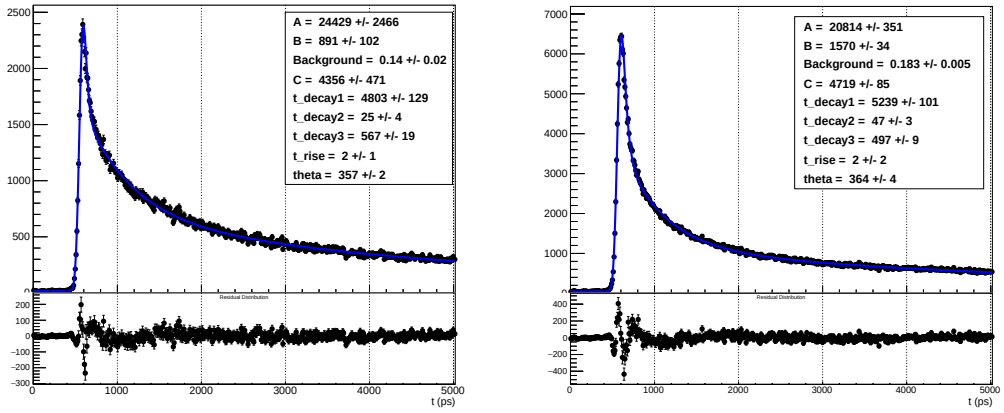

Figure 6.10: CdSe/ZnS NPLs timing performance under laser excitation measured in 2016 using the 5 ns sweeping range and an IRF of 36.5 ps. Left: CdSe/ZnS, Right: CdSe/ZnS with washed ligands.

6.3 X-ray excitation of NC thin films

The excitation of nanocrystals using ionizing radiation has been poorly studied so far. Recent studies developed in 2013 [26] using pulsed electron excitation and films of CdSe/ZnS core/shell quantum dots concluded in an ultrafast blue-shifted light emission with very low quantum efficiencies. The outcome of this work pointed towards materials with a high suppression of the Auger recombination rate to avoid the weak ultrafast emission. Therefore, we find the study of newly developed Auger suppressed nanocrystals under ionizing radiation a key step in the characterization and exploration of these materials for their future application in the radiation detector field. The time performance of NPLs and GS QDs thin films under pulsed X-ray excitation and measured in transmission mode will be presented in the following sections. The emission of CdSe/ZnS core/shell nanoplatelets excited by X-rays was under the photodetection limit of the streak camera which is at the level of 200 ph/MeV for a transparent and dense material.

6.3.1 CdSe nanoplatelets

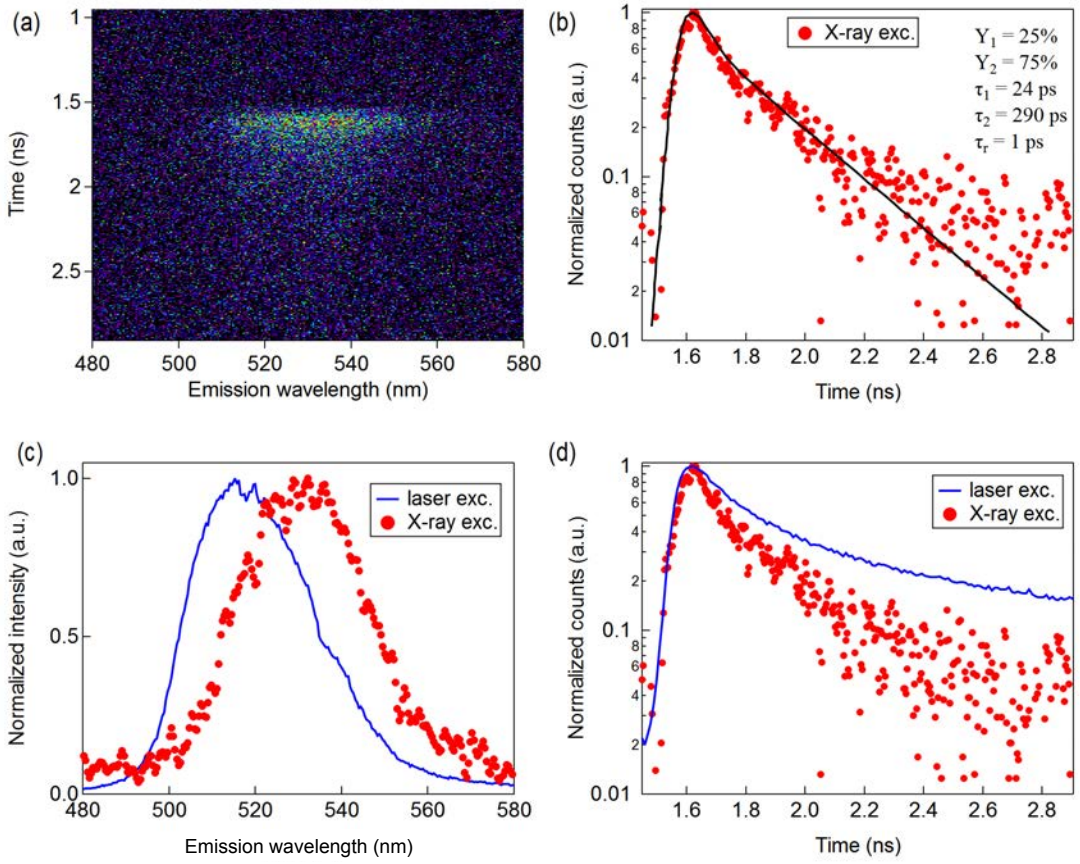

Figure 6.11: **X-ray excitation of a CdSe NPL film on glass**. (a) Streak image showing the X-ray excited CdSe NPL time-resolved emission spectrum. (b) Spectral integration of the full signal shown in panel (a). (c) X-ray excited spectrum compared to the spectrum obtained under low intensity laser excitation. Spectra were obtained by temporal integration of the respective streak camera images. A 500 μm spectrometer entrance slit was used in both cases. (d) Comparison of the X-ray and laser excited PL time dynamics. Together, (c) and (d) indicate significant biexciton or multiexciton emission under X-ray excitation.

As described in the section above, close-packed NC thin films were prepared by sequential drops from toluene onto 100 μm glass cover-slips The CdSe NPL film thickness was roughly 11 μm, determined from the solution concentration, volume deposited, and film area. The streak image in Figure 6.11(a) shows the time-resolved emission spectrum centered at about 530 nm of CdSe NPLs under X-ray excitation. Figure 6.11(c) shows that this spectrum is red-shifted compared to low-intensity laser excitation, which is consistent with biexciton (XX) or multiexciton (MX) emission. Both spectra are broad compared to the spectrum shown in Figure 6.3 since they were taken with a 500 μm spectrometer entrance slit to improve light collection.

Further evidence of XX/MX emission is provided by comparing the X-ray and laser excited emission rates in Figure 6.11(c). Under low-intensity laser excitation, the effective lifetime of 520 ps is indicative of purely excitonic emission. Conversely, a significant portion of

the energy from 40 keV X-ray excitation will be deposited in dense clusters, exciting multiple carriers in each NPL, which results in the observed fast, spectrally shifted XX/MX emission.

It is interesting to notice that the NPLs spectral emission under X-ray excitation is centered at 530 nm which is exactly the wavelength of the stimulated emission peak seen in the NPLs under femtosecond and c.w. pumped excitation. The question if ionizing radiation could create enough localized energy density for the NPLs to reach population inversion seems to come as a natural extrapolation of the previous measurements.

The excitation threshold to obtain stimulated emission when pumping CdSe NPLs using a femtosecond laser is about 6 μJ/cm^2. Converted to electron-volts will be around 4×10^{19} eV/cm^2. On the other hand, we know that "hot" electrons when thermalizing along a semiconductor can create, by the end of the track, a number of electron hole pairs as high as 10^{20} eh/cm^3. Converted to electron-volts, this give around 2-3$\times10^{20}$ eV/cm^3. As one can see, we will need the stimulated emission threshold expressed as a volumetric density in order to have an exact comparison.

6.3.2 CdSe/CdS giant shell quantum dots

As mentioned above, GS QDs have several features that make them a promising material class for radiation detection. Importantly, the large CdS shell reduces carrier losses due to defect trapping by passivating traps on the CdSe surface and providing separation from the external environment. This results in both high quantum yields and enhanced photostability compared to core-only or thin shell QDs. An undesirable consequence of the CdS shell for the present work is a reduced oscillator strength due to electron delocalization in the CdS shell and hole confinement in the CdSe core. This results in the radiative lifetime increasing with shell thickness [27], and longer lifetimes than CdSe NPLs (see Figure 6.5).

However, similar to the CdSe NPLs above, the results shown in Figure 6.12 demonstrate faster emission dynamics under X-ray excitation than under low intensity laser excitation. Possible sources of these faster dynamics can be excited state [129] and MX recombination, both of which are characteristically blue shifted for QDs. Auger recombination in the XX population could also play a role in shortening the lifetime. Examining the streak image in Figure 6.12(a) confirms these possibilities, with the faster dynamics occurring on the blue side of the emission spectrum (Figure 6.12(d). The blue shift also excludes the possibility that the fast lifetimes in GS QDs are due to sample heating, which would be characterized by a red-shifted spectrum. Further, the 82 meV blue shift of the early time spectrum points towards higher order MX generation beyond biexcitons [130].

When looking into the multiexcitonic dynamics under laser excitation we find that in the 5 ns gate there is just biexcitonic emission which is centered at around 620 nm as confirmed in Figure 6.5, section 6.2. This overlaps with the blue-shifted emission seen in the 5 ns gate X-ray excite data when integrating for only the first 200 ps as shown in Figure 6.13 (left).

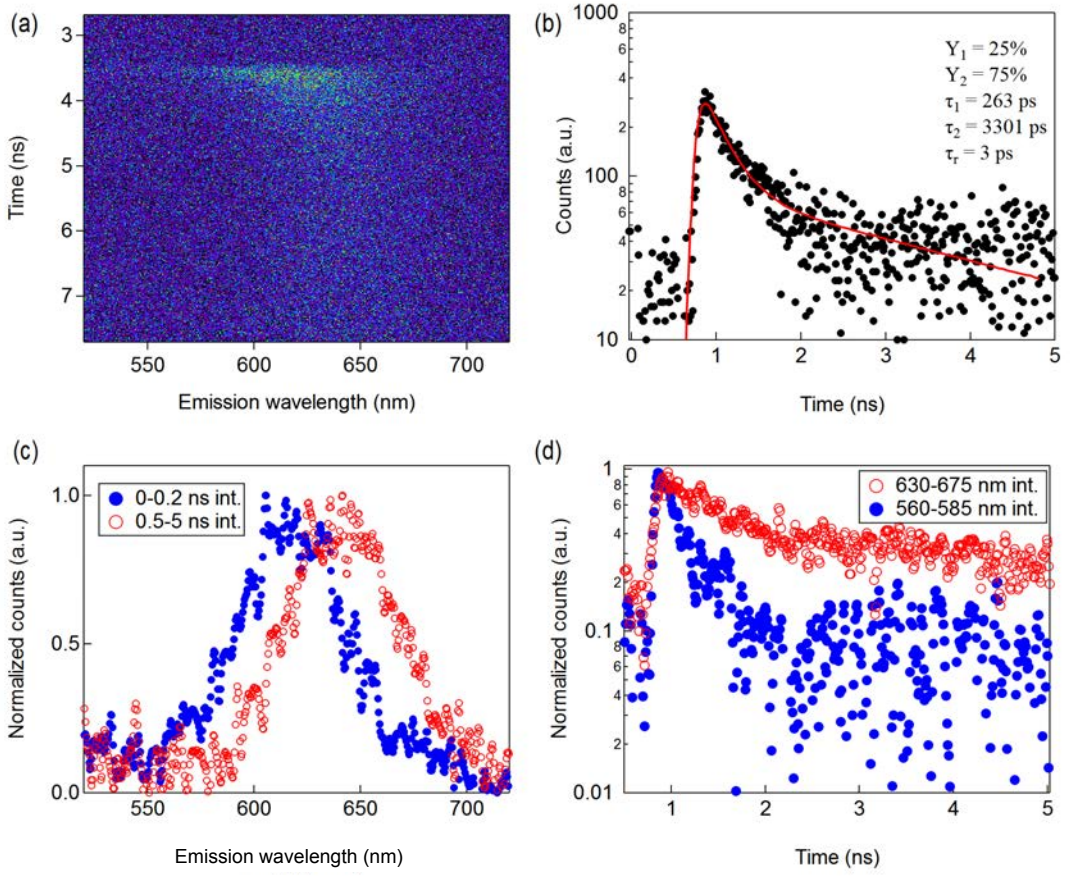

Figure 6.12: **X-ray excitation of CdSe/CdS GS QDs film**. (a) Streak image showing the GS QDs time-resolved emission spectrum. (b) Spectral integration of the full signal shown in panel (a). (c) Early time (0-0.2 ns) and later time (0.5-5 ns) spectra reveals a blue-shifted spectrum at early times. (d) Spectral integration of narrower slices on the red and blue side of GS QDs emission peak in panel (a). Together, (c) and (d) point towards multiexciton generation under X-ray excitation.

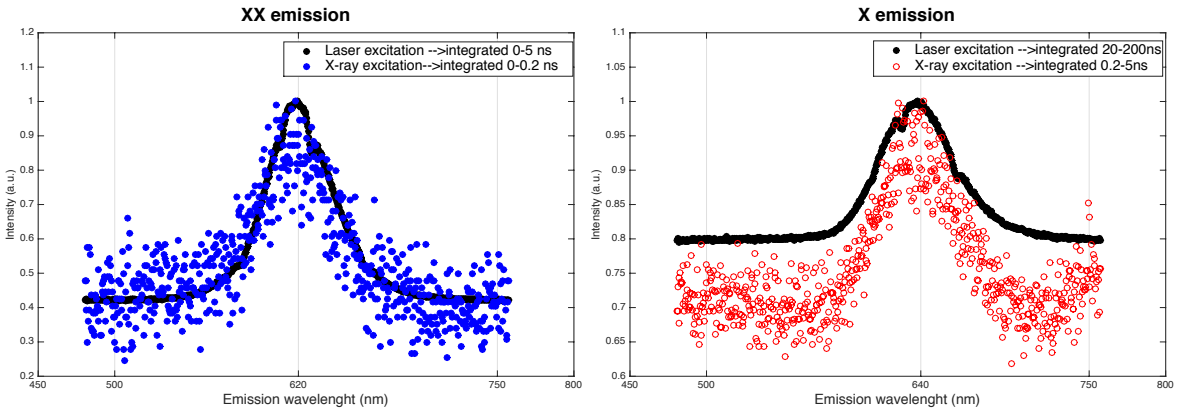

Figure 6.13: Early time (0-0.2ns) and later time (0.2-5ns) integrated data of GS QDs film under X-ray excitation (Figure 6.12 c)) as compared to excitonic (X→20-200ns) and biexcitonic (XX→0-5ns) emission under laser excitation.

So it seems that the blue shifted emission under X-ray excitation is mainly XX emission, however due to the low signal-to-noise ratio, this is not enough to confirm it. The rest of the emission under X-ray excitation between 200 ps and 5 ns seems to overlap with the excitonic emission seen under laser excitation between 20-200 ns. They are both centered at 640 nm as shown in Figure 6.13 (right). The rising edge for longer wavelength seen for the X-ray excited data in Figure 6.13 (right) is the second harmonic of the laser excitation centered at 744 nm.

6.3.3 Discussion

The lifetimes, component yields, and fraction of light emitted in the first 10 ps and 100 ps for CdSe NPLs and CdSe/CdS GS QDs are summarized in Table 6.1, where both the NPLs and GS QDs have components in the lower sub-ns region. Under X-ray excitation, these fast components have larger relative amplitudes than under low-intensity laser excitation (see Figure 6.5). The analysis done for the red and blue shifted emission coming from GS QDs is done using the laser IRF due to reduced signal-to-noise in the narrower spectral slices. Since the fit using the laser IRF is done analytically instead of by numerical methods, it will introduce a better error estimation for low signal-to-noise data. Apart from the normalized yields for each decay component, an effective lifetime, $\tau_{eff} = \sum A_i \cdot \tau_i / A_i$, is calculated for the different configurations using the amplitude of each component.

Table 6.1: **Summary of the laser and X-ray excited photoluminescence lifetimes with corresponding integrated photon yield fractions for NC thin films on glass substrates**. The effective lifetimes, $\tau_{eff} = \sum A_i \cdot \tau_i / A_i$ were calculated using the respective amplitudes of each component. The GS QD results include lifetimes obtained for the slower red and faster blue sides of the spectrum, integrated over the spectral ranges shown in Figure 6.12.

NCs	Fits	laser IRF NCs_{full}^{laser}		total IRF NCs_{full}^{X-rays}
NPLs	τ_1	187 ± 10^{-3} ps		24 ± 8 ps
	Y_1	26%		25%
	τ_2	1392 ± 10^{-4}ps		290 ± 11 ps
	Y_2	74%		75%
	τ_{eff}	520 ps		77 ps
	Yield 10 ps	1.3%		7.6%
	Yield 100 ps	15%		44%
NCs	Fits	NCs_{red}^{X-rays}	NCs_{blue}^{X-rays}	NCs_{full}^{X-rays}
GS QDs	τ_1	445 ± 45 ps	281 ± 18 ps	263 ± 25 ps
	Y_1	18%	100%	25%
	τ_2	3490 ± 321 ps	-	3301 ± 631 ps
	Y_2	82%	-	75%
	τ_{eff}	1564 ps	281 ps	849 ps
	Yield 10 ps	0.7%	3.5%	0.8%
	Yield 100 ps	8.5%	30%	10%

For CdSe NPLs, taking $\tau_{eff} = 520$ ps from low intensity laser excitation and $\tau_{eff} = 77$ ps from X-ray excitation (Table 6.1), the ratio of the slower laser excited emission to the faster X-ray excited emission is 6.7. Considering that Auger recombination will typically lead to an order of magnitude or higher lifetime shortening [81], this indicates that it may not play a significant role in the fast emission dynamics of CdSe NPLs under X-ray excitation.

For GS QDs the τ_{eff} under laser excitation is around 30 ns considering a 100 ns window where we can measure X and XX emission. Comparing the τ_{eff} under laser and X-ray excitation we get a factor 34 difference between them. If the blue-shifted emission seen under ionizing radiation is due to the creation of MX a factor 30 might not be a strong indicator to arrive to conclusions concerning the degree of Auger suppression. However, if the blue shifted emission is only XX we could derive that the Auger recombination rate increases considerably when using ionizing radiation. A higher signal-to-noise ratio to precisely characterize possible long components is absolutely necessary at this stage.

6.4 Transmission measurements

The transmission of the NPLs and GS QDs films was measured using a commercial Lambda 650 UV/Vis PerkinElmer spectrophotometer and the results are shown in Figure 6.14. The measurement included the transmission of the glass where the films of few micrometer thickness were deposited and a LYSO cubic crystal so that we have a comparative scenario. The absolute values of transmission will change for different film thickness but the qualitative information regarding cut-off and transmission plateau can be extracted. The NPLs and GS QDs photoluminescence main emission is highlighted in the wavelength axis together with the cut-off characteristic of the glass around 300 nm. The intrinsic problem of these nanomaterials regarding their transparency is clearly shown in Figure 6.14, especially for the CdSe NPLs where the 515 nm emission under laser excitation coincide with the cut-off edge of the transmission curve. GS QDs show better results due to their higher Stokes shift with the 640 nm photoluminescence main emission in the middle of the edge of the transmission curve.

The different nature of multiexcitonic dynamic exhibited by NPLs and QDs will change the transmission for the light emitted under ionizing radiation. For example, we have seen in the previous section that CdSe NPLs have a biexcitonic and multiexcitonic (XX/MX) emission centered, not at 515 nm which is the typical emission for the excitons, but is red-shifted to 530 nm. The transmission curve at 530 nm is already at the plateau which contributes with the very small Stokes shift that CdSe NPLs present. However, for GS QDs due to a blue-shifted multiexcitonic population, even though the Stokes shift is higher than that for NPLs, the transmission for 620 nm is indeed very low. In this way, the 1D-quantum confined system seems to be more in line with the requirements of a radiation detector system.

The light output of GS QDs films was measured using samples with different thickness and a Hamamatsu high gain, low cross-talk 3×3 mm^2 SiPM. The goal of this test is to

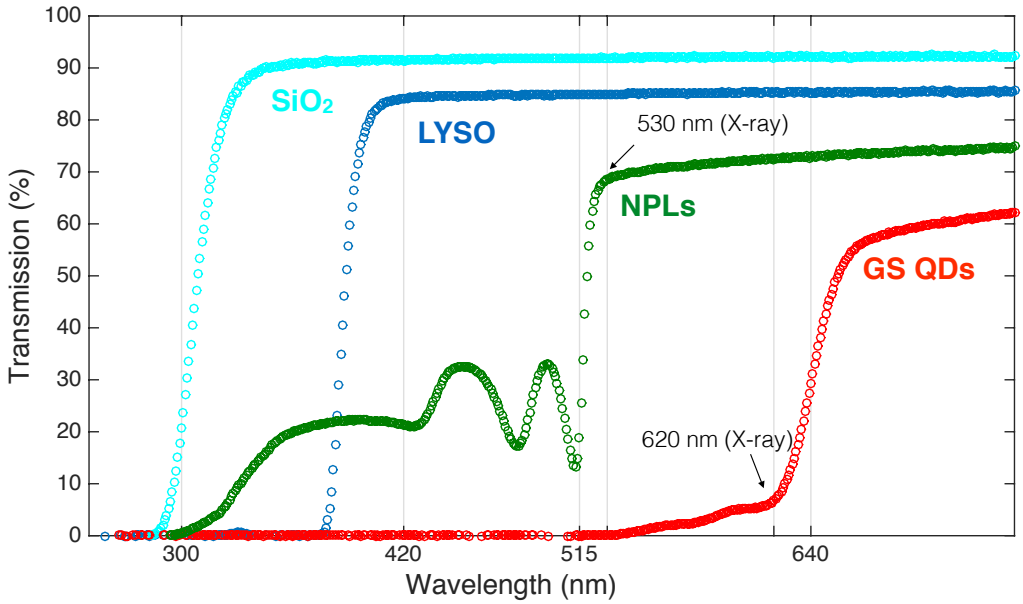

Figure 6.14: Transmission measured for NPLs and GS QDs films together with the glass were the nanocrystals where deposited and a cubic LYSO crystal.

check for light emission linearity as a function of film thickness. This will allow us to find the optimum film thickness where re-absorption is not limiting the amount of light transmitted. The SiPM is placed at the back of the microscope slips where the nanocrystals are deposited as shown to the left-hand side of Figure 6.15. The breakdown voltage is set to 52.5 V and the trigger is provided by the streak camera which also triggers the laser and therefore the X-ray tube. The SiPM is connected to an oscilloscope where the distribution of the charge integration is acquired forming what is known as 'finger plots', which can be observed at the right-hand side of Figure 6.15. The gate is open for 20 ns after the X-rays are triggered with the objective of measuring mainly the GS QDs fast component.

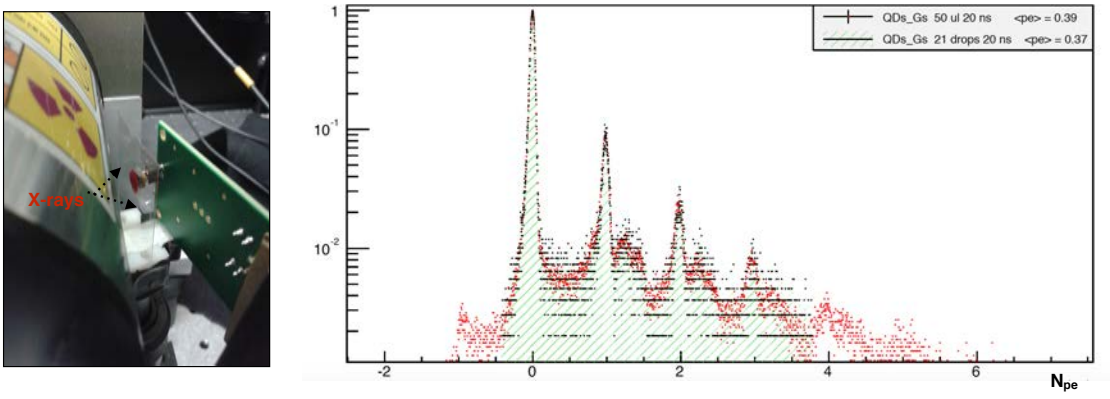

Figure 6.15: Left: Setup to measure the light output of CdSe/CdS films with different thickness using a SiPM placed at the back of the glass substrate. The film is situated in front of the X-ray tube. Right: 'Finger plot' representing the number of photoelectrons detected when irradiating the GS QDs films using pulsed X-rays with a 4 MHz repetition rate.

The finger plots are analyzed using Poisson statistic in order to find the mean number of photoelectrons detected. For this, we use the probability of detecting zero photoelectrons which relates to the mean value following the simple relation:

$$P(k) = \frac{\lambda^k e^{-\lambda}}{k!} \quad \therefore \quad P(0) = \frac{N_{counts}(0_{peak})}{N_{total}} = e^{-\lambda} \quad \therefore \quad \lambda = -log\{\frac{N_{counts}(0_{peak})}{N_{total}}\} \quad (6.1)$$

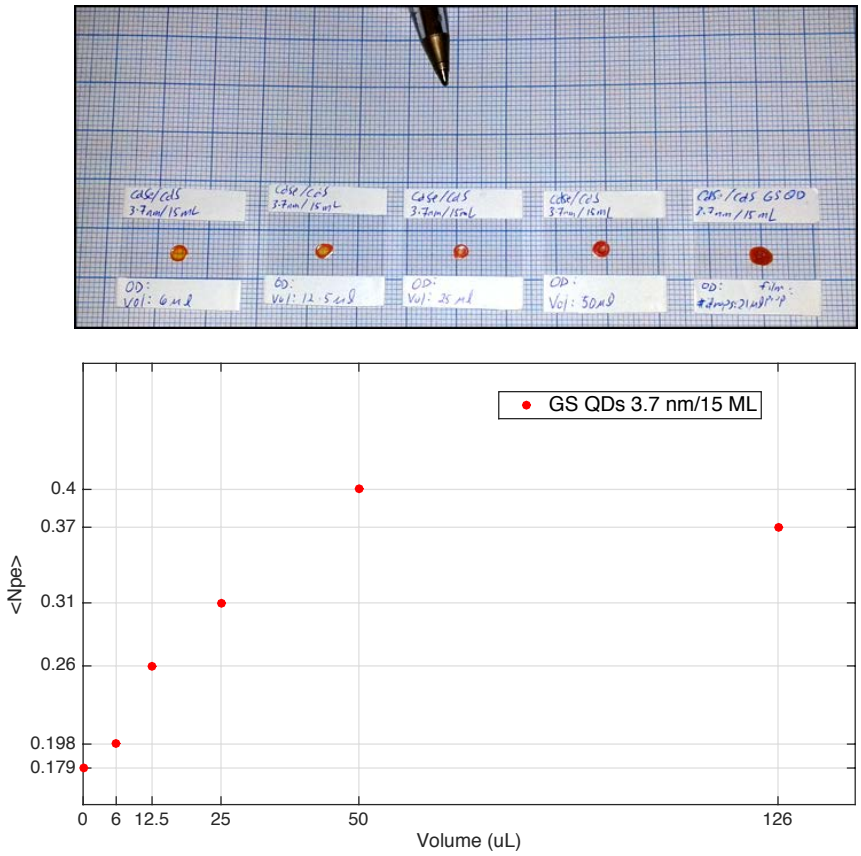

Figure 6.16: Mean number of photoelectrons measured with a Hamamatsu 3×3 mm^2 SiPM as a function of CdSe/CdS GS QDs volume for five different samples using pulsed X-ray excitation.

In this way, the mean number of photoelectrons, i.e. λ, was calculated for five different films which were deposited approximately covering the same area as shown in Figure 6.16. The volume of solution used to prepare the films was 6, 12, 25, 50 μL for the first four films. The last film was done by depositing 21 drops which is around 130 μL assuming each drop is around 6μL.

The value reported for a film of 0 μL in Figure 6.16 represents the background level of our measurements. The background includes contributions from the X-rays which are able to trigger the avalanche somewhere deep in the SPAD. There is also some contribution coming from the laser triggering the X-rays which bounces around in the bench. To set the background, we measure it by placing the SiPM at the back of a microscope slip without

film. The procedure is repeated every time before a film is measured so that we have control over the laser contribution.

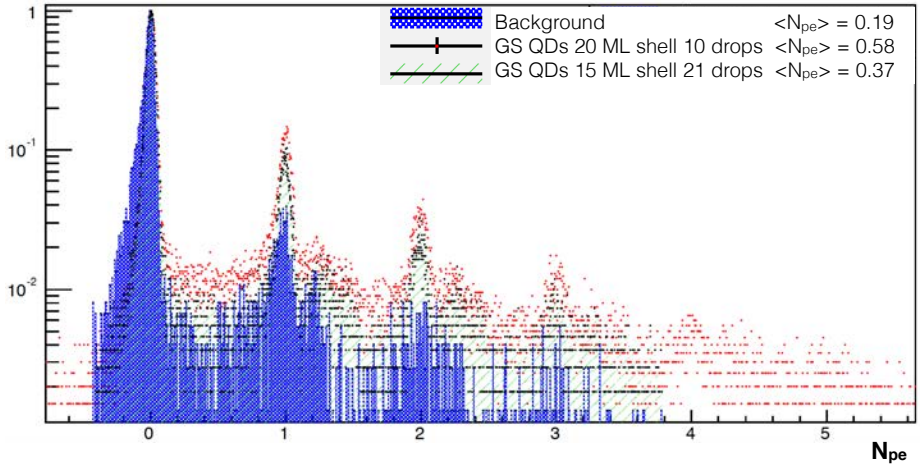

Figure 6.17: Mean number of photoelectrons measured above background with a Hamamatsu 3×3 mm^2 SiPM for two different CdSe/CdS GS QDs samples using pulsed X-ray excitation.

Together with the sample of CdSe/CdS (core: 3.7 nm, shell: 15 ML) GS QDs, we performed the same SiPM test with a second sample whose shell was 20 ML. The results are shown in Figure 6.17. The higher quantum efficiency of the second sample is attributed to the presence of a thicker shell, probably around 18 nm. The quality of the film is also higher for the latter due to a better homogeneity.

6.5 Nanoplasmonics

A complementary strategy to tailor the emission dynamics of nanocrystals is by modifying their electromagnetic environment with plasmonics. The use of silver nanoparticles deposited in the vicinity or surrounding CdSe-based nanocrystals could be used to enhance the photoluminescence recombination times and the quantum efficiency even further. We use silver because the surface plasmon of these metallic nanoparticles can be tuned between 500-700 nm. In this way, the radiative modes centered at 515 nm and 640 nm for NPLs and GS QDs, respectively can be coupled to the plasmonic modes of the silver. This effect can be classically understood as the Purcell effect but instead of a cavity, the modes available will have a plasmonic nature. The two silver nanoparticles used in this section are shown in Figure 6.18. The former one has a decahedral shape, a diameter of around 100 nm (Figure 6.18 top left) and its surface plasmon resonance matches the CdSe NPLs emission. The particles are suspended in a colloidal solution which can be used to form thin films of CdSe NPLs+Ag. The second one, is more like a 3D structure of coral silver (Figure 6.18 right) and they will be used as a matrix to deposit GS QDs. Its porous shape may allow NCs to permeate the structure, where they are surrounded by the strong electric fields of localized surface plasmons.

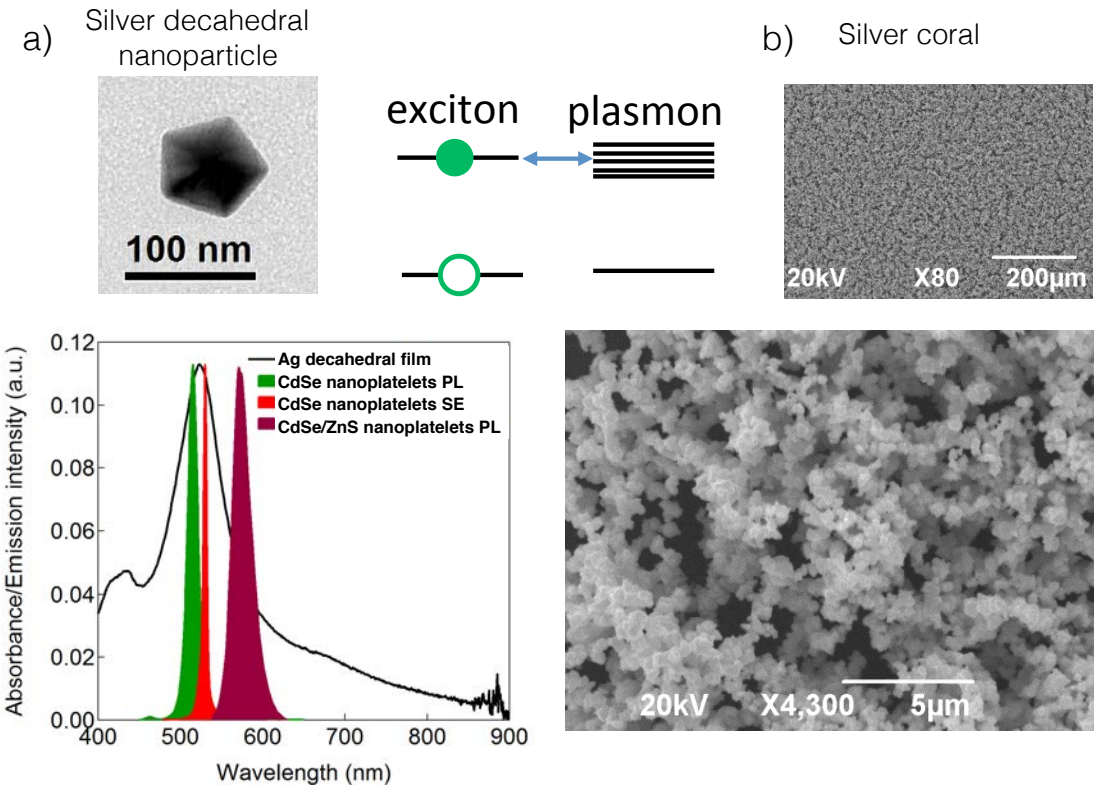

Figure 6.18: Silver decahedral nanoparticles (a) and 3D coral structure (b) used to enhance the photoluminescence recombination time by coupling their plasmonic modes to the excitonic emission of CdSe NPLs and CdSe/CdS GS QDs, respectively. In collaboration with Joel Grim [131].

The enhancement of a fast emission component is clear when looking at Figure 6.19. To the left we see the spectral-time resolved image taken with the streak camera in the 1 ns gate when measuring CdSe NPLs under laser excitation. The time profile follows the values reported in section 6.2 where we report 26% of the photons emitted with a decay time of around 200 ps and a second long component where 74% of the photons decays with a 1.4 ns constant (Figure 6.5 a)). The same measurement is repeated with a film made by drop-casting 20 times from a CdSe NPLs colloidal solution and 10 times from Ag nanoparticles colloidal solution. As a result, the pulse shrinks in time and the new decay components can be seen to the left in Figure 6.20. Both images in Figure 6.19 are taken under the same setup characteristics, so time and spectral resolution are identical as it can be inferred from the width of the laser pulse which is around 40 ps FWHM (centered at 375 nm).

The new timing characteristics of the film composed by CdSe NPLs and silver nanoparticles are shown to the left in Figure 6.20. There is one first component as fast as the laser IRF, which is highlighted in green as $\tau_1 = 0 \pm 5$ ps with an abundance of 26%. The rest of the components follow the timing properties of the CdSe NPLs pure film with a first decay of 145 ps and a long second one of 1.4 ns.

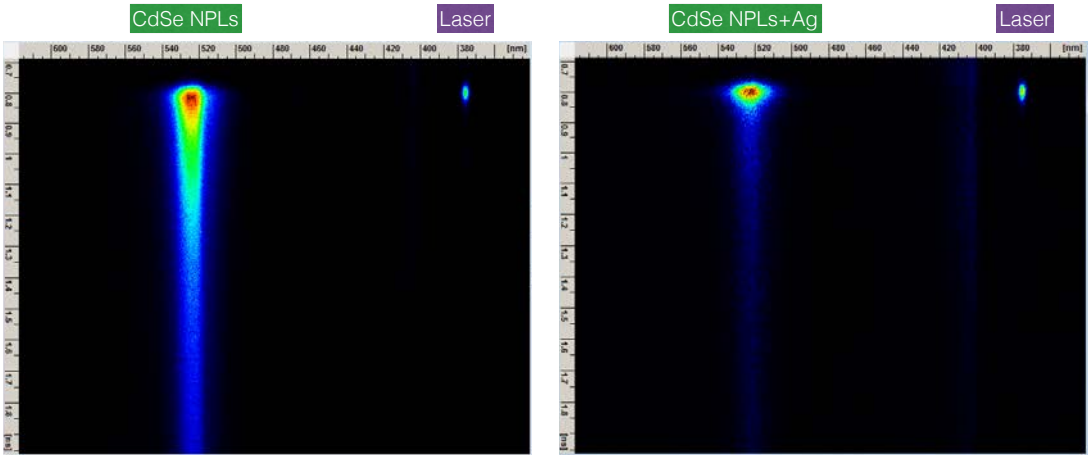

Figure 6.19: Spectral-time resolved photoluminescence of two CdSe NPLs films in 1 ns gate. Left: CdSe NPLs. Right: CdSe NPLs film mixed with Ag nanoparticles with a plasmon resonance between 505-625 nm.

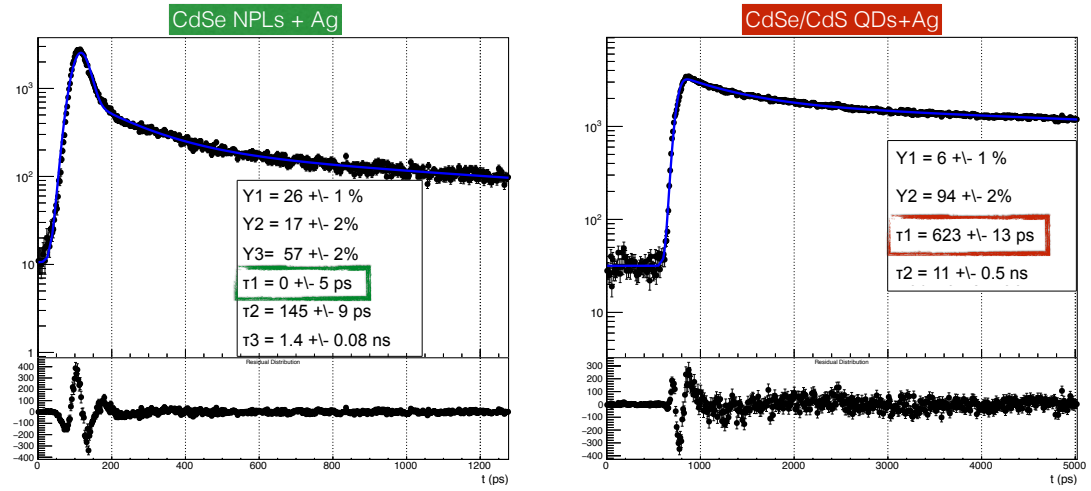

Figure 6.20: Enhanced time-resolved photoluminescence using nanoplasmonics. Left: CdSe NPLs close-packed film where Ag nanoparticles have been deposited. Right: CdSe/CdS GS QDs deposited in an Ag coral matrix.

A similar effect is seen for the long recombination times exhibited by GS QDs, i.e. a monoexponential decay time of 15 ns in the 5 ns gate. Coupling the 640 nm excitonic emission to the coral Ag plasmonic modes results in a fast decay component of around 600 ps as shown to the right-hand side of Figure 6.20. The fast component can change from point to point in the same sample due to the inhomogeneities of Ag and QDs distribution. The nanoplasmonic enhancement is also distance dependent, so it will reach a maximum for certain values of quantum dot-Ag nanoparticle separation. Balancing radiative enhancement with loss is a persistent challenge in the field of plasmonics, particularly for short emitter-metal distances. GS QDs provide a facile means of reaching this balance, with the CdS shell creating a separation between the emitting CdSe core and the Ag surface. The random distribution of particles in the film guarantees the appearance of the effect, however this is far for being a controlled process.

The X-ray excitation of these nanoplasmonic samples has been limited due to the low transparency of the films. The optical alignment between sample and streak camera is better achieved in transmission mode and this configuration is not possible for the Ag coral sample. The streak camera alignment was changed to reflection mode just to have an idea of the recombination times under X-ray excitation of the QDs film with and without silver. Unfortunately, the time resolution for this configuration is rather bad and the comparison can only be done qualitatively. The spectra and time profiles of pure and Ag GS QDs film are shown in Figure 6.21. The Ag coral matrix seems to enhance what is known as p-states, which is usually a very fast emission centered at 570 nm. If the (average) plasmon resonance is closer to 570 nm than 650 nm, the emission rate from the excited state population could be enhanced.

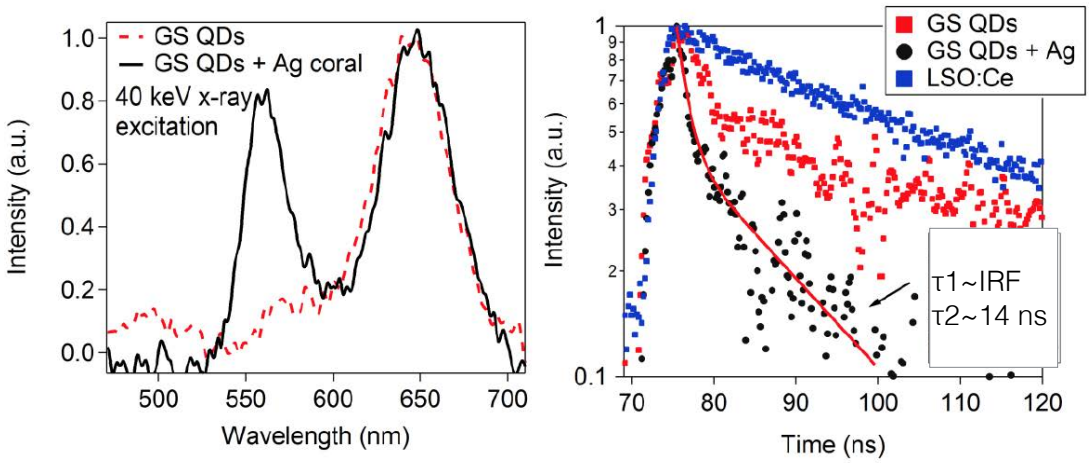

Figure 6.21: X-ray excitation of a GS QD pure film compared to a film deposited on an Ag coral. In collaboration with Joel Grim [131].

6.6 Conclusions

As shown in this chapter, CdSe NPLs and CdSe/CdS GS QDs are promising candidates for prompt photon emission under ionizing radiation. We have demonstrated that the emission rates of these NCs under pulsed X-ray excitation are much faster than traditional mechanisms in bulk scintillators, i.e. 5d-4f transitions. CdSe NPLs have a sub-100 ps effective decay time of 77 ps and CdSe/CdS GS QDs exhibit a sub-ns value of 849 ps. Further, the respective CdSe NPL and CdSe/CdS GS QD X-ray excited photoluminescence have the emission characteristics of excitons (X) and multiexcitons (MX), with the MXs providing additional prospects for fast timing with substantially shorter lifetimes. The CdSe nanoplatelets and giant shell quantum dots studied here overcome many of the challenges that earlier generations of NCs faced under ionizing radiation. Notably, non-radiative Auger recombination, which also deteriorates bulk scintillator performance, is suppressed in both systems. Further, the large shell of the CdSe/CdS GS QDs overcomes several other challenges, such as re-absorption of

emitted light by separating emission and absorption bands. However its blue-shifted emission under ionizing radiation makes them a less transparent system compared to CdSe NPLs. These features can in principle also be extended to NPLs via the growth of a larger bandgap shell such as CdS or ZnS.

CdSe nanoplatelets with a ZnS shell show high instability with respect to their spectral and timing characteristics which deteriorate and change in time. Spectral-time resolved measurements performed with a lapse time of one year, are able to proof so. However, this particular system encloses the best characteristics of both CdSe NPLs and CdSe/CdS GS QDs, so it should be kept in mind for future studies.

Transmission measurements performed with the NPLs and the GS QDs point towards CdSe NPLs as a better material to apply to radiation detectors systems due to their red-shift emission under ionizing radiation. However, the quality of the film obtained by drop-casting straight from its solution is not comparable with the film obtained with CdSe/CdS giant shell quantum dots, where an almost homogeneous layer is created when depositing on a glass substrate. This prevents us to measure the light output response as a function of film thickness as it was done for the CdSe/CdS giant shells.

The light output of the quantum dots under X-ray excitation increases when increasing the thickness of the shell. This result can be inferred from an increase in the quantum efficiency of the material under laser excitation when thicker shells are grown. However, the thicker the shell the longer the recombinations times exhibit by these materials so a compromise should be found for future applications. CdSe/CdS GS QDs with a core of 3.75 nm and a shell of 15 monolayers show a re-absorption of light when the thickness of the film starts to be larger than 100 μm. For this reason, we will work with films of around 10 μm in the next chapter.

Plasmonics offers a promising route to enhance emission rates of NCs. It also provides a means to compensate for the reduced oscillator strengths that result from growth of passivating shell layers, which are necessary to ensure stable, bright NCs. The results presented above confirm the feasibility of this approach under both laser and X-ray excitation. However, the disadvantage regarding the transparency of metallic nanoparticles is clear when measurements in transmission mode are no longer possible. Optimizing the overlap between the localized plasmon resonance and NC emission frequencies is an obvious future direction, together with the study of organized systems in which the light can be manipulated as in a photonic crystal array.

Chapter 7

Nanocrystal-based scintillators

7.1 Introduction

The feasibility to bring nanocrystals' localized high-performance properties into bulk materials suitable for radiation detectors, remains still as the main question, especially for timing measurements. Important features of a radiation detector, i.e. its stopping power and transparency, are still major challenges to overcome when using nanocrystal-based scintillator materials.

To address the technical implications and ultimately give proof of concept of an actual high-time-resolution system with nanocrystal-based scintillators, i.e. for both low (511 keV) and high energy radiation detection constitutes the main bottleneck in the application of these materials in a macroscopic system. This chapter deals with typical detector issues, such as e.g. overall detector density and its stopping power, using conventional scintillators and dense substances, like nanocomposite hosts or inactive layers, in combination with the fast emitting NCs. Such a detector could be constructed from nanocomposites, either bulk or as thin layers, or from stacks of thin wafers of bulk scintillators with NC-films coated on their surfaces. Another issue is the efficient transport of prompt photons to the photodetector. This requires high transparency or the design and fabrication of a light guiding system. For this purpose, a dense and transparent stopper could be envisaged that acts as a light-sharing waveguide coupled to a lateral readout photodetector.

In this chapter the aforementioned bottleneck of transferring the nanocrystal vast potential to the bulk material domain will be addressed following two main lines: (1) nanocrystals as part of a heterostructure and (2) nanocomposites, where the nanocrystals are embedded in a matrix host.

7.2 Colloidal nanocrystals and bulk scintillator heterostructures

Building up the thickness of nanocrystal films to fully stop high energy particles is challenging. One solution is to construct hybrid NC-bulk materials. In this approach, NCs can be used for the specialized task of fast timing while the bulk scintillator provides stopping power and scintillation light for tasks such as resolving particle energy. Such a detector could be constructed from stacks of thin wafers of bulk scintillators with films of NCs coating their surfaces. The design of this heterostructure for fast γ-ray tagging, for example, could be accomplished by making the dense bulk scintillator layer thinner than the recoil electron range, allowing energy transfer to the nanocrystal thin film [132].

In the following sections, we investigate this concept by depositing CdSe NPL films and GS QD films on the surfaces of LSO:Ce and LuAG:Ce, respectively. In this way, photoluminescence coming from NCs and conventional scintillators can be spectrally resolved in one streak image, which allows the efficiency of the NCs to be estimated by comparing to known light yield values of the bulk scintillators. A schematic view of the measurement can be seen in Figure 7.1 together with a streak image taken under laser excitation with the NPL heterostructure.

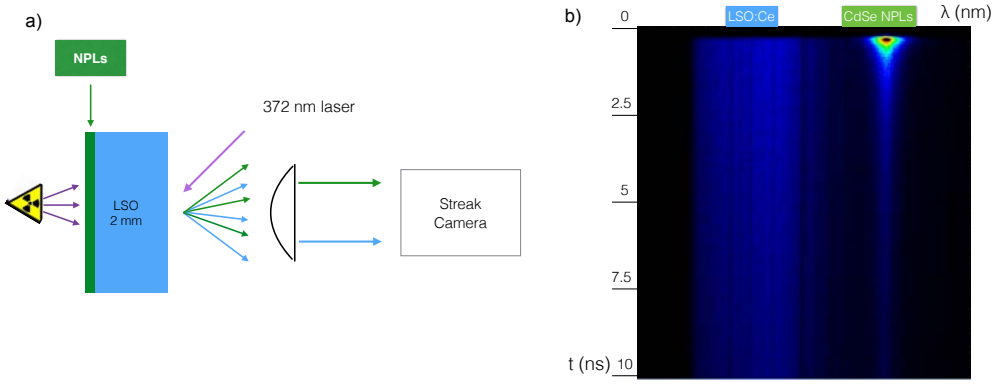

Figure 7.1: (a) Schematic view of the setup used to measure the heterostructure emission using laser and X-ray excitation. (b) Photoluminescence of the NPLs/LSO:Ce heterostructure under laser excitation.

7.2.1 CdSe NPLs deposited on LSO:Ce

A thin film of CdSe NPLs was deposited on one of the large faces of a $2 \times 6 \times 8\ mm^3$ LSO:Ce crystal. X-rays directly excite the NPLs film and the energy that has not been deposited in the NCs then reaches the scintillator along the 2 mm long axis. Light imaged from a $500 \times 100\ \mu m^2$ spot is shown in Figure 7.2 a), where ultrafast CdSe NPL emission is seen between 505-550 nm, spectrally shifted from the LSO:Ce photoluminescence. The sweeping range was set to 2 ns, which allows us to resolve the first NPL decay component and directly compare to the intrinsic dynamics of NPLs presented in the previous section. A long tail

which follows the LSO:Ce decay time characteristics is also present due to LSO:Ce blue light absorbed and re-emitted as green light from the CdSe NPLs. However, the majority of the CdSe NPL emission occurs during the LSO:Ce rise time.

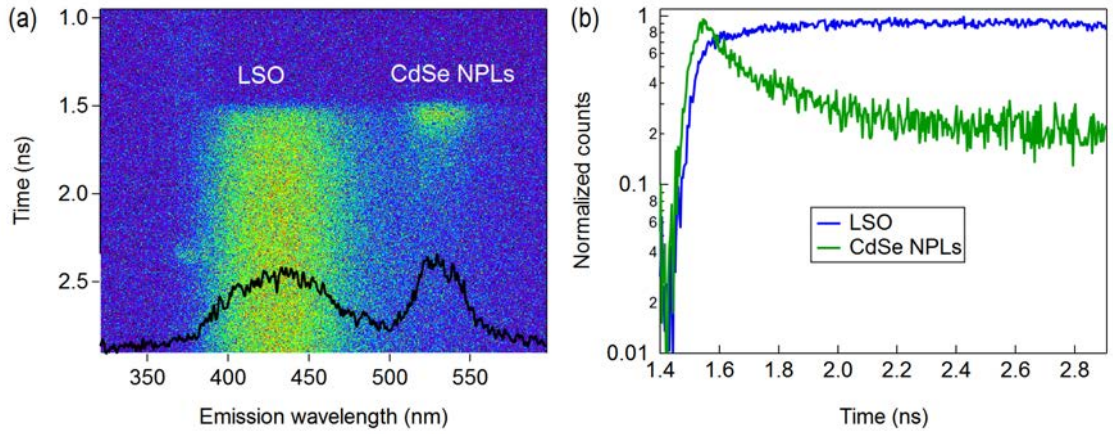

Figure 7.2: X-ray excitation of CdSe NPLs film deposited on a $2 \times 6 \times 8$ mm^3 LSO:Ce scintillating crystal. (a) Spectrally resolved streak image sweeping at 2 ns. (b) Spectral integration of the streak image to yield the decay traces for LSO:Ce and CdSe NPLs.

7.2.2 CdSe/CdS GS QDs deposited on LuAG:Ce

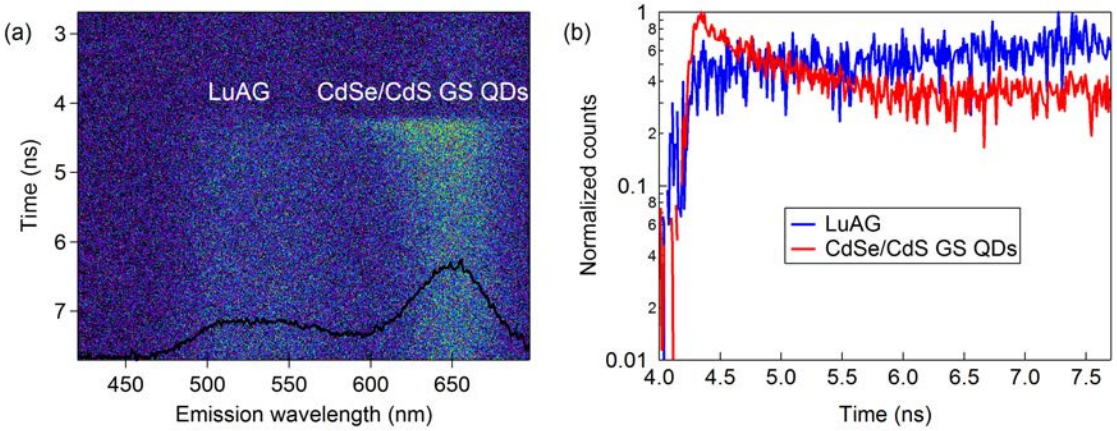

Figure 7.3: X-ray excitation of CdSe/CdS GS QDs film deposited on $1{\times}5{\times}5$ mm^3 LuAG:Ce scintillating crystal. a). Spectrally resolved streak image sweeping at 5 ns. b) Timing performance of LuAG:Ce and GS QDs emission.

A CdSe/CdS GS QDs film was deposited on the large face of a $1{\times}5{\times}5$ mm^3 LuAG:Ce crystal. The film was placed in front of the X-ray tube window and the sample was measured in transmission mode through the 1 mm long axis. Light was collected from a 500×100 μm^2 spot and both scintillation (LuAG:Ce) and ultrafast (QDs) emission are produced, which is shown in Figure 7.3 a). There is a very fast QD component that occurs during the 500 ps rise time of the LuAG:Ce scintillation and a long tail which can be due to either the slow component seen in CdSe/CdS GS QDs [27], or absorption of LuAG:Ce light which is re-

emitted with the typical LuAG:Ce decay characteristics. The LuAG emission does not stop rising in the 3.5 ns gate as shown in Figure 7.3 b), which corroborates the non-absorption of green light by the QDs in the very first nanoseconds of the scintillating pulse.

7.2.3 NCs Light yield estimations

The light yield of the NC films under X-ray excitation can be estimated by comparing to the LSO:Ce and LuAG:Ce emission in Figure 7.2 a) and Figure 7.3 a), respectively. Simulations using Geant4 [94] were used to determine the X-ray energy spectrum of the tungsten tube as well as the total energy deposited in the NC layer and scintillator after X-ray irradiation. Since the thickness of the heterostructure layer is unknown, simulations were run for thicknesses ranging from 100 nm to 100 μm. In the simulations, the NC films are declared using a filling factor of 50% to account for the presence of organic surface ligands, which decreases the overall density of the film. The total amount of photons emitted by the heterostructure is proportional to the energy deposited in each material and follows the relation:

$$LY_{NPLs} = \frac{\alpha_{NPLs}}{Y_{200ps}} \times LY_{LSO}|_{t=1.5ns} \frac{E_{dep}^{LSO}}{E_{dep}^{NPLs}} \tag{7.1}$$

$$LY_{QDs} = \frac{\alpha_{QDs}}{Y_{300ps}} \times LY_{LuAG}|_{t=3.5ns} \frac{E_{dep}^{LuAG}}{E_{dep}^{QDs}} \tag{7.2}$$

Here, α is the ratio between the total number of photons emitted by the NCs and the bulk scintillator. This ratio is taken from the integrated time profile. Since a rigorous calculation will have to account for the amount of light reabsorbed and emitted by the NCs, the estimations are done by taking the number of photons emitted at early times of 0 to 200 ps for NPLs and 0 to 300 ps for GS QDs where no re-absorption seems to take place. Using the time characteristics of NPLs and GS QDs under X-ray excitation obtained in the previous chapter we can estimate the percentage of photons emitted at time 200 ps and 300 ps, respectively. This factor is represented in the formula by Y_{200ps} which is equal to 0.61 and Y_{300ps} that has a value of 0.23. The relative wavelength dependence of the streak photocathode quantum efficiency and the efficiency of the spectrograph grating are also taken into account. Doing a background correction and comparing integrals of blue and green light, we calculate $\alpha_{NPLs} = 0.1$ for the green photons emitted between 0 and 200 ps. In the case of QDs/LuAG,we have $\alpha_{QDs} = 1$ for red photons emitted between 0 and 300 ps.

Considering the LSO intrinsic light yield as 40'000 ph/MeV, the amount of light emitted in the first 1.5 ns will be $\sim$ 1500 ph/MeV, represented by the term $LY_{LSO}|_{t=1.5ns}$. In the case of GS QDs/LuAG, we have taken an intrinsic light yield of 23'000 ph/MeV based on comparative light yield measurements [8]. Since LuAG:Ce has a second decay tail up to 1063 ns and the repetition rate is 250 ns, the $LY_{LuAG}|_t$ for t<3.5 ns is approximately 500 ph/MeV. This calculation considers a rise time of 535 ps, and 2 decay components with different yields: 70 ns (44%) and 1063 ns (56%) as reported in [12].

The values of mean energy deposited are computed and presented as normalized values for the 100 μm thickness in Figure 7.4 c) and d). The ratio between both curves will give the energy weighted factor and increases by an order of magnitude with decreasing thickness.

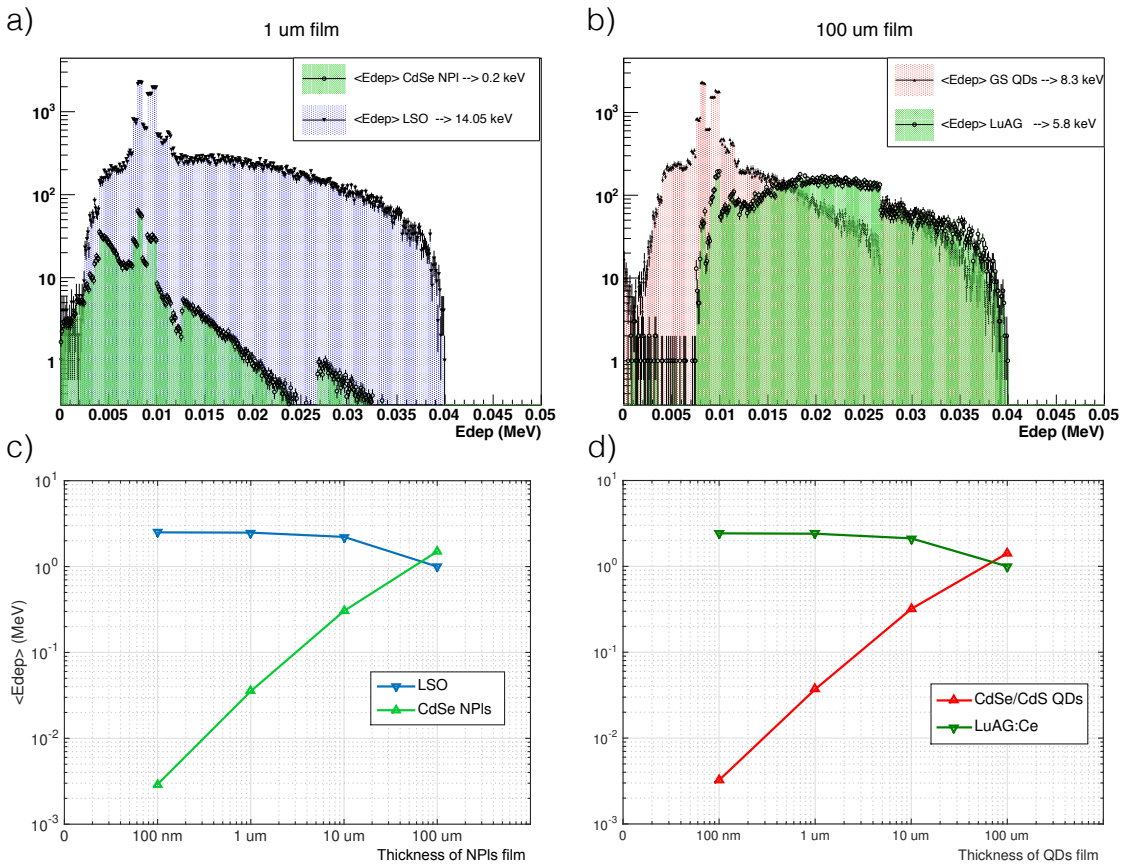

Figure 7.4: NC light yield estimations under 40 keV X-ray excitation as a function of film thickness. (a) Simulated spectrum of the energy deposited on NPLs/LSO heterostructure for each material when the film thickness is 1 μm. (b) Simulated spectrum of the energy deposited on QDs/LuAG heterostructure for each material when the film thickness is 100 μm. c) and d) Values of mean energy deposited on NPLs/LSO and QDs/LuAG heterostructure for different film thickness, respectively.

Measuring the light yield for NC films under X-ray excitation is a challenging task, and it is part of ongoing work. Some of the crucial requirements for this measurement are constant thickness of the films and a known packing density. In the present work, NC films were prepared by drop-casting from toluene solutions since this technique enables building up relatively thick films with sequential and concentrated drops. However, the NC films prepared for this work had considerable variation in thickness. We estimated an average thickness on the order of 10 μm, determined from the solution concentration, volume deposited, and film area. This is a rough estimate, and does not account for the variation in film thickness. Given this uncertainty and the assumed 50% packing density, we calculated the light yield for a range of both NPL and QD film thicknesses, with the results summarized in Table 7.1.

Table 7.1: **Inferred light yield (ph/MeV) for CdSe NPLs and GS QDs, calculated for a range of film thicknesses**. The estimated average thickness for the NC films used in this work was 10 μm, shown in bold (k=1000).

Thickness	LY_{NPLs} (ph/MeV)	LY_{QDs} (ph/MeV)
1 μm	$25k$	$220k$
5 μm	$5k$	$44k$
10μm	**2.5**k	**22**k
15 μm	$1.7k$	$14.7k$

7.2.4 Discussion

It is evident from the heterostructure results shown in Figure 7.2 and 7.3 that an additional longer decay component emerges due to absorption of the bulk scintillator light by the NC films. This is shown in Figure 7.5 for CdSe NPLs, where a long tail with a lifetime characteristic of the LSO:Ce decay time is present. However, the relative weights of the first and second decay components are now different by a factor of two (1 and 2% in the heterostructure) instead of a factor of three (25 and 75%). This indicates negligible absorption/re-emission at early times (0-300 ps) of the scintillating pulse. Fitting the LSO:Ce rise time (Figure 7.5 b), the first two NPL decay components occur within the same timescale as the direct and delayed excitation of the Ce^{3+} luminescent centers, represented by τ_{r1} and τ_{r2}, respectively. Similarly, a long decay component following the LuAG emission lifetime appears for the GS QDs/LuAG heterostructure. In both cases, the secondary excitation by the bulk scintillator and the intrinsic longer lifetime components of the NCs can be reduced by isolating the fast MX emission via spectral filtering. This may serve as an important strategy when considering practical devices in which repeated layers of NC/bulk scintillators are involved. In such devices, eliminating longer lifetime components will enable faster cycle times (or frame rates).

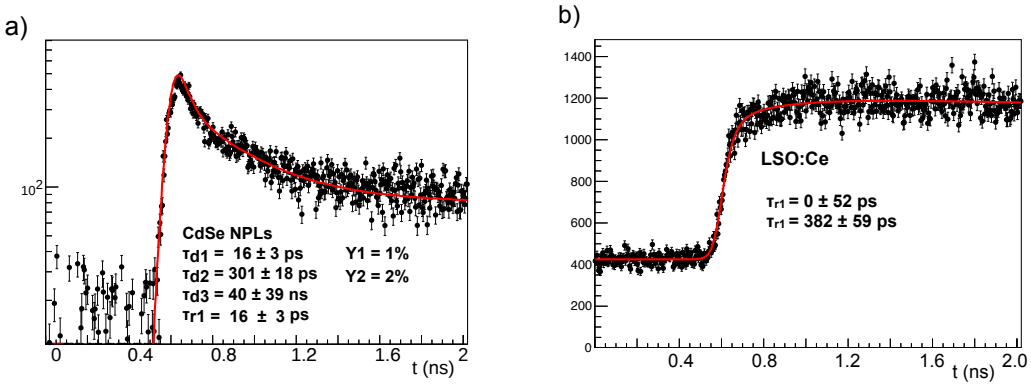

Figure 7.5: a) Timing performance of the NPLs film when deposited on top of LSO:Ce. b) Timing performance of a conventional scintillator, i.e. LSO:Ce in the first 1.5 ns.

7.2.5 Sampling calorimeter simulations

The following section is dedicated to calculate the feasibility of having a crystal of 10-20 mm length sampled with LYSO and CdSe NPLs layers to detect a 511 keV gamma. This geometry implies a lateral photodetector readout since as seen in the previous section there is absorption of blue light by the CdSe NPLs. The main idea is to use the energy carried by the electron coming from the photoeffect or Compton interaction as the source of excitation for the fast emission. In this way, the LYSO scintillating light could be used to measure the energy and the fast CdSe NPLs emission could be used as a time tag of the gamma event. This implies to have energy deposition in both systems, i.e. LYSO and CdSe NPLs, for each gamma event. To guarantee the recoil electron reaches the adjacent layer, the LYSO has to be sampled with a thickness of at least the order of the range of the recoil electron characteristic of the Compton edge which is about 340 keV. If we look in the NIST database the range for electrons of about 350 keV calculated by continuous slowing down approximation is around 240 μm. So as a maximum, the LYSO layers have to be 200 μm thick so that there is some energy transfer to the CdSe NPLs layers. This will be 100% the case for the electron coming from the photoeffect and from the recoil electrons which are close to the Compton edge.

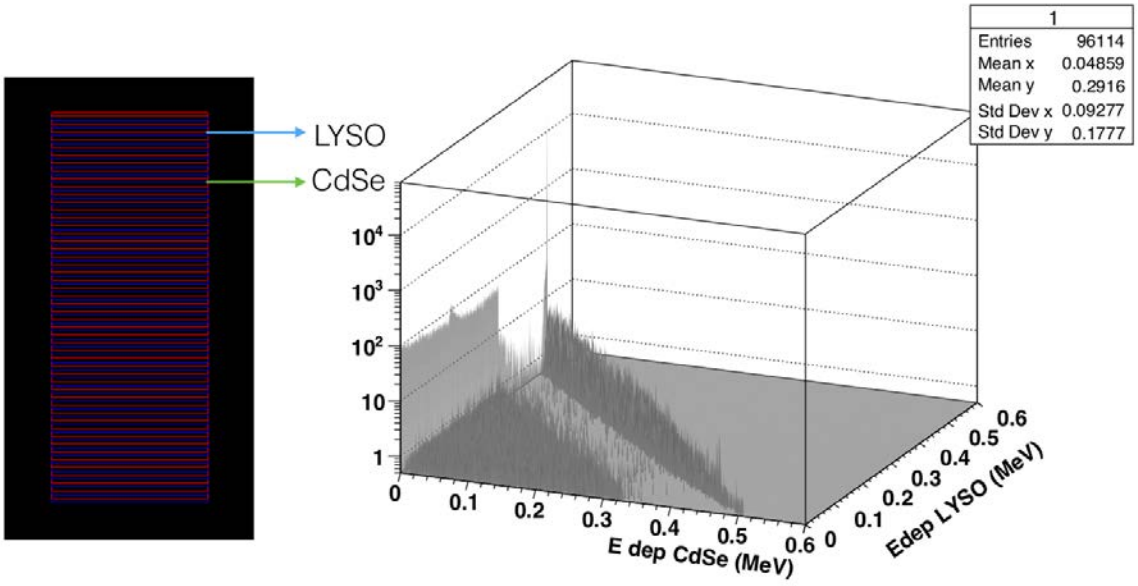

Figure 7.6: Left: Crystal sampled with 50 LYSO layers of 200 μm and 50 CdSe NPLs film layers of 100 μm. Right: Energy deposited in both systems when shooting 511 keV gammas.

In this way, a sampled crystal has been built using the Geant4 framework by stacking layers of LYSO coated with CdSe NPLs as shown in Figure 7.6. Since the LYSO layers need to be 200 μm thick and the stopping power will be carried mainly by the LYSO, we stack 50 of these layers which is equivalent to 10 mm long crystal and do a run using CdSe NPLs layers of 100 μm, so a 15 mm long crystal in total. The CdSe layers are defined using a 50% filling between nanoplatelets and ligands giving a final mean density of 3.55 g/cm^3.

The energies deposited in both systems are plotted to the right-hand side of Figure 7.6, where the energy spectrum of a homogeneous crystal can be seen when the energy deposited in the NPLs film is zero. For this configuration there is three times more events which deposit energy in the LYSO compared to the ones which are counted in the NPLs films. When counting all the events which deposit some energy in one of two systems the mean energy deposited in the NPLs is as low as 48.59 keV. However, if we do the weighted sum only taking into account the number of events which are actually interacting in the NPLs film, the mean energy moves towards 145 keV as shown in Figure 7.7 a). If we assume a light yield with an estimated value of 2500 ph/MeV (Table 6.1), this configuration will give a mean value of 360 photons.

If instead the simulations are done for a crystal with 50 layers of 200 μm LYSO and 200 μm CdSe NPLs film, the number of events detected in the NPLs film is 50% of the total number of gamma detected. The mean energy deposited moves to 175 keV and the spectrum will look like Figure 7.7 b). For this case, there is already few events that are able to deposit 511 keV which will emit around 1200 photons in total.

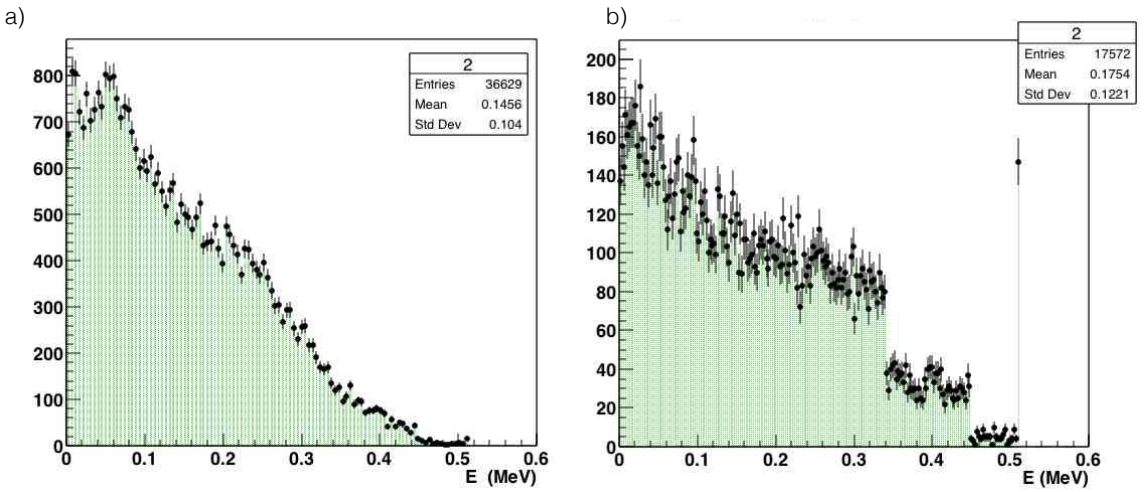

Figure 7.7: Spectra of energy deposited in the CdSe NPLs layers counting only events interacting in those layers for two different sampled crystals. a) 50 layers of 200 μm LYSO and 100 μm CdSe NPLs film and b) 50 layers of 200 μm LYSO and 200 μm CdSe NPLs film.

The idea of sampling a crystal using multilayers of LYSO coated with NCs films seems technologically very challenging without mentioning that the whole photodetector readout concept will need to change probably to a lateral configuration. To reach 100% of the photons detected by both systems we need either to decrease the thickness of the LYSO layers or to increase the thickness of the non-transparent CdSe NCs film larger than 200 μm. With these ideas in mind, we move the attention to nanocomposites, where the nanocrystals are embedded in a matrix which acts as the energy transfer medium.

7.3 ZnO:Ga nanocomposites

7.3.1 Introduction

Moving to wide-gap semiconductors, ZnO has proven to present excitonic radiative recombination on the sub-nanosecond scale [41]. However, the density of emitting centers is temperature dependent showing multi-exponential decay components and low light yield at room temperature [133]. New ways to fabricate this material making use of ZnO:Ga nanopowder and following the method reported in [21] combine excellent scintillating characteristics in terms of radioluminescence intensity (comparable to BGO light yield if co-doped with lanthanum) and a superfast monoexponential time response (photoluminescence with 400 ps decay time) at room temperature.

In the following sections we present spectral-time resolved measurements of ZnO:Ga composites under pulsed X-ray excitation and CTR measurements under gamma and MIPs irradiation. Two different approaches for preparing the nanocomposites were followed in order to provide higher light yield and better transparency (nanopowder layer deposited on a substrate) or increase the energy deposition via ionization in the scintillating material (nanopowder embedded in a host).

The ZnO:Ga nanopowder used to produce the composites presents a crystallite size of 80-100 nm, which agglomerates to create particles of size about 1 μm as it has been reported in [21] and shown in Figure 7.8 (inset). The nanocrystallite size determined from XRPD measurements gives the idea about the single nanocrystal volume available for the coherent exciton state and is within the range where the oscillator strength finds a maximum in the weak quantum confinement regime [41]. For the first sample, ZnO:Ga nanopowder was deposited by spin coating on a SiO_2 substrate and annealed at 400°C in air as the last preparative step, according to [134]. Here the scintillation will be produced in a submicrometric non-homogeneous thin layer. The thickness is determined using a profilometer yielding a mean value of 600 nm. This method of producing a nanocomposite compromises the stopping power of the sample, however, it guarantees the scintillation efficiency of the emitting centers. A second sample uses the same ZnO:Ga nanopowder dispersed within a Polystyrene (PS) host matrix, following the procedure previously reported [23]. This ZnO:Ga@PS nanocomposite consists of 10% weight ZnO:Ga with an average density of 1.5 g/cm^3. However, the light yield reported is 20% of BGO, i.e. 4-5% of LYSO [23]. A picture of the sample produced with different thicknesses is shown in Figure 7.8 (bottom). The transparency of the sample is clearly deteriorated for the 1 mm thick sample.

Samples were spectral-time characterized using pulsed X-rays up to 40 keV and a Hamamatsu C10910 streak camera with an intrinsic time resolution of 18 ps. A Hamamatsu N5084 X-ray tube is triggered by a picosecond diode laser PiLAS with a repetition rate of 4 MHz. Light is collected in transmission mode and focused into a spectrograph 2300i. The spectral resolution is determined using a 150 g/mm grating and a 500 μm open slit which result in a

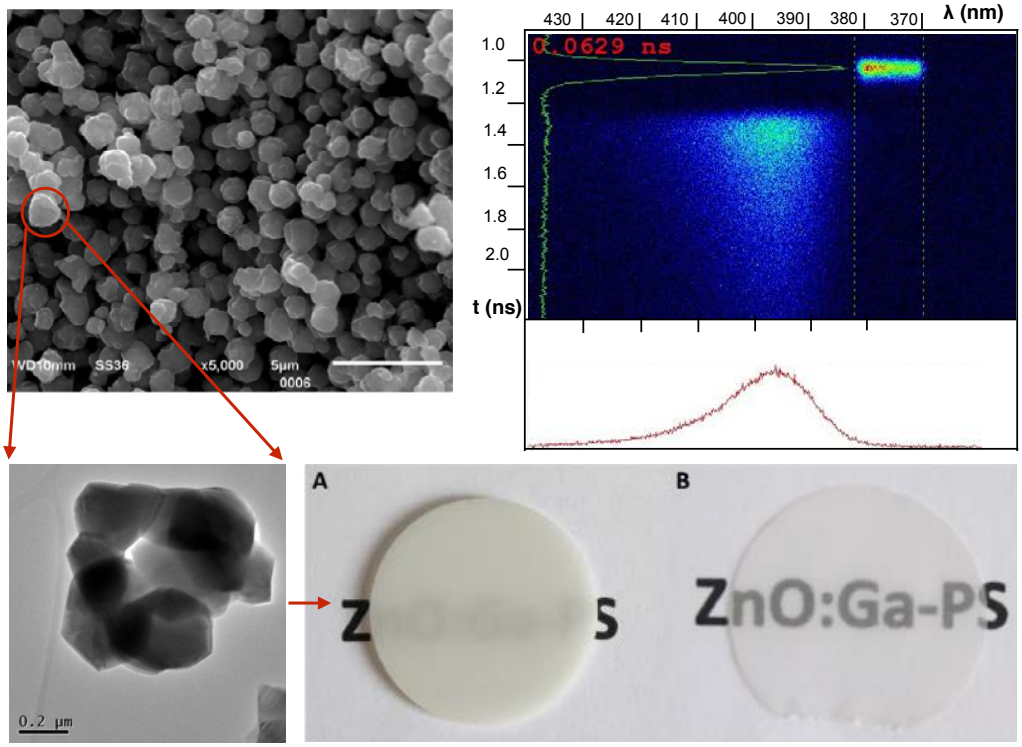

Figure 7.8: Top left: SEM image of ZnO:Ga nanopowder after two-step annealing process which causes the agglomeration of the single nanocrystals in particles of 1 μm diameter size. The SEM zoom of a typical nanocrystallite agglomeration is shown as inset. Top right: ZnO:Ga@PS spectral-time resolved radioluminescence measurement using 2 ns sweeping range. The laser IRF is shown to the right of the ZnO:Ga@PS emission. Bottom: ZnO:Ga@PS 1 mm thick sample (A) is shown next to a 0.1 mm thick sample (B).

broadened spectrum of around 10 nm for the laser line as shown in Figure 7.8. The photoelectrons are swept within 2 ns or 5 ns gate, every 250 ns, and the signal is recorded in single photon counting mode.

The impulse response function (IRF) of the system has been determined measuring the laser time profile using the same settings as for the X-ray measurements, i.e. optical path, photocathode slit aperture and sweeping range. The result for 50 μm slit aperture and 5 ns gate is a Gaussian of 80 ps FWHM, which is then convolved with the X-ray tube asymmetric time profile, resulting in a final IRF of 90 ps FWHM. The 2 ns gate streak image taken for the ZnO:Ga@PS sample is shown in Figure 7.8 together with the laser IRF (FWHM equals to 63 ps) which results in a total IRF of 75 ps.

Coincidence time resolution (CTR) measurements using 511 keV were performed with a ZnO:Ga@PS $3 \times 3 \times 1$ mm^3 thick sample. CTR measurements follow the method reported in [5] and [8]. Both samples were brought to test beam in order to characterize their performance under minimum ionizing excitation provided by a 150 GeV pion beam. Concerning the ZnO:Ga@SiO_2 sample, negligible energy deposition within the scintillating layer under gamma irradiation was found, which prevents the realization of the CTR test under 511 keV gamma for this sample.

7.3.2 Spectral-time resolved measurements using X-ray excitation

Spectrally integrated data obtained by pulsed X-ray excitation is shown in Figure 7.9 (left) for both samples, together with the system IRF. Time profiles were analyzed for several wavelength ranges, showing no differences in timing. Light is emitted between 380-420 nm with no presence of the polystyrene host radio-luminescence emission between 300-350 nm as already reported in [23]. A higher signal-to-background ratio (factor 2), is seen for the ZnO:Ga@PS sample. However, the total energy deposition for the ZnO:Ga@PS is a factor of 30 higher compared to ZnO:Ga@SiO_2, when considering a homogeneous submicrometric layer with a thickness of 600 nm. Even though the transparency of both samples is not similar, the light output of the ZnO:Ga@SiO_2 can be expected to be one order of magnitude higher as compared to ZnO:Ga@PS, if the energy deposition is taken into account. Both samples present similar mono-exponential decay time, showing an agreement within 8%, independent of the preparation method. A separate measurement, sweeping at 2 ns, was done to discard any fast components which could bring a bi-exponential behavior at early times. The results measured with 75 ps IRF present a mono-exponential decay time of 541 ± 5 ps and is shown in Figure 7.9 (right).

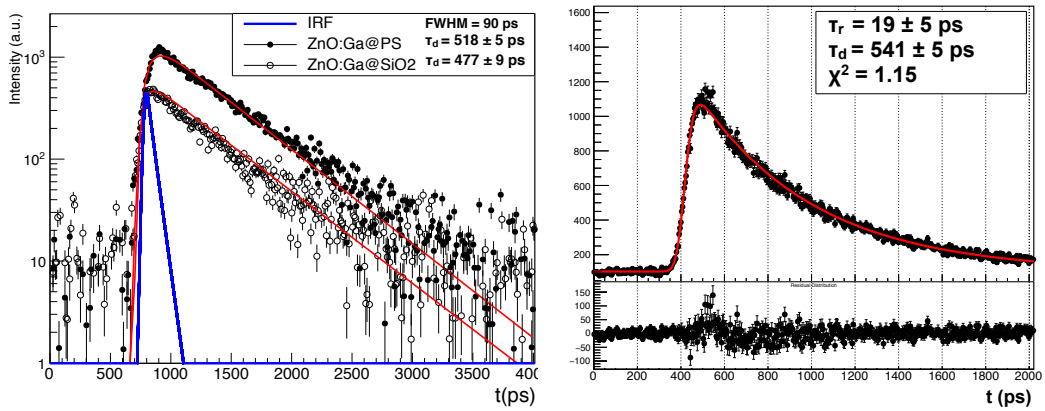

Figure 7.9: Left: ZnO:Ga nanocomposites timing performance under pulsed X-ray excitation plotted alongside with the system IRF using 5 ns sweeping range. Right: Spectrally integrated time profile of ZnO:Ga@PS sample under X-ray excitation using 2 ns sweeping range and an IRF of 75 ps FWHM.

7.3.3 CTR measurements in test beam

The timing performance when measuring two ZnO:Ga@PS $3\times3\times1$ mm^3 plates in coincidence is determined under 150 GeV pion excitation. The high energetic particles passed through the samples depositing energy uniformly along the 1 mm thick axis of the polystyrene and 5 mm thick axis of SiO_2. The procedure for these measurements is reported in [9]. Since Cherenkov photons will be created in the ZnO:Ga@SiO_2 sample, the coincidence measurements were also performed for a SiO_2 bare sample, in order to distinguish any contribution coming from the ZnO:Ga thin layer.

For small detectors, 150 GeV pions will interact as minimum ionizing particles with a mean energy deposition of 250 ± 87 keV for the ZnO:Ga@PS sample specifications. The data presented in Figure 7.10 were measured coupling each $3 \times 3 \times 1$ mm^3 ZnO:Ga@PS plate to a HPK Hamamatsu 3×3 mm^2 SiPM with an amplification coupling of 3.3 pF, bias voltage of 58 V and SiPM coupling of 100 pF. The corrected CTR of 50 ps sigma contrasts with 25 ps sigma obtained when using LYSO:Ce under the same irradiation conditions and SiPM readout.

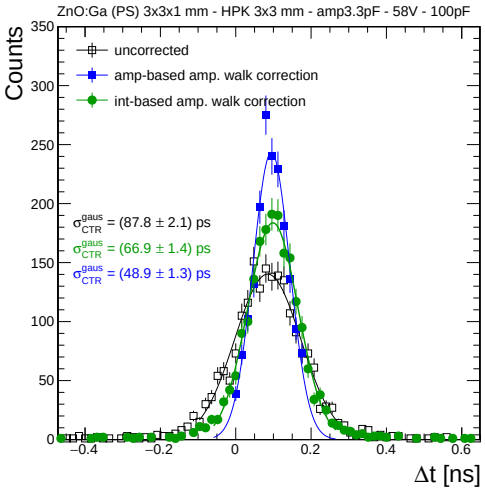

Figure 7.10: Time resolution of two ZnO:Ga@PS $3 \times 3 \times 1$ mm^3 plates coupled to a HPK 3×3 mm^2 SiPM, measured in coincidence under 150 GeV pions excitation.

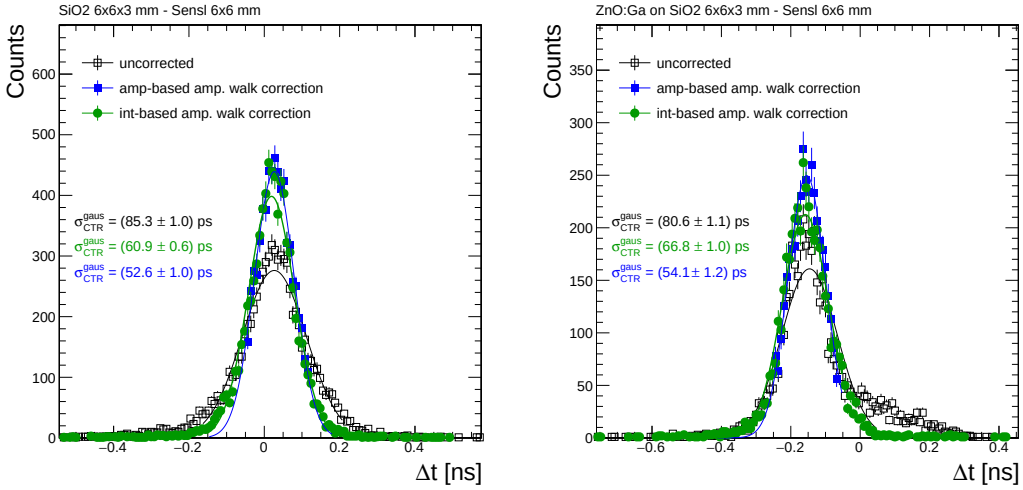

Figure 7.11: Coincidence time resolution measured for a $6 \times 6 \times 5$ mm^3 SiO_2 sample (left) and a $6 \times 6 \times 5$ mm^3 ZnO:Ga@SiO_2 (right) under pion beam excitation using LSO:Ce:Ca as the reference crystal.

For the ZnO:Ga deposited as a layer on a $6 \times 6 \times 5$ mm^3 SiO_2 substrate, the measurements were carried out comparing CTR values of ZnO:Ga@SiO_2 and SiO_2 in coincidence with a $2 \times 2 \times 5$ mm^3 LSO:Ce:Ca reference crystal. The similarities among CTR values obtained for both samples shown in Figure 7.11 allow us to arrive to the conclusion that there is no significant energy deposition in the 10 μm thick layer not even by minimum ionizing particles.

The energy spectrum measured for both samples under pion excitation is shown in Figure 7.12. The difference in pulse shape is negligible and most of the photons created and detected are Cherenkov photons.

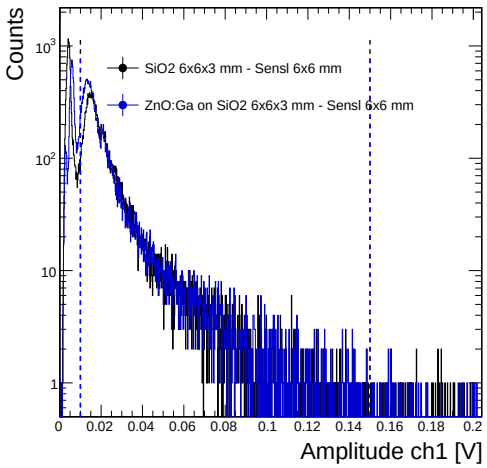

Figure 7.12: Energy spectrum measured for a $6 \times 6 \times 5$ mm^3 SiO_2 and a $6 \times 6 \times 5$ mm^3 ZnO:Ga@SiO_2 samples under pion beam excitation.

7.3.4 CTR measurements with 511 keV

The ZnO:Ga@PS $3 \times 3 \times 1$ mm^3 sample was coupled to a FBK NUV-HD 4×4 mm^2 SiPM using Meltmount glue and Teflon wrapping. The calibration of the SiPM single photoelectron response has been performed, correcting for the optical crosstalk probability of the SiPM. Gamma interactions of few hundreds of keV will deposit energy mainly through Compton scattering while photoelectric events will appear as a smeared out distribution with poor energy resolution. Geant4 simulations of 511 keV gamma interactions show a very low probability of photoelectric absorption as illustrated in the inset of Figure 7.13.

CTR measurements were done using a ^{22}Na source and a $2 \times 2 \times 10$ mm^3 LSO:Ce (0.4% Ca) reference crystal coupled to a NUV-HD FBK SiPM in coincidence with the ZnO:Ga@PS sample. Stated CTR values are corrected for the time resolution of the reference detector (70 ps FWHM) in order to obtain a CTR value as if two identical ZnO:Ga@PS detectors were operated in coincidence [12]. It should be noted that the single time resolution of one ZnO:Ga@PS would be the stated CTR value divided by $\sqrt{2}$. The bias voltage was set to 33 V and the NINO leading edge threshold to 80 mV corresponding to 1 photoelectron equivalent signal amplitude. CTR values were calculated applying different photoelectron cuts with a binning of around 1.4 pe in the ZnO:Ga@PS energy spectrum. Figure 7.13 shows the CTR values as a function of the number of photoelectrons used as cut. The CTR dependency with the square root of the number of photoelectrons (or photoelectron density) has been previously studied and understood [12] and it writes as CTR$\propto \sqrt{\tau_r \tau_d / N_{pe}}$. In this way, data shown in Figure 7.13 follows the parametrization of such formula.

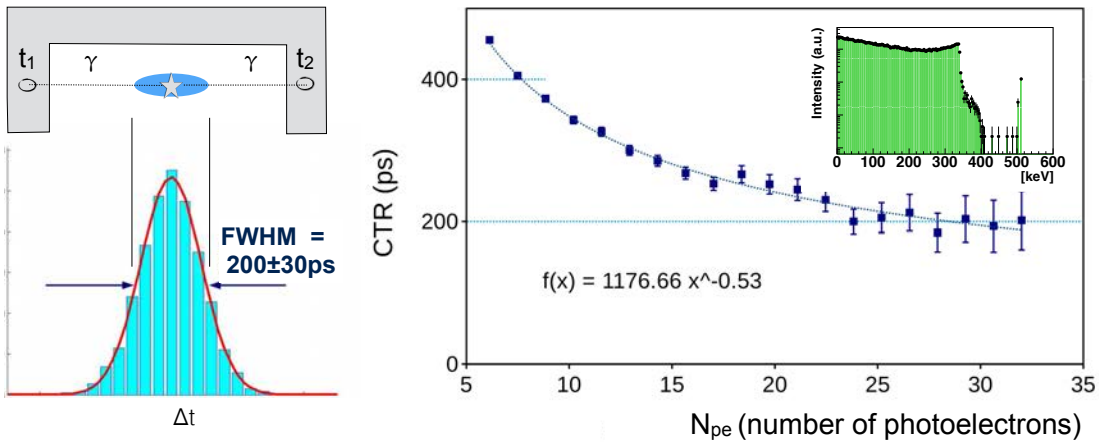

Figure 7.13: Coincidence time resolution of ZnO:Ga@PS $3 \times 3 \times 1$ mm^3 coupled to a NUV-HD 4×4 mm^2 FBK SiPM as a function of number of photoelectrons detected. The simulations done for 511 keV energy deposition are shown as inset.

7.3.5 Discussion and outlook

The poor photoelectron signal due to low light yield and low transparency counteracts the fast decay time of the sample when performing CTR measurements. However, the potential of the material as a new generation scintillator to reach sub-20 ps time resolution is clear when comparing the nanopowder's light distribution properties with the figure of merit among scintillators. Lu_2SiO_5:Ce 0.4% Ca co-doped constitutes one of the best materials for timing applications nowadays with a rise time reported as 20 ps, an effective decay time of 30 ns [12] and a light output of around 18'000 ph/MeV when using Teflon wrapping and grease coupling for a $2 \times 2 \times 10$ mm^3 all faces polished crystal. CTR values achieved for this configuration using FBK NUV-HD devices are of the order of 100 ps [8].

The comparison of ZnO:Ga@PS versus Lu_2SiO_5:Ce 0.4% Ca co-doped is done by calculating the photoelectron cumulative distribution functions along the first 500 ps of the scintillating pulse, as shown in Figure 7.14. In this way, we determine at what time, after the scintillating pulse starts, the number of photoelectrons detected reaches the same probability. Calculations are done for the actual performance of the ZnO:Ga@PS and LSO:Ce:Ca samples and a hypothetical ZnO:Ga sample with a number of photoelectron detected of the order of 1000, which reaches the 10 pe line at the very first 15 ps. The 10 pe 'probability threshold' line is crossed at a time similar to the CTR measured for LSO:Ce and ZnO:Ga@PS samples. A factor 80 higher photon density for ZnO:Ga due to its fast decay time, as compared to LSO:Ce Ca co-doped, could bring the CTR down to sub-20 ps values if the amount of photoelectrons detected would be on the order of 1'000 as proven to be the radioluminescence yield of ZnO:Ga:La nanopowders when not yet embedded in a host matrix. Extrapolating to this amount of photoelectrons when using the equation obtained in Figure 7.13, corroborates the potential of reaching sub-20 ps CTR values using ZnO:Ga nanopowder.

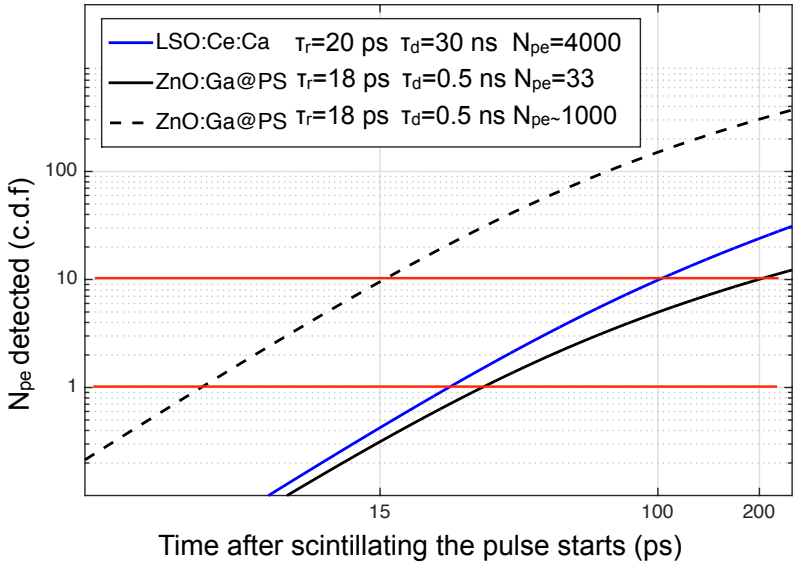

Figure 7.14: ZnO:Ga nanocrystal's potential to improve coincidence time resolution to sub-20 ps values.

Looking at the formula that defines the light yield theoretical limit for scintillators, we can determine the parameters that need future improvement.

$$LY_{out}^{lim}[ph/MeV] = LTE \cdot \frac{S \cdot Q}{b \cdot E_G[MeV]} \tag{7.3}$$

Here, LTE stands for light transfer efficiency of the material and depends on the transparency, index of refraction and the crystal's attenuation length. S and Q represent the transfer and quantum efficiencies of the scintillating process. The denominator represents the energy necessary to create and electron-hole (eh) pair, which multiplies the phonon losses in the thermalization stage (b) and the band gap energy. With an E_{eh} of 9.75 eV for ZnO (E_G=3.25 eV and b=3 [33]) and 14.4 eV for LSO (E_G=7.2 eV and b=2 [33]), these values translate to a maximum of 100'000 eh/MeV for the ZnO and 70'000 eh/MeV for LSO, having almost a factor of 1.5 different compared to the theoretical limit. Assuming that 33 photoelectrons correspond to 511 keV energy deposition and considering a photon detection efficiency of 0.3 (SiPM and Meltmount transmission for 390 nm) the estimated light output for the ZnO:Ga@PS sample is around 200 ph/MeV. From this calculation, it is clear that the energy transfer and quantum efficiency of the ZnO:Ga@PS needs further development together with the light transfer efficiency (LTE).

As it follows from temperature dependence of UV excitonic emission in ZnO:Ga,La nanopowder, [21] the quantum efficiency of this kind of materials around 300 K is much less than 1. One of the most common strategies to increase the quantum efficiency of nanocrystals is to passivate surface traps through core/shell heterostructures [27], [127]. Photo-instability effects and quenching at the surface of the materials come as a result of the high surface to volume ratios present in materials grown in the nano-scale and from the fact that we

are dealing with a Wannier-like emitting state, which is in its nature migrating inside the nanocrystal within its lifetime. In this direction, the synthesis of ZnO:Ga nanocrystals with a shell of ZnMgO could highly increase the photoluminescence efficiency when embedding free-standing nanopowders in a polystyrene host. Equally important will be to avoid agglomeration of nanopowders. High opacity of the presently studied ZnO:Ga@PS, see transmission spectra in [23], is due to aggregation of ZnO:Ga nanocrystals into submicrometric-sized objects. Better dispersion of the nanopowder dramatically decreases the light scattering effects and sample transparency [135], which improves considerably the scintillation light collection. Regarding the improvements needed for the energy transfer efficiency, the possibility of creating a chemical bond between the nanocrystals and the host, in order to channel efficiently carrier mobility from the PS host towards ZnO:Ga nanocrystals, should be also investigated. Such concepts of chemically bonded organic-inorganic scintillation nanocomposite systems have been already reported in literature [136], [137]. The introduction of a host which presents higher density is also important to analyze in order to increase the stopping power of the sample for TOF-PET applications. Reaching the particle size that maximize the oscillator strength and limits light scattering while retaining all the luminescence and scintillation properties is one of the challenges for this technology.

7.4 Conclusions

We have demonstrated that a new generation of colloidal nanocrystals holds significant potential as a material class to generate a prompt photo-response to ionizing particles. The study of NCs film deposited on conventional scintillators confirmed the simultaneous emission from both scintillating systems. However, as shown in section 7.2 there is indeed a re-absorption of the scintillating light by the nanocrystals especially for the long components. Assuming a light yield of 2500 ph/MeV for the CdSe NPLs, we conclude that a 511 keV gamma energy deposition will bring around 95 prompt photons in the first 10 ps and around 500 photons distributed between 0 and 100 ps. Doing the calculations for the GS QDs, their intrinsically slower recombination time yields a very few prompt photons in the first 10 ps (around 8). However, due to its higher light yield there will be around 1000 photons emitted in the first 100 ps after a 511 keV deposition.

Simulations performed in order to evaluate the possibility of a sampling calorimeter approach have shown the intrinsic challenge of this idea, where the layers will need to be extremely thin and energy fluctuations will dominate.

Decay- and rise-time have been measured for two ZnO:Ga nanopowder-based composites showing very similar results for both samples independent of the host. For ZnO:Ga on a SiO_2 substrate, we observe a negligible energy deposition within the submicrometric scintillating layer both for 511 keV and minimum ionizing particles. For the polystyrene sample, CTR measurements using 511 keV excitation present a minimum FWHM of 200 $\pm$ 30 ps for events

with maximum energy deposition. When comparing to the timing performance of LSO:Ce:Ca, the ZnO:Ga@PS shows a time resolution deteriorated by a factor 2, which is well understood due to the poor light output of the sample combined with a low stopping power and no energy resolution. The presented nanocomposite timing performance could pave the research path towards sub-20 ps time resolution as shown in this contribution. Already, a material with just 33 photoelectrons detected is able to deliver a CTR of 200 ps FWHM. However, an efficiency and transparency boost when placing nanopowders in a denser host still constitutes the main challenge in order to benefit from sub-nanosecond recombination times [138].

Conclusions and Perspective

This thesis investigated the technical feasibility of reaching a sub-20 ps time resolution using scintillator-based radiation detectors. The implications of such time resolution in the medical imaging and high energy physics fields are outstanding. For TOF-PET studies, 10 ps coincidence time resolution would provide with a direct imaging without reconstruction and at least a ten-fold increase in sensitivity. In the high energetic regime reached at the LHC, it would bring a considerable pile-up rejection factor which is needed for event reconstruction in the future high luminosity colliders. We have characterized the limits of state-of-the-art scintillating crystals and investigated a novel class of materials able to produce a prompt photon response to the passage of ionizing particles.

The study started with the validation of the simulation framework used to track optical photons produced and transported in the scintillating crystals. After comparison with experimental data, simulations were used to estimate the light transfer efficiency of 20 mm long LYSO crystals using different coupling configurations. This sets the intrinsic light yield of LYSO crystals in a range between 34'000-44'000 ph/MeV. As a second study, the light extraction maximum gain obtained by shaping the readout face of cuboid scintillating crystals was calculated. The crystals were cut according to the parameters tested in the simulations and the light output measurements were able to confirm a light output gain of 30%. The potential of a new highly pixelated PET module for higher spatial resolution and DOI encoding information was also evaluated, yielding positive results for one configuration.

Following these studies, the LYSO intrinsic light yield was measured in a dedicated setup. The intrinsic light yield sets a limit to the value that N_{pe} could theoretically reach using state-of-the-art photodetectors. The results are 40'000 $\pm$ 3% (stat) $\pm$ 9% (syst) ph/MeV, which indicate that around 50% of the photons are lost in a 20 mm long crystal. This implies a factor of 0.7 in CTR improvement if all the light produced will be extracted. Dedicated efforts to increase the photon detection efficiency (PDE) of SiPMs to the maximum value could provide another factor of two in N_{pe}, which converts to a factor of 0.5 in CTR improvement. Hence, both optimizations in light extraction and PDE are unable to provide an order of magnitude leap in the time resolution. In this way, the identification of potential materials for prompt photon emission is carried out by looking into Auger suppressed nanocrystals (NCs).

On the other hand, the rise time of a large set of scintillating crystals was also measured using X-ray pulsed excitation and an impulse response function of 60-134 ps. The study included lutetium based scintillating crystals, with and without Ca^{2+} co-doping, and a set of garnets (YAG, GaGG, LuAG) with and without Mg^{2+} co-doping. Two rise time components have been identified for most of the non co-doped crystals except for LGSO, which could be an indication of direct ($\tau_{r1} \sim$ O(10)ps) and delayed ($\tau_{r2} \sim$ O(100)ps) excitation of the activator centers. Co-doping with Ca^{2+} [119] or Mg^{2+} [120] species was proven to improve rise and decay time of the scintillating signal, especially for the garnets. However, this method finds poor impact on coincidence time resolution (CTR) measurements (a maximum factor 0.5 for the garnets) as long as a similar improvement on the SPTR of SiPMs is not achieved [8]. Regarding the decay time and as reported in [121], 16 ns features as a limiting value for lutetium based cerium doped scintillators.

Thus, as proven along the Chapters 3 to 5, traditional scintillators with their associated light production and their limitations in photon-extraction and -transfer, build an intrinsic barrier to attaining the sub-20 ps domain in time resolution when using 511 keV gamma excitation, requiring that new approaches to achieving a prompt photo-response must be explored.

Processes such as Cherenkov radiation [122, 123, 106] and hot intraband emission [124, 43] have been investigated for this purpose, though both suffer from poor light yield. Exploiting the Cherenkov prompt emission has lead to CTR values of 270 ps using $2 \times 2 \times 3$ mm^3 BGO crystals (τ_d=300 ns). According to Cràmer-Rao lower bound calculations, the number of prompt photons needed, along with the scintillation emission, is as high as 500-1000 photons if a CTR of 10 ps is to be reached [12, 57]. These numbers already assume a considerable improvement of the SPTR of state-of-the-art photodetectors as low as the SPTR of a single SPAD (single photon avalanche diode), which is around 10 ps. Therefore, the need for fast emitting materials or a source of sufficiently 'prompt' photons under ionizing radiation is essential in the research path of sub-20 ps time resolution detectors.

This motivates research not only towards ultrafast sub-nanosecond performance but also to materials that have the potential to produce prompt photons with sufficiently high yield under ionizing irradiation. A new class of materials, with unparalleled energy conversion efficiency has been found to be a proliferating source of prompt photons under ionizing radiation: nanocrystals.

Nanocrystals (NCs), i.e. semiconductors grown at the nano-scale (<100 nm) with a size-dependent band-gap structure, are capable of meeting many of the challenges in the current R&D of scintillating detectors. Their tunable optoelectronic properties, combined with recent advances in controlling their size, shape, heterostructure and surface chemistry have enabled their use in a wide range of photonic applications, such as low-threshold lasing [15], photovoltaic cells [18], single photon sources for quantum information [19, 20] and bio-labeling [87]. Their high quantum yields and ultrafast recombination time at the sub-ns level have

already generated interest in their use as low-cost, high-performance scintillators for radiation detection. Earlier high energy excitation studies [91, 25] have identified several important issues and deficiencies that degrade the light emitting properties of NCs, predominantly non-radiative Auger recombination [26], photo-instability [24], and losses due to the re-absorption of emitted light. However, significant progress has been made to overcome these barriers and to advance this technology for applications outlined above. Auger recombination, for example, has been considerably suppressed with the appearance of 2D-nanoplatelets [16, 15] and heterostructured core/shell quantum dots [127, 27]. Further improvements were made by embedding ZnO:Ga nanoparticles [21] in a host material leading to efficient synthesis of composites using dry nanopowders [23, 134].

The response of NCs to ionizing radiation was characterized using a Hamamatsu streak camera C10910 and a pulsed X-ray tube with an impulse response function of 60-134 ps FWHM (depending on sweeping range). We investigated three classes of colloidal NCs: two-dimensional CdSe nanoplatelets (NPLs), spherical CdSe/CdS core/giant shell quantum dots (GS QDs) and two-dimensional core/shell CdSe/ZnS nanoplatelets. We demonstrated that the emission rates of the first two NCs under pulsed X-ray excitation are much faster than traditional mechanisms in bulk scintillators, i.e. 5d-4f transitions characteristic of Ce^{3+}. CdSe NPLs have a sub-100 ps effective decay time of 77 ps (25% of the photons with a τ_{d1} of 24 ps and 75% with a τ_{d2} of 290 ps). CdSe/CdS GS QDs exhibit a sub-ns effective decay time of 849 ps (25% of the photons with a τ_{d1} of 263 ps and 75% with a τ_{d2} of 3.3 ns). Further, the respective CdSe NPL and CdSe/CdS GS QD X-ray excited photoluminescence have the emission characteristics of excitons (X) and multiexcitons (MX), with the MXs providing additional prospects for fast timing with substantially shorter lifetimes. The different multi-excitonic dynamics seen for both types of NCs under ionizing excitation, makes CdSe NPL the best performing material due to its red-shifted MX population. The study using CdSe/ZnS core shell NPLs showed spectral and timing deteriorated properties along the timeline of this thesis. Further optimization will be needed to guarantee long term stability of this very promising type of nanocrystal.

The implementation of nanocrystal-based scintillators as a new generation of ultrafast particle detectors was explored using two main lines: (1) nanocrystals as part of a heterostructure and (2) nanocomposites, where the nanocrystals are embedded in a host matrix. Initial studies comprised colloidal CdSe NPLs film of ~ 10 μm thickness deposited on the back of a LSO scintillator and CdSe/CdS GS QDs film of ~ 10 μm deposited on LuAG:Ce. The measurements revealed the NCs ultrafast emission under pulsed X-ray excitation along with the LYSO/LuAG scintillation emission. The study confirmed the presence of an additional longer decay component due to absorption of the bulk scintillator light by the NC film. In both cases, the secondary excitation by the bulk scintillator and the intrinsic longer lifetime components of the NCs can be reduced by isolating the fast MX emission via spectral filtering. Figure 7.15, left plot, shows a spectral time-resolved image of the light emitted from the CdSe-NPLs-LSO heterostructure generated by pulsed X-rays up to 40 keV. The black line denotes the time-integrated profile for the first 100 ps. After normalizing to the total energy

deposited in both materials, the NPLs photoelectron density is one order of magnitude higher as compared to LSO. Estimated light yield values for these two materials are of the order of 10^3 and 10^4 ph/MeV for NPLs and GS QDs, respectively. Assuming an energy deposition of 511 keV, CdSe NPLs have a prompt emission of 95 photons for the first 10 ps and around 500 photons for the first 100 ps. For the GS QDs case, CdSe/CdS presents around 8 prompt photons emitted within 10 ps and of the order of 1000 photons emitted in the first 100 ps. This feature defines them as a potential material class to generate a prompt photo-response at the level of O(10)ps.

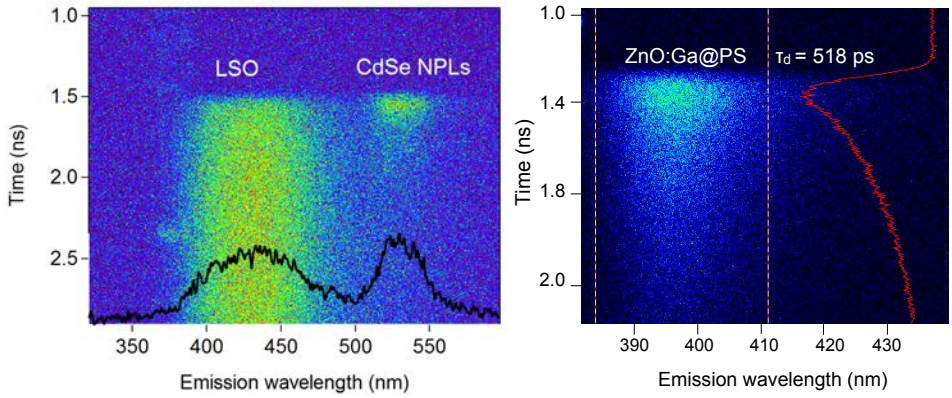

Figure 7.15: Ultrafast performance of colloidal CdSe NPLs deposited on LSO crystals (left) and a ZnO:Ga-polystyrene nanocomposite (right) under ionizing radiation.

In an attempt to fabricate a feasible detector, ZnO:Ga nanopowder embedded in a polystyrene (PS) matrix was used, where the plastic (polystyrene) scintillator acted as host, transferring non-radiative energy to the nanoparticles. This nanocomposite shows a single-exponential decay time of 518 ps and a rise time of $\leq$18 ps (see Figure 7.15, right plot).

The calculations shown in Figure 7.16 give evidence that photon emission in a 1 mm thick ZnO:Ga@PS sample (first-generation nanocomposite production), albeit its significantly lower photoelectron (pe) yield of 33 pe for 511 keV gammas, reaches the probability threshold of 10 detected pe at a time of 200 ps, only a factor of two inferior than LSO:Ce:Ca (0.4%), as was also confirmed experimentally [138]. The green curve defining the N_{pe} cumulative density function for CdSe NPLs, which crosses the 10 pe line as early as 7 ps, assumes a bulk material with time and light yield characteristics given in Table 6.1. The upper of the two calculated ZnO:Ga-curves (dashed black) assumes a N_{pe} comparable the radioluminescence yield by ZnO:Ga:La nanopowders when not yet embedded in a matrix, which is equivalent to BGO. Basically, the ultrafast emission seen in nanocrystals needs to be transported to a bulk, transparent material able to stop 511 keV. This would be possible for very few events when a crystal is sampled using LYSO and CdSe NPLs layers of around 200 μm each. In this case, the photodetector read out would need to be changed. Concerning the development of nanocomposites, a core/shell structure is needed in order to isolate the nanocrystals from the host which could bring significant changes in the lifetime of core-only materials. The technology of nanopowder production that avoid the crystallite agglomeration is another challenge of the composite production.

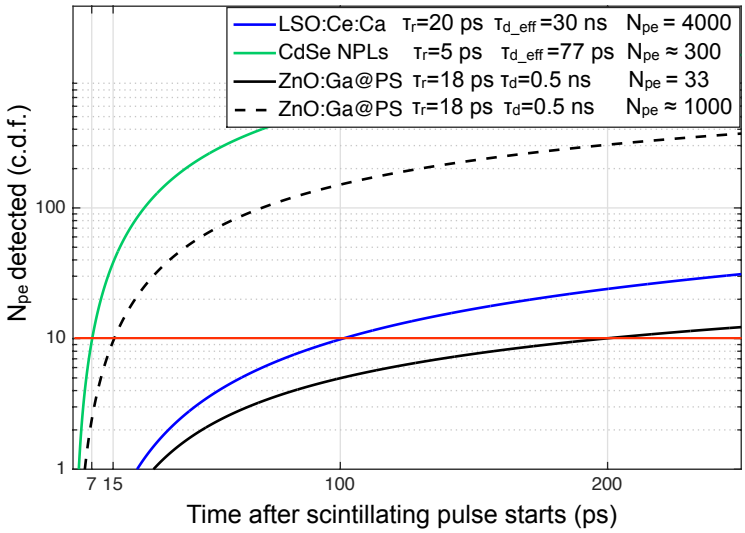

Figure 7.16: The nanocrystals' photoelectron density reaches values of 10 detected photoelectrons in the first 20 ps of the scintillating signal. This proof the NCs capacity to improve the time resolution to sub-20 ps values assuming that their potential would be transferred to a bulk, transparent material.

In conclusion, we have demonstrated that a new generation of nanocrystals hold significant potential as a material class to generate a prompt photo-response to ionizing particles. NC radiative emission lifetimes are shown to be significantly shorter than traditional scintillation mechanisms. The CdSe nanoplatelets and giant shell quantum dots studied here overcome many of the challenges that earlier generations of NCs faced under ionizing radiation. Notably, non-radiative Auger recombination, which also deteriorates bulk scintillator performance, is suppressed in both systems.

The large shell of the CdSe/CdS GS QDs overcomes several other challenges, such as re-absorption of emitted light by separating emission and absorption bands. However its blue-shifted emission under ionizing radiation makes them a less transparent system compared to CdSe NPLs. These features can in principle also be extended to NPLs via the growth of a larger bandgap shell such as CdS or ZnS. Although a stable syntheses method needs to be developed.

Outlook

We have shown that nanocrystal-based scintillators are a promising approach to fast timing detectors and provide a feasible path towards sub-20 ps time resolution. Future lines of research will be directed towards NCs as part of an efficient heterostructure which provides high stopping power, energy transfer to the nano-emitters and light-guiding system to the photodetector. For this, a periodic arrangement of the nanocrystals, preferably nanoplatelets with a shell, will have to be implemented in order to guarantee maximum transparency in some preferential direction in line with the photodetector readout axis.

Plasmonics offer a promising route to enhance emission rates of NCs. It also provides a mean to compensate for the reduced oscillator strength that result from growth of passivating shell layers, which are necessary to ensure stable and bright NCs. The results presented above confirm the feasibility of this approach under both laser and X-ray excitation. However, the disadvantage regarding the transparency of metallic nanoparticles is clear when measurements in transmission mode are no longer possible. Optimizing the overlap between the localized plasmon resonance and the NC emission frequencies is an obvious future direction, together with the study of organized systems in which the light can be manipulated as in a photonic crystal array.

These studies demonstrate the large development potential of NC technology and justify the rigorous research in this field to make NCs a viable option for superfast timing in many domains such as HEP and medical imaging.

Glossary

PET	Positron Emission Tomography
HEP	High Energy Physics
TOF-PET	Time-Of-Flight Positron Emission Tomography
FWHM	Full Width Half Maximum
CTR	Coincidence Time Resolution
LOR	Line Of Response
$\mathbf{N}_{pe}$	Number of Photoelectrons
HL-LHC	High Luminosity Large Hadron Collider
FLC	Future Linear Collider
SiPMs	Silicons PhotoMultipliers
FBK	Fondazione Bruno Kessler
NCs	Nanocrystals
NPLs	Nanoplatelets
GS QDs	Giant Shell Quantum Dots
PTS	Photon Travel Spread
SPTR	Single Photon Time Resolution
GOST	Giant Oscillator Strength Transition
LTE	Light Transfer Efficiency
SPE	Single Photoelectron
QE	Quantum Efficiency
IBL	Intra-Band Luminescence
ECAL	Electromagnetic Calorimeter
IRF	Impulse Response Function
CM	Carrier Multiplication
AR	Auger Recombination
X	Exciton
XX	Biexciton
MX	Multiexciton

List of Tables

List of Figures

Bibliography

[1] C. W. E. van Eijk, "Inorganic scintillators in medical imaging," *Physics in Medicine and Biology*, vol. 47, no. 8, p. R85, 2002. [Online]. Available: http://stacks.iop.org/0031-9155/47/i=8/a=201 Cited on 1

[2] P. Lecoq, "Development of new scintillators for medical applications," *Nuclear Instruments and Methods in Physics Research Section A*, vol. 809, pp. 130 – 139, 2016. [Online]. Available: http://www.sciencedirect.com/science/article/pii/S0168900215009754 Cited on 1

[3] M. Nikl, "Scintillation detectors for x-rays," *Measurement Science and Technology*, vol. 17, no. 4, p. R37, 2006. [Online]. Available: http://stacks.iop.org/0957-0233/17/i=4/a=R01 Cited on 1, 24, 25, 29, 155

[4] D. del Re, "Timing performance of the CMS ECAL and prospects for the future," *Journal of Physics: Conference Series*, vol. 587, no. 1, p. 012003, 2015. [Online]. Available: http://stacks.iop.org/1742-6596/587/i=1/a=012003 Cited on 1, 30

[5] S. Gundacker, E. Auffray, B. Frisch, P. Jarron, A. Knapitsch, T. Meyer, M. Pizzichemi, and P. Lecoq, "Time of flight positron emission tomography towards 100ps resolution with L(Y)SO: an experimental and theoretical analysis," *Journal of Instrumentation*, pp. 1–28, 2013. Cited on 1, 32, 138

[6] E. Auffray, F. B. M. B. Hadj, D. Cortinovis, K. Doroud, E. Garutti, P. Lecoq, Z. Liu, R. Martinez, M. Paganoni, M. Pizzichemi, A. Silenzi, C. Xu, and M. Zvolsk, "Characterization studies of silicon photomultipliers and crystals matrices for a novel time of flight PET detector," *Journal of Instrumentation*, vol. 10, no. 06, p. P06009, 2015. [Online]. Available: http://stacks.iop.org/1748-0221/10/i=06/a=P06009 Cited on 1, 2, 32, 71

[7] M. Miller, J. Zhang, K. Binzel, J. Griesmer, T. Laurence, and M. Narayanan, "Characterization of the Vereos Digital Photon Counting PET System," *J Nucl Med.*, vol. 56, 2015. Cited on 1, 31

[8] S. Gundacker, F. Acerbi, E. Auffray, A. Ferri, A. Gola, M. Nemallapudi, G. Paternoster, C. Piemonte, and P. Lecoq, "State-of-the-art timing in TOF-PET detectors with LuAG, GaGG and L(Y)SO scintillators of various sites coupled to FBK-SiPMs." *Journal of Instrumentation*, vol. 11, no. 8, p. P08008., 2016. Cited on 1, 2, 32, 33, 90, 107, 132, 138, 142, 148

[9] A. Benaglia, S. Gundacker, P. Lecoq, M. T. Lucchini, A. Para, K. Pauwels, and E. Auffray, "Detection of high energy muons with sub-20 ps timing resolution using L(Y)SO crystals and SiPM readout," *Nuclear Instruments and Methods in Physics Research A*, vol. 830, no. 11,, pp. 30–35, 2016. Cited on 1, 2, 33, 139

[10] G. Borghi, B. J. Peet, V. Tabacchini, and D. R. Schaart, "A 32mm×32mm×22mm monolithic LYSO:Ce detector with dual-sided digital photon counter readout for ultrahigh-performance TOF-PET and TOF-PET/MRI," *Physics in Medicine and Biology*, vol. 61, no. 13, p. 4929, 2016. [Online]. Available: http://stacks.iop.org/0031-9155/61/i=13/a=4929 Cited on 1, 33

[11] G. Borghi, V. Tabacchini, R. Bakker, and D. R. Schaart, "TOF-PET imaging with sub-3 mm resolution and 215 ps coincidence resolving time using digital SiPM based monolithic scintillator detectors in a 70 cm diameter tomographic setup," *J. Nucl. Med.*, vol. 57, no. 2, p. 104, 2016. Cited on 1, 33

[12] S. Gundacker, E. Auffray, K. Pauwels, and P. Lecoq, "Measurement of intrinsic rise times for various L(Y)SO and LuAG scintillators with a general study of prompt photons to achieve 10 ps in TOF-PET," *Physics in Medicine and Biology*, vol. 61, pp. 2802–2837, 2016. Cited on 2, 25, 32, 36, 90, 91, 95, 100, 107, 108, 132, 141, 142, 148

[13] S. Ithurria, M. D. Tessier, B. Mahler, R. P. S. M. Lobo, and B. D. A. L. Efros, "Colloidal nanoplatelets with two-dimensional electronic structure." *Nature materials*, vol. 10, no. 12, p. 936, dec 2011. [Online]. Available: http://dx.doi.org/10.1038/nmat3145 Cited on 3, 108

[14] A. Naeem, F. Masia, S. Christodoulou, I. Moreels, P. Borri, and W. Langbein, "Giant exciton oscillator strength and radiatively limited dephasing in two-dimensional platelets," *Physics Review Letters B*, vol. 91, p. 121302, Mar 2015. [Online]. Available: http://link.aps.org/doi/10.1103/PhysRevB.91.121302 Cited on 3, 108

[15] J. Q. Grim, S. Christodoulou, F. D. Stasio, R. Krahne, R. Cingolani, L. Manna, and I. Moreels, "Continuous-wave biexciton lasing at room temperature using solution-processed quantum wells," *Nature Nanotechnology*, vol. 9, pp. 891–895, 2014. Cited on 3, 54, 108, 109, 110, 112, 148, 149

[16] B. Guzelturk, Y. Kelestemur, M. Olutas, S. Delikanli, and H. V. Demir, "Amplified spontaneous emission and lasing in colloidal nanoplatelets," *ACS Nano*, vol. 8, no. 7, pp. 6599–6605, 2014, pMID: 24882737. [Online]. Available: http://dx.doi.org/10.1021/nn5022296 Cited on 3, 54, 109, 149

[17] V. I. Klimov, A. A. Mikhailovsky, S. Xu, A. Malko, J. A. Hollingsworth, C. A. Leatherdale, H.-J. Eisler, and M. G. Bawendi, "Optical gain and stimulated emission in nanocrystal quantum dots," *Science*, vol. 290, no. 5490, pp. 314–317, 2000. [Online]. Available: http://science.sciencemag.org/content/290/5490/314 Cited on 3, 54, 109

[18] F. Meinardi, A. Colombo, K. A. Velizhanin, R. Simonutti, M. Lorenzon, L. Beverina, R. Viswanatha, V. I. Klimov, and S. Brovelli, "Large-area luminescent solar concentrators based on Stokes-shift-engineered nanocrystals in a mass-polymerized PMMA matrix," *Nature Photonics*, vol. 8, no. 5, p. 392, apr 2014. [Online]. Available: http://dx.doi.org/10.1038/nphoton.2014.54 Cited on 3, 54, 109, 148

[19] F. Pisanello, L. Martiradonna, G. Lemènager, P. Spinicelli, A. Fiore, L. Manna, J.-P. Hermier, R. Cingolani, E. Giacobino, M. De Vittorio, and A. Bramati, "Room temperature-dipolelike single photon source with a colloidal dot-in-rod," *Applied Physics Letters*, vol. 96, no. 3, 2010. [Online]. Available: http://scitation.aip.org/content/aip/journal/apl/96/3/10.1063/1.3291849 Cited on 3, 54, 109, 148

[20] M. A. M. Versteegh, M. E. Reimer, K. D. Jons, D. Dalacu, P. J. Poole, A. Gulinatti, A. Giudice, and V. Zwiller, "Observation of strongly entangled photon pairs from a nanowire quantum dot," *Nature Communications*, vol. 5, no. 5298, 2014. Cited on 3, 54, 109, 148

[21] L. Procházková, T. Gbur, V. Čuba, V. Jarý, and M. Nikl, "Fabrication of highly efficient ZnO nanoscintillators," *Optical Materials*, vol. 47, pp. 67–71, Sep. 2015. Cited on 3, 54, 109, 137, 143, 149

[22] C. Liu, T. J. Hajagos, D. Kishpaugh, Y. Jin, W. Hu, Q. Chen, and Q. Pei, "Facile single-precursor synthesis and surface modification of hafnium oxide nanoparticles for nanocomposite γ-ray scintillators," *Advanced Functional Materials*, vol. 25, no. 29, pp. 4607–4616, 2015. [Online]. Available: http://dx.doi.org/10.1002/adfm.201501439 Cited on 3, 54, 109

[23] H. Burešová, L. Procházková, R. M. Turtos, V. Jarý, E. Mihóková, A. Beitlerová, R. Pjatkan, S. Gundacker, E. Auffray, P. Lecoq, M. Nikl, and V. Čuba, "Preparation and luminescence properties of ZnO:Ga polystyrene composite scintillator," *Opt. Express*, vol. 24, no. 14, pp. 15 289–15 298, Jul 2016. [Online]. Available: http://www.opticsexpress.org/abstract.cfm?URI=oe-24-14-15289 Cited on 3, 109, 137, 139, 144, 149

[24] N. J. Withers, K. Sankar, B. A. Akins, T. A. Memon, T. Gu, J. Gu, G. A. Smolyakov, M. R. Greenberg, T. J. Boyle, and M. Osiński, "Rapid degradation of CdSe-ZnS colloidal quantum dots exposed to gamma irradiation," *Applied Physics Letters*, vol. 93, no. 17, 2008. [Online]. Available: http://scitation.aip.org/content/aip/journal/apl/93/17/10.1063/1.2978073 Cited on 3, 109, 149

[25] S. E. Létant and T. Wang, "Semiconductor quantum dot scintillation under γ-ray irradiation," *Nano Letters*, vol. 6, no. 12, pp. 2877–2880, 2006, pMID: 17163723. [Online]. Available: http://dx.doi.org/10.1021/nl0620942 Cited on 3, 54, 109, 149

[26] L. A. Padilha, W. K. Bae, V. I. Klimov, J. M. Pietryga, and R. D. Schaller, "Response of semiconductor nanocrystals to extremely energetic excitation," *Nano Letters*, vol. 13, no. 3, pp. 925–932, 2013, pMID: 23373470. [Online]. Available: http://dx.doi.org/10.1021/nl400141w Cited on 3, 54, 109, 115, 149

[27] S. Christodoulou, G. Vaccaro, V. Pinchetti, F. De Donato, J. Q. Grim, A. Casu, A. Genovese, G. Vicidomini, A. Diaspro, S. Brovelli, L. Manna, and I. Moreels, "Synthesis of highly luminescent wurtzite CdSe/CdS giant-shell nanocrystals using a fast continuous injection route," *J. Mater. Chem. C*, vol. 2, pp. 3439–3447, 2014. [Online]. Available: http://dx.doi.org/10.1039/C4TC00280F Cited on 3, 110, 112, 117, 131, 143, 149

[28] P. Lecoq, *Scintillation and Inorganic Scintillators.* Berlin, Heidelberg: Springer, 2006, pp. 1–34. [Online]. Available: http://dx.doi.org/10.1007/3-540-27768-4_1 Cited on 7

[29] B. K. Ridley, *Quantum processes in semiconductors.* Oxford, OX2 6DP, UK: Oxford University Press, 2013, pp. 1–51. Cited on 9, 14, 16, 17

[30] P. Harrison and A. Valavais, *Quantum wells, wires and dots.* West Sussex, P019 8SQ, UK: Jhon Wiley & Sons, Ltd, 2016, pp. 1–77. Cited on 10, 11

[31] N. W. Ashcroft and N. D. Mermin, *Solid State Physics*. Philadelphia, USA: Saunders College Publishing, 1976, p. 99. Cited on 13

[32] M. Combescot and S.-Y. Shiau, *Excitons and Cooper Pairs, two composite boson in many body physics*, first edition ed., O. U. press, Ed. Cited on 16, 17

[33] P. A. Rodnyi, P. Dorenbos, and C. W. E. van Eijk, "Energy loss in inorganic scintillators," *pss (b)*, vol. 187, no. 1, pp. 15–29, 1995. [Online]. Available: http://dx.doi.org/10.1002/pssb.2221870102 Cited on 20, 143

[34] I. V. Khodyuk, F. G. A. Quarati, M. S. Alekhin, and P. Dorenbos, "Energy resolution and related charge carrier mobility in LaBr3:Ce scintillators," *Journal of Applied Physics*, vol. 114, no. 12, 2013. [Online]. Available: http://scitation.aip.org/content/aip/journal/jap/114/12/10.1063/1.4823737 Cited on 20, 21, 157

[35] J. Q. Grim, K. B. Ucer, A. Burger, P. Bhattacharya, E. Tupitsyn, E. Rowe, V. M. Buliga, L. Trefilova, A. Gektin, G. A. Bizarri, W. W. Moses, and R. T. Williams, "Nonlinear quenching of densely excited states in wide-gap solids," *Physics Review Letters B*, vol. 87, p. 125117, Mar 2013. [Online]. Available: http://link.aps.org/doi/10.1103/PhysRevB.87.125117 Cited on 21, 22, 109

[36] J. Q. Grim, Q. Li, K. B. Ucer, A. Burger, G. A. Bizarri, W. W. Moses, and R. T. Williams, "The roles of thermalized and hot carrier diffusion in determining light yield and proportionality of scintillators," *Phys. Status Solidi A*, vol. 209, no. 12, pp. 2421–2426, 2012. Cited on 21

[37] X. Lu, Q. Li, G. A. Bizarri, K. Yang, M. R. Mayhugh, P. R. Menge, and R. T. Williams, "Coupled rate and transport equations modeling proportionality of light yield in high-energy electron tracks: CsI at 295 K and 100 K; CsI:Tl at 295 K," *Phys. Rev. B*, vol. 92, p. 115207, 2015. Cited on 21

[38] Z. Wang, Y. Xie, B. D. Cannon, L. W. Campbell, F. Gao, and S. Kerisit, "Computer simulation of electron thermalization in CsI and CsI(Tl)," *Journal of Applied Physics*, vol. 110, no. 6, 2011. [Online]. Available: http://scitation.aip.org/content/aip/journal/jap/110/6/10.1063/1.3632969 Cited on 22

[39] Z. Wang, Y. Xie, L. W. Campbell, F. Gao, and S. Kerisit, "Monte Carlo simulations of electron thermalization in alkali iodide and alkaline-earth fluoride scintillators," *Journal of Applied Physics*, vol. 112, no. 1, 2012. [Online]. Available: http://scitation.aip.org/content/aip/journal/jap/112/1/10.1063/1.4736088 Cited on 22

[40] C. Pédrini, "Scintillation mechanisms and limiting factors on each step of relaxation of electronic excitations," *Physics of the Solid State*, vol. 47, no. 8, pp. 1406–1411, 2005. [Online]. Available: http://dx.doi.org/10.1134/1.2014478 Cited on 22, 23, 24

[41] J. Wilkinson, K. Ucer, and R. Williams, "Picosecond excitonic luminescence in ZnO and other wide-gap semiconductors," *Radiation Measurements*, vol. 38, no. 46, pp. 501 – 505, 2004, proceedings of the 5th European Conference on Luminescent Detectors and Transformers of Ionizing Radiation (LUMDETR 2003). [Online]. Available: http://www.sciencedirect.com/science/article/pii/S1350448704000289 Cited on 26, 137

[42] P. Rodnyi, "Progress in fast scintillators," *Radiation Measurements*, vol. 33, no. 5, pp. 605 – 614, 2001, proceedings of the International Symposium on Luminescent Detecto rs and Transformers of Ionizing Radiation. [Online]. Available: http://www.sciencedirect.com/science/article/pii/S1350448701000683 Cited on 26

[43] P. Lecoq, M. Korzhik, and A. Vasil'ev, "Can transient phenomena help improving time resolution in scintillators?" *IEEE Transactions on Nuclear Science*, vol. 61, no. 1, pp. 229–234, Feb 2014. Cited on 27, 108, 148, 157

[44] S. I. Omelkov, V. Nagirnyi, E. Feldbach, R. M. Turtos, E. Auffray, M. Kirm, and P. Lecoq, "Intraband luminescence excited in new ways: low-power x-ray and electron beams," *Journal of Luminescence*, vol. submitted, 2016. Cited on 27

[45] S. Vandenberghe, E. Mikhaylova, E. D'Hoe, P. Mollet, and J. S. Karp, "Recent developments in time-of-flight PET," *EJNMMI Physics*, vol. 3, no. 1, p. 3, 2016. [Online]. Available: http://dx.doi.org/10.1186/s40658-016-0138-3 Cited on 31, 32

[46] J. A. Kolthammer, K. H. Su, A. Grover, M. Narayanan, D. W. Jordan, and R. F. Muzic, "Performance evaluation of the Ingenuity TF PET/CT scanner with a focus on high count-rate conditions," *Phys Med Biol*, vol. 59, 2014. [Online]. Available: http://dx.doi.org/10.1088/0031-9155/59/14/3843 Cited on 31

[47] B. W. Jakoby, Y. Bercier, M. Conti, M. E. Casey, B. Bendriem, and D. W. Townsend, "Physical and clinical performance of the mCT time-of-flight PET/CT scanner," *Phys Med Biol*, vol. 56, 2011. [Online]. Available: http://dx.doi.org/10.1088/0031-9155/56/8/004 Cited on 31

[48] V. Bettinardi, L. Presotto, E. Rapisarda, M. Picchio, L. Gianolli, and M. C. Gilardi, "Physical performance of the new hybrid PET/CT Discovery-690," *Med Phys.*, vol. 38, 2011. [Online]. Available: http://dx.doi.org/10.1118/1.3635220 Cited on 31

[49] K. C. Burr, G.-C. Wang, G. Mann, K. Balakrishnan, J. Wang, and et al, "A new modular and scalable detector for a time-of-flight pet scanner," in *Nuclear Science Symposium and Medical Imaging Conference (NSS/MIC)*. IEEE, 2012, pp. 2830–834. Cited on 31

[50] M. Conti., "State of the art and challenges of time-of-flight PET," *Physica Medica*, vol. 25, pp. 1–11, 2009. Cited on 32

[51] T. F. Budinger, "Time-of-flight positron emission tomography: status relative to conventional PET," *J Nucl Med.*, vol. 24, pp. 73–8, 1983. Cited on 32, 33

[52] S. Gundacker, "Time resolution in scintillator based detector for positron emission tomography," Ph.D. dissertation, Vienna University of Technology, 2014. [Online]. Available: https://cds.cern.ch/record/1700603?ln=en Cited on 32, 64

[53] G. Stringhini, M. Pizzichemi, A. Ghezzi, A. Stojkovic, M. Paganoni, and E. Auffray, "Development and evaluation of a practical method to measure the depth of interaction function for a single side readout pet detector," *Journal of Instrumentation*, vol. 11, no. 11, p. P11014, 2016. [Online]. Available: http://stacks.iop.org/1748-0221/11/i=11/a=P11014 Cited on 34, 75

[54] M. Pizzichemi, G. Stringhini, T. Niknejad, Z. Liu, P. Lecoq, S. Tavernier, J. Varela, M. Paganoni, and E. Auffray, "A new method for depth of interaction determination in PET detectors," *Physics in Medicine and Biology*, vol. 61, no. 12, p. 4679, 2016. [Online]. Available: http://stacks.iop.org/0031-9155/61/i=12/a=4679 Cited on 34, 75

[55] S. I. Kwon, A. Gola, A. Ferri, C. Piemonte, and S. R. Cherry, "Bismuth germanate coupled to near ultraviolet silicon photomultipliers for time-of-flight PET," *Physics in Medicine and Biology*, vol. 61, no. 18, p. L38, 2016. [Online]. Available: http://stacks.iop.org/0031-9155/61/i=18/a=L38 Cited on 34

[56] N. Efthimiou, "Technical report of the STSM FAST COST action TD1401: Implementation of TOF reconstruction for STIR toolkit." 2016. Cited on 34

[57] R. M. Turtos, S. Gundacker, A. Polovitsyn, S. Christodoulou, M. Salomoni, E. Auffray, I. Moreels, P. Lecoq, and J. Grim, "Ultrafast emission from colloidal nanocrystals under pulsed x-ray excitation," *Journal of Instrumentation*, vol. 11, no. 10, p. P10015, 2016. [Online]. Available: http://stacks.iop.org/1748-0221/11/i=10/a=P10015 Cited on 36, 108, 148

[58] C. B. Murray, D. J. Norris, and M. G. Bawendi, " Synthesis and characterization of nearly monodisperse CdE (E=S, Se,Te) semiconductor nanocrystallites," *Journal of the American Chemical Society*, vol. 115, pp. 8706–15, 1993. Cited on 37

[59] L. Qu and X. Peng, "Control of photoluminescence properties of CdSe nanocrystals in growth," *Journal of the American Chemical Society*, vol. 124, pp. 2024–55, 2003. Cited on 37

[60] X. G. Peng, L. Manna, W. D. Yang, J. Wickham, E. Scher, and et al., "Shape control of CdSe nanocrystals," *Nature*, vol. 404, pp. 59–61, 2000. Cited on 37

[61] L. Manna, E. C. Scher, and A. P. Alivisatos, "Synthesis of soluble and processable rod-, arrow-, teardrop-, and tetrapod-shaped CdSe nanocrystals," *Journal of the American Chemical Society*, vol. 122, pp. 12 700–6, 2000. Cited on 37

[62] M. A. Hines and P. Guyot-Sionnest, "Synthesis and characterization of strongly luminescing ZnS-capped CdSe nanocrystals," *Journal of Physical Chemistry*, vol. 100, pp. 468–71, 1996. Cited on 38

[63] X. Peng, M. C. Schlamp, A. V. Kadavanich, and A. P. Alivisatos, "Epitaxial growth of highly luminescent CdSe/CdS core/shell nanocrystals with photostability and electronic accessibility," *Journal of the American Chemical Society*, vol. 119, pp. 7019–29, 1997. Cited on 38

[64] S. A. Ivanov, J. Nanda, A. Piryatinski, M. Achermann, L. P. Balet, and et al, "Light amplification using inverted core/shel nanocrystals: towards lasing in the single exciton regime," *Journal of Physical Chemistry B*, vol. 108, pp. 10 625–30, 2004. Cited on 38

[65] H. Kim, M. Achermann, J. A. Hollingsworth, and V. I. Klimov, "Synthesis and characterization of Co/CdSe core/shell nanocomposites: bi-functional magnetic optical nanocrystals," *Journal of the American Chemical Society*, vol. 127, pp. 544–46, 2005. Cited on 38

[66] M. Achermann, J. A. Hollingsworth, and V. I. Klimov, "Multiexcitons confined within a subexcitonic volume: spectroscopic and dynamical signatures of neutral and charged biexcitons in ultrasmall semiconductor nanocrystals," *Phys Rev. B*, vol. 68, p. 245302, 2003. Cited on 38

[67] A. L. Efros, V. A. Kharchenko, and M. Rosen, "Breaking the phonon bottleneck in nanometer quantum dots: role of auger-like processes," *Solid State Commun.*, vol. 93, p. 28184, 1995. Cited on 38

[68] V. I. Klimov and D. W. McBranch, "Femtosecond 1p-to-1s electron relaxation in strongly-confined semiconductor nanocrystals," *Phys. Rev. Lett*, vol. 80, p. 402831, 1998. Cited on 38

[69] P. Guyot-Sionnest, M. Shim, C. Matranga, and M. Hines, "Intraband relaxation in CdSe quantum dots," *Phys. Rev. Lett*, vol. 60, p. 218184, 1999. Cited on 38

[70] V. I. Klimov, A. A. Mikhailovsky, D. W. McBranch, C. A. Leatherdale, and M. G. Bawendi, "Mechanisms for intraband energy relaxation in semiconductor quantum dots: the role of electron-hole interactions," *Phys. Rev. Lett*, vol. 61, p. 1334952, 2000. Cited on 38

[71] R. D. Schaller and V. I. Klimov, "High efficiency carrier multiplication in PbSe nanocrystals: implications for solar-energy conversion," *Phys. Rev. Lett.*, vol. 92, p. 186601, 2004. Cited on 38

[72] V. I. Klimov, "Spectral and dynamical properties of multiexcitons in semiconductor nanocrystals," *Annu. Rev. Phys. Chem.*, vol. 58, p. 63573, 2007. Cited on 41, 46, 47, 48

[73] ——, "Multicarrier Interactions semiconductor nanocrystals in relation to the phenomena of Auger recombination and carrier multiplication," *Annu. Rev. Condens. Matter Phys.*, vol. 5, pp. 285–316, 2014. Cited on 41, 47, 48

[74] V. I. Klimov, A. A. Mikhailovsky, D. W. McBranch, C. A. Leatherdale, and M. G. Bawendi, "Quantization of multiparticle auger rates in semiconductor quantum dots," *Science*, vol. 287, pp. 1011–13, 2010. Cited on 41, 52

[75] H. Htoon, J. A. Hollingsworth, R. Dickerson, and V. I. Klimov, "Effect of Zero- to One-Dimensional Transformation on Multiparticle Auger Recombination in Semiconductor Quantum Rods," *Phys. Rev. Lett.*, vol. 91, p. 227401, Nov 2003. [Online]. Available: http://link.aps.org/doi/10.1103/PhysRevLett.91.227401 Cited on 41, 49, 52

[76] L.-W. Wang, M. Califano, A. Zunger, and A. Franceschetti, "Pseudopotential theory of Auger processes in CdSe quantum dots," *Phys. Rev. Lett.*, vol. 91, p. 056404, Jul 2003. [Online]. Available: http://link.aps.org/doi/10.1103/PhysRevLett.91.056404 Cited on 41, 42

[77] D. J. Norris, A. Sacra, C. B. Murray, and M. G. Bawendi, "Measurement of the size dependent hole spectrum in CdSe quantum dots," *Phys. Rev. Lett.*, vol. 72, pp. 2612–2615, Apr 1994. [Online]. Available: http://link.aps.org/doi/10.1103/PhysRevLett.72.2612 Cited on 42

[78] V. Kharchenko and M. Rosen, "Auger relaxation processes in semiconductor nanocrystals and quantum wells," *Journal of Luminescence*, vol. 70, no. 1, pp. 158 – 169, 1996. [Online]. Available: http://www.sciencedirect.com/science/article/pii/002223139600052X Cited on 42

[79] B. Saleh and M. Teich, *Fundamentals of Photonics*. John Wiley & Sons Inc. Cited on 45

[80] A. I. Ekimov, F. Hache, M. C. Schanne-Klein, D. Ricard, C. Flytzanis, I. A. Kudryavtsev, T. V. Yazeva, A. V. Rodina, and A. L. Efros, "Absorption and intensity-dependent photoluminescence measurements on CdSe quantum dots: assignment of

the first electronic transitions," *J. Opt. Soc. Am. B*, vol. 10, no. 1, pp. 100–107, Jan 1993. [Online]. Available: http://josab.osa.org/abstract.cfm?URI=josab-10-1-100 Cited on 45

[81] C. Dang, J. Lee, C. Breen, J. S. Steckel, S. Coe-Sullivan, and A. Nurmikko, "Red, green and blue lasing enabled by single-exciton gain in colloidal quantum dot films." *Nature nanotechnology*, vol. 7, no. 5, p. 335, may 2012. [Online]. Available: http://dx.doi.org/10.1038/nnano.2012.61 Cited on 50, 120

[82] V. I. Klimov, S. A. Ivanov, J. Nanda, M. Achermann, I. Bezel, J. A. McGuire, and A. Piryatinski, "Single-exciton optical gain in semiconductor nanocrystals," *Nature*, vol. 447, pp. 441–46, 2007. Cited on 53

[83] X. Wang, X. Ren, K. Kahen, M. A. Hahn, M. Rajeswaran, S. Maccagnano-Zacher, J. Silcox, G. E. Cragg, A. L. Efros, and T. D. Krauss, "Non-blinking semiconductor nanocrystals," *Nature*, vol. 459, pp. 686–689, 2009. Cited on 54

[84] S. Nizamoglu, T. Erdem, X. W. Sun, and H. V. Demir, "Warm-white light-emitting diodes integrated with colloidal quantum dots for high luminous efficacy and color rendering," *Optics Letters*, vol. 35, pp. 3372–3374, 2010. Cited on 54

[85] A. M. Malyarevich, I. A. Denisov, K. V. Yumashev, O. S. Dymshits, and A. A. Zhilin, "Optical absorption and luminescence study of Cobalt-doped magnesium aluminosilicate glass ceramics," *Journal of the Optical Society of America B*, vol. 19, pp. 1815–1821, 2002. Cited on 54

[86] A. W. Achtstein, A. V. Prudnikau, M. V. Ermolenko, L. I. Gurinovich, S. V. Gaponenko, U. Woggon, A. V. Baranov, M. Y. Leonov, I. D. Rukhlenko, A. V. Fedorov, and M. V. Artemyev, "Electroabsorption by 0D, 1D, and 2D nanocrystals: a comparative study of CdSe colloidal quantum dots, nanorods, and nanoplatelets," *ACS Nano*, vol. 8, p. 76787686, 2014. Cited on 54

[87] D. Deng, Y. Chen, J. Cao, J. Tian, Z. Qian, S. Achilefu, and Y. Gu, "High-quality CuInS_2-ZnS quantum dots for in vitro and in vivo bioimaging," *Chemistry of Materials*, vol. 24, no. 15, pp. 3029–3037, 2012. [Online]. Available: http://dx.doi.org/10.1021/cm3015594 Cited on 54, 109, 148

[88] J. Lim, M. Park, W. K. Bae, D. Lee, S. Lee, C. Lee, and K. Char, "Highly efficient Cadmium-free quantum dot light-emitting diodes enabled by the direct formation of excitons within InP@ZnSeS quantum dots," *ACS Nano*, vol. 7, no. 10, pp. 9019–9026, 2013, pMID: 24063589. [Online]. Available: http://dx.doi.org/10.1021/nn403594j Cited on 54

[89] J.-S. Lee, M. V. Kovalenko, J. Huang, D. S. Chung, and D. V. Talapin, "Band-like transport, high electron mobility and high photoconductivity in all-inorganic nanocrystal arrays," *Nature Nano*, vol. 6, pp. 348–352, 2011. Cited on 54

[90] W. C. W. Chan and S. Nie, "Quantum dot bioconjugates for ultrasensitive nonisotopic detection," *Science*, vol. 281, no. 5385, pp. 2016–2018, 1998. [Online]. Available: http://science.sciencemag.org/content/281/5385/2016 Cited on 54

[91] S. Létant and T. Wang, "First study of nano-composite scintillators under alpha irradiation," *Applied Physics Letters*, vol. 88, Jun 2005. [Online]. Available: http://www.osti.gov/scitech/servlets/purl/884768 Cited on 54, 109, 149

[92] P. Brůža, D. Pànek, V. Fidler, P. Benedikt, V. Čuba, T. Gbur, P. Boháček, and M. Nikl, "Applications of a table-top time-resolved luminescence spectrometer with nanosecond soft x-ray pulse excitation," *IEEE Transactions on Nuclear Science*, vol. 61, no. 1, pp. 448–451, Feb 2014. Cited on 54, 109

[93] E. Auffray, B. Frisch, F. Geraci, A. Ghezzi, S. Gundacker, H. Hillemanns, P. Jarron, T. Meyer, M. Paganoni, K. Pauwels, M. Pizzichemi, and P. Lecoq, "A comprehensive & systematic study of coincidence time resolution and light yield using scintillators of different size, wrapping and doping," in *Nuclear Science Symposium and Medical Imaging Conference (NSS/MIC)*. IEEE, 2011, pp. 64 – 71. Cited on 58

[94] S. Agostinelli and et al., "Geant4 - a simulation toolkit," *Nuclear Instruments and Methods in Physics Research A*, vol. 506, p. 250, 2003. Cited on 59, 62, 65, 132

[95] (2006-2015) Crystal photonics inc. [Online]. Available: http://crystal-photonics.com/ Cited on 60

[96] Vikuity. (2003) Vikuiti Enhanced Specular Reflector (ESR. [Online]. Available: http://multimedia.3m.com/mws/media/193294O/vikuiti-tm-esr-application-guidelines.pdf?fn=ESR_family_AppGuide.pdf Cited on 60, 69

[97] D. J. van der Laan, D. R. Schaart, M. C. Maas, F. J. Beekman, P. Bruyndonckx, and C. W. E. van Eijk, "Optical simulation of monolithic scintillator detectors using GATE/GEANT4," *Physics in Medicine and Biology*, vol. 55, pp. 1659–1675, 2010. Cited on 62

[98] R. Kitamura, L. Pilon, and M. Jonasz, "Optical constants of silica glass from extreme ultraviolet to far infrared at near room temperature," *Applied Optics*, vol. 46, no. 33, pp. 8118–8133, 2007. Cited on 62

[99] D. Motta and S. Schonert, "Optical properties of bialkali photocathodes," *Nuclear Instruments and Methods in Physics Research A*, vol. 539, pp. 217–235, 2005. Cited on 62

[100] K. Pauwels, E. Auffray, S. Gundacker, A. Knapitsch, and P. Lecoq, "Effect of aspect ratio on the light output of scintillators," *IEEE Transactions on Nuclear Science*, vol. 59, no. 5, pp. 2340–2345, October 2012. Cited on 64

[101] M. Janecek and W. W. Moses, "Simulating scintillator light collection using measured optical reflectance," *IEEE Transactions on Nuclear Science*, vol. 57, no. 3, pp. 964–970, June 2010. Cited on 65

[102] J. W. Cates, J. P. Hayward, and X. Zhang, "Increased light extraction from inorganic scintillators with laser-etched microstructures," *IEEE Transactions on Nuclear Science*, vol. 60, no. 2, pp. 1027–1032, April 2013. Cited on 66

[103] A. Knapitsch, E. Auffray, C. W. Fabjan, J. L. Leclercq, X. Letartre, R. Mazurczyk, and P. Lecoq, "Effects of photonic crystals on the light output of heavy inorganic scintillators," *IEEE Transactions on Nuclear Science*, vol. 60, no. 3, pp. 2322–2329, June 2013. Cited on 66

[104] M. V. Nemallapudi, S. Gundacker, R. M. Turtos, M. Vangeleyn, N. Brillouet, P. Lecoq, and E. Auffray, "Alternative geometries for improved light output of inorganic scintillating crystals," *IEEE Transactions on Nuclear Science*, vol. 63, no. 2, pp. 649–55, 2016. Cited on 69, 75

[105] R. M. Turtos, S. Gundacker, M. Pizzichemi, K. Pauwels, A. Ghezzi, E. Auffray, P. Lecoq, and M. Paganoni, "Measurement of LYSO intrinsic light yield using electron excitation," *IEEE Transactions on Nuclear Science*, vol. 63, no. 2, pp. 475–479, April 2016. Cited on 75, 86, 107

[106] P. Lecoq, E. Auffray, S. Brunner, H. Hillemanns, P. Jarron, A. Knapitsch, T. Meyer, and F. Powolny, "Factors influencing time resolution of scintillators and ways to improve them," *IEEE Transactions on Nuclear Science*, vol. 57, no. 5, pp. 2411–16, 2010. Cited on 77, 108, 148

[107] M. Kronberger, E. Auffray, and P. Lecoq, "Determination of the absolute light yields of LuYAP and LYSO," in *IEEE Nuclear Science Symposium Conference Record*, 2008, pp. 1153–1157. Cited on 77

[108] M. Moszynski, M. Kapusta, M. Mayhugh, D. Wolski, and S. Flyckt, "Absolute light output of scintillators," *IEEE Transactions on Nuclear Science*, vol. 44, no. 3, pp. 1052–61, 1997. Cited on 77

[109] J. S. Salacka and M. K. Bacrania, "A comprehensive technique for determining the intrinsic light yield of scintillators," *IEEE Transactions on Nuclear Science*, pp. 901–909, 2010. Cited on 77

[110] J. de Haas, P. Dorenbos, and C. van Eijk, "Measuring the absolute light yield of scintillators," *Nuclear Instruments and Methods in Physics Research A*, vol. 537, pp. 97–100, 2005. Cited on 77

[111] X. Yang, E. Downie, T. Farrell, and H. Peng, "Study of light transport inside scintillation crystals for PET detectors," *Physics in Medicine and Biology*, pp. 2143–2161, 2013. Cited on 78, 81

[112] J. Schouwenberg, "Technical report of the CERN Summer School program 2014: Developing a beta source based setup for pixel sensor characterization." 2014. Cited on 83

[113] A. Knapitsch, E. Auffray, G. Barbastathis, C. Chevalier, C.-H. Hsieh, J.-G. Kim, S. Li, M. S. J. Marshall, R. Mazurczyk, P. Modrzynski, V. Nagarkar, I. Papakonstantinou, B. Singh, A. Taylor, and I. Paul Lecoq, Fellow, "Large scale production of photonic crystals on scintillators," *IEEE Transactions on Nuclear Science*, vol. 63, no. 2, pp. 639–43, 2016. Cited on 86

[114] A. Knapitsch and P. Lecoq, "Review on photonic crystal coatings for scintillators," *International Journal of Modern Physics A*, vol. 29, no. 30, p. 1430070, 2014. [Online]. Available: http://www.worldscientific.com/doi/abs/10.1142/S0217751X14300701 Cited on 86

[115] S. E. Derenzo, M. J. Weber, W. W. Moses, and C. DuJardin, "Measurements of the intrinsic rise times of common inorganic scintillators," *IEEE Transactions in Nuclear Science*, vol. 47, pp. 860–864, 2000. Cited on 89

[116] D. N. ter Weele, D. R. Schaart, and P. Dorenbos, "Intrinsic scintillation pulse shape measurements by means of picosecond x-ray excitation for fast timing applications," *Nuclear Instrument and Methods A*, vol. 767, pp. 206–211, 2014. Cited on 90

[117] W. Eadie, D. Drijard, F.James, M. Roos, and B. Sadoulet, *Statistical Methods in Experimental Physics.* North-Holland, 1971. Cited on 91

[118] S. C. Blankespoor, S. E. Derenzo, W. W. Moses, M. Ito, and K. Oba, "Characterization of a pulsed x-ray source for fluorescent lifetime measurements," in *1993 IEEE Conference Record Nuclear Science Symposium and Medical Imaging Conference*, Oct 1993, pp. 9–13. Cited on 106

[119] M. A. Spurrier, P. Szupryczynski, K. Yang, A. A. Carey, and C. L. Melcher, "Effects of Ca^{2+} co-doping on the scintillation properties of LSO:Ce," *IEEE Transactions on Nuclear Science*, vol. 55, no. 3, pp. 1178–1182, June 2008. Cited on 107, 148

[120] S. Liu, X. Feng, Z. Zhou, M. Nikl, Y. Shi, and Y. Pan, "Effect of Mg^{2+} co-doping on the scintillation performance of LuAG:Ce ceramics," *pss (RRL) Rapid Research Letters*, vol. 8, no. 1, pp. 105–109, 2014. [Online]. Available: http://dx.doi.org/10.1002/pssr.201308199 Cited on 107, 148

[121] P. Dorenbos, "Fundamental limitations in the performance of Ce^{3+}, Pr^{3+}, and Eu^{2+} activated scintillators," *IEEE Transactions on Nuclear Science*, vol. 57, no. 3, pp. 1162–1167, June 2010. Cited on 107, 109, 148

[122] S. E. Brunner, L. Gruber, J. Marton, K. Suzuki, and A. Hirtl, "Studies on the Cherenkov effect for improved time resolution of TOF-PET," *IEEE Transactions on Nuclear Science*, vol. 61, no. 1, pp. 443–447, Feb 2014. Cited on 108, 148

[123] S. Korpar, R. Dolenec, P. Križan, R. Pestotnik, and A. Stanovnik, "Study of TOF-PET using Cherenkov light," *Physics Procedia*, vol. 37, pp. 1531 – 1536, 2012, proceedings of the 2nd International Conference on Technology and Instrumentation in Particle Physics (TIPP 2011). [Online]. Available: http://www.sciencedirect.com/science/article/pii/S1875389212018718 Cited on 108, 148

[124] S. Omelkov, V. Nagirnyi, A. Vasil'ev, and M. Kirm, "New features of hot intraband luminescence for fast timing," *Journal of Luminescence*, vol. 176, pp. 309 – 317, 2016. [Online]. Available: http://www.sciencedirect.com/science/article/pii/S0022231316301004 Cited on 108, 148

[125] R. T. Williams, J. Q. Grim, Q. Li, K. B. Ucer, and W. W. Moses, "Excitation density, diffusion-drift, and proportionality in scintillators," *physica status solidi (b)*, vol. 248, no. 2, pp. 426–438, 2011. [Online]. Available: http://dx.doi.org/10.1002/pssb.201000610 Cited on 109

[126] L. T. Kunneman, M. D. Tessier, H. Heuclin, B. Dubertret, Y. V. Aulin, F. C. Grozema, J. M. Schins, and L. D. A. Siebbeles, "Bimolecular Auger recombination of electron-hole pairs in two-dimensional CdSe and CdSe/CdZnS core/shell nanoplatelets," *The Journal of Physical Chemistry Letters*, vol. 4, no. 21, pp. 3574–3578, 2013. [Online]. Available: http://dx.doi.org/10.1021/jz401970p Cited on 109

[127] F. G. Santamaría, Y. Chen, J. Vela, R. D. Schaller, J. A. Hollingsworth, and V. I. Klimov, "Suppressed Auger recombination in giant nanocrystals boosts optical gain performance," *Nano Letters*, vol. 9, no. 10, pp. 3482–3488, 2009, pMID: 19505082. [Online]. Available: http://dx.doi.org/10.1021/nl901681d Cited on 109, 110, 143, 149

[128] A. W. Achtstein and et al, "Electronic structure and exciton-phonon interaction in two-dimensional colloidal CdSe nanosheets," *Nano Lett.*, vol. 12, pp. 3151–3157, 2012. Cited on 111

[129] G. Rainò, I. Moreels, A. Hassinen, T. Stöferle, Z. Hens, and R. F. Mahrt, "Exciton dynamics within the band-edge manifold states: The onset of an acoustic phonon bottleneck," *Nano Letters*, vol. 12, no. 10, pp. 5224–5229, 2012, pMID: 23016932. [Online]. Available: http://dx.doi.org/10.1021/nl302390b Cited on 117

[130] H. Htoon, A. V. Malko, D. Bussian, J. Vela, Y. Chen, J. A. Hollingsworth, and V. I. Klimov, "Highly Emissive Multiexcitons in Steady-State Photoluminescence of Individual Giant CdSe/CdS Core-Shell Nanocrystals," *Nano Letters*, vol. 10, no. 7, pp. 2401–2407, 2010, pMID: 20515013. [Online]. Available: http://dx.doi.org/10.1021/nl1004652 Cited on 117

[131] J. Grim, "Technical report of the STSM FAST COST action TD1401: Ultrafast timing using shape-controlled colloidal nanocrystals." Cited on 124, 126, 161

[132] P. Lecoq, "Metamaterials for novel x- or gamma-ray detector designs," in *2008 IEEE Conference Record Nuclear Science Symposium and Medical Imaging Conference*, vol. 680, 2008, pp. 07–1. Cited on 130

[133] S. E. Derenzo, M. J. Weber, and M. K. Klintenberg, "Temperature dependence of the fast, near-band-edge scintillation from CuI, HgI_2, PbI_2, ZnO:Ga and CdS:In," *Nuclear Instrument and Methods A*, vol. 486, no. 12, pp. 214 – 219, 2002. [Online]. Available: http://www.sciencedirect.com/science/article/pii/S0168900202007052 Cited on 137

[134] L. Procházková, V. Čuba, J. Mrázek, A. Beitlerová, V. Jarý, and M. Nikl, "Preparation of Zn(Cd)O:GaSiO2 composite scintillating materials," *Radiation Measurements*, vol. 90, pp. 59 – 63, 2016. [Online]. Available: http://www.sciencedirect.com/science/article/pii/S1350448715301190 Cited on 137, 149

[135] E. A. McKigney, R. E. D. Sesto, L. G. Jacobsohn, P. A. Santi, R. E. Muenchausen, K. C. Ott, T. M. McCleskey, B. L. Bennett, J. F. Smith, and D. W. Cooke, "Nanocomposite scintillators for radiation detection and nuclear spectroscopy," *Nuclear Instrument and Methods A*, vol. 579, pp. 15–18, 2007. Cited on 144

[136] K. Shibuya, M. Koshimizu, H. Murakami, Y. Muroya, Y. Katsumura, and K. Asai, "Development of ultra-fast semiconducting scintillators using quantum confinement effect," *Japanese Journal of Applied Physics*, vol. 43, no. 10B, pp. L1333–L1336, 2004. Cited on 144

[137] S. Kishimoto, K. Shibuya, F. Nishikido, M. Koshimizu, R. Haruki, and Y. Yoda, "Subnanosecond time-resolved x-ray measurements using an organic-inorganic perovskite scintillator," *Applied Physics Letters*, vol. 93, no. 26, 2008. [Online]. Available: http://scitation.aip.org/content/aip/journal/apl/93/26/10.1063/1.3059562 Cited on 144

[138] R. M. Turtos, S. Gundacker, M. T. Lucchini, L. Procházková, V. Čuba, H. Burešová, J. Mrázek, M. Nikl, P. Lecoq, and E. Auffray, "Timing performance of ZnO:Ga nanopowder composite scintillators," *physica status solidi (RRL) Rapid Research Letters*, vol. 10, no. 11, pp. 843–847, 2016. [Online]. Available: http://dx.doi.org/10.1002/pssr.201600288 Cited on 145, 150

Appendix A

Rise time measurements of the garnet's family

The measurements performed with the following crystals are considered as preliminary results. The calibration file used for fitting the data is not specific for each crystal emission and a generic calibration file which integrates white light is used instead. For this reason, some of the values related to different rise time components might change making the abundance of each component not relevant. However, the improvement seen in the rise time of Mg^{2+} co-doped samples is remarkable. Scintillating crystals as LuAG, GaGG and YAG have a very slow rise time of the order of few nanoseconds, which is dependent on the Ce^{3+} concentration. Co-doping with Mg^{2+} reduces the slowest rise time components from O(1)ns to O(100)ps leading to a time response as fast the one presented in LSO:Ce Ca^{2+} crystals. Figure A.1 illustrates the difference in time profile of a YAG:Ce(0.5%) (left) and a YAG:Ce(0.5%) co-doped with Mg^{2+} (3000 ppm) (right) crystals, where the τ_{r1} is reduced from 272 ps to 21 ps and τ_{r2} from 2.7 ns to 146 ps.

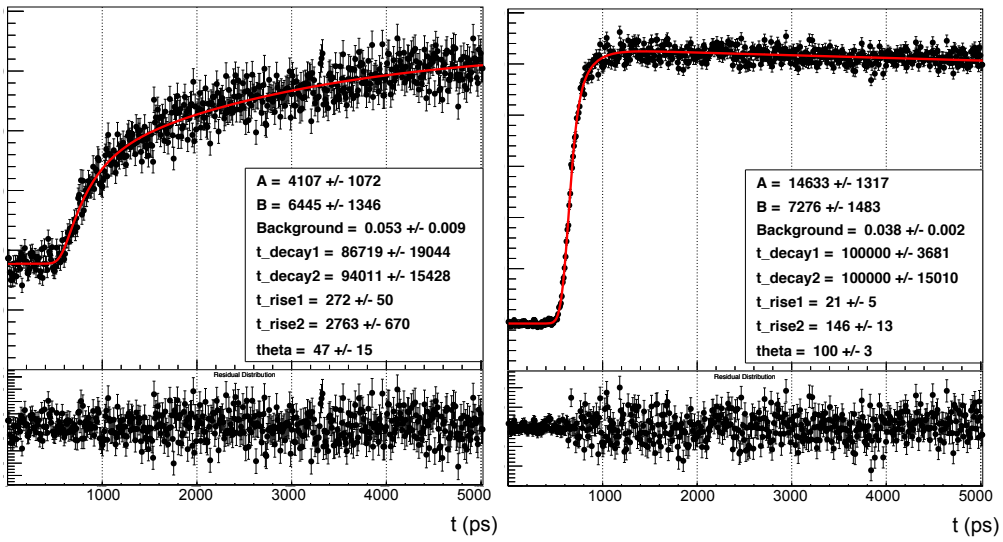

Figure A.1: Time-resolved scintillating signal in the 5 ns gate measured for a YAG:Ce(0.5%) (left) and a YAG:Ce(0.5%) co-doped with Mg^{2+} (3000 ppm) (right)

A summary of the results is present in Table A.1. The measurements with an IRF of 600 ps were measured with a gate of 20 ns in order to resolve the long component. The two measurements with IRF of 134 ps (5 ns gate) and 600 ps (20 ns gate) should be taken as complementary. The first one to resolve τ_{r1} and the second one to determine τ_{r2}. The IRF dependence with the sweeping range is one of the weakness of the streak camera.

Table A.1: **Rise time of different garnets Ce^{3+} doped scintillators with and without Mg^2 co-doping**.

Crystal	IRF	τ_{r1}	τ_{r2}
LuAG:Ce (0.3%) 128	134 ps	82 ± 21 ps	835 ± 106 ps
LuAG:Ce (0.3%) 128	600 ps	0 ± 150 ps	713 ± 245 ps
LuAG:Ce (0.5%) 2952	134 ps	292 ± 48 ps	2757 ± 801 ps
LuAG:Ce (0.5%) 2952	600 ps	479 ± 87 ps	5020 ± 100 ps
LuAG:Ce (0.5%) Mg (3000 ppm) 2953	134 ps	30 ± 7 ps $40 \pm 4\%$	242 ± 7 ps $60 \pm 2\%$
LuAG:Ce (0.5%) Mg (6000 ppm) 2963	134 ps	0 ± 5 ps $27 \pm 2\%$	185 ± 60 ps $73 \pm 11\%$
YAG:Ce (0.5%) 2954	134 ps	272 ± 50 ps $39 \pm 10\%$	2763 ± 670 ps $61 \pm 13\%$
YAG:Ce (0.5%) 2954	600 ps	463 ± 59 ps $49 \pm 8\%$	4015 ± 374 ps $51 \pm 3\%$
YAG:Ce (0.5%) Mg (3000 ppm) 2955	134 ps	21 ± 5 ps $67 \pm 6\%$	146 ± 13 ps $33 \pm 7\%$
YAG:Ce (0.5%) Mg (6000 ppm) 2964	134 ps	37 ± 7 ps $82 \pm 7\%$	263 ± 48 ps $18 \pm 16\%$
GaGG:Ce 2586	134 ps	151 ± 18 ps $64 \pm 5\%$	2164 ± 551 ps $36 \pm 10\%$
GaGG:Ce 2975	134 ps	320 ± 45 ps $34 \pm 4\%$	5248 ± 1063 ps $66 \pm 19\%$
GaGG:Ce 2975	600 ps	0 ± 17 ps $42 \pm 16\%$	6842 ± 735 ps $58 \pm 8\%$
GaGG:Ce Mg 2978	134 ps	0 ± 8 ps	219 ± 14 ps

Appendix B

Spectral-time resolved measurements using the C10910 Universal streak camera.

B.1 Protocol to align the 2 lenses-2 mirrors optical system and operate the X-ray tube.

1. Place the sample (preferably a scintillating crystal with dimensions of $2\times2\times10$ mm^3) in front of the X-ray windows, as close as possible to the tube. The axis defining the shortest dimension, 2 mm in this case, should be placed in the direction of collection of the first lens.
2. Put safety goggles on.
3. Make sure the flipping mirror is up before turning on the laser.
4. Illuminate the sample with the laser. The laser beam should pass through the center of a 10 cm focal length biconvex lens and reach the sample in a point near the center of the X-ray window.
5. Check the height of the system by placing the reference laser in the box and confirming both laser points coincide in the same spot of the sample. Remove pointer laser. The photocathode of the streak camera is placed at 16 cm from the table floor.
6. Project the image coming from the sample into the spectrograph slit, guiding the light through 2 lenses and 2 mirrors:
    - Place the 6 cm focal length lens in front of the point illuminated by the laser. Project the parallel beam created by the lens at the center of the first mirror.
    - Make the first mirror parallel to the second mirror, in a way that the parallel beam pass through the center of the 15 cm focal length lens.
    - If placed in line with the spectrograph slit, the 15 cm focal length lens will focus down the parallel beam into the streak camera.
    - Use the streak camera focus mode to optimize the signal, finding precisely the focal spot and moving it into the first slit. A bigger signal will be visible at the display. Reduce spectrograph and streak camera slit if needed.

7. If the system is already aligned, when changing samples, just find the focal spot by moving back and forth one of the translating stages.

8. After the optimization of the signal, make sure the laser is off, flip down the mirror and turn laser on. Make sure the photocathode of the tube is homogeneously illuminated and remove the laser filter if needed.

9. Close the box and start acquiring data.

10. When measurement is over, turn off the laser and the X-ray tube. Put MCP gain down to zero and close both slits before opening the box.

B.2 Safety issues concerning the streak camera operation

1. Do not remove the filter laser. If you have to measure UV emission please be completely aware that if the laser shines into the spectrograph slit and you have wide open slits you can burn the photocathode of the streak camera. The laser is so intense that you might see it even with when the manual slit is at the zero μm position.

2. Do not open the box intermediately after turning OFF the X-ray tube. Remember to press F8 to automatically close the shutter or close the slit manually. The X-ray measurements are usually done with wide open slits (spectrograph and streak camera). If you open the box with wide open slits, the streak camera photocathode will saturate intermediately. If the light source if too bright you can burn the photocathode.

3. The X-ray tube Beryllium window is placed at around 1 cm from the output window. Therefore, placing crystals or any other sample in front of the X-ray tube has to be done with extreme precaution.

4. The X-ray tube photocathode is placed very close to the lens used to dis-focus the laser beam. The manipulation of this lens has to be done with extreme caution, making sure is always fixed to the optical table. The use of screwdrivers and/or any other tool near the photocathode zone should be avoided unless the lens needs to be changed.

5. Do not use the X-ray tube unnecessarily, its a has a finite lifetime.

6. The laser spot reaching the X-ray tube photocathode should be of the same than the active area ($\sim$ 1 cm in diameter). If the laser spot is not defocus properly the photocathode will age in-homogeneously.

7. When doing the warm-up of the tube, please make sure there is some light shining into the photocathode.

8. The use of safety goggles is mandatory meanwhile aligning and/or the laser is ON

9. The laser box should be placed at a height where is always visible whether is ON or OFF.

10. The streak camera slit should remain closed if the system is not in operation. From time to time the images taken with 5 μm slit aperture will show up with a line pattern characteristic of dust particles in the slit. If this happens the slit should be cleaned following this procedure:

- Make sure the streak camera is off (shutter closed). All the manipulations explained below must be done very carefully. The pieces should not be dropped or hit by any means.
- Loosen up the wheel connecting the spectrograph with the streak camera slit as shown in the picture by the solid arrow. Unscrew all the way to the left and disconnect the spectrograph from the rest by pulling softly the black rings towards the spectrograph. A gap will open in the position marked by the dashed arrow.

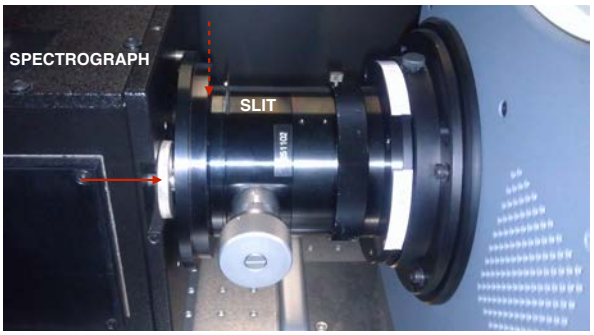

- Unscrew the fours screws marked in the picture. Remove all the central piece and place it in a safe surface.

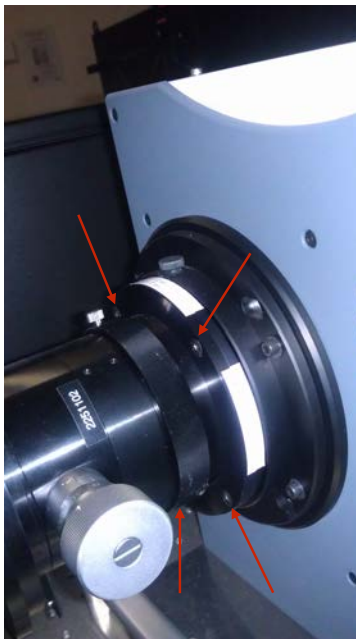

- Now, loosen up 3 screws as the ones marked in the following picture. It is very important that the screws that will be loosen up are the ones closer to the slit. The screws marked with the DO NOT TOUCH label are the ones aligning the optics between slit and the photocathode streak. If by any chance these screws are loosen up the streak camera must be send to Hamamatsu. Loosen up the screws to the left of the picture will disconnect the slit piece from the rest. Handle with careful both pieces.
- Take the slit central piece and use paper for optical lenses with some alcohol to clean the sharp blades of the slit. Do not touch the slit with your fingers or any metallic device.

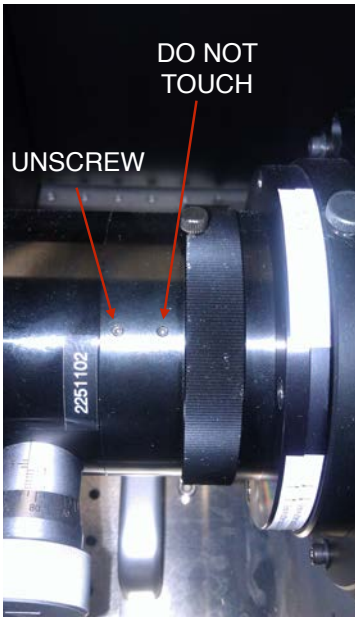

- Once everything is clean, proceed to put everything back together in the right order. Do not connect the spectrograph with the central piece yet.
- First, you should fix the entire central piece to the streak camera and make sure the photocathode and the slit are horizontally aligned. You should turn on the streak camera and in Focus mode align the emission with a horizontal line placed in the middle image.
- Once the emission is horizontal you can tighten up the 3 screws which are closer to the streak and put back the spectrograph in its original position.

11. Do not remove any box and/or tool from the streak camera room. The spectrograph and the streak camera need the original packaging to be send back to the producers if calibration and/or reparation is required.